Alma Mater Studiorum · Università di Bologna

DOTTORATO DI RICERCA IN
Automatica e Ricerca Operativa

Ciclo   XXVIII

Settore Concorsuale di Afferenza: 09/G1
Settore Scientifico Disciplinare: ING-INF/04

Online Trajectory Planning
for Vibration Suppression
and Perfect Tracking

Presentata da: **LORENZO MORIELLO**

Coordinatore di Dottorato: Relatore:
Chiar.mo Prof.   **Chiar.mo Prof.**
DANIELE VIGO   **CLAUDIO MELCHIORRI**

Correlatore:
Prof.
LUIGI BIAGIOTTI

Esame Finale Anno 2016

Online Trajectory Planning for Vibration Suppression
and Perfect Tracking

by

Lorenzo Moriello

Submitted to the

Department of Electrical, Electronic and Information Engineering (DEI),

in partial fulfillment of the requirements
for the degree of

Ph.D on Automatic Control and Operational Research

Abstract

In this thesis the problem of trajectory planning for automatic machines is addressed, considering in particular the problem of vibration suppression and perfect tracking. In particular two novel trajectory generators based on dynamic filters are developed and implemented. The proposed trajectory planners are designed respectively for residual vibrations suppression and perfect tracking of periodic trajectories. Both solutions are very effective and easy to implement, exploiting the realization of dynamic filters by means of FIR filters.

In the first part of the thesis the problem of residual vibrations in motion control of robots is addressed, pointing out the need to eliminate vibrations to achieve high performance. Chapters 1 to 4 report the most widespread feed-forward techniques for residual vibration suppression such as Input Shaping, filtering, system dynamic inversion and proper trajectory planning. In a review fashion all these techniques are analyzed in detail and implemented in simulation to verify the effect of vibration reduction on a typical second order system. Moreover all the analysis are performed with a control system perspective in order to give a unified point of view allowing to compare all the solutions despite their differences.

Then in Chapter 5 a novel trajectory generator based on Exponential Filters is presented, analyzed and compared with the most commonly used feed-forward techniques for vibration suppression, proving comparable performances with the state of the art. The analysis and comparison procedure is performed both in simulation and in experimental activities. In particular this new method is developed first for simple SISO LTI systems and then extended to MIMO systems showing great effectiveness ranging from simple elastic transmissions up to robotic arms with compliant joints.

In Chapter 6 a new repetitive control scheme based on B-Spline Trajectory Generator that exploits dynamic filters is presented. The novel scheme integrates the trajectory generator and the repetitive controller in a single discrete time feedback loop achieving perfect tracking for periodic motions. Tracking performance and stability are demonstrate both analytically and experimentally showing also a considerable ease of implementation even on commercial robotic devices with unaccessible factory controller.

In appendix A, a more technologically oriented activity is reported, concerning on the development of a 6-axis Force/Torque sensor for underwater activities based on optoelectronic components. The description covers the entire process from the concept to the development of a simulation model and finally to the prototype realization. Also the experimental activities about calibration and performance evaluation are presented, paying much attention on how different solutions adopted for sealing the sensor affect the performances.

Thesis Supervisor: Prof. Claudio Melchiorri

"Anyone who stops learning is old,

whether at twenty or eighty.

Anyone who keeps learning stays young.

The greatest thing in life is to keep your mind young."

Henry Ford

Acknowledgments

At the end of a journey the results we get are never just because of our own ability, but also of people and events that happen along the way. For this reason I want to thank Prof. Claudio Melchiorri for bringing me to undertake this journey and giving me the resources and the tools to carry it through to the best I could do. My sincere thanks also goes to Luigi and Gianluca who have followed me in the different phases of my work and taught me not only notions but also a working method.
Of course all of this wouldn't have been sufficient without the ongoing support of my family, a silent support but tremendously effective. At the same time nothing would have been the same without Chiara, which in five years by my side never missed a chance to push me to give my very best. Finally thanks to all the friends who accompanied me all the way here, especially the LAR crew, with whom every drama is resolved with a good laugh and any insane idea becomes a business plan. In short, if I came up here it is thanks to all of you.

Lorenzo

Contents

Chapter 1

Feed-Forward Techniques for Vibration Suppression

Reducing vibrations has always been a key issue in automation. In general, vibrations are due to the motion itself since moving any inertial load could excite the resonant frequencies of the body structures. This is a very undesirable condition since it affects both the accuracy of the control system and the reliability of the structures. Typically this problem was roughly avoided by slowing down any motion, especially in older automatic machines which handle large inertias. Obviously this was not sufficient, also lightening of robot's structures, reducing frictions and the introduction of elastic elements in the transmissions have made vibrations a more and more relevant issue. Moreover the demand for ever faster motions led to the development of methods that aims to reduce vibrations without compromising performances.

In literature both feedback and feed-forward schemes have been proposed in order to suppress vibrations and among these, methods based on feed-forward action are of great relevance. Feed-forward schemes are used to shape the command input, that usually is a step, in order to provide a proper trajectory that minimizes both vibrations and duration of the motion. The major advantage of this approach is that it can be applied on any controlled system since it doesn't need any change on the control architecture or additional sensors.

Earliest forms of command shaping were mechanical design techniques of high-speed

cams. A huge literature refers to design methods of cam profiles based on proper motion shaping in order to avoid the excitement of system resonances [66].

Focusing on control techniques, one of the first attempts was the posicast control developed in the 1950's [95, 100, 96]. The method consists of exciting several transient oscillations of the system, splitting up the input command into several fragments properly delayed in time. In this way if the resultant sum of the transient oscillations is zero, one can obtain a deadbeat step response from a very lightly damped system. Unfortunately at that time digital controllers were just born and the implementation of posicast control schemes could only be carried out with discrete elements and delay lines. As a result implementing those schemes was a challenging task, mainly for lack of robustness.

A well-known technique for minimizing the residual vibration in point-to-point motions is represented by input shaping [86, 106]. Basically it is a filtering technique where the reference command is convolved with a train of properly designed impulses, resulting a shaped command that aims to reduce or suppress residual vibration in a controlled plant. The theory and the concept behind input shaping were exactly the same of posicast control, but only in late 1980's this technique become very popular. This was mainly due to a discrete time reformulation and analysis, plus the possibility to easily implement input shapers with digital controllers. Input shapers have been successfully used in a number of practical applications, such as reduction of crane oscillations, [42], control of industrial machines like XY stages, [34], vibration suppression in flexible robotic arms, [59]. A deep review of input shapers is presented in Chapter 2.

Alternative approaches for vibrations reduction by means of command shaping are based on low-pass and notch filters, expressed either as finite or infinite impulse response filters. In this case the method is quite simple and rely on filtering those spectral components of the command input that could excite system resonances, but it is worth noticing that filters do not guarantee complete vibration cancellation [90]. A technique that assures residual vibrations suppression exploits the dynamic inversion of a flexible plant [79]. This approach lead to a vibration free motion but the

2

need of the complete knowledge on the plant system made it not so attractive for practical applications.

More recently, methods for vibration reduction directly based on a proper definition of the reference signal have been presented, see [52, 13, 7]. These techniques rely on the limitation of jerk impulses, whose duration must be carefully chosen on the basis of the dynamics characteristics of the resonant system. Constant jerk trajectories are the simplest example of this approach, but they assure complete vibration cancellation only in case of totally undamped plants. An improvement has been presented in [7], where asymmetric jerk profiles are used to take into account the damping coefficient of the flexible system. This approach, which has been generalized and improved, will be discussed in Chapter 5.

1.1   Modelling Vibratory System

The problem of residual vibrations affects very different kind of machines. In order to evaluate the features and the effects of any method for vibration suppression, the motion system shown in Fig. 1-1 can been considered because of its significance in the industrial field, where a number of applications can be modeled in this way: a properly controlled electric motor is used to actuate an inertial load, whose inertial coefficient is J_l, by means an elastic transmission lightly damped, characterized by an elastic constant k_t and a damping coefficient b_t [55, 6, 60]. By assuming that, because of the control, the actuator behaves like an ideal position source, i.e. $q_m(t) \simeq q_{ref}(t)$, only the mathematical model of the system describing the elastic linkage, which causes vibrations, and the load has been taken into account. It is a SISO (Single Input Single Output) LTI (Linear Time Invariant) system that can be modelled with the transfer function

$$G_{ml}(s) = \frac{Q_l(s)}{Q_m(s)} = \frac{2\delta\omega_n s + \omega_n^2}{s^2 + 2\delta\omega_n s + \omega_n^2} \tag{1.1}$$

with

$$\omega_n = \sqrt{\frac{k_t}{J_l}}, \quad \delta = \frac{b_t}{2\sqrt{k_t J_l}}$$

3

Figure 1-1: Lumped constant model of a motion system with elastic linkage (a) and related block-scheme representation (b).

where $Q_m(s) = \mathcal{L}\{q_m(t)\}$ and $Q_l(s) = \mathcal{L}\{q_l(t)\}$ are the Laplace transforms of the motor and load position, respectively. Note that the inertia J_m of the motor has no influence on this model. From (1.1), it follows that the dynamic relation between the motor position, supposed to be equal to the reference trajectory $q_{ref}(t)$, and the tracking error $\varepsilon(t)$ is

$$\frac{E(s)}{Q_{ref}(s)} = \frac{-s^2}{s^2 + 2\delta\omega_n s + \omega_n^2} \quad \Rightarrow \quad \frac{E(s)}{\ddot{Q}_{ref}(s)} = \frac{-1}{s^2 + 2\delta\omega_n s + \omega_n^2} \tag{1.2}$$

and where $E(s) = \mathcal{L}\{\varepsilon(t)\}$, $Q_{ref}(s) = \mathcal{L}\{q_{ref}(t)\}$ and $\ddot{Q}_{ref}(s) = \mathcal{L}\{\ddot{q}_{ref}(t)\}$.

As a matter of fact it can be noted that both transfer functions in (1.1) and (1.2) are of the form

$$F(s) = \frac{N(s)}{s^2 + 2\delta\omega_n s + \omega_n^2}$$

that is, the difference between the above equations rely on the numerator only, while the denominator refers always at the same complex conjugate poles couple. Indeed,

$$\delta = 0 \qquad\qquad \delta = 0.1$$

(a)

(b)

Figure 1-2: Step response (a) and Pole-Zero diagram (b) of the considered plant $G(s)$, with $\omega_n = 2\pi$ and with different damping value.

in terms of impulse response it can be proven that in general

$$f(t) = \left[Me^{-\delta\omega_n(t)}\right]\sin\left(\omega_n\sqrt{1-\delta^2}t + \phi\right),$$

where M and ϕ only depends on the numerator $N(s)$ that affects the amplitude and the initial phase of the impulse response. Therefore in lieu of simplicity and generality, an uncoupled linear vibratory systems it can be assumed modelled as a common second order SISO (Single Input Single Output) LTI (Linear Time Invariant) system plant

$$G(s) = \frac{\omega_n^2}{s^2 + 2\delta\omega_n s + \omega_n^2} \tag{1.3}$$

5

Such a system fed with a unitary impulse, produces a decaying sinusoidal response

$$y(t) = \left[\frac{\omega_n}{\sqrt{1 - \delta^2}} e^{-\delta \omega_n t} \right] \sin \left(\omega_n \sqrt{1 - \delta^2} t \right) \qquad (1.4)$$

where ω_n is the undamped natural frequency of the plant, δ is the damping ratio of the plant and t is time. Thus once the damping coefficient δ and natural frequency ω_n of the system are known, the system and accordingly its vibrating response is defined. In practical experience when the parameters are unknown, with standard procedures it is possible to directly deduce their values from the response of the plant to input signals that cause vibrations. For instance, the residual vibrations consequent to a step input are given by

$$\varepsilon_{step}(t) = -\frac{1}{\sqrt{1 - \delta^2}} e^{-\delta \omega_n t} \cos \left(\omega_n \sqrt{1 - \delta^2} \, t + \varphi_0 \right)$$

where $\varphi_0 = \arctan \left(\frac{\delta}{\sqrt{1-\delta^2}} \right)$. Therefore, if a measurement of the oscillation is available, it is sufficient to detect two subsequent peak values, as highlighted in Fig. 1-3(a), and compute the exponential decay and the time period of the oscillation as

$$T_0 = t_2 - t_1$$
$$\alpha = \frac{1}{T_0} \ln \left(\frac{p_2}{p_1} \right)$$

where the meaning of t_1, t_2, p_1, p_2 is explained in the figure. Note that the period of the oscillation and its decay rate depend on the system, and they do not change also if different type of reference inputs are considered. For instance, second order trajectories, with discontinuous acceleration, can be used in order to provide the actuator with a feasible trajectory and to avoid an excessive strain on the plant (see fig. 1-3(b)).

(a)

(b)
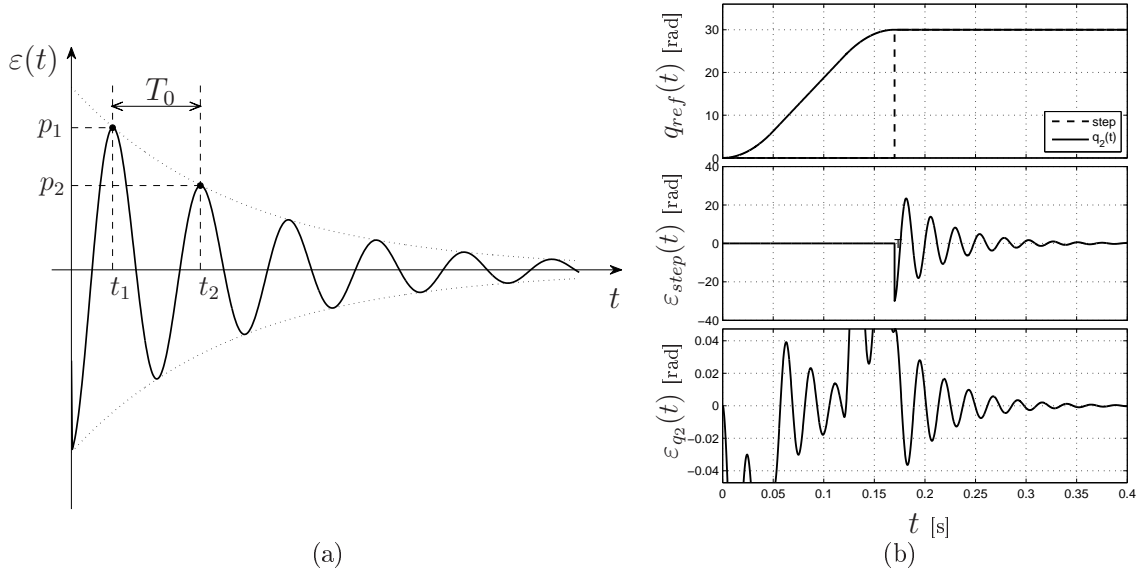
Figure 1-3: Residual vibrations caused by the applications of a step input to the system (1.3) (a) and comparison between residual vibrations caused by the application of a step input and of a second order trajectory $q_2(t)$ to a vibratory system G(s) (b).

Finally the parameters δ and ω_n can be made explicit by means of the relations

$$\alpha = -\delta\,\omega_n \tag{1.5}$$

$$T_0 = k\,\frac{2\pi}{\omega_n\sqrt{1-\delta^2}} \qquad\qquad k \in \mathbb{N}.$$

1.2   Performance Measurement of Command Shapers

Evaluating performances of any feed-forward technique, also referred as command shapers (CS), is a key factor in order to choose the proper solution for any given problem. As well as the many design solutions, in literature are proposed several review papers that suggest various points of view to compare different CS ([108, 47, 53] among many others). Besides the measurement of the magnitude of residual vibrations, several approaches take into account the duration of the shaped command (distortion), while others for example introduce benchmarks based on the energy content of residual vibrations.

7

1.2.1 Robustness

Typically the most important feature to evaluate CS performances is the robustness to errors in parameters definition. Since, usually, they are designed to nullify vibrations at a certain nominal frequency, in this way the focus is on the behaviour of an CS in the neighborhood of the nominal frequency. This is crucial because rarely the real plant parameters match the model's. Moreover, CS are often applied to already controlled plants whose parameters are unknown, and therefore to be estimated. Obviously the estimation by means of proper identification techniques involves uncertainties on model parameters and CS design is required to assure a certain level of robustness. The analysis of the robustness comes directly from the measurement of the residual vibration and its reduction by means of command shaping. First, Residual Vibration (RV) is defined as the measure of the maximum displacement of a response from equilibrium, from the time when the command ends. Traditionally, as maximum displacement is meant the magnitude of the dissipation envelope of the response, so RV refers to the value of that decaying envelope at the time when the shaped command ends. Starting from RV is possible to define the Percent Residual Vibration (PRV) as the ratio between Residual Vibrations from a shaped command and from an unshaped command

$$PRV = \frac{RV_s}{RV_u}. \tag{1.6}$$

Finally robustness is evaluated according to the PRV's sensitivity function to errors in parameters ω_n and δ, that represents the level of vibrations induced by a shaped command when applied to a system with different values of natural frequency or damping

$$PRV(\omega, \delta) = \frac{RV_s(\omega, \delta)}{RV_u(\omega, \delta)}. \tag{1.7}$$

It is worth noting that usually PRV refers directly to the function in (1.7) that is expressed in terms of percentage and normalized frequency or damping.

In fig. 1-4 a common PRV function with respect to errors in natural frequency is shown: the plot easily highlight the behaviour of the shaper in nominal condition ($\omega = \omega_n$) and for any other frequency.

8
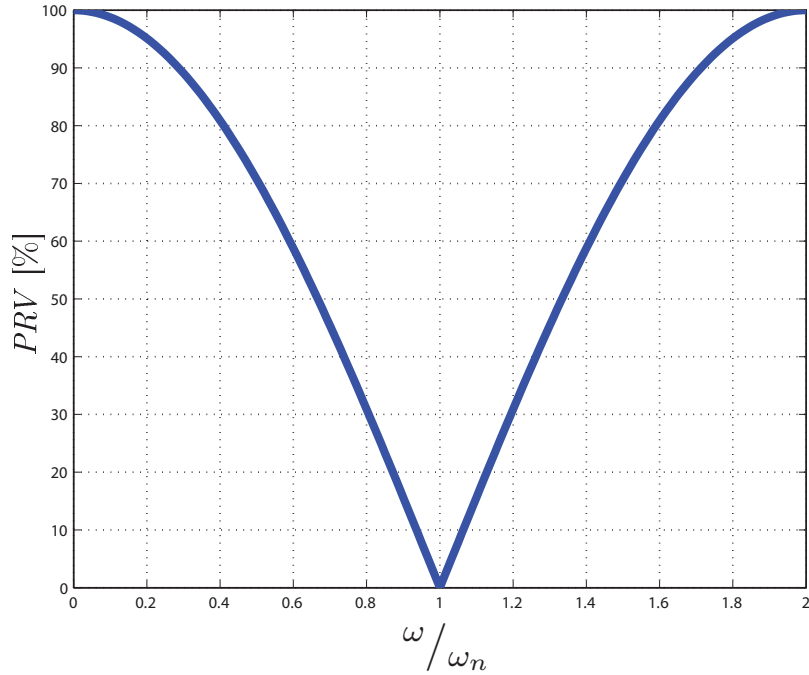
Figure 1-4: Typical Percent Residual Vibration function with respect to frequency variations.

1.2.2 Filter Based Approach

In (1.6) the PRV is given for a generic CS. However, a part from particular solutions that lead to a proper formula, the PRV function needs to analyse responses in time domain, therefore the calculation of the RV that could be tricky.

A very effective approach to evaluate the the PRV function exploits the analogy with the filter's theory. First, a completely undamped second order system $(\delta = 0)$ is considered, representing also the worst condition in terms of vibrations

$$G(s) = \frac{\omega_n^2}{s^2 + \omega_n^2}. \tag{1.8}$$

Moreover, $H(s)$ is the transfer function of a generic CS for the system in (1.8) and it is assumed to command an impulsive input to the system $G(s)$. From (1.6) in order to define the PRV function is required to calculate the value of RV in both shaped and unshaped case. Since the unshaped case is basically the impulse response and $G(s)$ an elastic undamped system, the result is simply a sinusoidal response with frequency ω_n, see fig. 1-5(a). Therefore RV_u is the amplitude of the sinusoidal response, $RV_u = X$.

9

Regarding the shaped case, RV_s refers to the amplitude of the vibration of the system response, at the time when the shaping effect of $H(s)$ ends. However, in fig. 1-5(b) is shown that the same system response could be obtained from the shaper $H(s)$, fed by a sinusoidal signal of frequency ω_n, thanks to the commutativity property of linear systems. In this way, recalling the theory on frequency response function of linear systems, is well known that for an asymptotically stable LTI system fed by a sinusoidal input, the output is a sinusoidal function as well, once completed an initial transient

$$y(t) = Y(\omega_n)\sin[\omega_n t + \varphi(\omega_n)], \tag{1.9}$$

where

$$Y(\omega_n) = XH(\omega_n) \tag{1.10}$$

with X the amplitude of the sinusoidal input and $H(\omega_n)$ the frequency response of $H(s)$ at frequency ω_n. This consideration is very useful since the mentioned transient lasts exactly the duration of the shaping effect, so the residual vibration can be determined by the frequency response, in particular

$$RV_s = Y(\omega_n)e^{j\varphi(\omega_n)} = X|H(j\omega_n)| \tag{1.11}$$

where X is the amplitude of the sinusoidal response of $G(s)$, but also $RV_u = X$ as stated before, so from (1.6) holds that

$$PRV = \frac{RV_s}{RV_u} = \frac{X|H(j\omega_n)|}{X} = |H(j\omega_n)|. \tag{1.12}$$

Finally the result result in (1.12) can be extended to the PRV's sensitivity function to errors in frequency parameter

$$PRV(\omega) = |H(j\omega)|. \tag{1.13}$$

The relation in (1.13) although valid to evaluate robustness with respect to frequency variations only, is quite important since it allows to connect a widely used tool for

10
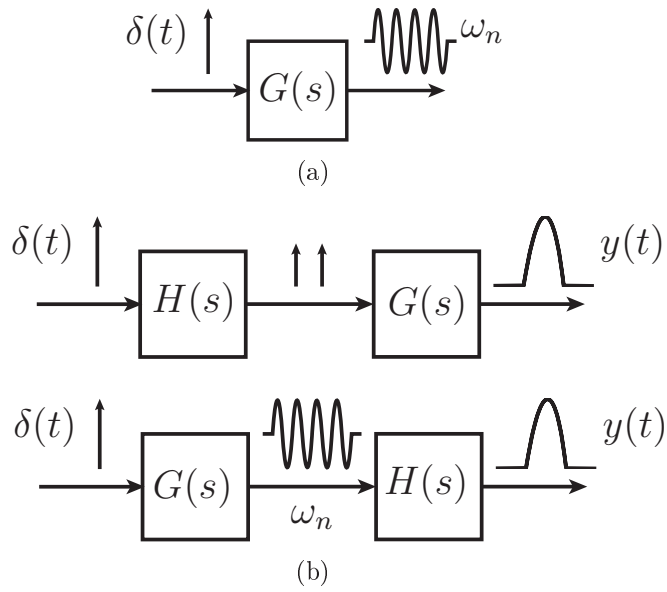
Figure 1-5: Definition of PRV for a typical elastic system with both unshaped (a) and shaped (b) command.
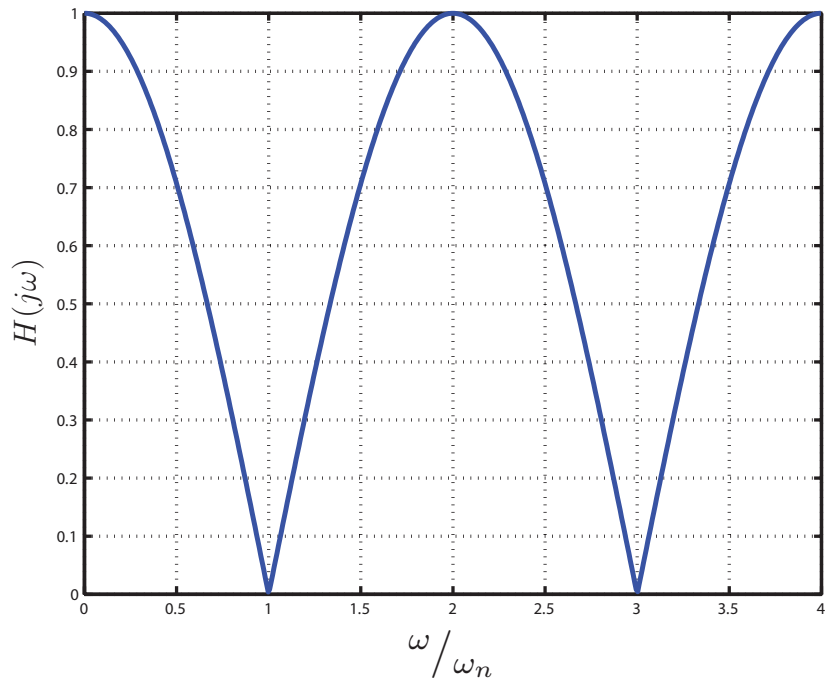
Figure 1-6: Frequency response of the input shaper $H(j\omega)$.

evaluating and design CS such as PRV function, and an analysis approach based on control system theory. Assuming to have a plant like in (1.8) and a common CS $H(z)$ whose PRV's sensitivity function to ω_n is like the one in fig. 1-4, if the amplitude axis were expressed in terms of PRV (i.e. from 0 to 1) instead of percentage of PRV, the result would be exactly the frequency response $H(j\omega)$ in fig. 1-6. Obviously this equivalence allows to consider CS like particular filters. Indeed, looking at the problem in the complex plane, the system (1.13) is described by a couple of complex conjugate poles at frequencies $\pm j\omega_n$. Therefore in order to nullify vibrations caused by the poles by means of a filter, it should have at least a couple of zeroes able to cancel the poles (see fig. 1-7), that is exactly what is described by $H(j\omega)$.

It has to be noted that besides the assumption of undamped system, these considerations allow to use filtering techniques to design CS even for generic systems with damping, since the design method based on the zero placement on the complex plane permit to easily adapt the shaper for any value of δ as will be discussed later. Moreover with respect to robustness, this discussion permit to assume frequency response as a preliminary tool for evaluation of command shapers. In fact it will be explained that the effect of damping on CS design is a simple frequency translation of the CS with $\delta = 0$.

Looking at fig. 1-8 the difference between damped and undamped case can be visualized on the complex plane with a couple of complex conjugate poles with $\delta = 0$ and $\delta \neq 0$. It is well known that for a given natural frequency, the effect of damping is simply a translation on a circular trajectory of radius ω_n, such that $\phi = \arccos \delta$.
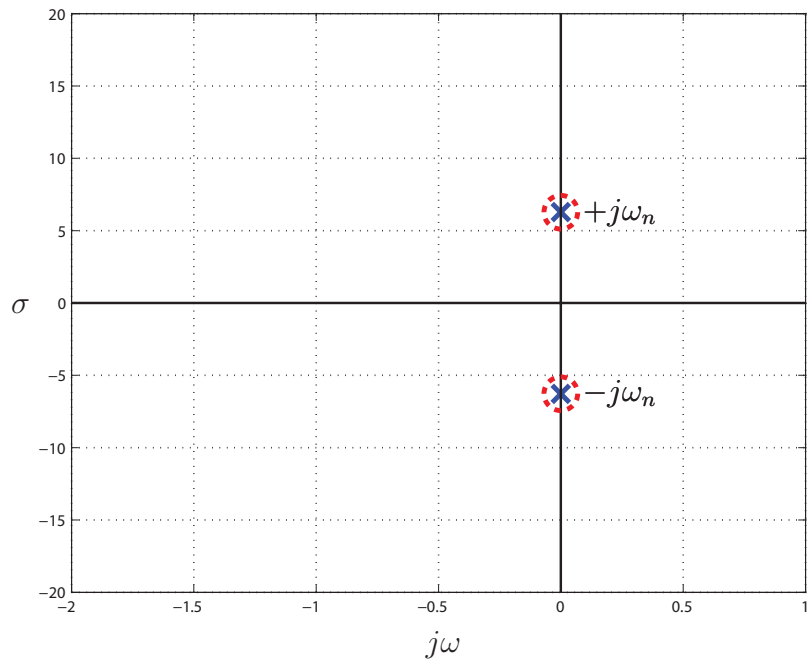
Figure 1-7: Shaper design using the complex plane: the poles of the system in (1.13) are reported in blue along with the desired zeroes (in red).
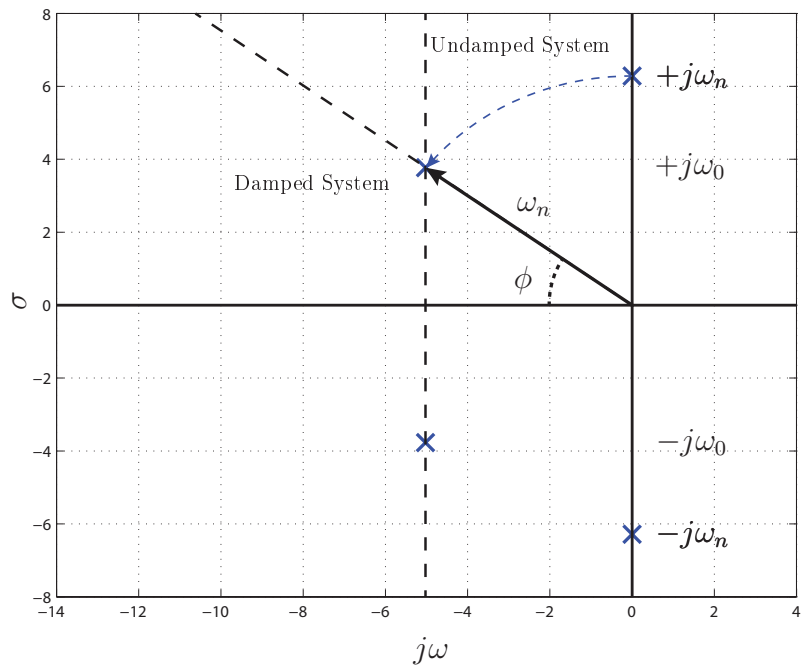
Figure 1-8: Effect of damping on a couple of complex conjugate poles in S-Plane.

Chapter 2

Input Shapers: a Review

2.1 Input Shaping Technique

Input shaping is one of the most popular command generation technique. Basically it is a filtering technique where the reference command is convolved with a train of properly designed impulses, resulting a shaped command that aims to reduce or suppress residual vibration in a controlled plant.

In order to understand how to cancel vibrations, a typical vibratory system as in Sec 1.1 has to be considered. In fig. 2-1 the system response to an impulse is reported according to the equation in (1.4), that is de facto the vibration that has to be cancelled. The easiest way to cancel the vibration is to add the same vibration in phase opposition, like as it is shown with a dashed line. Since any impulse can provide the same response in (1.4) with amplitude proportional to the impulse amplitude itself, it is clear that a second virtual vibration can be overposed to the first by applying a second command impulse properly delayed in time and with an amplitude that assure to eliminate the first vibration. In this way the desired command is split in two (or more) impulses that represents the shaped command. In particular the shaped command assures the completion of the motion within the end of the train of impulses and the vibration suppression at the end of the command.

The same result can be obtained analitically by exploiting the superposition property of linear systems. Being (1.4) the generic impulse response of a second order system
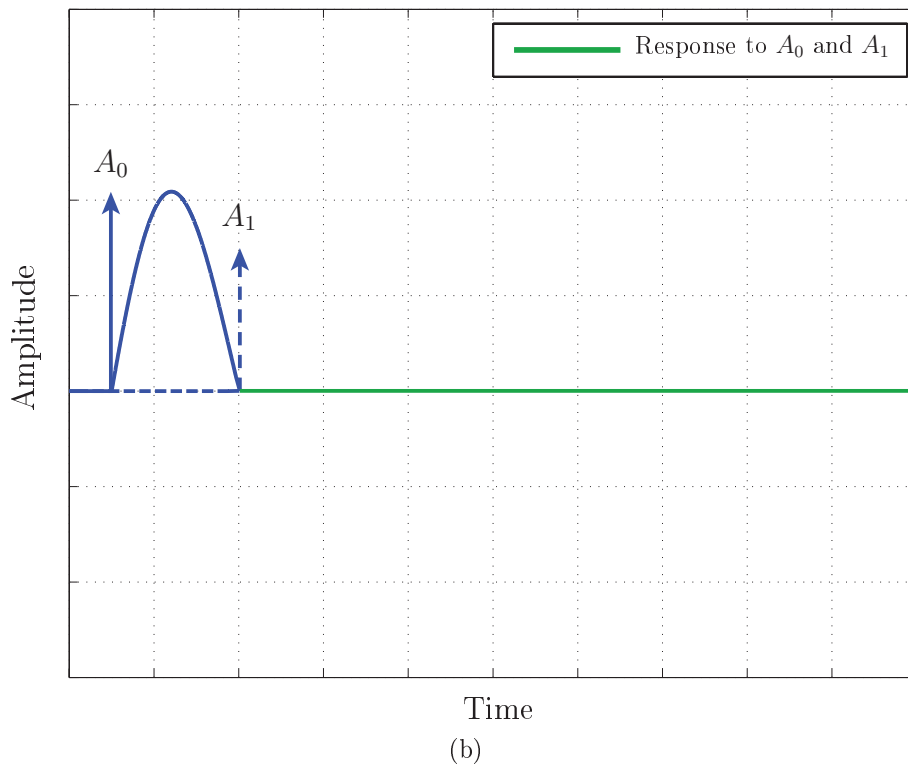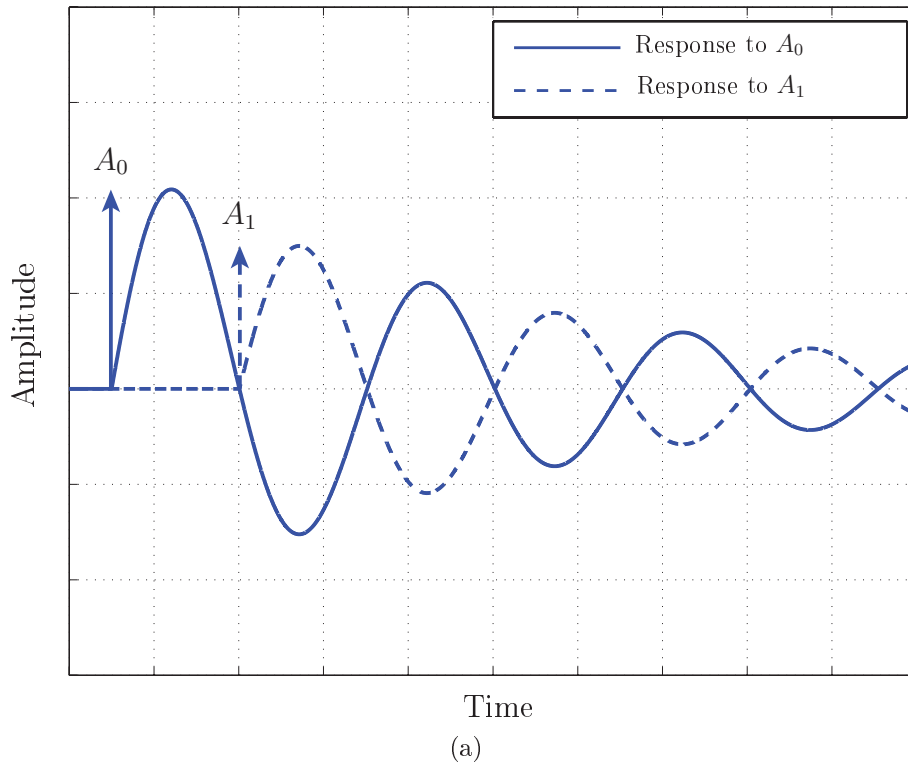
Figure 2-1: Impulse responses of the second order system and system response to the sequence of impulses A_0 and A_1 that cancel vibrations.

16

and known that for an LTI system holds that

$$B_0 \sin(\omega t + \phi_0) + B_1 \sin(\omega t + \phi_1) = B_{res} \sin(\omega t + \phi_{res}) \tag{2.1}$$

it is clear that the resultant output depends on the amplitude of the impulses and the time instants in which they are commanded. Moreover, in order to cancel vibration it is sufficient to assure that $B_{res} = 0$ after the last impulse. From (1.4) and (2.1) and generalizing for N impulses, results

$$B_{res} = \sqrt{\left(\sum_{j=0}^{N-1} B_j \cos \phi_j \right)^2 + \left(\sum_{j=0}^{N-1} B_j \sin \phi_j \right)^2}$$

where

$$B_j = A_j \frac{\omega_n}{\sqrt{(1 - \delta^2)}} e^{-\delta \omega_n (t_{N-1} - t_j)},$$

$$\phi_j = \omega_n \sqrt{1 - \delta^2} t_j$$

(2.2)

with A_j the amplitude of the j-th impulse, t_j the time of the j-th impulse and t_{N-1} the time of the last impulse of the shaped command. Further simplifications of (2.2) lead to the following conditions that assure complete residual vibration suppression for an N-impulses IS [85, 86]

$$\sum_{j=0}^{N-1} A_j e^{-\delta \omega_n (t_{N-1} - t_j)} \sin \left(t_j \omega_n \sqrt{(1 - \delta^2)} \right) = 0$$

$$\sum_{j=0}^{N-1} A_j e^{-\delta \omega_n (t_{N-1} - t_j)} \cos \left(t_j \omega_n \sqrt{(1 - \delta^2)} \right) = 0 \tag{2.3}$$

2.1.1 Robustness Analysis

The robustness analysis of an Input Shaper (IS) is usually given by means of the PRV function. However since a generic IS produces a train of N impulses and being the system response to any impulse of the type in (1.4), the RV can be easily calculated

as

$$RV = \frac{e^{-\delta \omega_n t_{N-1}}}{\sqrt{(1-\delta^2)}} \sqrt{C^2 + S^2} \tag{2.4}$$

where

$$
\begin{aligned}
C &= \sum_{j=0}^{N-1} A_j e^{\delta \omega_n t_j} \cos \left(t_j \omega_n \sqrt{(1-\delta^2)} \right), \\
S &= \sum_{j=0}^{N-1} A_j e^{\delta \omega_n t_j} \sin \left(t_j \omega_n \sqrt{(1-\delta^2)} \right)
\end{aligned}
\tag{2.5}
$$

with A_j the amplitude of the j-th impulse, t_j the time of the j-th impulse and $N-1$ refers to the last impulse of the command. Starting from RV is possible to define the Percent Residual Vibration as in (1.6), in particular PRV for IS is the ratio between RV's from a train of impulses and from a single unity magnitude impulse. From (2.4) and (1.6) descends

$$PRV = e^{-\delta \omega_n t_{N-1}} \sqrt{C^2 + S^2}, \tag{2.6}$$

where C and S are defined in (2.4).

Finally robustness is evaluated according to (1.7)

$$PRV(\omega, \delta) = e^{-\delta \omega t_{N-1}} \sqrt{[C(\omega, \delta)]^2 + [S(\omega, \delta)]^2}. \tag{2.7}$$

2.1.2 Vector Diagram Description of Input Shapers

Vector diagrams are graphical representations of impulse sequences, introduced in early papers dealing with IS [94, 89]. Basically a vector diagram is a description of the impulse train in polar coordinates that results quite useful in both design and evaluation of IS. In particular the diagram is created treating every impulse as a vector of norm equal to the impulse amplitude and angle θ_i such that

$$\theta_i = \omega t_i, \tag{2.8}$$

where t_i is the time of the impulse, as can be seen in fig. 2-2.
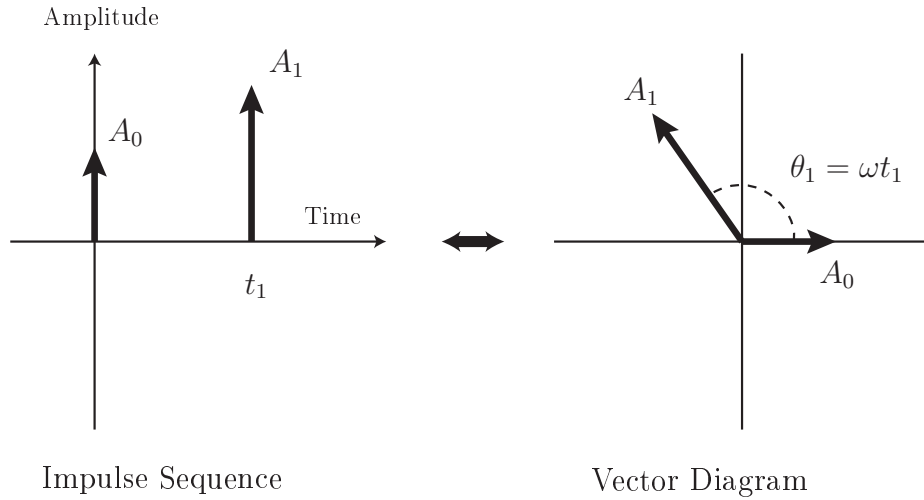
Figure 2-2:   Representation of an impulse sequence by means of vector diagram.

The vector diagram turns into an important tool for the design of IS if ω is chosen as the system frequency. Such a construction method permits to make interesting considerations on residual vibrations for a second order system fed by a shaped command from a generic N-impulses IS. That is, the resultant of the vectorial sum of all impulses has magnitude proportional to the amplitude of residual vibrations and angle equal to the phase of the vibratory response. Accordingly, both design and evaluation of IS can be obtained by means of geometrical analysis on vectors.

The first achievement is that for any train of N arbitrarily chosen impulses, it is always possible to define an IS with $N + 1$ impulses that guarantees zero residual vibration. Being

$$
\begin{aligned}
|R_N| &= \sqrt{|R_x|^2 + |R_y|^2}, \\
\theta_R &= \arctan \frac{R_y}{R_x}
\end{aligned}
\tag{2.9}
$$

with

$$
R_x = \sum_{i=0}^{N-1} A_i \cos \theta_i \quad \text{and} \quad R_y = \sum_{i=0}^{N-1} A_i \sin \theta_i
\tag{2.10}
$$

19
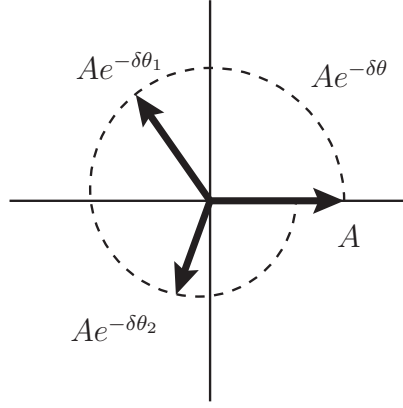
Figure 2-3: Effect of the scaling on the vector diagram for a damped system.

the resultant of a train of N impulses, vibration free motion is assured by adding one more impulse such that

$$|A_N| = |R_N|,$$
$$\theta_N = \theta_R + \pi.$$

(2.11)

It has to be noted that all these considerations are valid even in case of damped system by taking into account the damping effect on both angle and amplitude, that is introducing the effective amplitude $|A_{damp}|$ and frequency θ_{damp} in the above relations

$$|A_{damp}| = \frac{|A|}{e^{-\delta\theta}},$$
$$\theta_{damp} = \omega_n t \sqrt{1 - \delta^2}.$$

(2.12)

In particular the scaling of the amplitude is referred to the decay of the response to the first impulse at time zero, in order to take into account the same effective amplitude $|A_{damp}|$ for any impulse at a certain time t. Graphically the scaling can be represented on the vector diagram by superimposing the spiral $Ae^{-\delta\theta}$ like in fig. 2-3. Besides the calculation of a resultant that is proportional to the residual vibration amplitude, vector diagrams permit to easily work on robustness. This is thanks to the assumption that $\theta_i = \omega t_i$ which describes a rotation of the vectors depending on the frequency. In this manner the evaluation of robustness can be geometrically

20

performed by rotation of the vectors, moreover the design for particular sensitivity behaviours (asymmetric, humped, ...) can be achieved by imposing proper geometrical conditions.

The vector diagram approach also reveals a strong relationship between IS and filters. In fact considering $\delta = 0$, and being the impulse train described as vectors in polar coordinates it is possible to define a generic impulse as

$$\hat{A}_i = A_i e^{j\theta} = A_i e^{j\omega_n t}. \tag{2.13}$$

Therefore the resultant from a train of N impulses of an IS becomes

$$R_N = A_0 + A_1 e^{j\omega_n t_1} + A_2 e^{j\omega_n t_2} + \ldots + A_{N-1} e^{j\omega_n t_{N-1}}, \tag{2.14}$$

so, from (2.9) and using Euler formula

$$|R_N| = \left| \sum_{i=0}^{N-1} A_1 e^{j\omega_n t_i} \right| = \sqrt{\left(\sum_{i=0}^{N-1} A_1 \cos(\omega_n t_i) \right)^2 + \left(\sum_{i=0}^{N-1} A_1 \sin(\omega_n t_i) \right)^2}. \tag{2.15}$$

This result become relevant if approaching IS with a system theory perspective. In fact being a generic IS described by

$$h(t) = A_0 \delta(t) + A_1 \delta(t - t_1) + A_2 \delta(t - t_2) + \ldots + A_{N-1} \delta(t - t_{N-1}) \tag{2.16}$$

where $\delta(t)$ is the Dirac impulse, it is well known that the transfer function results

$$H(s) = A_0 + A_1 e^{-st_1} + A_2 e^{-st_2} + \ldots + A_{N-1} e^{-st_{N-1}}, \tag{2.17}$$

therefore its frequency response is

$$H(j\omega) = A_0 + A_1 e^{-j\omega t_1} + A_2 e^{-j\omega t_2} + \ldots + A_{N-1} e^{-j\omega t_{N-1}}, \tag{2.18}$$

21

and from (2.14) it is easy to affirm that

$$RN = H^\star(j\omega_n). \tag{2.19}$$

Finally, assuming to vary the frequency ω in (2.14) to evaluate robustness, it descend that

$$|R_N(\omega)| = |H(j\omega)|. \tag{2.20}$$

2.2 Zero Vibration Input Shaper

The Zero Vibration IS (ZV IS) is the simplest input shaper that assures complete residual vibration suppression at a given system frequency of a second order plant. The definition of the ZV IS descends directly from the considerations in Section 2.1, and in particular is the simplest solution of the zero vibration conditions in (2.3), by means of only two impulses

$$h_{ZV}(t) = \frac{1}{1+K}\delta(t) + \frac{K}{1+K}\delta(t-T) \tag{2.21}$$

with

$$\begin{aligned} K &= e^{\frac{-\delta\pi}{\sqrt{1-\delta^2}}}, \\ T &= \frac{\pi}{\omega_n\sqrt{1-\delta^2}}, \end{aligned} \tag{2.22}$$

where δ is damping, ω_n is the natural undamped frequency of the system and T the time delay of the second impulse. The effect of the ZV IS is exactly that described in fig. 2-1, in fact the delay T is half period of the vibration and the amplitude is such that vibration is eliminated in phase opposition. In fig. 2-4(a) is reported the effect of complete vibration suppression with a shaped step command in both damped and undamped case. Also in fig. 2-4(a) and fig. 2-4(b) it can be noted the effect of damping in the design of the shaper, i.e. the ratio between the two impulses depends on δ. In fig. 2-4(c) the *PRV* function has been reported with respect to natural frequency ω_n.

In order to analyze the ZV IS with a filter perspective as proposed in Section 1.2.2, the definition in (2.21) can be easily rewritten in terms of transfer function

$$H_{ZV}(s) = \frac{1 + Ke^{-sT}}{1 + K}. \tag{2.23}$$

In fig. 2-5(a) analysis of (2.23) in the complex plane shows the effect of the ZV IS that performs a Pole-Zero cancellation of the pole's couple that cause vibrations. Also in fig. 2-5(b) and fig. 2-5(c) is reported the IS function with different values of σ and $j\omega$ in order to obtain a description of the ZV IS in the whole S-Plane. These representations of the ZV IS show the zeroing effect of the shaper for nominal parameters, since the value of the response is null in correspondence of the zeros position. However since contour lines represent linearly spaced amplitude values, their proximity each other means a rapid grow of the response when small variations are present. This can be easily seen also in the 3-dimensional representation of fig. 2-6.

Plots in fig. 2-4(a) and fig. 2-4(c) demonstrate that ZV IS really suppresses vibration when it is designed with exact plant's parameters. Moreover it is very easy to implement and introduces very low distortion since, being T_0 the period of the vibration at system frequency ω_0, the shaped command only lasts a time $T = {}^{T_0}/_2$. However from fig. 2-4(c) and fig. 2-5 it can be seen that the suppression effect rapidly decrease as the real parameters differs from the nominal ones.
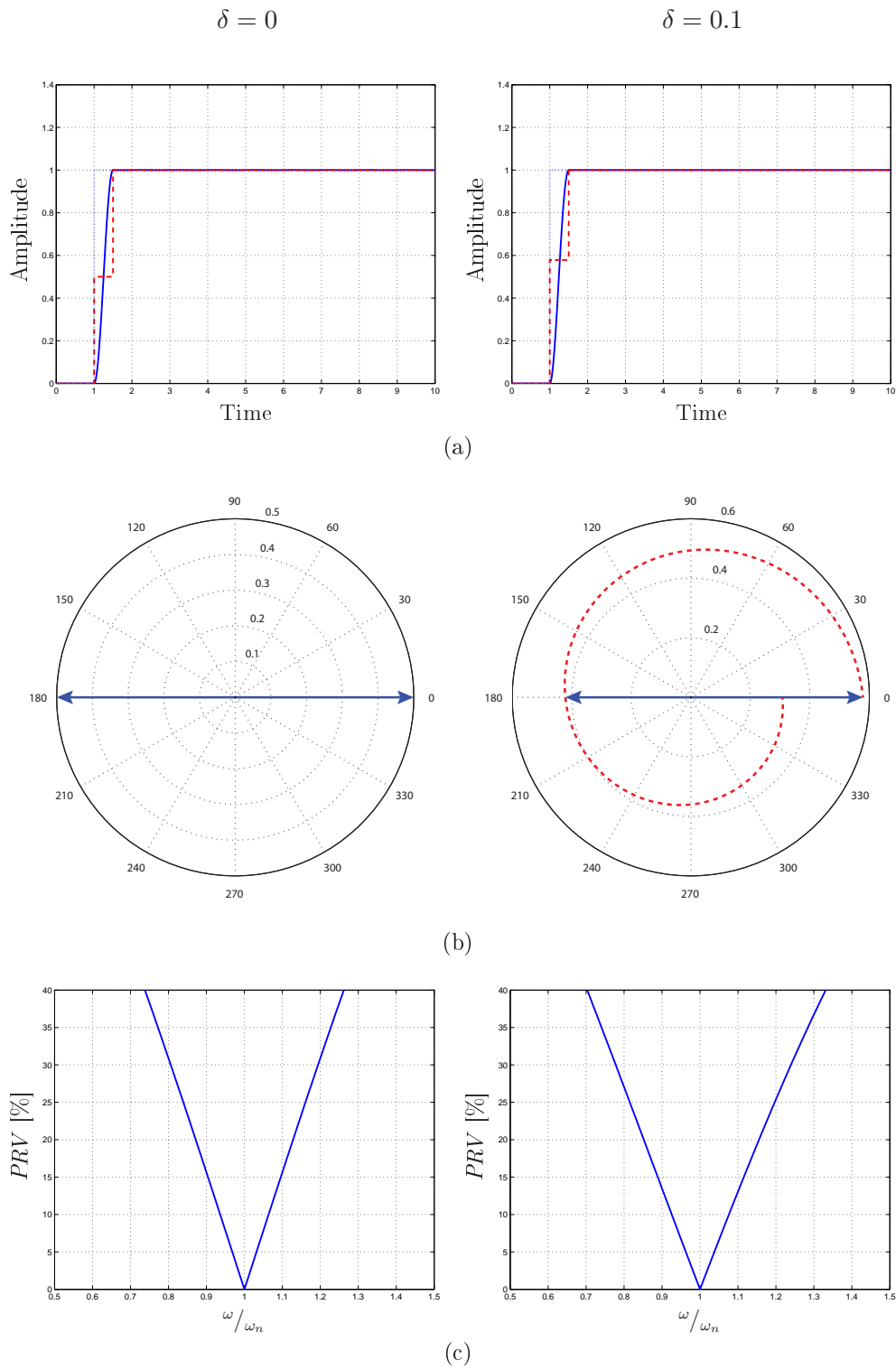
Figure 2-4: Step response of the system with ZV IS (a), impulses description by means of vector diagram (b) and PRV function of the ZV IS with respect to variation of natural frequency (c).

$\delta = 0$ $\delta = 0.1$

(a)

(b)

(c)
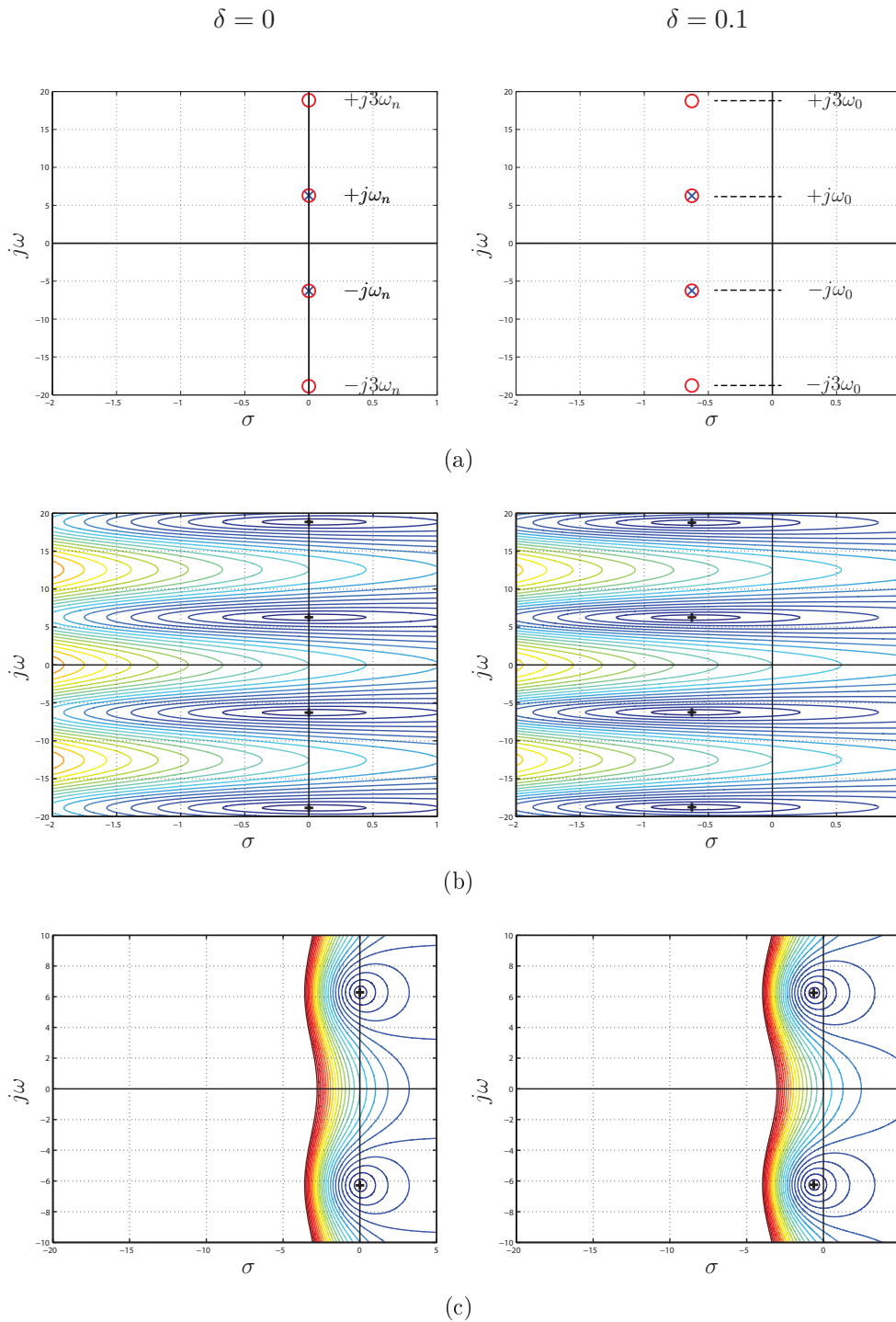
Figure 2-5: Pole-Zero diagram of the system with ZV IS (a) and description of $H_{ZV}(s)$ as function of σ and $j\omega$ (b,c). In (c) the same plot of (b) is reported with equal scale on x and y axis in order to better understand the behavior of the system response. In (b) and (c) the contour lines are equally spaced of 0.1 and the zeroes position is highlighted with a black cross.
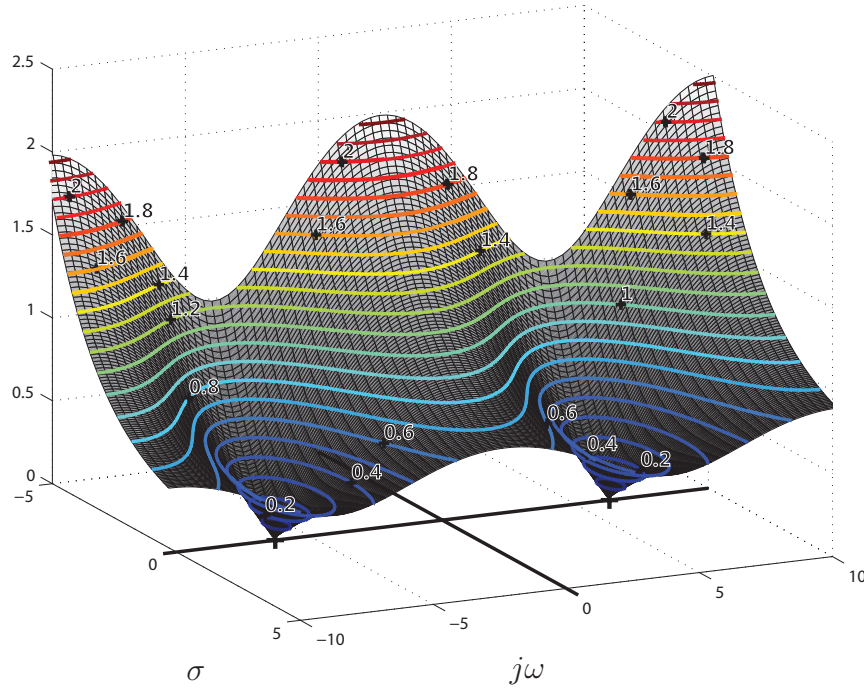
Figure 2-6: 3-D view of $H_{ZV}(s)$ with $\delta = 0$ as function of σ and $j\omega$. The contour lines are equally spaced of 0.1 and the zeroes position is highlighted with a black cross.

2.3 Zero Vibration Derivative Input Shaper

The Zero Vibration Derivative Input Shaper (ZVD IS) has been introduced in order to increase robustness of the ZV IS. As seen in Section 2.2 the ZV IS suffers from lack of robustness in parameters definition which makes it rather unsuitable for implementation in real cases. ZVD IS is the earliest form of robust IS and still descends from the the zero vibration conditions in (2.3), but adds additional conditions on the behavior of the IS near the nominal parameters. That is, equations in (2.3) are enriched with the condition on the derivative of PRV with respect to frequency variations

$$\frac{\partial}{\partial \omega} \left(e^{-\delta \omega t_n} \sqrt{[C(\omega, \delta)]^2 + [S(\omega, \delta)]^2} \right) = 0. \tag{2.24}$$

The result from (2.3) and (2.24) is a three-impulses IS whose transfer function is

$$H_{ZVD}(s) = \frac{1}{1 + 2K + K^2} + \frac{2K}{1 + 2K + K^2} e^{-sT} + \frac{K^2}{1 + 2K + K^2} e^{-s2T} \tag{2.25}$$

26

where

$$K = e^{\frac{-\delta\pi}{\sqrt{1-\delta^2}}},$$

$$T = \frac{\pi}{\omega_n\sqrt{1-\delta^2}},$$

(2.26)

that are the same of (2.22). As can be seen in fig. 2-7(a) and fig. 2-7(c) the vibrations are suppressed as well, but the robustness is significantly increased resulting in a smoother PRV function thanks to the derivative condition. However, it has to be noted that the introduction of an additional impulse doubles the time duration of the shaping effect, resulting in a total time $2T$ that equals the time T_0 of the period of the vibration at system frequency ω_0.

The increased robustness can be explained by simply manipulating (2.25) that results

$$H_{ZVD}(s) = \left(\frac{1 + Kz^{-1}}{1 + K}\right)^2 = (H_{ZV}(s))^2,$$

(2.27)

that is basically to double the effect of a simple ZV IS. Also on the complex plane, looking at fig. 2-8(a) is visible that the effect the derivative condition is exactly to double the zeroes of the ZV IS. Therefore, the zeroing effect is wider as can be seen in fig. 2-8(b) and fig. 2-8(c) where the contour lines although at same levels of fig. 2-5, appears much more spread in the neighborhood of the zeroes of the ZDV IS.

$\delta = 0$ $\delta = 0.1$

(a)

(b)

(c)
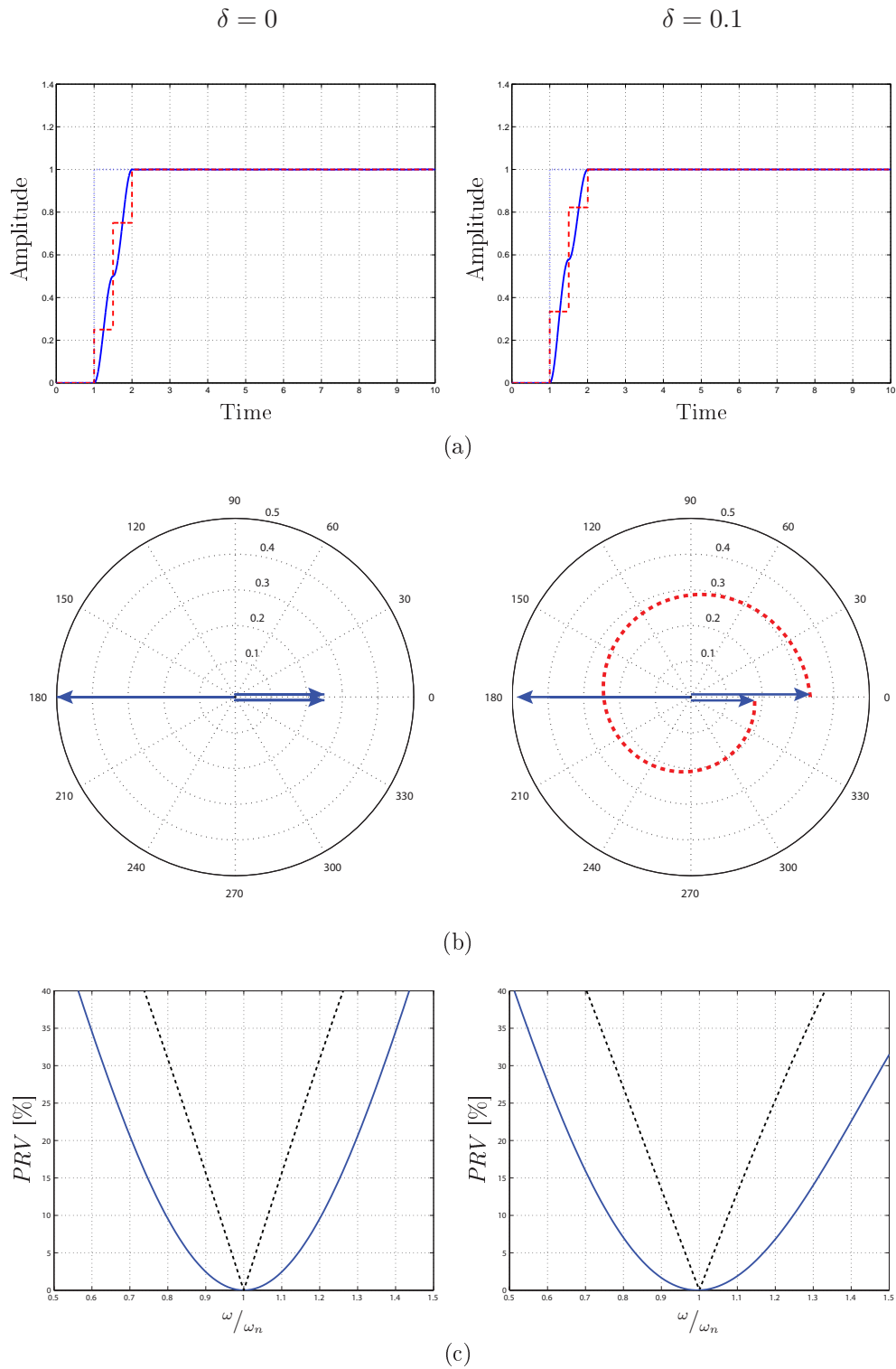
Figure 2-7: Step response of the system with ZVD IS (a), impulses description by means of vector diagram (b) and PRV function of the ZVD IS compared to ZV IS in black dotted line (c).

28
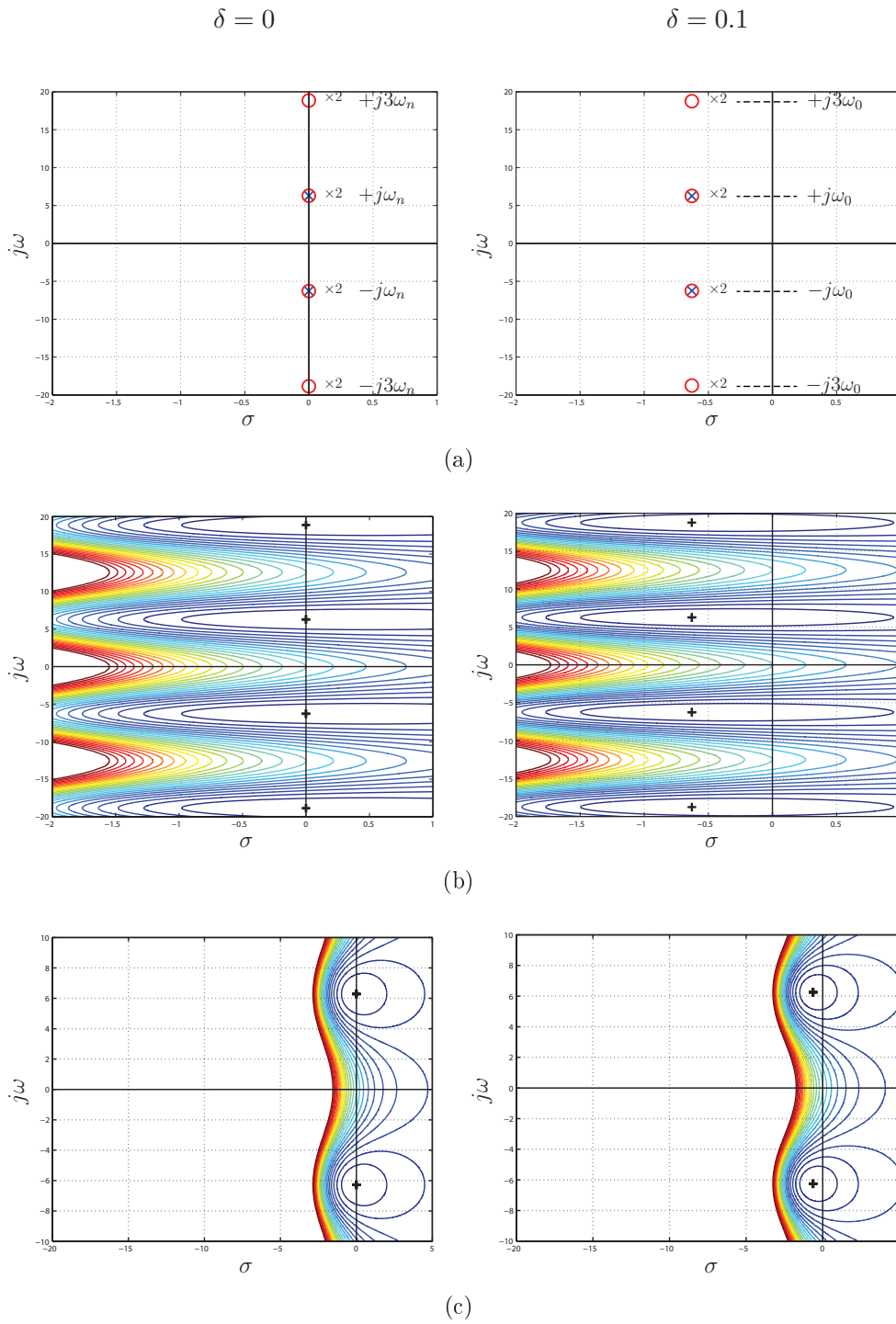
Figure 2-8:   Pole-Zero diagram of the system with ZVD IS (a) and description of $H_{ZVD}(s)$ as function of σ and $j\omega$ (b,c). In (c) the same plot of (b) is reported with equal scale on x and y axis in order to better understand the behavior of the system response. In (b) and (c) the contour lines are equally spaced of 0.1 and the zeroes position is highlighted with a black cross.

2.4 Zero Vibration n-Derivative Input Shapers

Starting from the ZVD IS an entire family of robust input shapers has been introduced and defined by means of derivative methods. Basically adding to (2.3) and (2.24) further derivative conditions of the type

$$\frac{\partial^n}{\partial \omega^n} \left(e^{-\delta \omega t_n} \sqrt{[C(\omega, \delta)]^2 + [S(\omega, \delta)]^2} \right) = 0 \qquad (2.28)$$

with n the derivative order, an ever-increasing level of robustness can be achieved. In this way it is possible to define the so-called Zero Vibration n-Derivative Input Shapers (ZVD^n IS), whose general transfer function results

$$H_{ZVD^n}(s) = \left(\frac{1 + Ke^{-sT}}{1 + K} \right)^n . \qquad (2.29)$$

where K and the sample time T are defined as in (2.22) as well.

The effect of adding constraints on null derivatives is visible in fig. 2-9(b) where the smoothness of the PRV function is greater as the degree of the null derivative increases, that is robustness increases as well. Unfortunately for every additional condition, ie for every null derivative grade, an extra impulse is needed, resulting in ever longer sequences in terms of duration of the shaping effect (see fig. 2-9(a)), therefore causing an undesirable distortion of the command input when a high order of derivatives as set to zero. Moreover it has to be noted that robustness increases less and less as the number of impulses grows, so usually derivative methods are not taken into account over the second or third derivatives. In particular these are the Zero Vibration Double Derivative IS (ZVDD IS) and the Zero Vibration Triple Derivative IS (ZVDDD IS), which are defined by means of conditions in (2.3) and (2.24) plus the additional constraint in (2.28) with $n = 2$ and $n = 2, 3$ respectively. This is confirmed also from a system theory point of view. Indeed looking at fig. 2-10(a) it is clear that the effect of any further constraint on derivatives set to zero is to increase of one the multiplicity of all zeroes in the complex plane. This obviously increase the nullifying effect of the zeroes as can be seen also in fig. 2-10(b) and fig. 2-

ZVDD   ZVDDD

(a)

(b)
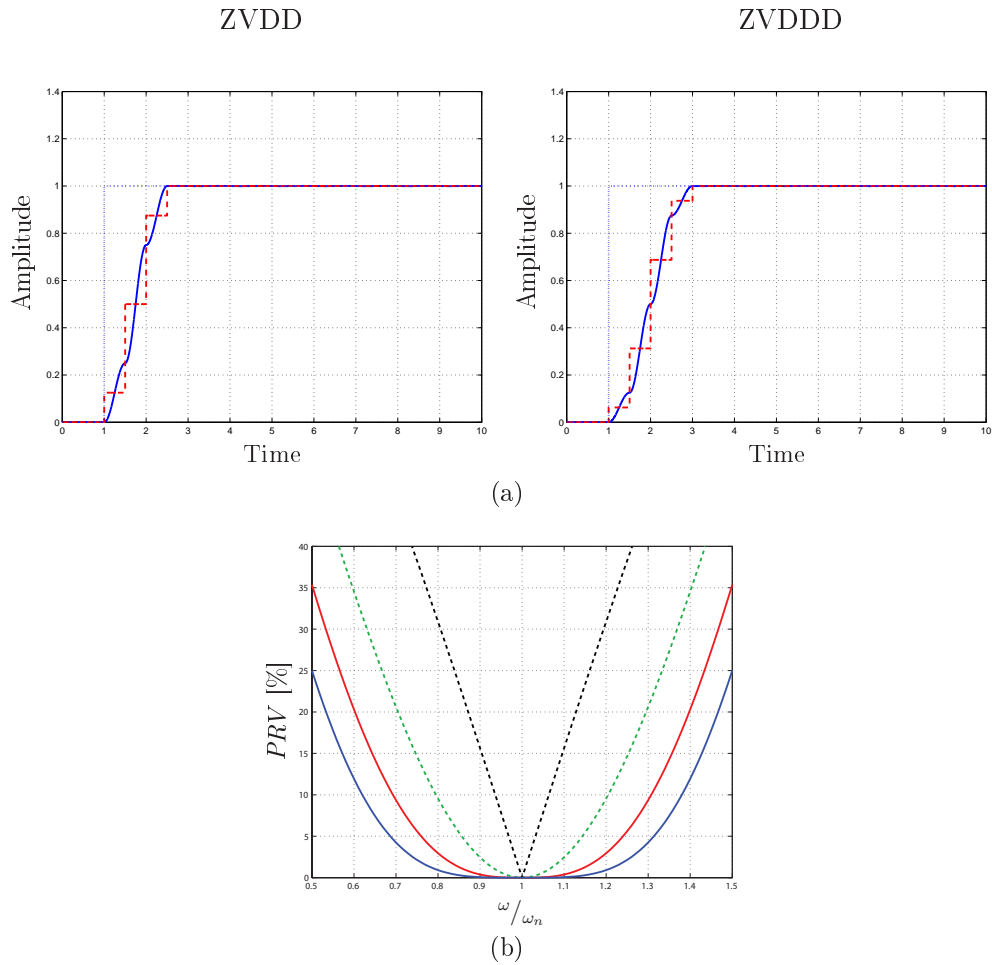
Figure 2-9: Step response of the system with $\delta = 0$ using ZVDD IS and ZVDDD IS (a) and PRV function of the ZVDD IS and ZVDDD IS, compared to ZV IS in black dotted line and ZVD IS in green dotted line (b).

10(c) where $H_{ZVDD}(s)$ and $H_{ZVDDD}(s)$ show large areas with very low amplitude. However it has to be noted that the difference is appreciable only very close to nominal parameters while the overall function doesn't change so much with respect to fig. 2-5(c) and fig. 2-8(c).

ZVDD   ZVDDD

(a)

(b)

(c)
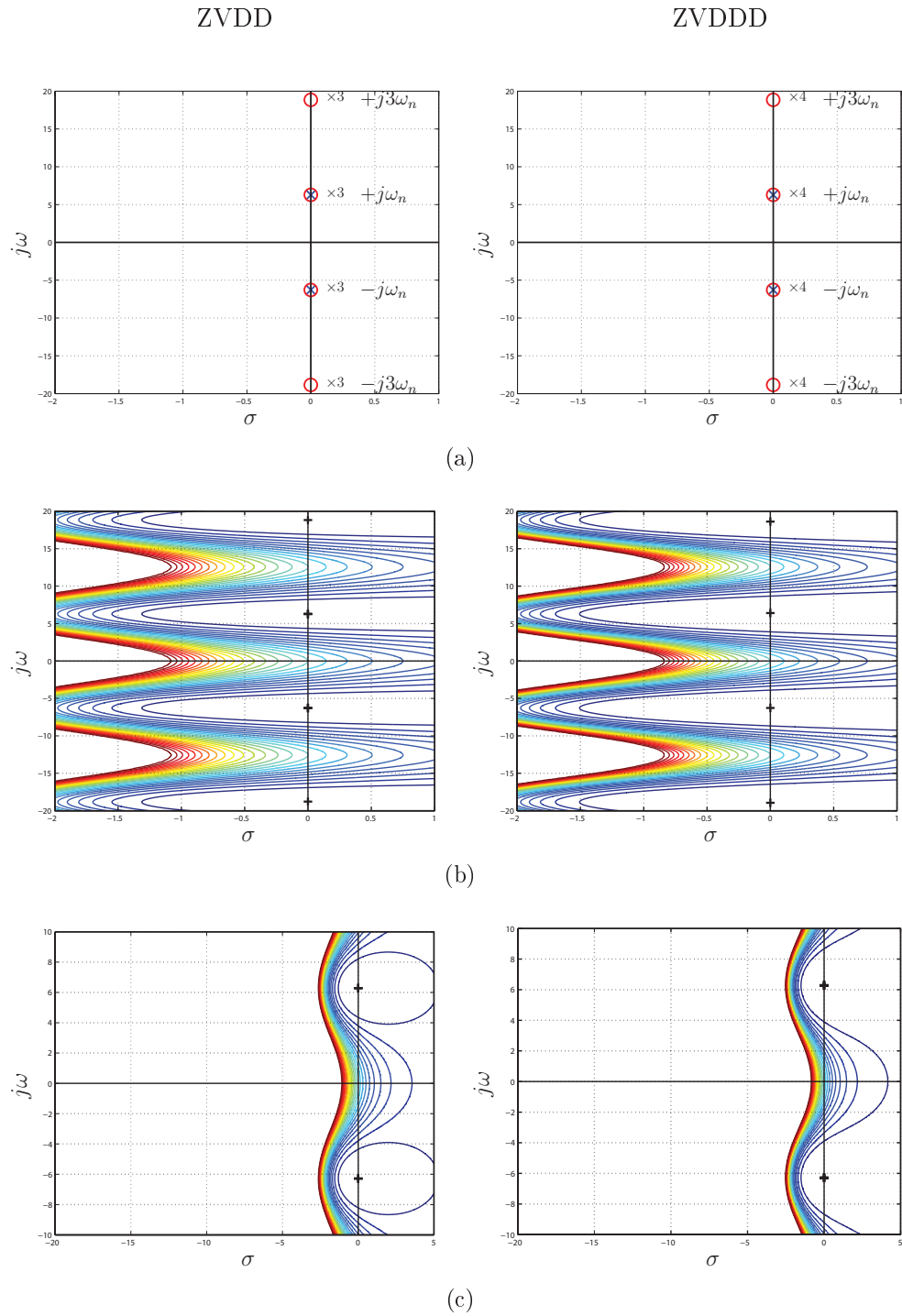
Figure 2-10: Pole-Zero diagram of the system with derivative IS (a) and description of $H_{ZVDD}(s)$ and $H_{ZVDDD}(s)$ as function of σ and $j\omega$ (b,c). In (c) the same plot of (b) is reported with equal scale on x and y axis in order to better understand the behavior of the system response. In (b) and (c) the contour lines are equally spaced of 0.1 and the zeroes position is highlighted with a black cross.
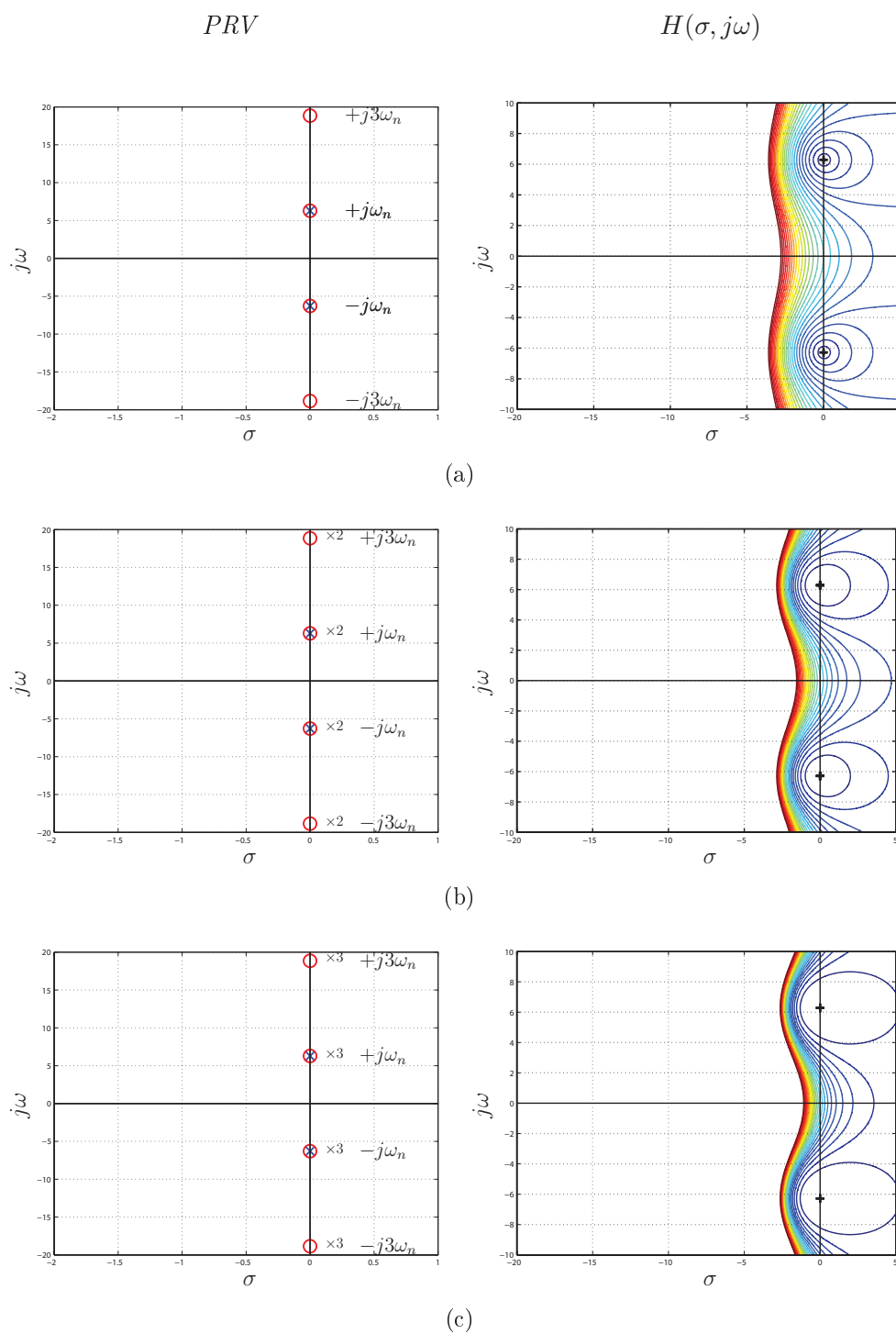
Figure 2-11: Comparison of Pole-Zero diagram and transfer function description on the complex plane of respectively ZV IS (a), ZVD IS (b) and ZVDD IS (c).

2.5 Extra Insensitive Input Shaper

In Section 2.4 has been shown how robust IS based on derivative methods soon become too much complicated compared with less and less effectiveness in increasing robustness. Extra Insensitive IS (EI IS) instead are based on the concept of allowing a certain amount of residual vibration, in order to guarantee the vibration reduction effect for a wider range of frequencies. This idea is mainly driven by practical experience, since it is known that real implementations rarely match the simulation models. Moreover for many real applications an augmented robustness with respect to variation of parameters is more important than the complete suppression of vibration, although within certain limits.

EI IS has been introduced in [94, 89] by means of the vector diagram approach for a system with damping $\delta = 0$. As said before the idea is to relax the null vibration condition for nominal parameters, assuming to allow a certain level of PRV, typically not more than 10%. Starting from a ZVD IS, it is proven that when the sum of the three impulses at modelling frequency is set equal to a vibration limit V_{lim}, the PRV function presents an "hump" of amplitude V_{lim} that drops down to zero symmetrically with respect to the nominal frequency, as shown in fig. 2-12. Moreover by only modifying amplitudes of a ZVD IS impulses, the 3-impulse sequence that yields maximum robustness for a given vibration limit can be obtained.

By means of geometrical relationship between PRV and vector diagram representation given in Section 2.1.2, the behavior of the EI IS for $\delta = 0$ in fig. 2-12(b) is easily explainable. Unlike the ZVD IS, the amplitude of the three impulses is chosen such that the vectorial sum in fig. 2-13(a) is non null

$$|A_0| - |A_1| + |A_2| = V_{lim}(|A_0| + |A_1| + |A_2|), \qquad \omega = \omega_n. \qquad (2.30)$$

Being the angle of each impulse in the vector diagram related to frequency by $\theta_i = \omega_i t_i$, it is straightforward that for each value of ω the angle of the third vector θ_3 is always twice the angle of the second vector θ_2. Therefore by means of simple geometrical considerations it can be demonstrated that the vectorial sum can be set to zero at

34
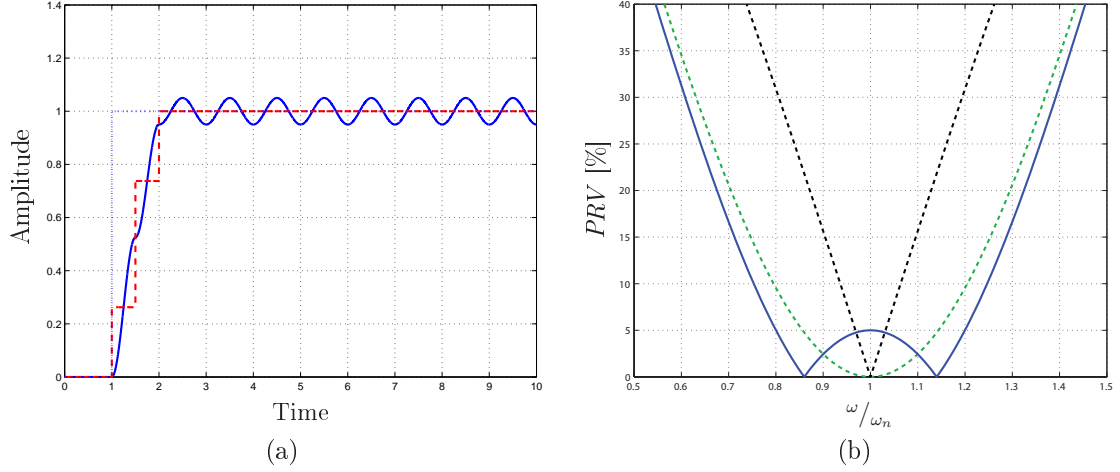
Figure 2-12: Step response of the system with $\delta = 0$ shaped by EI IS with $V_{lim} = 0.05$ (a) and PRV function of the EI IS compared to ZV IS in black dotted line and ZVD IS in green dotted line (b).

certain angles that represent two frequency values equidistant from ω_n as described in fig. 2-13(b).

However recalling the relationship between vector diagram, PRV function and frequency response with $\delta = 0$, the same problem can be posed in a more formal way looking at it in a filter perspective. First of all the EI IS can be described in Laplace domain as

$$H_{EI}(s) = A_0 + A_1 e^{-sT} + A_2 e^{-s2T} \tag{2.31}$$

where

$$T = \frac{\pi}{\omega_n} \tag{2.32}$$

being $\delta = 0$. Then in order to obtain a frequency response $|H_{EI}(j\omega)|$ shaped like the PRV function in fig. 2-12(b), amplitudes A_0, A_1, A_2 must satisfy the following equations

$$\begin{cases} |H_{EI}(j\omega)| = 1 & , \omega = 0 \\ |H_{EI}(j\omega)| = V_{lim} & , \omega = \omega_n \\ |H_{EI}(j\omega)| = 0 & , \omega = \omega_A \\ |H_{EI}(j\omega)| = 0 & , \omega = \omega_B \end{cases} \tag{2.33}$$

35
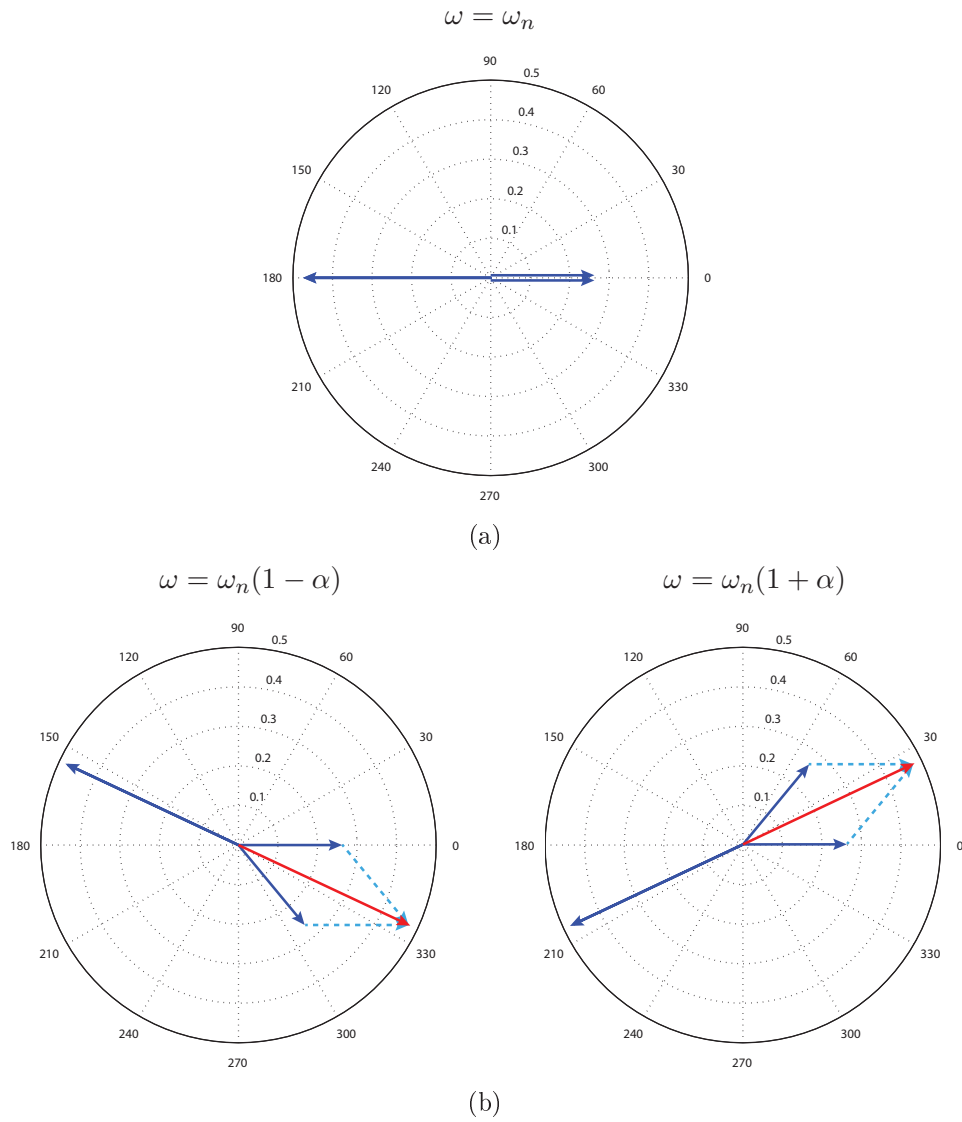
Figure 2-13: Vector diagram representation of the EI IS in nominal condition (a) and for ω that cause zero vibration (b).

where

$$|H_{EI}(j\omega)| = \left| \sum_{i=0}^{2} A_i e^{-ji\omega T} \right| \qquad (2.34)$$

and

$$\omega_A = \omega_n(1-\alpha), \quad \omega_B = \omega_n(1+\alpha), \qquad (2.35)$$

being $2\alpha\omega_n$ the total frequency width of the hump in terms of normalized frequency. The solution of (2.33) confirms the one of the authors in [94, 89]

$$\begin{cases} A_0 = \frac{1+V_{lim}}{4} \\[2mm] A_1 = \frac{1-V_{lim}}{2} \\[2mm] A_2 = \frac{1+V_{lim}}{4} \\[2mm] \cos(\alpha\omega_n T) = \frac{1-V_{lim}}{1+V_{lim}} \end{cases} \qquad (2.36)$$

Moreover the last equation in (2.36) gives a direct correspondence between the allowed residual vibration V_{lim} and the width of the hump. In particular it is interesting to note that for $\alpha = 0$ the hump collapses in $\omega = \omega_n$ and the shaper becomes a simple ZVD IS, while for $\alpha = 0.5$ results $V_{lim} = 1$ that is no shaping effect on vibration at $\omega = \omega_n$. In fact for $\alpha = 0.5$ the EI IS behaves like a ZV IS designed for a frequency $\hat{\omega}_n = \omega_n/2$. Therefore an EI IS for an undamped system is properly defined with

$$0 < \alpha < 0.5. \qquad (2.37)$$

In fig. 2-14 the the Pole-Zero description and the behavior in the complex plane of $H_{EI}(s)$ with proper amplitudes in (2.36) is shown. In particular comparing fig. 2-14(c) and fig. 2-8(c) for a ZVD IS, it is evident that the effect of EI IS is to widen the area of the S-Plane in which the shaper is able to reduce vibrations, using the same number of impulses of a ZVD IS. Actually, has been already demonstrated that if a certain $V_{lim} \neq 0$ is assumed, the impulses of a ZVD IS change in amplitude according to (2.36). This modification has a clear impact on the zero placement of the transfer function $H_{EI}(s)$ in fig. 2-14(a) with respect to $H_{ZVD}(s)$ in fig. 2-8(a). As told before
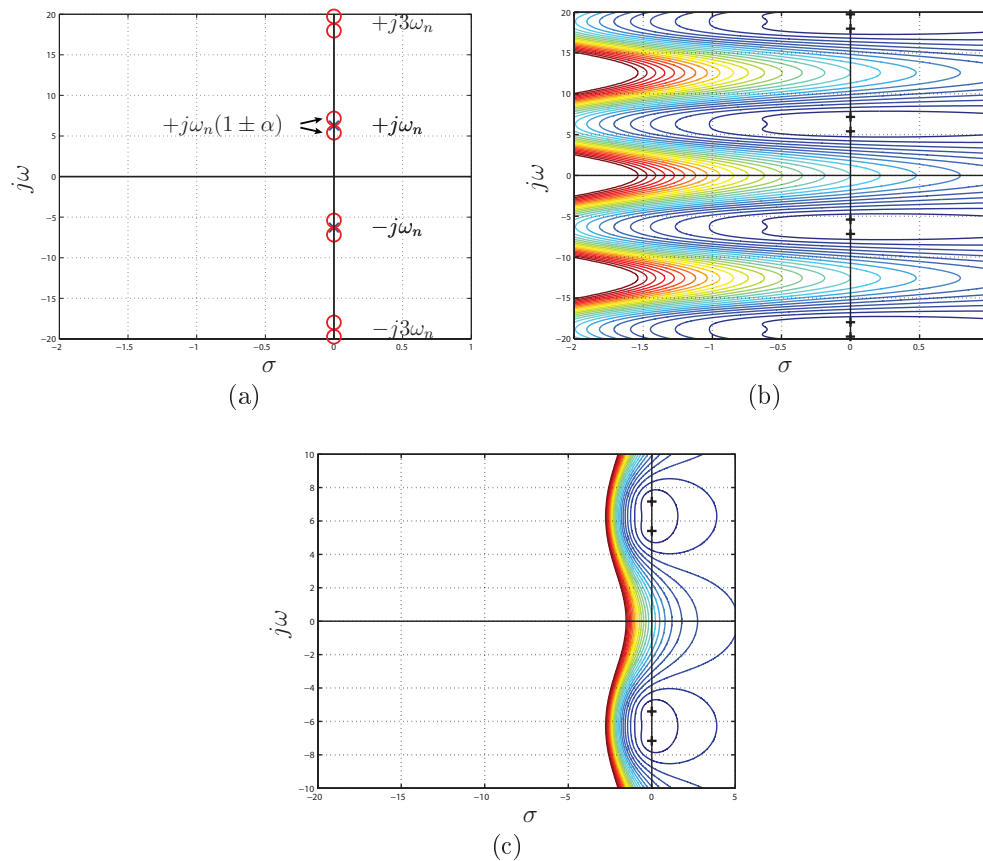
Figure 2-14: Pole-Zero diagram of the system with $\delta = 0$ shaped by EI IS with $V_{lim} = 0.05$ (a) and description of $H_{EI}(s)$ as function of σ and $j\omega$ (b,c). In (c) the same plot of (b) is reported with full scale axis in order to better understand the behavior of the system response. In (b) and (c) the contour lines are equally spaced of 0.1 and the zeroes position is highlighted with a black cross.

a ZVD IS can be considered as a particular EI IS for $V_{lim} = 0$, therefore $\alpha = 0$ and $H_{ZVD}(s)$ presents the typical complex conjugate couples of zeroes with multiplicity 2. On the contrary for an EI IS the effect of $\alpha \neq 0$ is graphically explained in fig. 2-15 as a split of the double zero of a ZVD IS into two single zeroes accordingly with α and equidistant from ω_n. However this is just a confirm of the result given by the PRV function and the frequency response but again shows the consistency of the Pole-Zero analysis for reducing vibrations, since a null value of PRV corresponds to a zero of the IS transfer function.

Unfortunately for damped system, an EI IS with a PRV like the one in fig. 2-7(b) can't be easily defined or simply derived from the undamped problem (2.33). In fact it is demonstrated that these constraint equations can't be solved in closed form, only numerical solutions are given for EI IS with $0 \leq \delta \leq 0.3$ and $0 \leq V_{lim} \leq 0.15$, namely

$$
\begin{aligned}
A_0 &= 0.24968 + 0.24962\, V_{lim} + 0.80008\, \delta + 1.23328\, \delta V_{lim} + 0.49599\, \delta^2 \\
&\quad + 3.17316\, \delta^2 V_{lim}, \\
A_1 &= 1 - (A_0 + A_2), \\
A_2 &= 0.25149 + 0.21474\, V_{lim} - 0.83249\, \delta + 1.41498\, \delta V_{lim} + 0.85181\, \delta^2 \\
&\quad - 4.90094\, \delta^2 V_{lim}
\end{aligned}
\tag{2.38}
$$
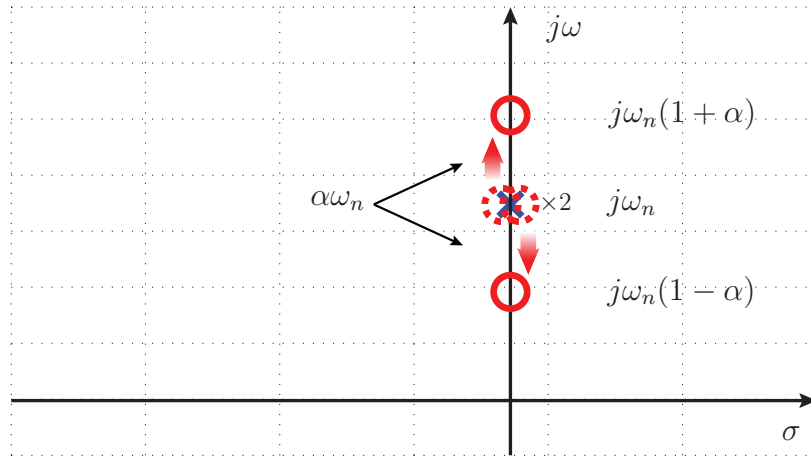
Figure 2-15: Effect of the introduction of an allowable amount of vibration in the placement of the zeroes of the transfer function $H_{EI}(s)$: as α increase from 0 the characteristic double zero of a ZVD IS is split into two single zeroes equally spaced from $j\omega_n$.

39

with

$$T_0 = 0,$$

$$
\begin{aligned}
T_1 = T_2(&0.49990 + 0.46159\,\delta V_{lim} + 4.26169\,\delta^2 V_{lim} + 1.75601\,\delta^3 V_{lim} \\
&+ 8.57843\,\delta V_{lim}^2 - 108.644\,\delta^2 V_{lim}^2 + 336.989\,\delta^3 V_{lim}^2),
\end{aligned}
$$

$$T_2 = 2T = \frac{2\pi}{\omega_n \sqrt{1 - \delta^2}}, \tag{2.39}$$

therefore the EI IS results

$$h_{EI}(t) = A_0\delta(t - T_0) + A_1\delta(t - T_1) + A_2\delta(t - T_2), \tag{2.40}$$

that is in terms of transfer function

$$H_{EI}(s) = A_0 + A_1 e^{-sT_1} + A_2 e^{-sT_2}. \tag{2.41}$$

In fig. 2-16(c) the *PRV* function of the IS designed in that way describes exactly the desired humped behavior like in fig. 2-12(b) and the step response in fig. 2-16(a) shows the response of the system with an EI IS that allows a certain level of vibration V_{lim}. Also it has to be noted that like in case of undamped system the total length of the impulse train is the same of a ZVD IS but the three impulses are not anymore equally spaced in time.

In fig. 2-17 the analysis of $H_{EI}(s)$ in the S-Plane shows the same effect of widening the area in which vibrations can be reduced. Again, this result is obtained by splitting the typical double zero of a ZVD IS according to the amount of allowed vibrations. Likewise the undamped case, the zeroes are split in order to match the zero values of the *PRV* function. Being the *PRV* defined as a function of ω_n, with $\delta \neq 0$ the split results taking place along a constant damping direction on the complex plane.

Unfortunately this constraint on the zeroes position, is the reason that makes the design of the EI IS possible only with the numerical solution in 2.38 and 2.39.

However an easier solution can be found tackling the problem with a system theory perspective. First of all it is proven that the EI IS is a particular ZVD IS in which

40
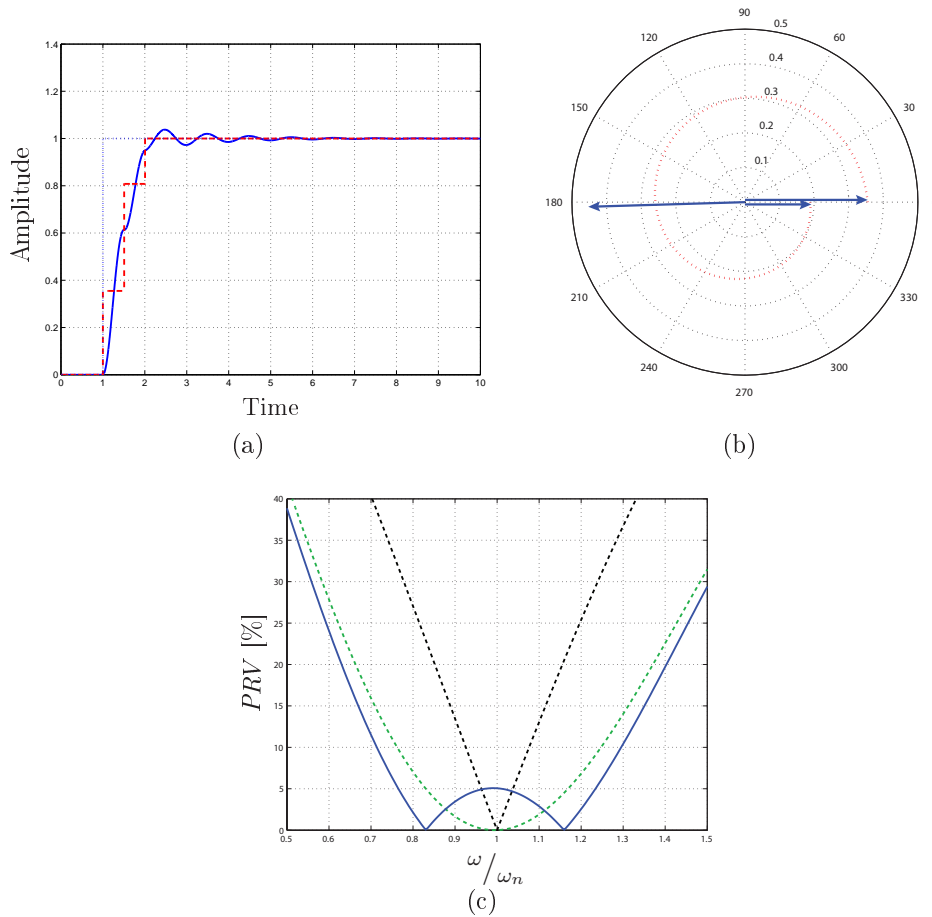
Figure 2-16: Step response of the system with $\delta = 0.1$ shaped by EI IS with $V_{lim} = 0.05$ (a), impulses description by means of vector diagram (b) and PRV function of the EI IS compared to ZV IS in black dotted line and ZVD IS in green dotted line (c).

the double zeroes are split in order to widen the zeroing effect. Then the precise use of the *PRV* function as a tool to define the shaper for damped system, lead to a difficult solution. In particular it can be proven that in all previous cases the effect of damping in IS design is a frequency translation of the zeroes for the undamped case and a frequency adjustment to the correct system frequency. In fact, being for example

$$H_{ZVD}(s) = \left(\frac{1 + e^{-sT}}{2} \right)^2 \tag{2.42}$$

41
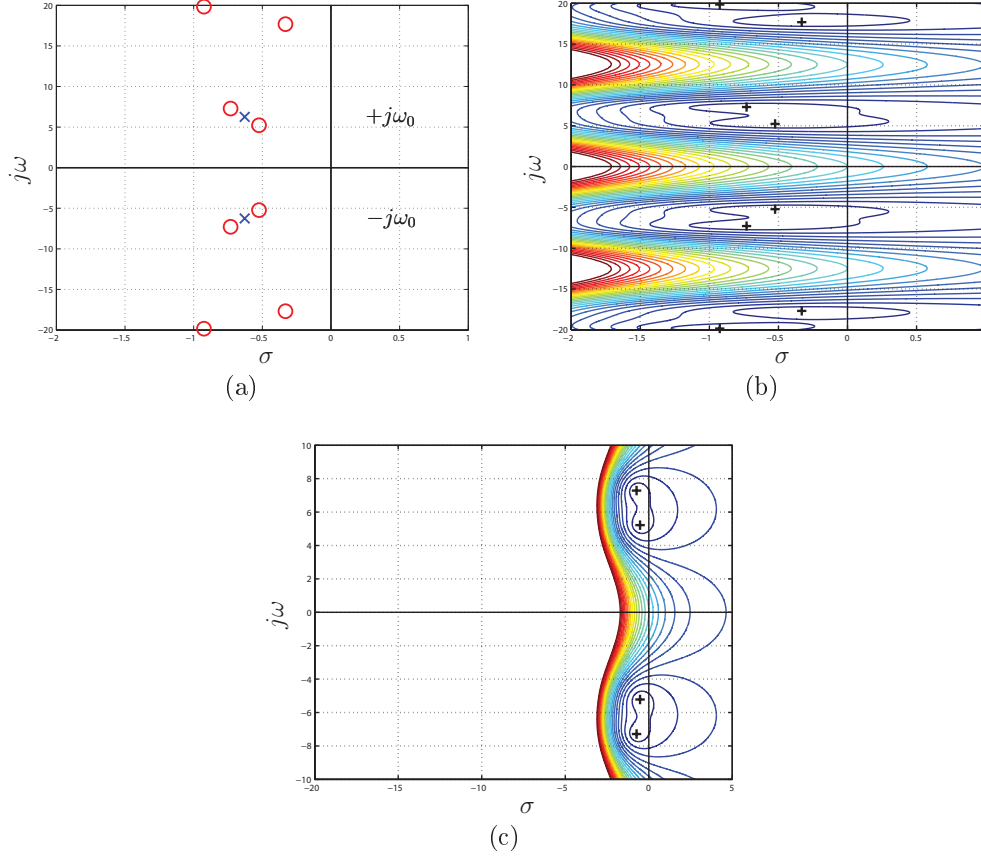
Figure 2-17: Pole-Zero diagram of the system with $\delta = 0.1$ shaped by EI IS with $V_{lim} = 0.05$ (a) and description of $H_{EI}(s)$ as function of σ and $j\omega$ (b,c). In (c) the same plot of (b) is reported with full scale axis in order to better understand the behavior of the system response. In (b) and (c) the contour lines are equally spaced of 0.1 and the zeroes position is highlighted with a black cross.

the transfer function of a ZVD IS for undamped system, and supposing $\hat{\sigma} = \delta\omega_n$ the desired translation, holds that

$$H_{ZVD}(s + \hat{\sigma}) = \left(\frac{1 + e^{-sT}e^{-\hat{\sigma}T}}{2}\right)^2, \tag{2.43}$$

where T is defined as usual

$$T = \frac{\pi}{\omega_n\sqrt{1 - \delta^2}}, \tag{2.44}$$

therefore solving the product $\hat{\sigma}T$, results

$$H_{ZVD}(s + \hat{\sigma}) = \left(\frac{1 + e^{-sT} e^{-\frac{\delta\pi}{\sqrt{1-\delta^2}}}}{2} \right)^2.$$

(2.45)

Finally recalling from (2.3)

$$K = e^{\frac{-\delta\pi}{\sqrt{1-\delta^2}}},$$

(2.46)

$H_{ZVD}(s + \hat{\sigma})$ becomes

$$H_{ZVD}(s + \hat{\sigma}) = \left(\frac{1 + Ke^{-sT}}{2} \right)^2 = H_{ZVD}(s)$$

(2.47)

which it is exactly the transfer function of a ZVD IS in (2.25), provided that the static gain is set to one.

Following the same approach it can be defined an IS whose behavior is very close to the EI IS, but without restrictions on the damping value and avoiding numerical solutions. In details, starting from the undamped case in (2.36) a 3-impulse train IS can be defined as follow

$$\begin{aligned} A_0 &= \frac{1 + V_{lim}}{4} \\ A_1 &= \frac{1 - V_{lim}}{2} K \\ A_2 &= \frac{1 + V_{lim}}{4} K^2 \end{aligned}$$

(2.48)

where

$$\begin{aligned} T_0 &= 0 \\ T_1 &= T \\ T_2 &= 2T \end{aligned}$$

(2.49)

with K and T defined as in (2.3). Therefore the transfer function result

$$H_{EI^\star}(s) = \frac{A_1 + A_2 e^{-sT} + A_3 e^{-s2T}}{A_1 + A_2 + A_3}.$$

(2.50)

43
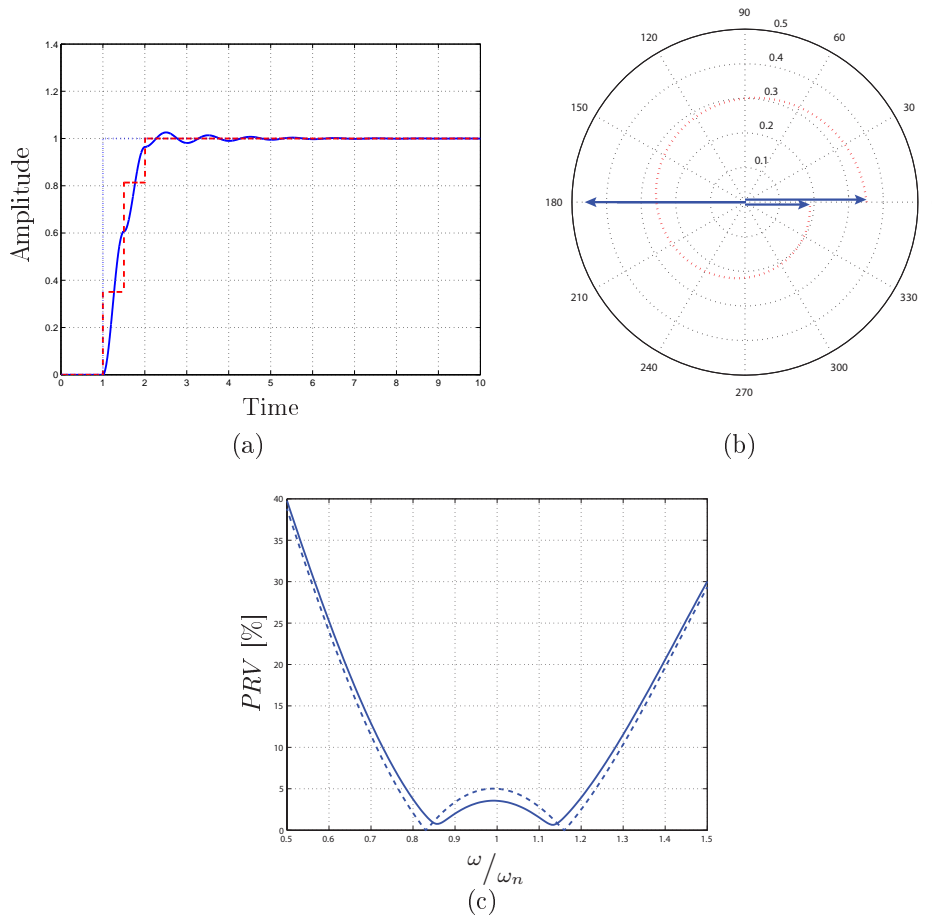
Figure 2-18: Step response of the system with $\delta = 0.1$ shaped by EI* IS with $V_{lim} = 0.05$ (a), impulses description by means of vector diagram (b) and PRV function of the EI* IS compared to EI IS designed by means of the numerical solution reported with dotted line (c).

The step response in fig. 2-18(a) shows that a small amount of vibrations are allowed like in fig. 2-16(a), also the PRV function of the EI* IS in fig. 2-18(c) demonstrates that residual vibrations are constrained under the desired value V_{lim} for a wide range of frequencies. In particular it can be seen that the range of variation of ω_n which satisfy the vibration limit it is comparable to the one of the EI IS designed by means of 2.38 and 2.39. On the contrary the EI* IS doesn't assure complete vibration suppression for any value of ω_n, but anyway the purpose of an EI IS is to extend the vibration reduction effect rather than nullify vibration.

In fig. 2-19 the analysis of EI* IS on the complex plane compared to the numerically

defined EI IS shows a very similar effect in terms of widening the plane's region in which the vibrations are consistently reduced, except that the zeroes are split along different directions. Even in this case the relation that links the allowed residual vibration V_{lim} and the frequency split by means of the parameter α holds, provided that the system frequency is considered instead of the natural frequency ω_n

$$\cos(\alpha \omega_0 T) = \frac{1 - V_{lim}}{1 + V_{lim}} \tag{2.51}$$

where

$$\omega_0 = \omega_n \sqrt{1 - \delta^2}. \tag{2.52}$$

Therefore for a given vibration limit V_{lim}, the zeroes are placed at frequencies

$$\omega_A^\star = \omega_0(1 - \alpha), \quad \omega_B^\star = \omega_0(1 + \alpha). \tag{2.53}$$

Also, being ω_0 and T defined for both damped and undamped system, we can assume the above equations as the general relationship between V_{lim} and the displacement of the zeroes. Moreover it has to be noted that the product $\omega_0 T$ is always equal to π, so α is uniquely defined by V_{lim} and totally independent from the damping. That is α is the ratio of the system frequency that identify the displacement of the zeroes from the system frequency itself, and also for damped system must satisfy the condition in (2.37).
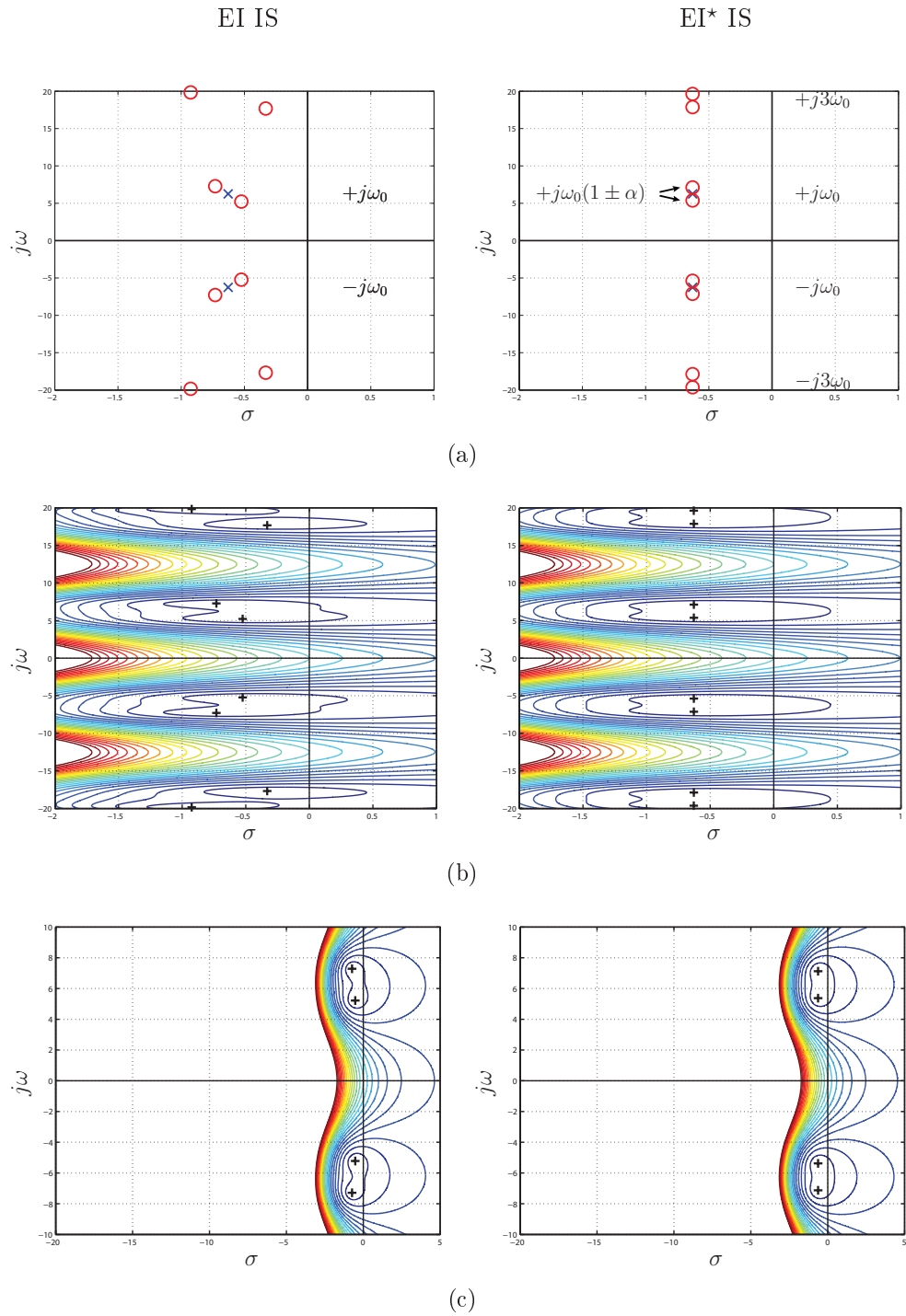
Figure 2-19: Pole-Zero diagrams of the system with $\delta = 0.1$ shaped by EI IS and EI* IS with $V_{lim} = 0.05$ (a) and description of both transfer functions in terms of σ and $j\omega$ variations (b,c). In (c) the same plot of (b) is reported with equal scale on x and y axis in order to better understand the behavior of the system response. In (b) and (c) the contour lines are equally spaced of 0.1 and the zeroes position is highlighted with a black cross.

2.6　Multi-Hump EI Input Shaper

Multi-Hump Extra Insensitive Input Shaper (n-Hump EI) are the natural extension of EI IS that are characterized by a hump-shaped PRV function. In a manner similar to ZVD^n IS in Section 2.4, the idea is to increase robustness by adding n constraint equations and n impulses of the IS. In particular, for the charateristic design approach of EI IS adding a further constraint means design an additional hump in the PRV function. Usually multi-hump IS refers to EI IS with only two or three humps, since any additional hump implies the use of one more impulse and the complexity of the design procedure rapidly grows. In [92, 93] the design algorithm of single-hump EI IS reported in Section 2.5 is extended for a 2-Hump EI and a 3-Hump EI. Similarly to EI IS the problem has been introduced for $\delta = 0$ by means of vector diagrams and can be described by means of constraints on frequency response. For a 2-Hump EI the transfer function of the shaper is

$$H_{2HEI}(s) = A_0 + A_1 e^{-sT} + A_2 e^{-s2T} + A_3 e^{-s3T} \tag{2.54}$$

with

$$T = \frac{\pi}{\omega_n \sqrt{1 - \delta^2}} \tag{2.55}$$

and amplitudes must satisfy

$$
\begin{cases}
|H_{2HEI}(j\omega)| = 1 & , \omega = 0 \\[6pt]
|H_{2HEI}(j\omega)| = 0 & , \omega = \omega_n \\[6pt]
|H_{2HEI}(j\omega)| = V_{lim} & , \omega = \omega_{H1} \\[6pt]
\frac{\partial}{\partial \omega}|H_{2HEI}(j\omega)| = 0 & , \omega = \omega_{H1} \\[6pt]
A_0 = A_3 \text{ and } A_1 = A_2
\end{cases}
\tag{2.56}
$$

where

$$|H_{2HEI}(j\omega)| = \left| \sum_{i=0}^{3} A_i e^{-ji\omega T} \right| \tag{2.57}$$

and

$$\omega_{H1} = \omega_n(1 - \beta) \tag{2.58}$$

is the frequency at which the hump for $\omega < \omega_n$ has the maximum value. Basically the constraints in (2.56) impose null vibration at nominal frequency, a residual vibration limit V_{lim} at a frequency ω_{H1} and that $PRV(\omega_{H1})$ is a local maximum. Moreover the last equation impose the symmetry of the PRV function with respect to ω_n, therefore for $\omega > \omega_n$ is implicitly defined an hump with a local maximum V_{lim} at a frequency

$$\omega_{H2} = \omega_n(1 + \beta) \tag{2.59}$$

where β, unlike α for EI IS, refers to the frequency range between the maximum of the two humps.

For a 2-Hump EI results

$$\begin{cases} A_0 = \frac{3X^2 + 2X + 3V_{lim}^2}{16X} \\ A_1 = \frac{1}{2} - A_0 \\ A_2 = A_3 \\ A_3 = A_0 \\ \cos(\beta\omega_n T) = \frac{1}{3}\left(1 + \frac{1}{4A_0}\right) \end{cases} \tag{2.60}$$

where

$$X = \sqrt[3]{V_{lim}^2\left(\sqrt{1 - V_{lim}^2} + 1\right)}. \tag{2.61}$$

In the same way a 3-Hump EI for an undamped system is defined as

$$H_{3HEI}(s) = A_0 + A_1 e^{-sT} + A_2 e^{-s2T} + A_3 e^{-s3T} + A_4 e^{-s4T} \tag{2.62}$$

with

$$T = \frac{\pi}{\omega_n\sqrt{1 - \delta^2}} \tag{2.63}$$

provided that amplitudes satisfy

$$
\begin{cases}
|H_{3HEI}(j\omega)| = 1 & , \omega = 0 \\[4pt]
|H_{3HEI}(j\omega)| = V_{lim} & , \omega = \omega_n \\[4pt]
|H_{3HEI}(j\omega)| = V_{lim} & , \omega = \omega_{H1} \\[4pt]
\frac{\partial}{\partial \omega}|H_{3HEI}(j\omega)| = 0 & , \omega = \omega_{H1} \\[4pt]
A_0 = A_4 \text{ and } A_1 = A_3 &
\end{cases}
\tag{2.64}
$$

where

$$
|H_{3HEI}(j\omega)| = \left| \sum_{i=0}^{4} A_i e^{-ji\omega T} \right|
\tag{2.65}
$$

and

$$
\omega_{H1} = \omega_n(1 - \gamma)
\tag{2.66}
$$

is again the frequency at which the hump for $\omega < \omega_n$ has the maximum value. However in this case the symmetry condition makes that one hump is centered on ω_n and the other two are at both sides with maximum value V_{lim} at frequencies ω_{H1} and ω_{H2} that is

$$
\omega_{H2} = \omega_n(1 + \gamma)
\tag{2.67}
$$

with γ again refers to the frequency range between the maximum of the two outer humps.

Amplitudes that solve (2.64) are

$$
\begin{cases}
A_0 = \frac{1 + 3V_{lim} + 2\sqrt{2(V_{lim}^2 + V_{lim})}}{16} \\[6pt]
A_1 = \frac{1 - V_{lim}}{4} \\[6pt]
A_2 = 1 - 2(A_0 + A_1) \\[6pt]
A_3 = A_1 \\[6pt]
A_4 = A_0 \\[6pt]
\cos(\gamma \omega_n T) = \frac{1 - V_{lim}}{16 A_0}
\end{cases}
\tag{2.68}
$$

2-Hump IS   3-Hump IS

(a)

(b)
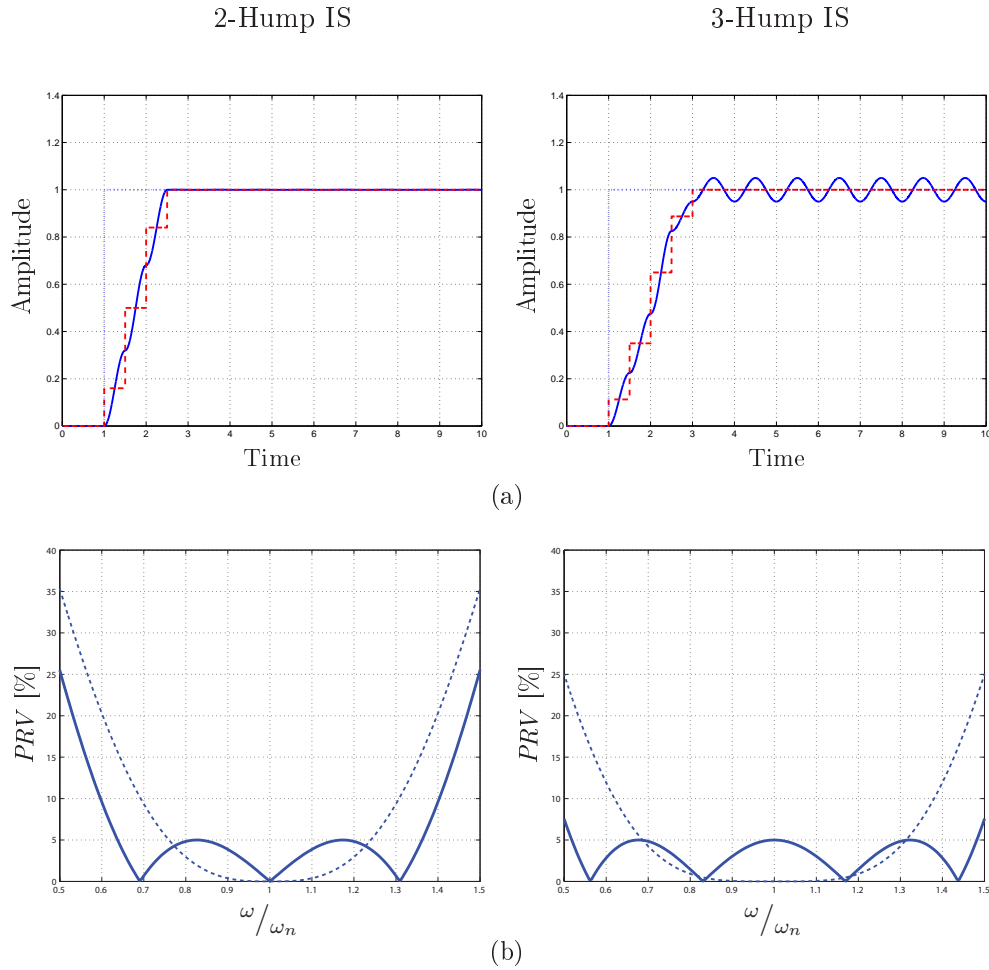
Figure 2-20: Step response of the system with $\delta = 0$ shaped by 2-Hump EI and 3-Hump EI with $V_{lim} = 0.05$ (a) and PRV functions of the IS compared respectively to ZVDD IS and ZVDDD IS (b).

In fig. 2-20(b) the *PRV* functions of the EI IS with two and three humps are shown, highlighting the robustness increase with respect to the ZVDD IS and the ZVDDD IS that have the same time length respectively. Also in fig. 2-20(a) the step response of the shaped system with nominal parameters present different behaviors according to the number of humps, since for odd numbers of humps the *PRV* function present a maximum in nominal conditions.

In fig. 2-21 the analysis of both the shapers on the complex plane describes the same effect of zero-splitting already seen for the single-hump case. In this case however it can be seen a different behavior depending on the number of zeros that are involved. In fact, the 2-Hump IS that descend from a ZVDD IS present three zeroes that are

50

2-Hump IS   3-Hump IS

(a)

(b)

(c)
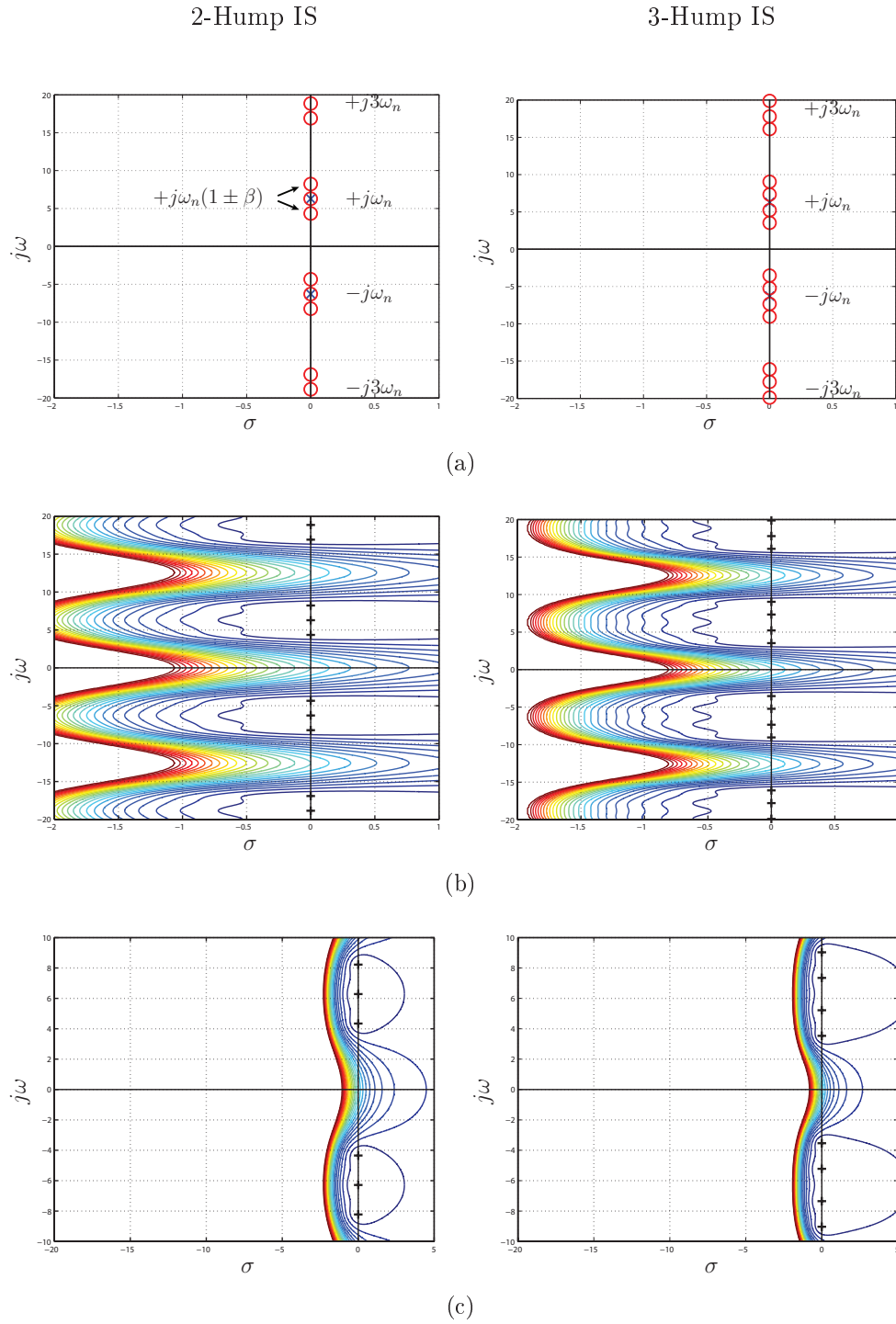
Figure 2-21: Pole-Zero diagrams of the system with $\delta = 0$ shaped by 2-Hump EI and 3-Hump EI with $V_{lim} = 0.05$ (a) and description of both transfer functions in terms of σ and $j\omega$ variations (b,c). In (c) the same plot of (b) is reported with equal scale on x and y axis in order to better understand the behavior of the system response. In (b) and (c) the contour lines are equally spaced of 0.1 and the zeroes position is highlighted with a black cross.

split symmetrically to ω_n a part from one zero that cancel the system pole. On the other hand the 3-Hump IS has four zeroes and the symmetric split doesn't cancel the system pole. This behavior obviously depend on the parity of the zeroes multiplicity and has a direct consequence in the shape of the PRV function.

For damped system a numerical solution have been proposed for both 2-Hump IS and 3-Hump IS, although only for $V_{lim} < 0.05$ and $0 \leq \delta \leq 0.3$. Coherently with the simple EI IS, the numerical solution permits to split the zeroes in the same way of the undamped case, along a constant damping direction as shown in fig. 2-19(a). However with the same approach of (2.48) based on frequency translation of the zeroes, an approximate solution can be derived for any values of δ starting from the amplitude values in (2.60) and (2.68) that is

$$
\begin{aligned}
A_0 &= \frac{3X^2 + 2X + 3V_{lim}^2}{16X} \\
A_1 &= \left(\frac{1}{2} - A_0 \right) K \\
A_2 &= A_3 K^2 \\
A_3 &= A_0 K^3
\end{aligned}
\tag{2.69}
$$

for 2-Hump IS and

$$
\begin{aligned}
A_0 &= \frac{1 + 3V_{lim} + 2\sqrt{2(V_{lim}^2 + V_{lim})}}{16} \\
A_1 &= \frac{1 - V_{lim}}{4} K \\
A_2 &= \left(1 - 2(A_0 + A_1) \right) K^2 \\
A_3 &= A_1 K^3 \\
A_4 &= A_0 K^4
\end{aligned}
\tag{2.70}
$$

for 3-Hump IS. The step responses and PRV functions in fig. 2-22 show that even if the shapers are designed with the frequency translation approach, the approximation is quite good and the implementation of that IS is very effective in order to obtain a vibration reduction for a wide range of frequencies. This is confirmed by the transfer

2-Hump IS   3-Hump IS

(a)

(b)
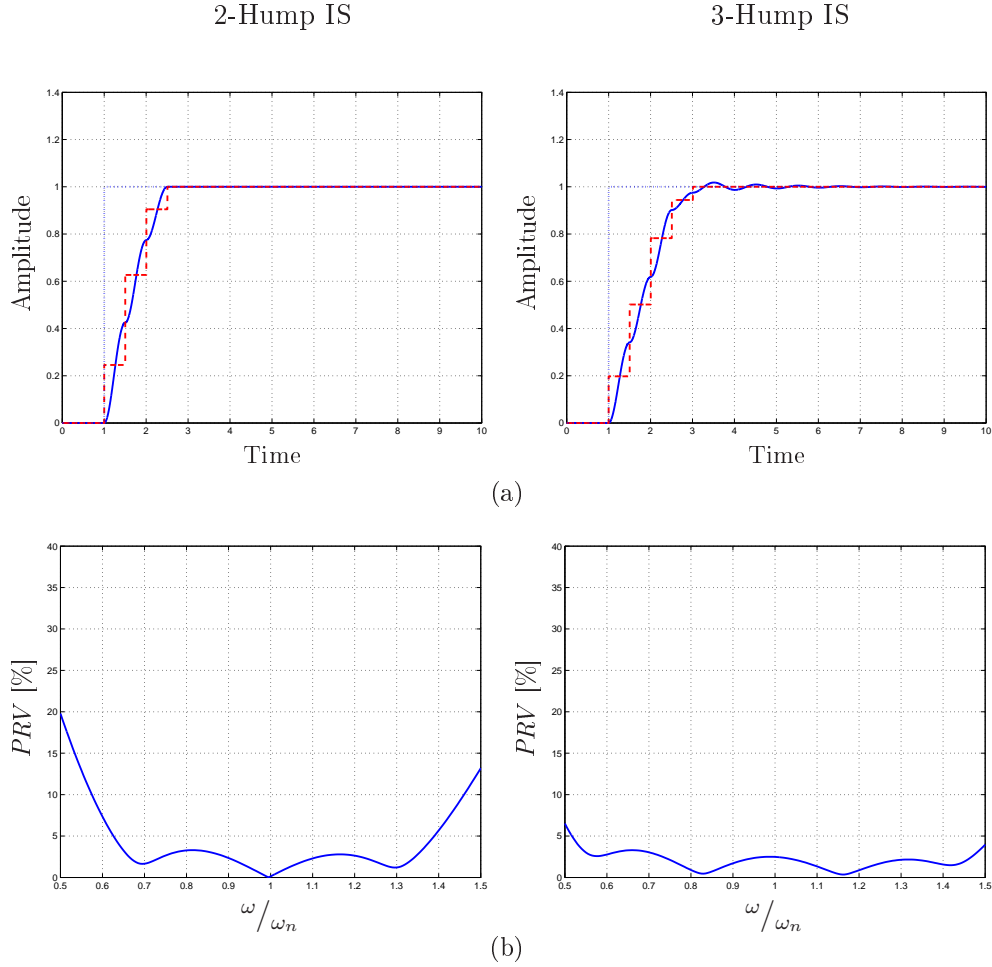
Figure 2-22: Step response of the system with $\delta = 0.1$ shaped by 2-Hump EI and 3-Hump EI with $V_{lim} = 0.05$ (a) and PRV functions of the IS (b). Both are designed with relations in (2.69) and (2.70).

functions analysis on the complex plane in fig. 2-23.

2.6.1   Approximate Design Techniques
for Multi-Hump EI Input Shaper

The proposed approximate method of design EI IS for damped system based on frequency translation in Sections 2.5 and 2.6 is validated also in some recent works. The truth is that the rigorous definition that is given by the authors in [94, 89] for a single-hump EI and in [92, 93] for a multi-hump EI, places limitations which reduce the attractiveness of these techniques for damped systems. On the contrary

53

2-Hump IS

3-Hump IS

(a)

(b)

(c)
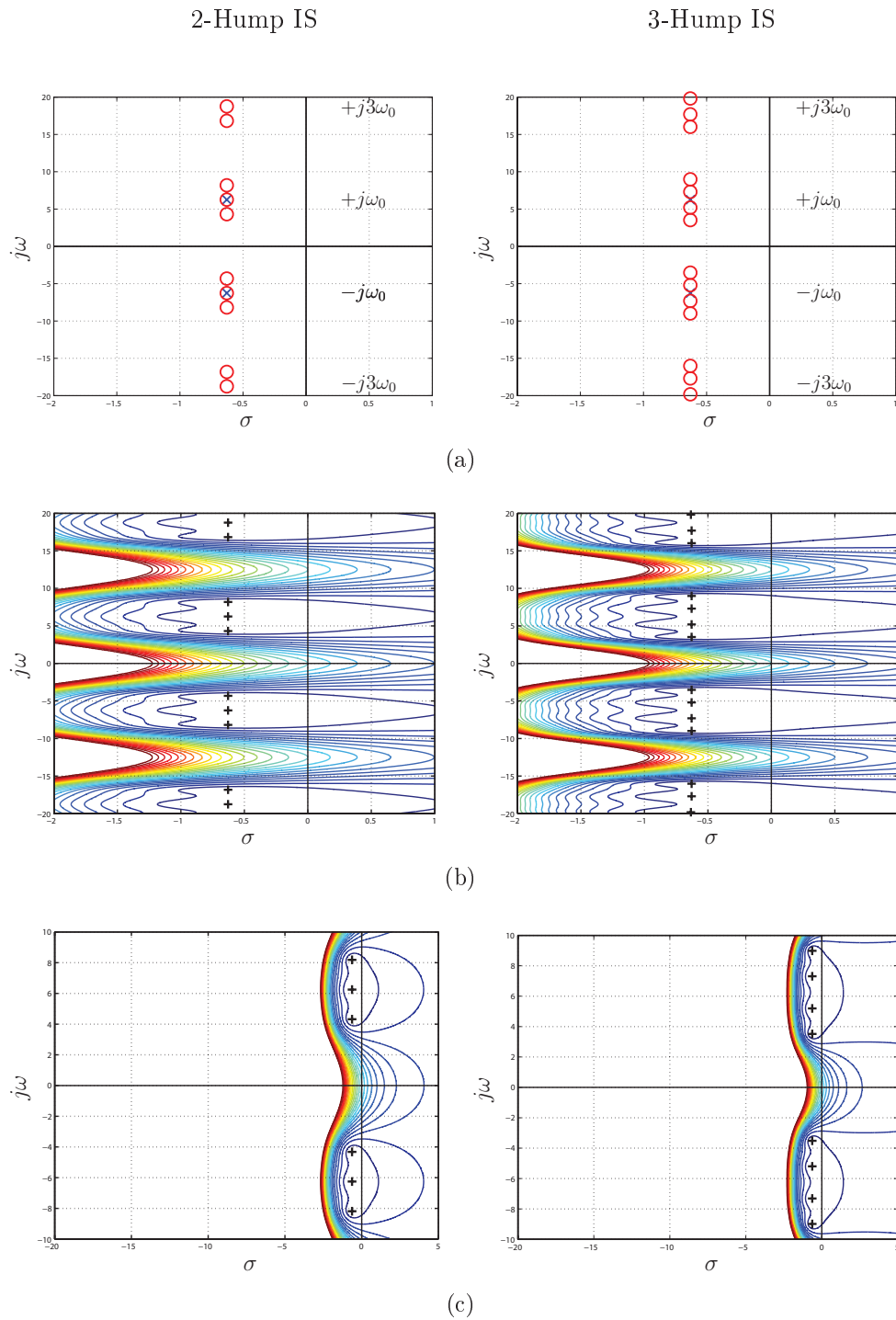
Figure 2-23: Pole-Zero diagrams of the system with $\delta = 0.1$ shaped by 2-Hump EI and 3-Hump EI with $V_{lim} = 0.05$ (a) and description of both transfer functions in terms of σ and $j\omega$ variations (b,c). In (c) the same plot of (b) is reported with equal scale on x and y axis in order to better understand the behavior of the system response. In (b) and (c) the contour lines are equally spaced of 0.1 and the zeroes position is highlighted with a black cross.
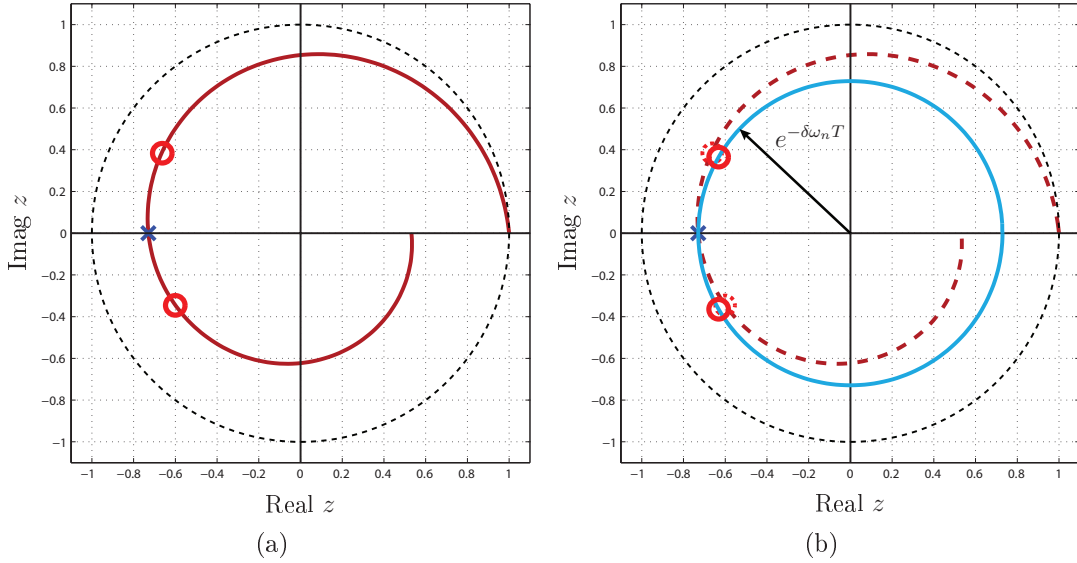
Figure 2-24: Representation of the system pole and the zeroes for an EI IS with respect to the system poles on the Z-Plane: in (a) the numerical solution let the zeroes lying on a constant damping spiral, in (b) the approximate solution places the zeroes on the circle whose radius is $e^{-\delta\omega_n T}$.

in a control systems perspective, methods that avoid numerical solutions are most appreciable, albeit with a certain degree of approximation.

In [74] a graphical approach based on zero placement on the Z-Plane is proposed. After a complete analysis of IS in discrete time domain together with the representation of the shaping effect on the Z-Plane, the authors come to highlight that the vibration suppression is due to a pole-zero cancellation and that EI IS basically split multiple zeroes in a proper way, as deeply discussed in previous sections. Moreover in an equivalent manner to what reported in Section 2.5, they assure that the numerical solution of EI IS is such that the zeroes are placed along a constant damping line that is represented as a spiral in fig. 2-24(a). Therefore, in order to achieve a closed form solution the graphical method proposes to place the zeroes on the circle whose radius $e^{-\delta\omega_n T}$ is such that the constant damping spiral is intersected in correspondence of the system poles (see fig. 2-24(b)).

However is easy to demonstrate that this graphical method is exactly the same of the one based on frequency translation in the S-Plane. In fact from [74] the two zeroes

are defined as

$$z_{1,2} = e^{-\delta\omega_n T + j\left(1\pm\frac{\Delta\omega}{\omega_n}\right)\pi},$$

(2.71)

then being actually $\frac{\Delta\omega}{\omega_n} = \alpha$ with α defined as in 2.35 and recalling T in (2.3), results

$$z_{1,2} = e^{-\delta\omega_n T + j\omega_n\sqrt{1-\delta^2}(1\pm\alpha)T},$$

(2.72)

and collecting T

$$z_{1,2} = e^{\left(-\delta\omega_n + j\omega_n\sqrt{1-\delta^2}(1\pm\alpha)\right)T}.$$

(2.73)

Finally being the relation between the discrete transfer function and the continuous transfer function $z = e^{sT}$, from 2.73 it can be obtained

$$s_{1,2} = -\delta\omega_n + j\omega_n\sqrt{1-\delta^2}\,(1\pm\alpha)\,,$$

(2.74)

that are the same zeroes of the solution in (2.48) reported in fig. 2-19.

In [48] instead, a partially analytical method is presented. First the three impulses are defined to be equally spaced of T and such that the vibration ratio for nominal condition is a certain V_{lim}. As a consequence the solution in (2.48) is derived. In addition the authors define an angle $\phi = \alpha\pi$ through which the constraint $PRV = 0$ is given for just one side of the hump. In this way is obtained a closed form solution for the amplitudes although it includes one unknown parameter which is a function of ϕ and has to be numerically solved. However this solution is much more simple than the rigorous one and the unknown parameter can be numerically solved for any value of V_{lim} and δ. Unfortunately the null-PRV condition on one side only of the hump does not assure that the PRV fall to zero either on the other side of the hump, moreover it causes robustness degradation for high V_{lim} values. This behaviour can be easily explained since in terms of poles-zeroes this method basically places one zero in order to be coincident to the numerical solution, while the other is left like in the solution in (2.48). Therefore the PRV function is no more symmetric and for large split of the zeroes the robustness degrades quickly.

In conclusion it has to be noted that the complication of numerical solutions, though partial, are motivated mostly by the fact that the PRV function is defined for variation of the natural frequency ω_n. Practically speaking is a fact that in evaluating parameters of an unknown damped system, what is actually measurable are the system frequency $\omega_0 = \omega_n\sqrt{1-\delta^2}$ and the decay rate $-\delta\omega_n$ of the vibratory response, that is the coordinates σ and $j\omega$ of the system poles on the S-Plane. Therefore potential errors in parameters estimation typically affect both δ and ω_n and defining the robustness for variation of ω_n or δ only is more a customary description than a real need. In addition from the analysis of the IS as a function of σ and $j\omega$ reported in previous sections, it can be noted that in general the vibration suppression effect rapidly vanishes as σ decreases, then the actual critical parameter in IS design is σ, so complicated numerical solutions are not so necessary.

2.7 IS Design for Multiple-Mode Vibrations Suppression

In many real applications, from cranes to flexible robotic arms, system modelling by means of a common second order LTI system as in Section 1.1 is not sufficient since other vibratory modes besides the fundamental one may be significant and then to be suppressed. In general IS for multiple-mode vibration suppression refers to higher order LTI system of the form

$$G_m(s) = \prod_{i=1}^{m} \frac{\omega_{ni}^2}{s^2 + 2\delta_i\omega_{ni}s + \omega_{ni}^2} \tag{2.75}$$

where m is the number of vibratory modes and δ_i, ω_{ni} are the parameters of the i-th mode. Basically in terms of poles of the transfer function, $G_m(s)$ can be represented by m couples of complex conjugate poles in the S-Plane. Therefore the natural approach to suppress m modes of vibration is to convolute m IS, each of which designed for

one of the m modes

$$H_m(s) = \prod_{i=1}^{m} H_i(s) \qquad (2.76)$$

where $H_i(s)$ is the IS for the i-th mode. In this way every IS cares to cancel only the poles for which it is designed and the convolution permits to achieve an overall pole-zero cancellation of $G_m(s)$.

Unfortunately this simple approach has a main drawback in terms of distortion, in fact the convolved shaper has total time duration equal to the sum of the shaping time of each IS. This means that if each IS is of the same kind and with a certain duration T_i, the worst case is represented by m modes closed to each other since results

$$T_{tot} = \sum_{i=0}^{m} T_i \approx mT_i. \qquad (2.77)$$

As a result the time dilatation may result in unfeasible solutions for some applications, therefore many approaches has been proposed that define IS which are designed to solve simultaneously the constraints for all the modes. The great advantage of all these methods is that in this way is always possible to achieve solutions with a time duration shorter than the convolved shaper.

2.7.1   Numerical Optimization Based Design

In [43, 87, 88] the design of IS for two or more vibratory modes is presented. Despite different assumptions related to the constraints of the case study in each papers, a general method can be deduced for the design of IS for multiple-modes vibration suppression based on numerical solution. Typically for an m-modes system $G_m(s)$ an overall problem is considered which contains the residual vibrations constraints for each mode along with additional constraints with respect to amplitudes of the impulses and robustness. Direct solving of such problems usually results in infinite possible solutions, therefore the IS is achieved choosing one of the feasible solution by means of optimization algorithms, typically for minimizing the shaper duration. These kind of IS reduce m vibratory modes and provide very low distortion, generally

58

in terms of number of impulses, the optimization procedure results in impulse trains of total $2m + 1$ impulses, where m is the number of the modes.

2.7.2 Zero-Placement Based Design

A different approach to achieve a multiple-mode IS is reported in [106] exploiting the zero placement technique in the Z-Plane to suppress vibrations. The assumption is that in order to suppress m vibratory modes of a given system $G_m(s)$, the IS must have at least $2m$ zeroes able to cancel the system poles

$$H_m(z) = \prod_{i=0}^{m} (z - p_i)(z - p_i^{\star}), \qquad (2.78)$$

where p_i, $p_i^{\star}$ are the i-th couple of complex conjugate poles of the system. In addition the above relation can be generalized in order to achieve augmented robustness for some critical modes by increasing the zeroes multiplicity n_i

$$H_m(z) = \prod_{i=0}^{m} (z - p_i)^{n_i} (z - p_i^{\star})^{n_i}. \qquad (2.79)$$

Then the IS is obtained in a discrete time fashion providing causality and minimum distortion of the command, that is equalize the degree of the zeroes with r poles at the Z-Plane origin

$$H_m(z) = \frac{C}{z^r} \prod_{i=0}^{m} (z - p_i)^{n_i} (z - p_i^{\star})^{n_i}, \qquad (2.80)$$

where

$$r = \sum_{i=0}^{m} n_i \qquad (2.81)$$

and C will provide also unitary static gain. Finally the impulse amplitudes are defined by means of the impulse response

$$h_m(t) = C \left(\delta(t) + \sum_{i=1}^{r} a_i \delta(t - iT) \right), \qquad (2.82)$$

where the coefficient a_i results from the polynomial expansion of the discrete transfer function $H_m(z)$. It has to be noted that $H_m(z)$ is derived assuming to know from the beginning the sample time T of the IS, as a matter of fact T is a design choice. In fact the authors propose to calculate the coefficients a_i by means of the poles of the continuous transfer function $G_m(s)$, therefore the amplitudes a_i are obtained as function of the sample time T. In this way the amplitudes can be chosen accordingly to the feasibility of a real implementation and minimizing T. At last C is chosen to provide unitary static gain.

This method allows to obtain suboptimal results for multiple-mode vibration suppression. This is due to the use of equally time spaced impulses, as a result in case of widely spaced modes of vibration IS derived in this way result typically longer than convolved shapers.

2.7.3 An Application of EI IS for a Two-Mode Vibratory System

In Section 2.5 a closed form solution for an EI IS has been derived by means of its frequency response and a good approximation for damped systems has been given by a frequency translation approach. Moreover the effect of zeroes split of EI IS has been deeply discussed and characterized. Namely the characteristic hump is due to two zeroes placed at frequencies in (2.53) which are symmetric with respect to the system frequency and whose distance is expressed in terms of the parameter α that is function of the system parameters and the desired vibration limit V_{lim} in (2.51).

Looking at the EI IS with a different perspective, the 3-impulse train cane be designed in order to suppress two undamped vibratory modes or two damped modes with the same decaying rate σ. In particular, being ω_1, ω_2 the frequencies of the two modes with $\omega_1 < \omega_2$, from (2.53) results

$$\alpha = \frac{\omega_2 - \omega_1}{\omega_2 + \omega_1} \tag{2.83}$$

60

and obviously

$$\omega_0^\star = \frac{\omega_2 + \omega_1}{2}, \tag{2.84}$$

where $\omega_0^\star$ is a virtual system frequency that defines also a virtual damping $\delta^\star$, for a given σ of the two modes. Then from (2.51), solving for the vibration limit descend

$$V_{lim}^\star = \frac{1 - \cos(\alpha \omega_0^\star T^\star)}{1 + \cos(\alpha \omega_0^\star T^\star)} \tag{2.85}$$

with $T^\star$ defined as usual in (2.22) by means of the virtual parameters $\omega_0^\star$ and $\delta^\star$. Therefore an EI IS design for a virtual system characterized by $\omega_0^\star$, $\delta^\star$ and $V_{lim}^\star$ assures complete vibration suppression of two modes at frequencies ω_1, ω_2. Moreover since the system poles are cancelled by zeroes with multiplicity of one, the robustness of the shaper with respect to each mode is comparable to a ZV IS.

This approach leads to a time optimal solution for suppression of two vibratory modes with equal decay rate σ. However it has to be noted that for widely placed modes this IS could introduce an undesirable effect of amplification between the two modes, i.e. in undamped case by means of the frequency response it can be seen that if $\omega_2 \gg \omega_1$ then $|H_{EI}(j\omega_n^\star)| > 1$. Anyway this effect can be avoided by imposing the constraint $0 < \alpha < 0.5$ from (2.37), since as been told before for $\alpha = 0.5$ results $|H_{EI}(j\omega_n^\star)| = V_{lim} = 1$. Therefore in terms of frequencies, for a given ω_1 the second mode must satisfy

$$\omega_1 > \omega_2 > 3\omega_1. \tag{2.86}$$

Chapter 3

Filtering Techniques and System-Inversion Based Planning for Vibration Reduction

3.1 Filter Based Methods for Vibration Reduction

The problem of vibrations suppression is often addressed by means of filtering techniques. In literature many works propose approaches based on commands shaped by either low-pass (LPF) or notch filters (BSF), as a solution to real case studies [2, 1, 4, 32, 33]. The motivation relies on the analysis of the vibratory system in terms of spectral components. In other words the plant is assumed to have one or more resonant frequencies which describes the modes of vibration, therefore the filter has the duty of eliminating those spectral components of the command input able to excite the system's resonances. In this way, since typical real controlled systems has low-pass behavior and being the focus on avoiding certain frequency components of the command, natural candidates for vibrations reduction by means of fiters are LPF or BSP when high dynamics are not expendable.

3.1.1 Low-Pass Filters

In order to describe the effect of shaping commands by means of filters, the case of a typical second order LTI system as in Section 1.1 fed by a step filtered by a LPF is presented first. Three of the most common filter's design techniques are considered to determine generalized considerations which relate to the filtering technique and not only to a particular design. Namely the filters used in simulation are Butterworth Filter, Chebyshev Filter and Elliptic Filter [107].

Butterworth filter assures a maximally flat magnitude response in the pass-band and an overall monotonic behavior. The design is achieved by means of the normalized Butterworth polynomials that are expressed in terms of the complex variable s assuming a cutoff frequency $\omega_c = 1$

$$
\begin{aligned}
B_n(s) &= \prod_{k=1}^{\frac{n}{2}} \left[s^2 - 2s \cos \left(\frac{2k+n-1}{2n} \pi \right) + 1 \right] \ , \ n = \text{even} \\
B_n(s) &= (s+1) \prod_{k=1}^{\frac{n-1}{2}} \left[s^2 - 2s \cos \left(\frac{2k+n-1}{2n} \pi \right) + 1 \right] \ , \ n = \text{odd}
\end{aligned}
\tag{3.1}
$$

where n is the polynomial order. Therefore the transfer function of a Butterworth filter with cutoff frequency ω_c and order n results

$$
H(s) = \frac{H_0}{B_n(\gamma)} \ , \ \text{where } \gamma = \frac{s}{\omega_c}
\tag{3.2}
$$

where H_0 is the static gain of the filter. In particular the transfer function is composed of n poles equally spaced around a circle of radius ω_c in the left half plane. Chebyshev filter has steeper transition band than Butterworth's, but admits a controlled amount of ripple of the gain amplitude in the pass-band or in the stop-band. Commonly Chebyshev filters refer to the case with equiripple behavior in the pass-band, whose frequency response for a LPF is

$$
|H(j\omega)| = \frac{1}{\sqrt{1 + \varepsilon^2 T_n^2 \left(\frac{\omega}{\omega_c} \right)}}
\tag{3.3}
$$

64

where ε is the ripple factor, ω_c is the cutoff frequency and T_n is a Chebyshev polynomial of order n. The transfer function of this filter can be defined analyzing the denominator of (3.3), in particular for an n-order filter results $2n$ poles arranged on an ellipse in the complex plane centered at the origin, with a real semi-axis of length

$$\sinh\left(\frac{1}{n}\sinh^{-1}\left(\frac{1}{\varepsilon}\right)\right) \tag{3.4}$$

and an imaginary semi-axis of length

$$\cosh\left(\frac{1}{n}\sinh^{-1}\left(\frac{1}{\varepsilon}\right)\right). \tag{3.5}$$

Moreover the $2n$ poles are symmetrically arranged on the ellipse with respect to the two axis, therefore in order to guarantee the stability of the filter the transfer function considers the poles of the left half plane p^- only. As a result the transfer function of a Chebyshev filter is

$$H(s) = \frac{1}{2^{n-1}\varepsilon} \prod_{i=1}^{n} \frac{1}{\left(s - p_i^-\right)}. \tag{3.6}$$

The Elliptic filter has faster transition between pass-band and stop-band compared to Chebyshev and Butterworth, and admits equiripple behavior in both pass-band and stop-band. It can be seen as a kind of generalization of both Chebyshev and Butterworth filters, since setting null ripple in one band defines a Chebyshev filter and setting null ripple in both bands defines a Butterworth filter. The frequency response of a low-pass elliptic filter is

$$|H(j\omega)| = \frac{1}{\sqrt{1 + \varepsilon^2 R_n^2\left(\xi, \frac{\omega}{\omega_c}\right)}} \tag{3.7}$$

where R_n is the elliptic rational function of order n, ω_c is the cutoff frequency, ε is the pass-band ripple factor and ξ is the selectivity factor which define the ripple in the stop-band as a function of ε. The transfer function of an Elliptic filter can be derived in a similar way to Chebyshev filter, that is the poles of the transfer function are the poles of the frequency response function and the zeroes result the poles of the
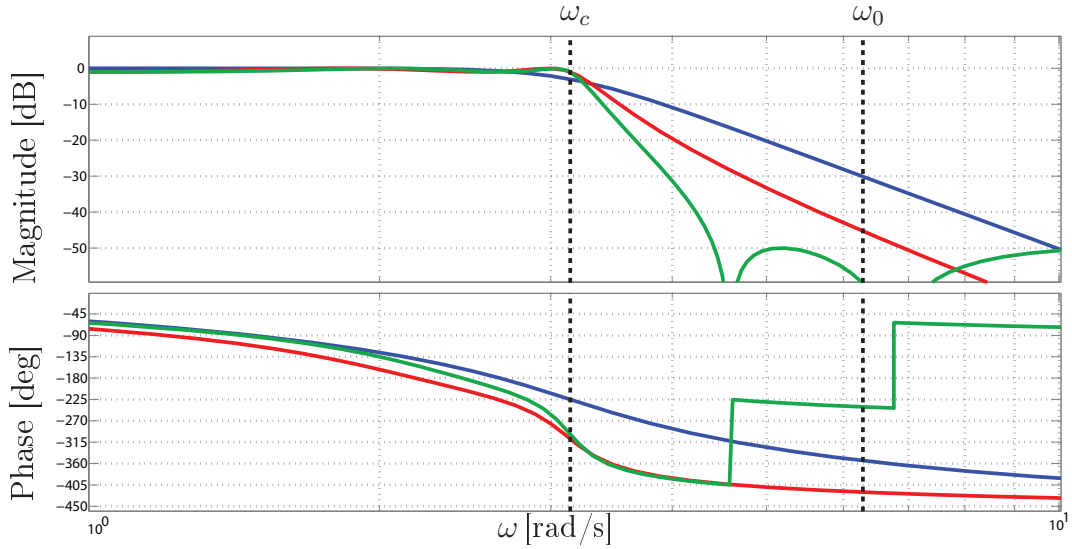
Figure 3-1: Magnitude and phase response of the considered filters with respect to frequency: in blue is reported the Butterworth filter, in red the Chebyshev filter and in green the Elliptic filter. The dashed lines identify the cutoff frequency ω_c and the system frequency ω_0.

elliptic rational function R_n.

In fig. 3-1 the Bode plots of the three LPF are reported to highlight the different behavior in terms of frequency response. All filters are of the fifth order and designed assuming a cutoff frequency one octave lower than the system frequency, $\omega_0 = 2\omega_c$, amplitude of the stop-band ripple equal to -50 dB for the Elliptic filter and amplitude of the pass-band ripple equal to 1 dB for both Elliptic and Chebyshev filter.

In fig. 3-2 also are reported the responses of an undamped second order system to a step command filtered by the three LPF. As can be seen the settling time of the filtered system is very long, moreover the vibration is reduced but not suppressed. In fact, filters does not assure vibration suppression and this can be explained by looking the pole-zero diagram of the filters in fig. 3-3 where it is clear that there is no zero able to cancel the system poles. Butterworth and Chebyshev cases are glaring since there are no zeroes at all, while the Elliptic filter has two couples of complex conjugate zeroes, but it has to be noted that usual design procedures do not refer explicitly to the placement of that zeroes.

As a matter of fact the filtering effect intended as by means of filters, doesn't rely on the presence of zeroes but in redistributing the residues of the system poles. This
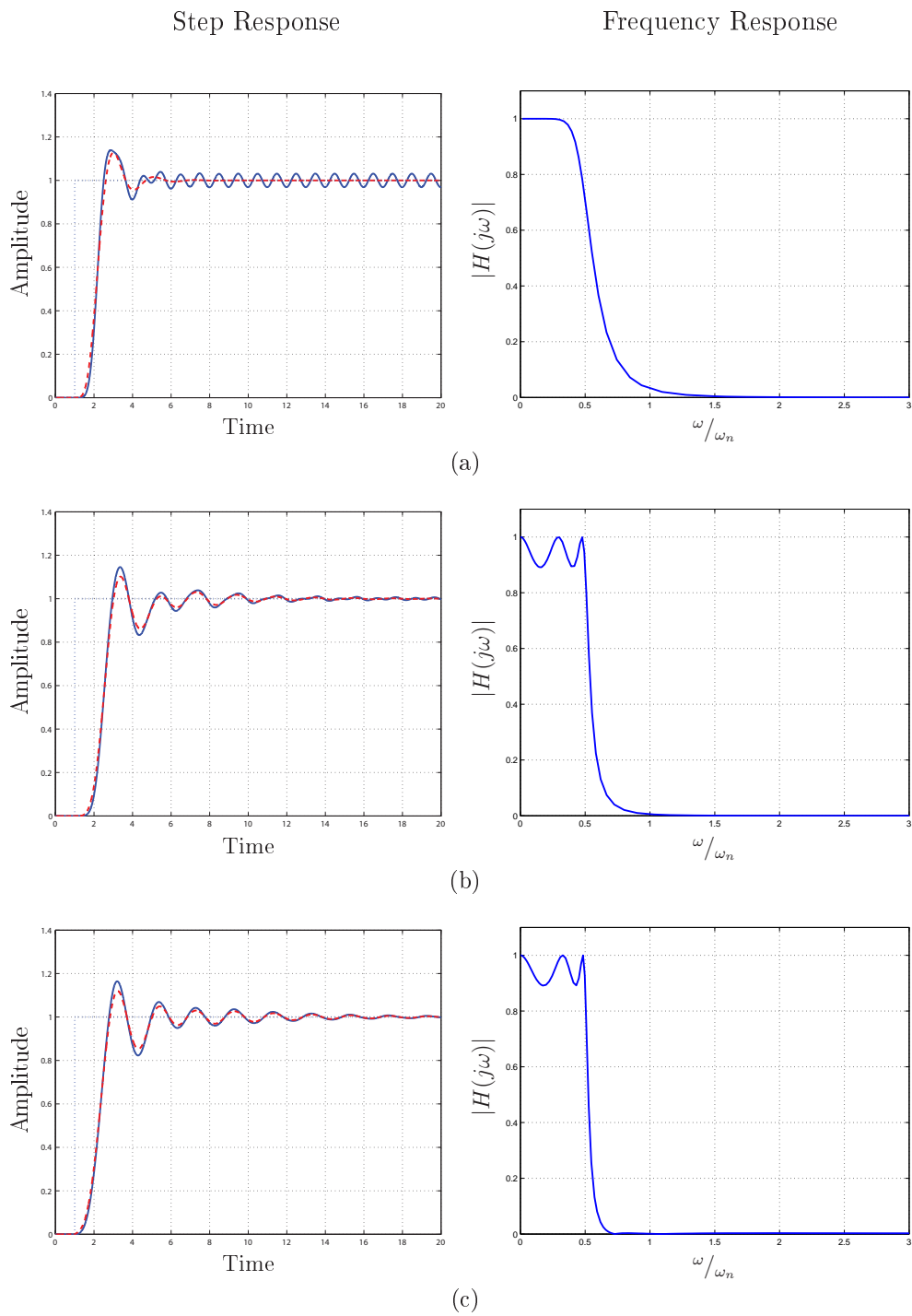
Figure 3-2: Response of the system $G(s)$ with $\delta = 0$ to a step filtered by means of Butterworth filter (a), Chebyshev filter (b) and Elliptic filter (c). Respective frequency responses of the considered filters are reported in linear scale on the right column.
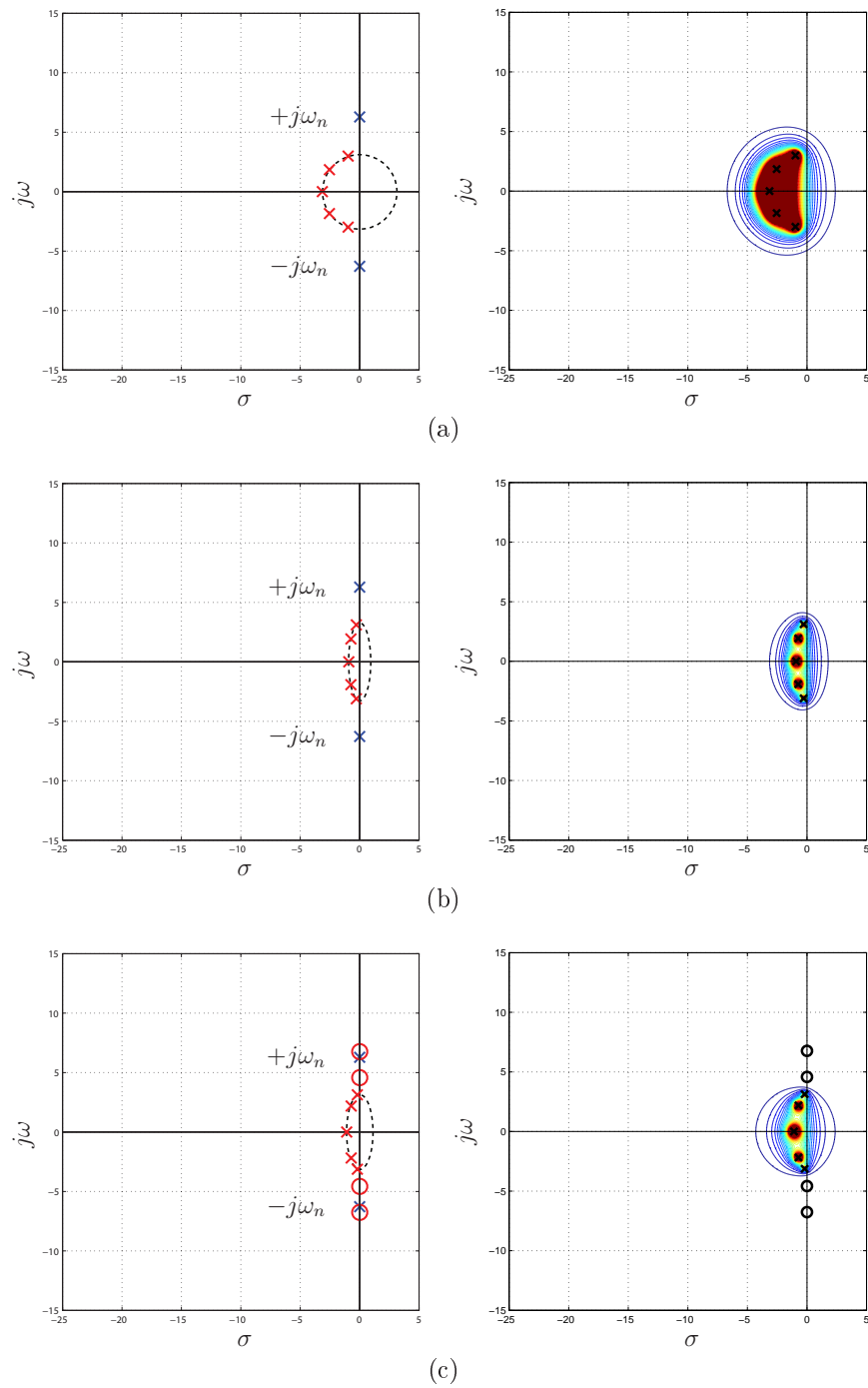
Figure 3-3: Pole-Zero diagrams of the system with $\delta = 0$ shaped by Butterworth filter (a), Chebyshev filter (b) and Elliptic filter (c). On the right the description of the filters in terms of σ and $j\omega$ variations is reported with equal scale on x and y axis. The contour lines are equally spaced of 0.1 and the filter's Pole-Zero position is highlighted with a black cross.

68
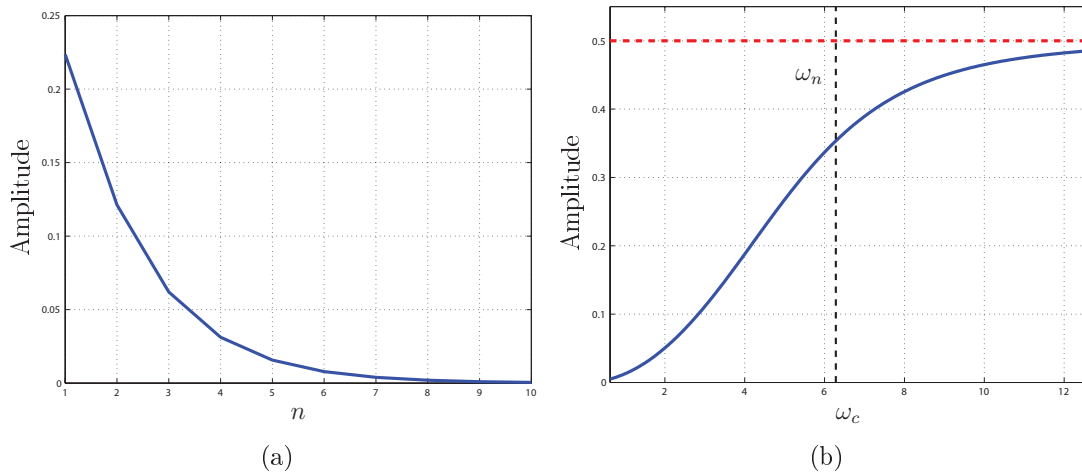
Figure 3-4: Residue associated to the system pole in case of a step filtered by a Butterworth filter. In (a) the amplitude of the residue is reported as a function of the order n of the filter with cutoff frequency such that $\omega_n = 2\omega_c$. In (b) the amplitude of the residue is reported as a function of the cutoff frequency ω_c in a second order filter. In red dashed line the unfiltered value of the residue is reported.

particular interaction can be explained assuming for example to filter a step reference commanded to an undamped second order system $G(s)$ by means of a simple Butterworth filter $H_{Bn}(s)$. In this way the Laplace transform of the step response results

$$R(s) = \frac{G(s)H_{Bn}(s)}{s} \tag{3.8}$$

then analyzing the residue of the poles of the vibratory system $G(s)$ it can be noted that the filter's parameters determine the reduction of the residue, therefore the decrease of the amplitude of that frequency component.

In fig. 3-4 is reported the amplitude of the residue of the system poles that cause the vibration as function of the filter's design parameters. Namely in fig. 3-4(a) is shown the effect of increasing the order n of the filter with a fixed cutoff frequency. In terms of frequency response this can be seen in a faster transition between pass-band and stop-band, therefore an augmented selectivity of the filter, that is a sharp reduction of the residue. In fig. 3-4(b) instead the effect of changing the cutoff frequency ω_c is reported for a given second order filter. In this case it is clear that the lower is the cutoff frequency the more the system frequency is filtered. This is exactly the behavior

69
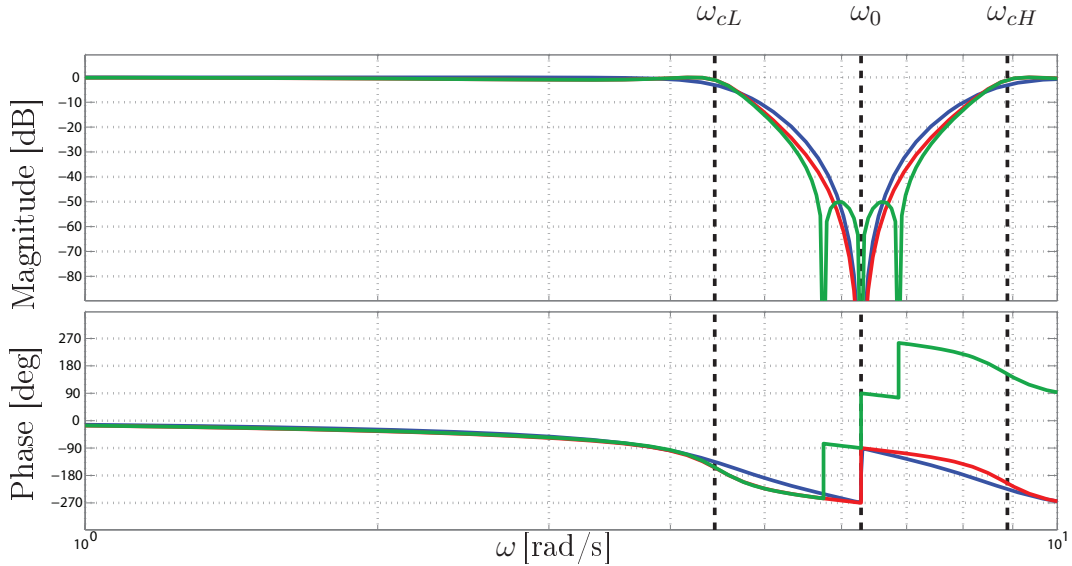
Figure 3-5: Magnitude and phase response of the considered notch filters with respect to frequency: in blue is reported the Butterworth filter, in red the Chebyshev filter and in green the Elliptic filter. The dashed lines identify the cutoff frequencies ω_{cL} and ω_{cH} and the system frequency ω_0.

described in fig. 3-4(b) where the residue grows as the cutoff frequency increases, in particular when $\omega_c > \omega_n$ the residue approaches to its unfiltered value.

3.1.2 Notch Filters

In many filtering approach to reduce vibrations, notch filters are considered instead of LPF. This is due to the possibility to reduce spectral components only in a limited frequency band without compromising eventual higher dynamics. Even in this case are considered BSF designed by means of Butterworth, Chebyshev and Elliptic filter prototypes. In particular all filters are of the third order and designed assuming a symmetric stop-band with respect to the system frequency ω_0 and a stop-band width of an octave

$$\omega_{cL} = \frac{\omega_0}{\sqrt{2}}, \ \omega_{cH} = \omega_0\sqrt{2}. \tag{3.9}$$

Also the amplitude of the stop-band ripple is set equal to -50 dB for the Elliptic filter and the amplitude of the pass-band ripple equal to 1 dB for both Elliptic and Chebyshev filter.

70

Step Response

Frequency Response

(a)

(b)

(c)
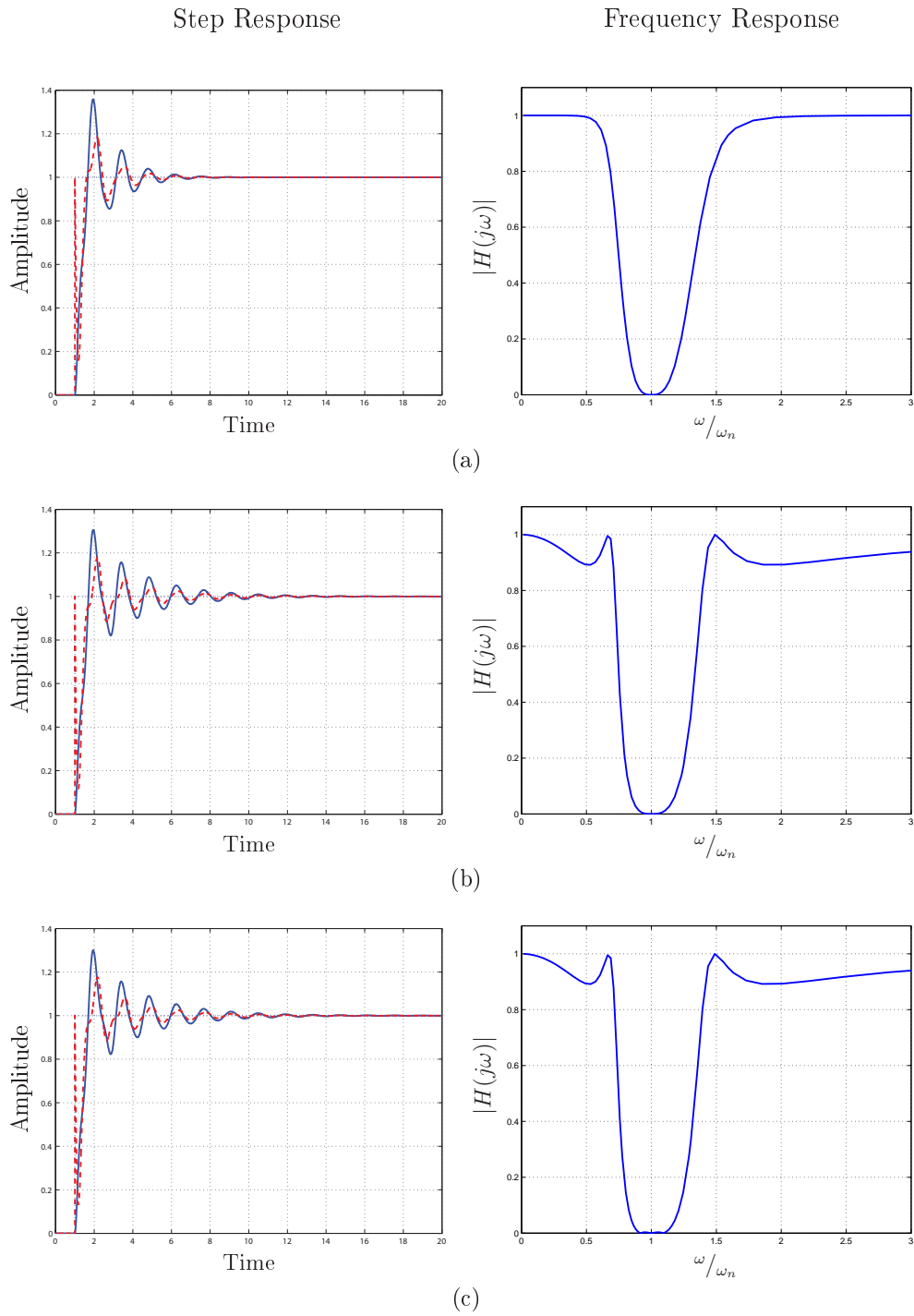
Figure 3-6: Response of the system $G(s)$ with $\delta = 0$ to a step filtered by means of Butterworth BSF (a), Chebyshev BSF (b) and Elliptic BSF (c). Respective frequency responses of the considered filters are reported in linear scale on the right column.
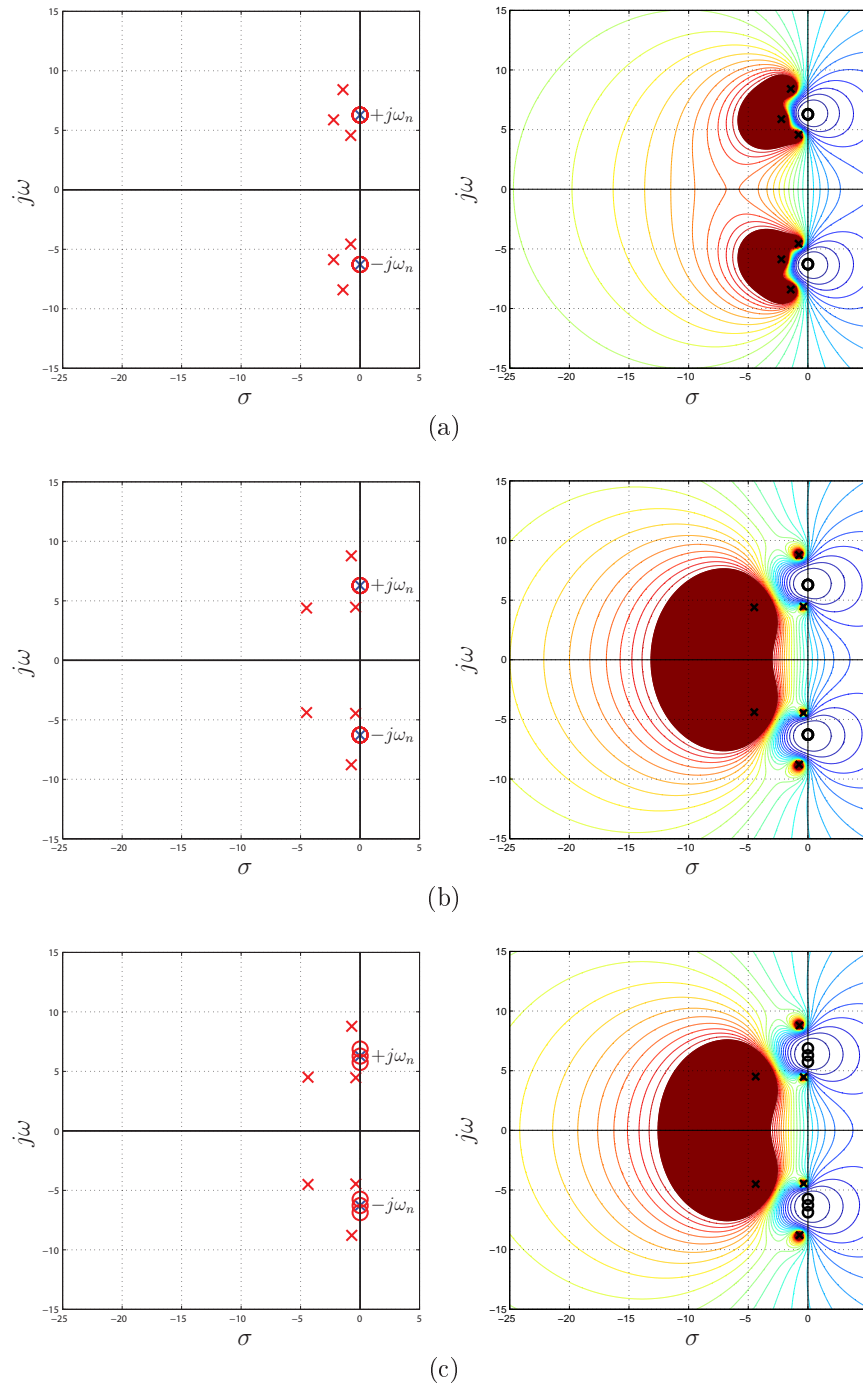
Figure 3-7: Pole-Zero diagrams of the system with $\delta = 0$ shaped by Butterworth BSF (a), Chebyshev BSF (b) and Elliptic BSF (c). On the right the description of the filters in terms of σ and $j\omega$ variations is reported with equal scale on x and y axis. The contour lines are equally spaced of 0.1 and the filter's Pole-Zero position is highlighted with a black cross.

In fig. 3-5 the Bode plots of the three BSF are reported showing the attenuation effect in the designed stop-band while outside the stop-band it can be noted that the magnitude of approximately 0 dB assures the substantial transparency of the filter for frequency components in the pass-band.

In fig. 3-6 the responses of an undamped second order system to a step command filtered by the three BSF are reported, showing better results in terms of both vibration reduction and delay, with respect to LPF in fig. 3-2. However some additional considerations have to be done by means of the pole-zero analysis in fig. 3-7. First of all the filters are designed in order to exploit the characteristic zeroes of notch filters to cancel the vibratory poles of the system $G(s)$. Therefore this can be considered the best condition to filter an undesired frequency. Also the reduced delay of BSF is influenced by the choice of third order filters while the considered LPF in Section 3.1.1 are of order 5. Anyway the delay introduced by BSF remains large with respect to other shaping techniques. This can be easily demonstrated by considering for example a ZVDD IS as reported in Section 2.4, whose effect is to cancel the vibratory poles with a couple of complex conjugate zeroes of multiplicity 3 like the BSF in fig. 3-7. In fact assuming to express the distortion introduced by the shapers in terms of periods of system vibration, while the ZVDD IS lasts 1.5 periods, the filters in fig. 3-7 last from about 8 to 12 times longer.

3.1.3 Considerations on Command Shaping by means of Filters

In Section 3.1.1 and 3.1.2 the effect of command shaping by means of typical filtering techniques has been presented, showing that filters basically can not assure vibrations suppression. Although the presence of zeroes, even BSF can not be considered as vibration suppressors, mainly because the typical design procedures doesn't rely on the complete suppression of a particular frequency, but in the attenuation of a band of frequencies. This behavior is even more evident in case of damped system as reported in fig. 3-8. It is well known that in case of a second order system $G(s)$ with $\delta \neq 0$ the

73

vibratory poles no more lie on the imaginary axis of the complex plane, therefore the pole-zero cancellation is impossible.

In several papers filters are compared to input shapers by means of deep experimental analysis showing a relevant performance gap in terms of vibration suppression [84, 90, 91]. In addition to the mentioned inability to assure complete vibration suppression, an other noticeable disadvantage is the large time delay introduced by the filters. This is one of the side effects of the mechanism of residues modification of filters. In fact, a part from the considerations on the cutoff frequency which has direct consequence on the overall dynamics, it can be seen that in general the higher is the filter order, the more effective is the filter. However raising the order of the filter means to increase the number of the poles introduced by the filter. As a result the poles introduced by means of usual filtering techniques add undesired dynamics visible as large overshoots in the presented step responses, and also imply a large phase delay therefore an undesired distortion.

In Section 3.1.1 and 3.1.2 only analog filters have been considered for brevity. As a matter of fact same results can be achieved with digital implementations by means of Infinite Impulse Response Filters (IIR). Moreover as reported in details in [84, 90, 91] even Finite Impulse Response Filters (FIR) designed by means of typical methods (windowing and Parks - McClellan above all) doesn't reach the benchmark of IS, although FIR filters shows better performances than analog and IIR in reducing vibrations.
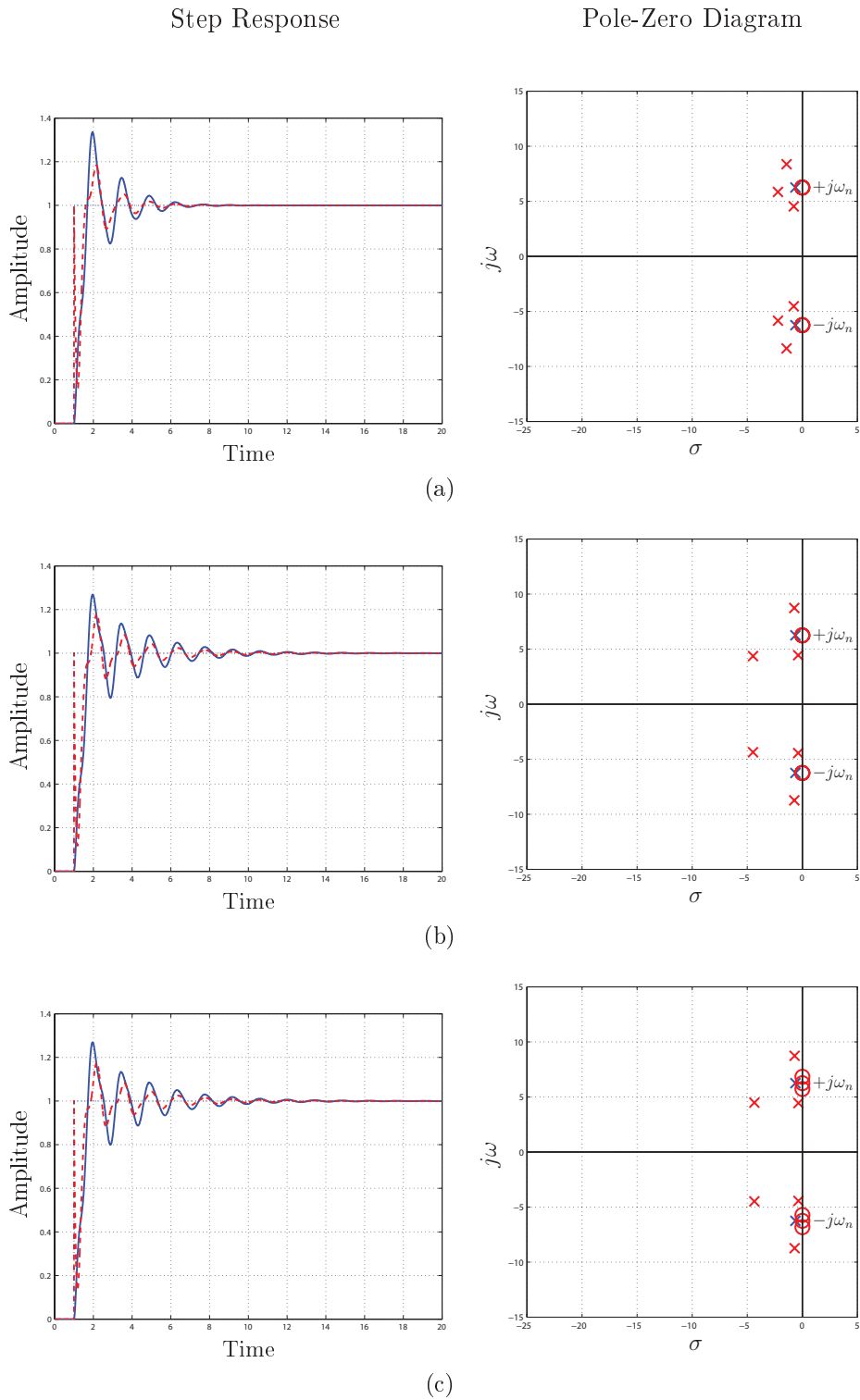
Figure 3-8: Response of the system $G(s)$ with $\delta = 0.1$ to a step filtered by means of Butterworth BSF (a), Chebyshev BSF (b) and Elliptic BSF (c). Respective Pole-Zero diagram of the considered filters are reported in the right column.

75

3.2 System Inversion Based Techniques for Vibration Suppression

In Section 3.1.3 has been reported that usual filter design techniques have no aim of vibration suppression. Roughly speaking, this is due to the fact that poles and zeroes are mainly exploited in terms of their characteristic behavior to reduce or increase the gain of the frequency response. In fact, filter designs by means of polynomials which basically define a pole-zero placement in order to achieve a desired shaping of the frequency response of the filter.

However considering BSF in Section 3.1.2, some additional considerations can be done by analyzing the pole-zero diagram in fig. 3-7 from another point of view. As said the particular design parameters choice in the treated filters, permitted to achieve a perfect cancellation of the undesired vibratory dynamic. Therefore assuming that the focus of a filter is to eliminate a certain frequency component indeed and the order n of the filter is the multiplicity of the zeroes devoted to that cancellation, then the polynomial prototypes may be intended as particular constraints by means of which n additional stable dynamics are introduced in order to guarantee causality of the filter. In theory according to this system inversion based perspective, the poles placement can be achieved in a more convenient way than by means of usual polynomials, such as by placing n arbitrarily fast stable real poles. As a matter of fact this trivial solution as some drawbacks, that is it doesn't take into account the actuator limits and there is no constraint on the gain of the frequency response, a part from the static gain.

Anyway the system inversion approach under reasonable conditions results very effective and several works in literature report methods that assure complete residual vibration suppression. In particular in [78, 79, 80] a method based on system inversion assures complete absence of oscillations during and at the end of a point-to-point motion, providing also a time minimization. This technique consists in a proper motion planning which takes into account the transfer function of a second order vibratory system and a desired vibration-free motion profile. Namely the authors propose to

76

define *a priori* and impose a polynomial of class $C^{(h)}$ as target function for the system output, in order to achieve monotonicity and h continuous derivatives. Therefore a family of $C^{(h-1)}$-class functions is obtained by means of dynamic inversion of the vibratory system and the target function. Finally by means of a numerical optimization algorithm the minimum time solution is selected.

This approach provides a very good motion assuring vibration suppression and also an arbitrary smoothness avoiding the typical step-like behavior of input shaping. In addition presents a time delay comparable to a ZVD IS that is the most common input shaper. However the main drawback is related to robustness since in general system inversion techniques require the complete knowledge of the system that has to be inverted. Obviously this can not be assured in general in real cases, where often feed-forward techniques are implemented to enhance performances of servo systems whose transfer function is unknown and then to be estimated.

Chapter 4

Filters for Online Trajectory Planning

Planning motion laws and trajectories for the actuation system of a robot has a key role not only from a functional point of view but also regarding the performance level achievable by a given system. During decades plenty of techniques have been presented for trajectory planning in order to meet many different requirements such as timing, physical limitations of the actuators, energy parameters but also other features related to the reliability like vibration reduction. In step with planning, many methods have been proposed regarding the generation of such trajectories and the implementation on real machines of proper trajectory generators, possibly capable of online generation of the motion profiles.

4.1 Analytical Trajectories for Point-to-Point Motions

Trajectories for point-to-point motions are of great importance as they are the basis for more complex movements. Some of these are very common in practical industrial applications since they allow to satisfy several mechanical requirements while maintaining a good ease of use.

4.1.1 Trapezoidal Velocity Trajectory

Trajectories with trapezoidal velocity are very common method to obtain trajectories with a continuous velocity profile. In terms of position set-point are characterized by linear motions joined with parabolic blends, in particular a single point-to-point motion can be divided into three parts. Assuming a positive displacement, i.e. $q_1 > q_0$, duration T_a of the acceleration phase equal to the duration T_d of the deceleration phase, and time $t_0 = 0$, the trajectory is defined as follows:

1. **Acceleration phase**, $t \in [0, T_a]$. The position, velocity and acceleration are expressed as

$$\begin{cases} q(t) &= a_0 + a_1 t + a_2 t^2 \\ \dot{q}(t) &= a_1 + 2a_2 t \\ \ddot{q}(t) &= 2a_2 \end{cases} \tag{4.1}$$

that is the acceleration is positive and constant, and therefore the velocity is a linear function of time and the position is a parabolic curve. The three parameters a_0, a_1, and a_2 are defined accordingly to the constraints on the initial position q_0 and velocity v_0, and on the constant velocity v_v desired at the end of the acceleration phase. Assuming initial velocity set to zero, results

$$\begin{cases} a_0 &= q_0 \\ a_1 &= 0 \\ a_2 &= \dfrac{v_v}{2T_a} \end{cases} \tag{4.2}$$

therefore the constant acceleration is v_v / T_a.

2. **Constant velocity phase**, $t \in [T_a, t_1 - T_a]$. The position, velocity and acceleration are expressed as

$$\begin{cases} q(t) &= b_0 + b_1 t \\ \dot{q}(t) &= b_1 \\ \ddot{q}(t) &= 0 \end{cases} \tag{4.3}$$

that is the acceleration is null, the velocity is constant and the position is a linear function of time. Also for continuity reasons results that $b_1 = v_v$ and

$$q(T_a) = q_0 + \frac{v_v T_a}{2} = b_0 + \frac{v_v}{T_a}, \tag{4.4}$$

therefore

$$b_0 = q_0 - \frac{v_v T_a}{2}. \tag{4.5}$$

3. **Deceleration phase**, $t \in [t_1 - T_a, t_1]$. The position, velocity and acceleration are expressed as

$$\begin{cases} q(t) &= c_0 + c_1 t + c_2 t^2 \\ \dot{q}(t) &= c_1 + 2c_2 t \\ \ddot{q}(t) &= 2c_2 \end{cases} \tag{4.6}$$

that is a constant negative acceleration is present, the velocity decreases linearly and the position is again a polynomial function of degree two. The parameters c_0, c_1, and c_2 are by means of the conditions on the final position q_1 and velocity v_1, and on the constant velocity v_v at the beginning of the deceleration phase. Assuming a null final velocity, results

$$\begin{cases} c_0 &= q_1 - \frac{v_v t_1^2}{2T_a} \\ c_1 &= \frac{v_v t_1}{T_a} \\ c_2 &= -\frac{v_v}{2T_a} \end{cases} \tag{4.7}$$

In conclusion, the position trajectory $q(t)$ in the general case $t_0 \neq 0$, can be defined as

$$q(t) = \begin{cases} q_0 + \frac{v_v}{2T_a}(t - t_0)^2, & t_0 \leq t < t_0 + T_a \\ q_0 + v_v \left(t - t_0 - \frac{T_a}{2} \right), & t_0 + T_a \leq t < t_1 - T_a \\ q_1 - \frac{v_v}{2T_a}(t_1 - t)^2, & t_1 - T_a \leq t \leq t_1 \end{cases} \tag{4.8}$$

In order to univocally determine the trapezoidal trajectory, some additional conditions must be specified. A typical condition concerns the time length of the acceleration
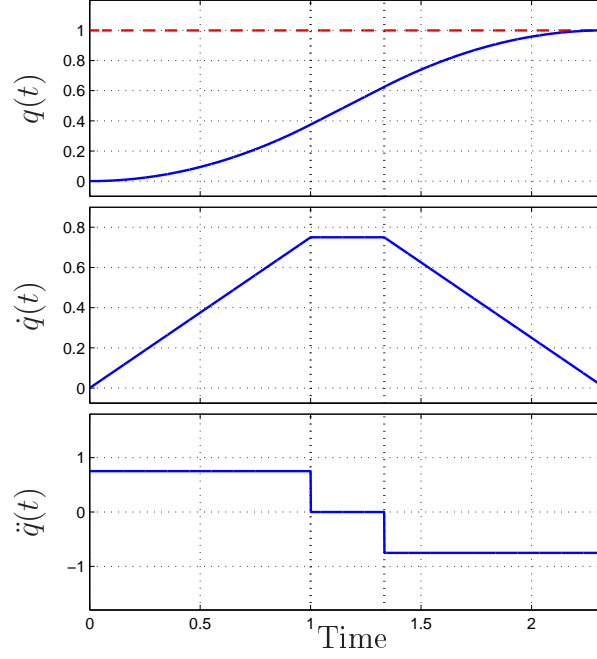
Figure 4-1: Position, velocity and acceleration of a point-to-point motion from 0 to q_1 by means of trapezoidal velocity trajectory.

and deceleration periods T_a, that must satisfy the obvious condition $T_a \leq T/2$ where T is the total duration of the motion. In addition some other constraints on the maximum velocity and acceleration of the actuation system can be imposed as deeply discussed in [9]. Obviously, these conditions affect the feasibility of the trajectory, therefore the given conditions must satisfy some geometric constraints. In particular, from the velocity continuity condition one can obtain the relation

$$a_a T_a = \frac{q_m - q_a}{T_m - T_a}, \quad \text{where} \quad \begin{cases} q_a &= q(t_0 + T_a) \\ q_m &= \frac{q_1 + q_0}{2} = q_0 + \frac{h}{2} \\ T_m &= \frac{t_1 - t_0}{2} = \frac{T}{2} \end{cases} \tag{4.9}$$

where a_a is the constant acceleration value in the first phase. Then by substituting results that

$$a_a T_a^2 - a_a(t_1 - t_0)T_a + (q_1 - q_0) = 0 \tag{4.10}$$

which is the geometric constraint that any couple (a_a, T_a) must satisfy in order to

82

achieve a feasible trapezoidal velocity trajectory.

4.1.2 Double-S Velocity Trajectory

Double-S velocity trajectories are an improvement of trapezoidal velocity trajectories of Section 4.1.1 in terms of smoothness and therefore on the stress and the vibrational effects generated on the transmission chain and on the load by the motion profile. A double-S trajectory is characterized by a continuous, linear piece-wise, acceleration profile instead of the typical discontinuous acceleration profile of trapezoidal one. In this manner, the resulting velocity is composed by linear segments connected by parabolic blends, thus the reason of the name double-S for this trajectory. It is known also as seven segments trajectory, because it is composed by seven different tracts with constant jerk, and it is precisely the typical step profile of the jerk which makes this trajectory much less stressful for the mechanical systems with respect to trapezoidal velocity trajectories which are characterized by an impulsive jerk profile.

Usually the double-S trajectory is defined assuming symmetrical actuator limits that is

$$j_{min} = -j_{max}, \quad a_{min} = -a_{max}, \quad v_{min} = -v_{max}, \tag{4.11}$$

where $j_{min/max}$, $a_{min/max}$, $v_{min/max}$, are the minimum and maximum values of respectively jerk, acceleration and velocity. Moreover in the usual definition the case $q_1 > q_0$ with $t_0 = 0$ is considered, and generic initial and final values of velocity v_0, v_1 are assumed, while accelerations a_0, a_1 are seto to zero. In addition the trajectory is reported by means of the following definitions:

T_{j1} : time interval in which the jerk is constant (j_{min} or j_{max}) during the acceleration phase;

T_{j2} : time interval in which the jerk is constant (j_{min} or j_{max}) during the deceleration phase;

T_a : acceleration period;

T_v : constant velocity period;

T_d : deceleration period;

T : total duration of the trajectory ($= T_a + T_v + T_d$).

In the same manner of Section 4.1.1 the trajectory can be easily described by distinguishing three phases, namely acceleration phase, maximum velocity phase and deceleration phase.

1. **Acceleration phase**, $t \in [0, T_a]$. The acceleration phase can be split according to the three segments of the jerk profile

   (a) $t \in [0, T_{j1}]$

   $$
   \begin{cases}
   q(t) & = q_0 + v_0 t + j_{max} \dfrac{t^3}{6} \\
   \dot{q}(t) & = v_0 + j_{max} \dfrac{t^2}{2} \\
   \ddot{q}(t) & = j_{max} t \\
   q^{(3)}(t) & = j_{max}
   \end{cases}
   \tag{4.12}
   $$

   (b) $t \in [T_{j1}, T_a - T_{j1}]$

   $$
   \begin{cases}
   q(t) & = q_0 + v_0 t + \dfrac{a_{max}}{6}(3t^2 - 3T_{j1}t + T_{j1}^2) \\
   \dot{q}(t) & = v_0 + a_{max}\left(t - \dfrac{T_{j1}}{2}\right) \\
   \ddot{q}(t) & = j_{max}T_{j1} = a_{max} \\
   q^{(3)}(t) & = 0
   \end{cases}
   \tag{4.13}
   $$

   (c) $t \in [T_a - T_{j1}, T_a]$

   $$
   \begin{cases}
   q(t) & = q_0 + (v_{max} + v_0)\dfrac{T_a}{2} - v_{max}(T_a - t) - j_{min}\dfrac{(T_a - t)^3}{6} \\
   \dot{q}(t) & = v_{max} + j_{min}\dfrac{(T_a - t)^2}{2} \\
   \ddot{q}(t) & = -j_{min}(T_a - t) \\
   q^{(3)}(t) & = j_{min} = -j_{max}
   \end{cases}
   \tag{4.14}
   $$

84

2. **Constant velocity phase**, $t \in [T_a, T_a + Tv]$. The position, velocity and acceleration are expressed as

$$
\begin{cases}
q(t) & = q_0 + (v_{max} + v_0)\dfrac{T_a}{2} + v_{max}(t - T_a) \\[2mm]
\dot{q}(t) & = v_{max} \\[2mm]
\ddot{q}(t) & = 0 \\[2mm]
q^{(3)}(t) & = 0
\end{cases}
\tag{4.15}
$$

3. **Deceleration phase**, $t \in [T - T_d, T]$. Again, the deceleration phase can be split according to the three segments of the jerk profile

(a) $t \in [T - T_d, T - T_d + T_{j2}]$

$$
\begin{cases}
q(t) & = q_1 - (v_{max} + v_1)\dfrac{T_d}{2} + v_{max}(t - T + T_d) - j_{max}\dfrac{(t - T + T_d)^3}{6} \\[2mm]
\dot{q}(t) & = v_{max} - j_{max}\dfrac{(t - T + T_d)^2}{2} \\[2mm]
\ddot{q}(t) & = -j_{max}(t - T + T_d) \\[2mm]
q^{(3)}(t) & = j_{min} = -j_{max}
\end{cases}
$$

$$\tag{4.16}$$

(b) $t \in [T - T_d + T_{j2}, T - T_{j2}]$

$$
\begin{cases}
q(t) & = q_1 - (v_{max} + v_1)\dfrac{T_d}{2} + v_{max}(t - T + T_d) + \\[2mm]
& \quad + \dfrac{a_{min}}{6}\left(3(t - T + T_d)^2 - 3T_{j2}(t - T + T_d) + T_{j2}^2\right) \\[2mm]
\dot{q}(t) & = v_{max} + a_{min}\left(t - T + T_d - \dfrac{T_{j2}}{2}\right) \\[2mm]
\ddot{q}(t) & = -j_{max}T_{j2} = a_{min} \\[2mm]
q^{(3)}(t) & = 0
\end{cases}
\tag{4.17}
$$
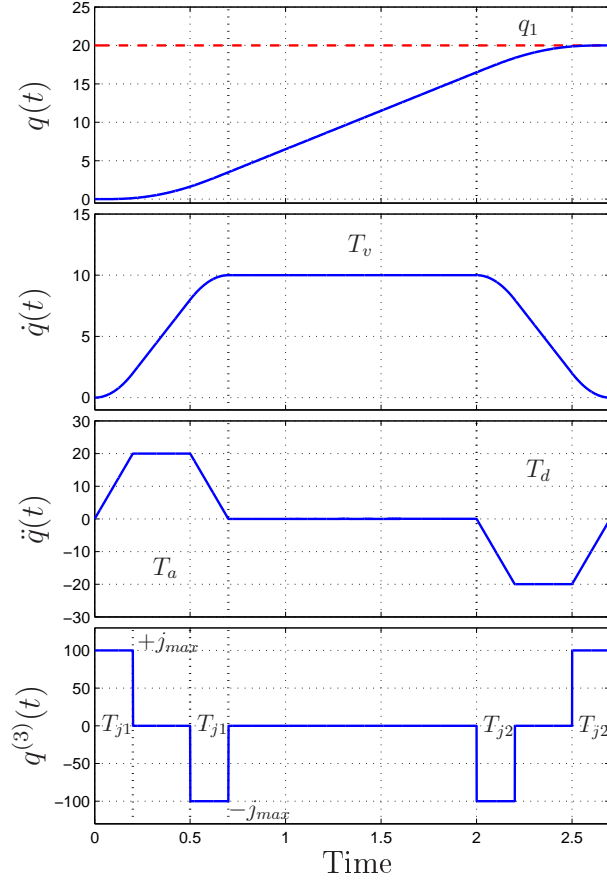
Figure 4-2: Position, velocity, acceleration and jerk of a point-to-point motion from 0 to q_1 by means of double-S velocity trajectory.

(c) $t \in [T - T_{j2}, T]$

$$
\begin{cases}
q(t) & = q_1 - v_1(T - t) - j_{max}\dfrac{(T - t)^3}{6} \\[2mm]
\dot{q}(t) & = v_1 + j_{max}\dfrac{(T - t)^2}{2} \\[2mm]
\ddot{q}(t) & = -j_{max}(T - t) \\[2mm]
q^{(3)}(t) & = j_{max}
\end{cases}
\qquad (4.18)
$$

Even in this case the correct execution of the double-S trajectory is subject to feasibility conditions, that is the existence of the mentioned phases, in particular it is required to perform the trajectory by means of a double jerk impulse. Moreover it can be demonstrated that a trajectory planned in order to reach, when possible, the maximum (minimum) value for jerk, acceleration and velocity, it is a minimum time trajectory. However the parameters definition of a double-S trajectory can be sub-

jected to several constraints in practical implementations, such as prescribed time length of some phase and different condition on initial and final velocity values. In [9] the planning of double-S trajectories with various constraints is addressed in details.

4.1.3 Harmonic Trajectory

Harmonic trajectories are characterized by an acceleration profile which is proportional to the position profile, with opposite sign. Geometrically the trajectory $q(t)$ can be described as the projection of a point p moving on a circle with constant velocity, on the diameter of the circle itself. In general form results

$$q(t) = \frac{q_1 - q_0}{2} \left(1 - \cos \frac{\pi(t - t_0)}{T} \right) + q_0, \tag{4.19}$$

where T is the total duration of the motion. Then by deriving

$$\dot{q}(t) = \frac{\pi h}{2T} \sin \left(\frac{\pi(t - t_0)}{T} \right)$$
$$\ddot{q}(t) = \frac{\pi^2 h}{2T^2} \cos \left(\frac{\pi(t - t_0)}{T} \right) \tag{4.20}$$
$$q^{(3)}(t) = -\frac{\pi^3 h}{2T^3} \sin \left(\frac{\pi(t - t_0)}{T} \right)$$

Harmonic trajectories are often used in more complex trajectories definition, characterized in general by polynomial segments connected by means of sinusoidal blends. This because the use of trigonometric functions permit to uniquely define all the requested derivative order of a trajectory by means of integration or derivation operations, given a single profile. Thus it may be of interest to plan trajectories by directly specifying the velocity or acceleration profile as a composition of constant segments connected by sinusoidal profiles, then the position, jerk, and so on, can be simply obtained. In particular trajectories with constant velocity/acceleration and harmonic blends are of rather used and described in [9].
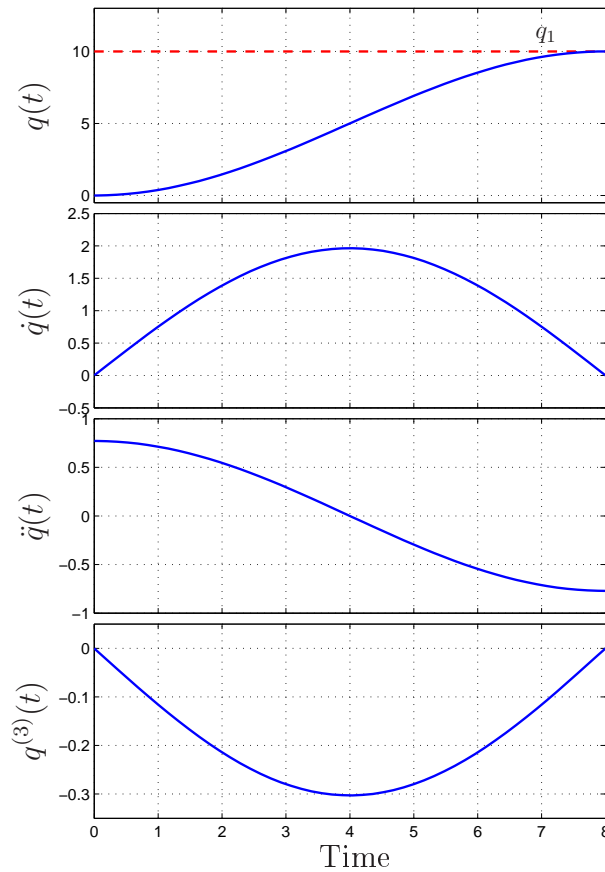
Figure 4-3: Position, velocity, acceleration and jerk of a point-to-point motion from 0 to q_1 by means of harmonic trajectory.

4.2 Analytical Trajectories for 3D Motions: Uniform B-Spline Trajectory

Spline functions are extensively used in planning trajectories for robots because of their flexibility. Tasks demanded to robots often require position profiles with complex shapes which are usually defined by means of a number of via-points. These via-points are then interpolated or approximated with smooth functions to be optimized in order to comply with the constraints imposed by the specific robot application, i.e. kinematic constraints (such as limit values of velocity, acceleration, jerk, etc.) or dynamic constraints on the maximum torque available. In general, such interpolation tasks are performed by means of cubic splines since they assure the continuity of velocity and acceleration and prevent large oscillations of the trajectory that can

result with high order polynomials [9]. That is when $n + 1$ points are given, in lieu of a unique interpolating polynomial of degree n it is possible to use n polynomials of degree $d = 3$, each one defining a segment of the trajectory. The overall function $q(t)$ defined in this manner is called cubic spline and results

$$q(t) = \{q_k(t),\ t \in [t_k, t_{k+1}]\,,\ k = 0, \ldots, n - 1\}\,,$$
$$q_k(t) = a_{k0} + a_{k1}\,(t - t_k) + a_{k2}\,(t - t_k)^2 + a_{k3}\,(t - t_k)^3\,. \tag{4.21}$$

In this way a complex motion composed of $n + 1$ via-points is completely defined by solving a linear system of n equations with a total number of $4n$ coefficients to be determined. In particular the solution is given by means of imposing several conditions which has to be satisfied:

- $2n$ conditions for the interpolation of the given via-points, since each cubic function must cross the points at its extremities;

- $n - 1$ conditions for the continuity of the velocities at the transition points;

- $n - 1$ conditions for the continuity of the accelerations at the transition points.

The remaining two degrees of freedom permit to impose two additional constraints that usually refer to boundary conditions of the spline derivatives. Moreover in literature several techniques have been presented in order to minimize some quantities, such as acceleration, jerk or the total traveling time of robot trajectories subject to constraints of velocity acceleration and jerk.

In some applications the requirement of planning trajectories with continuous derivatives up to a given order r makes preferable the adoption of splines in the so-called B-form, i.e. B-splines. Also the attractiveness of B-spline is because they are much simpler from the computational point of view, and because a local modification can be made quickly and easily without recomputing the entire trajectory.

A generic B-spline trajectory is defined as

$$q(t) = \sum_{j=0}^{m} \boldsymbol{p}_j\, \boldsymbol{B}_j^d(t), \qquad t_{min} \leq t \leq t_{max} \tag{4.22}$$

89
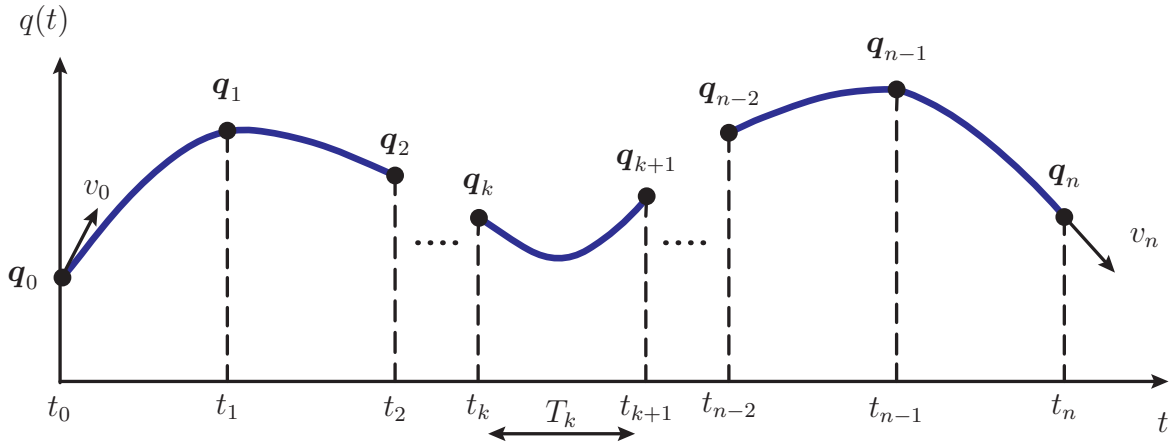
Figure 4-4: Spline trajectory through n + 1 points.

where $\boldsymbol{B}_j^d(t)$ is a B-spline basis function of degree d, and $\boldsymbol{p}_j$ are the control points, which are scalar parameters that determine the shape of the curve and must be computed by imposing interpolation conditions on the given data points $\boldsymbol{q}_k$. That is finding the values of the unknown parameters $\boldsymbol{p}_j$, $j = 0, \ldots, m$, which guarantee that given $n + 1$ via-points to be interpolated at their respective $n + 1$ time instants (also called knots), the B-spline function satisfies

$$q(t_k) = \boldsymbol{q}_k, \ k = 0, \ldots, n. \tag{4.23}$$

In particular the control points $\boldsymbol{p}_j$ can be defined by means of a linear system composed of $n + 1$ equations in $m + 1$ unknown of the form

$$q(t_k) = \begin{bmatrix} \boldsymbol{B}_0^d(t_k), & \boldsymbol{B}_1^d(t_k), & \ldots, & \boldsymbol{B}_{m-1}^d(t_k), & \boldsymbol{B}_m^d(t_k) \end{bmatrix} \begin{bmatrix} \boldsymbol{p}_0 \\ \boldsymbol{p}_1 \\ \vdots \\ \boldsymbol{p}_{m-1} \\ \boldsymbol{p}_m \end{bmatrix}. \tag{4.24}$$

Then, being the number of control points $m + 1 = (n + 1) + d - 1$ (for odd values of d, $m + 1 = (n + 1) + d$ when even value of d is considered), in order to achieve a

90
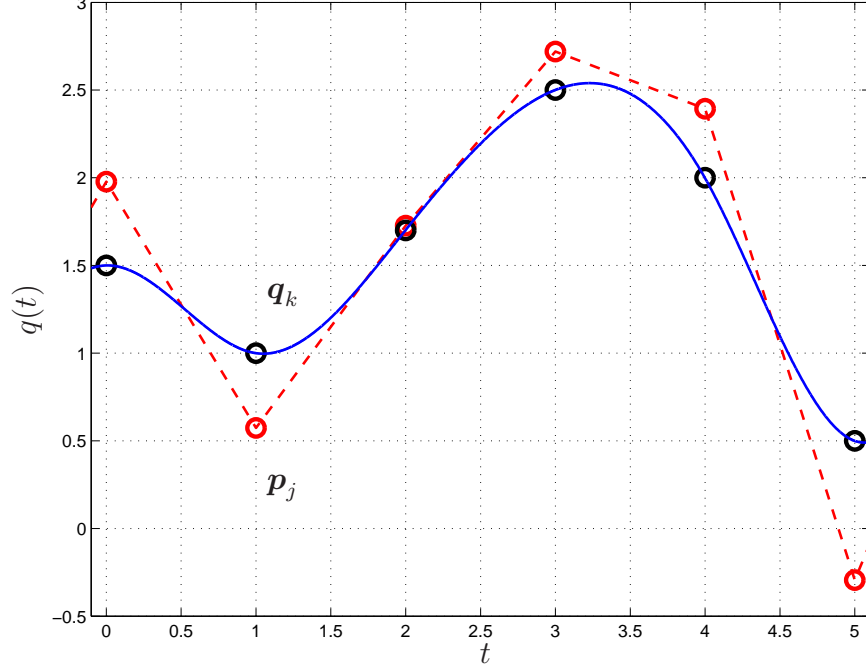
Figure 4-5: B-spline trajectory $q(t)$ passing through the desired via-points $\boldsymbol{q}_k$. In red the correspondent control points $\boldsymbol{p}_j$ are reported.

unique solution further $d - 1$ (or d) equations of the form

$$q^{(i)}(t_k) = \left[\boldsymbol{B}_0^{d(i)}(t_k),\ \boldsymbol{B}_1^{d(i)}(t_k),\ \ldots,\ \boldsymbol{B}_{m-1}^{d(i)}(t_k),\ \boldsymbol{B}_m^{d(i)}(t_k) \right] \begin{bmatrix} \boldsymbol{p}_0 \\ \boldsymbol{p}_1 \\ \vdots \\ \boldsymbol{p}_{m-1} \\ \boldsymbol{p}_m \end{bmatrix} \qquad (4.25)$$

has to be added imposing $d - 1$ (or d) conditions on higher order time derivatives of the curve. Alternatively $d - 1$ (or d) further equations can be added to impose continuity of the curve and its derivative at initial and final time instants (periodic B-spline).

Regarding the j-th B-spline basis function of degree d, is defined in a recursive manner as

$$\boldsymbol{B}_j^d(t) = \frac{t - t_j}{t_{j+d} - t_j} \boldsymbol{B}_j^{d-1}(t) + \frac{t_{j+d+1} - t}{t_{j+d+1} - t_{j+1}} \boldsymbol{B}_{j+1}^{d-1}(t) \qquad (4.26)$$

91

with

$$B_j^0(t) = \begin{cases} 1, & \text{if } t_j \leq t < t_{j+1} \\ 0, & \text{otherwise.} \end{cases} \qquad (4.27)$$

Therefore a B-spline basis function defined by means of (4.26) and (4.27) presents the following properties:

- $B_j^d(t)$ is a piecewise polynomial, defined for all $t \in [t_{min}, t_{max}]$;

- $B_j^d(t)$ is equal to zero everywhere except in the interval $t \in [t_j, t_{j+d+1})$;

- The interval $[t_k, t_{k+1})$ is called k-th *knot span* and can be of zero length in case of coincident knots;

- The B-spline basis functions are normalized so that

$$\sum_{j=0}^{m} B_j^d(t) = 1, \qquad t_{min} \leq t \leq t_{max} \qquad (4.28)$$

- In every knot span $[t_k, t_{k+1})$ at most $d+1$ basis functions are not null, namely $B_{k-d}^d, \ldots, B_k^d$.

A particular case of B-splines is represented by *uniform* B-splines, that are defined for an equally-spaced distribution of the knots, i.e. $t_{j+1} - t_j = T$, $j = 0, \ldots m - 1$. In this case, the basis functions for a given degree d are consistent under shifts:

$$B_{j+1}^d(t) = B_j^d(t - T), \qquad j = 0, \ldots, m - 1.$$

Therefore, for uniform B-splines it is possible to express the $(j+1)$-th basis function B_j^d in terms of the first basis function B_0^d, hereafter simply denoted by B^d:

$$B_j^d(t) = B^d(t - jT), \qquad j = 0, \ldots, m$$

and the B-spline can be rewritten as

$$q_u(t) = \sum_{j=0}^{m} p_j B^d(t - jT), \qquad 0 \leq t \leq mT. \qquad (4.29)$$

92

Moreover, for uniform B-splines, the definition (4.26) of the basis function $\boldsymbol{B}^d(t)$ of degree d is equivalent to

$$
\begin{aligned}
\boldsymbol{B}^d(t) &= \frac{1}{T}\boldsymbol{B}^{d-1} * \boldsymbol{B}^0 \\
&= \underbrace{\frac{1}{T}\boldsymbol{B}^0 * \frac{1}{T}\boldsymbol{B}^0 * \ldots * \frac{1}{T}\boldsymbol{B}^0}_{d \text{ times}} * \boldsymbol{B}^0,
\end{aligned}
\tag{4.30}
$$

with

$$
\boldsymbol{B}^0(t) = \begin{cases} 1, & \text{if } 0 \le t < T \\ 0, & \text{otherwise.} \end{cases}
$$
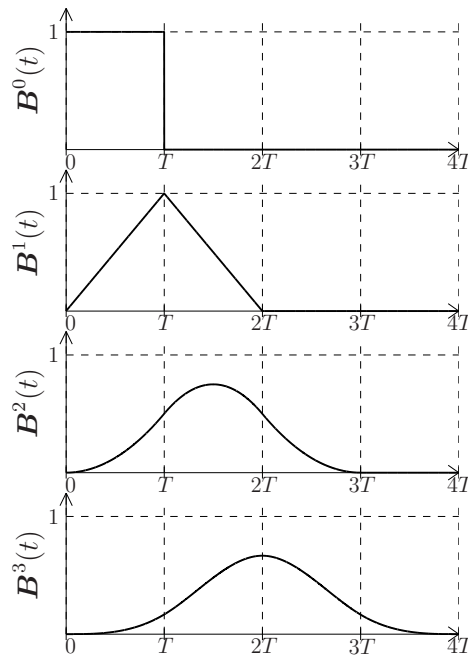
Figure 4-6: B-spline basis function $\boldsymbol{B}^d(t)$ obtained for different values of d.

4.3 Dynamic Filters for Trajectory Generation

4.3.1 Filter-Based Generator for Multi-Segment Polynomial Trajectories

The need of planning trajectories online has led to the development of a number of filters able to produce motion profiles with the desired degree of smoothness simply starting from rough reference signals, such as step functions, which set the desired final position. In [13] a very simple and effective approach based on dynamic filters is presented and allows to plan minimum-time trajectories for robots or automatic machines under constraints of velocity, acceleration, etc. In this case, the advantages of the filtering techniques, that allow to properly shape the frequency spectrum of a motion law, are combined with the features of multi-segment trajectories, whose parameters are generally defined with the only purpose of making the trajectories compliant with given bounds on velocity, acceleration, jerk, etc as reported in Section 4.1. The key point is the equivalence between time-optimal multi-segment polynomial trajectories with constraints on the first d derivatives and the output of a chain of d moving average filters, where the number d is the order of the trajectory. Therefore, in this case the filters are not used for making a given trajectory smoother but for online generating a trajectory starting from initial and final positions.

As described in Section 4.1, multi-segment trajectories are motion laws composed by several tracts, each one characterized by a specific analytical expression, properly joined in order to guarantee the desired degree of smoothness. In particular, time-optimal trajectories under constraints of velocity, acceleration, jerk, etc. are characterized by segments in which the velocity, the acceleration, and higher derivatives are saturated to the maximum allowed value. Thus in general, by imposing constraints on the first d derivatives one obtains a trajectory $q(t)$ of class $\mathcal{C}^{d-1}$, that is with the first $d-1$ derivatives that are continuous, while the d-th derivative $q^{(d)}(t)$ is a piece-wise constant function whose values belong to the set $\{q_{min}^{(d)}, 0, q_{max}^{(d)}\}$. With

94
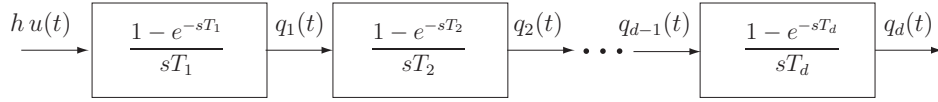
Figure 4-7: System composed by d filters for the computation of an optimal trajectory of class $\mathcal{C}^{d-1}$.

the additional condition of symmetric constraints:

$$q_{min}^{(i)} = -q_{max}^{(i)}, \quad i = 1, \ldots, d$$

one can show that such a kind of trajectories can be obtained by filtering a step input with a cascade of d dynamic filters, each one characterized by the transfer function

$$M_i(s) = \frac{1}{T_i} \frac{1 - e^{-sT_i}}{s} \tag{4.31}$$

where the parameter T_i (in general different for each filter composing the chain) is a time length, see Fig. 4-7. The possibility of obtaining time-optimal trajectories with the system of Fig. 4-7 fed by step input functions can be proved by exploiting a property of the convolution product (denoted with $*$) on the differentiation, i.e.

$$\frac{d}{dt}(f * g) = \frac{df}{dt} * g = f * \frac{dg}{dt}. \tag{4.32}$$

Consider the case of a single filter with a step input of generic magnitude h, i.e. $h\,u(t)$, being $u(t)$ the unit step function

$$u(t) = \begin{cases} 1, & t \geq 0 \\ 0, & t < 0. \end{cases}$$

In this case the output trajectory can be computed as

$$q_1(t) = h\,u(t) * m_1(t) \tag{4.33}$$

95

where

$$m_i(t) = \mathcal{L}^{-1}\{M_i(s)\} = \frac{1}{T_i}\big(u(t) - u(t - T_i)\big), \quad i = 1$$

is the impulse response corresponding to $M_i(s)$. Note that $m_i(t)$ is a rectangular function of duration T_i and magnitude $1/T_i$, see Fig. 4-8. This implies that, as well known, for any choice of T_i the area of the rectangular function is unitary, and accordingly the static gain of the corresponding function $M_i(s)$ is unitary as well:

$$M_i(0) = \int_0^\infty m_i(\tau)\, d\tau = 1.$$

By applying (4.32) to (4.33) one obtains

$$
\begin{aligned}
q_1(t) &= h\, u^{(1)}(t) * m_1(t) \\
&= h\, \delta(t) * m_1(t) = h\, m_1(t)
\end{aligned}
$$

where $\delta(t)$ is the unit impulse function. Therefore, by adopting a single filter $M_1(s)$ fed by a step function of amplitude h, the output consists in a trajectory $q_1(t)$ whose velocity has a rectangular profile with magnitude $v = h/T_1$. Then, it is immediate to obtain the value of the parameter T_1 which permits to impose a value of the velocity:

$$v = \frac{|h|}{T_1} = q_{max}^{(1)} \quad \rightarrow \quad T_1 = \frac{|h|}{q_{max}^{(1)}}. \tag{4.34}$$

Accordingly, when a step input of amplitude h is applied, the output of $M_1(s)$ will change from the initial to the final value (given by h) with a linear profile whose duration is exactly T_1.

If one adds a second filter $M_2(s)$, characterized by the parameter T_2, the resulting trajectory is

$$
\begin{aligned}
q_2(t) &= q_1(t) * m_2(t) \\
&= h\, u(t) * m_1(t) * m_2(t). \tag{4.35}
\end{aligned}
$$

96
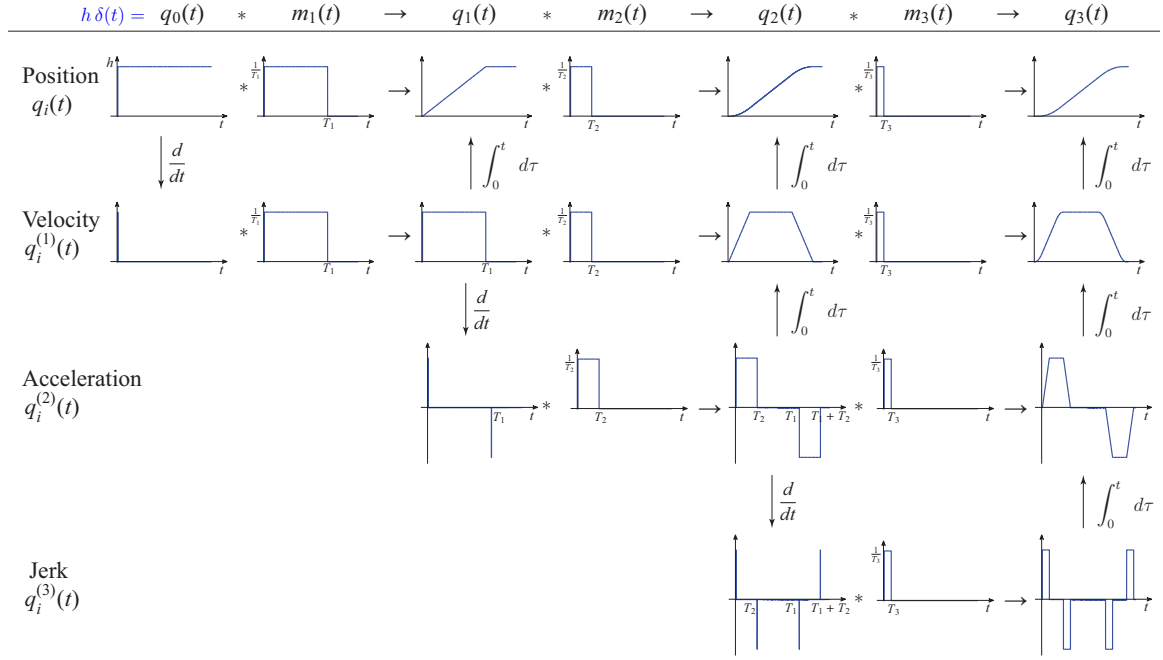
Figure 4-8: Relationships among the profiles of trajectories obtained by iterated averaging operations. Note that in the first row the algebraic relation $q_i(t) = q_{i-1}(t) * m_i(t)$, $i = 1, 2, 3$ is reported, while in the remaining rows a pictorial representation of the relationship among the trajectories of different orders and their derivatives is shown.

Therefore, the first derivative is

$$
\begin{aligned}
q_2^{(1)}(t) &= q_1^{(1)}(t) * m_2(t) \\
&= h\, m_1(t) * m_2(t)
\end{aligned}
\tag{4.36}
$$

and, by taking into account that

$$
m_1^{(1)}(t) = \frac{1}{T_1}\big(\delta(t) - \delta(t - T_1)\big)
$$

it is possible to deduce the second derivative

$$
\begin{aligned}
q_2^{(2)}(t) &= h\, m_1^{(1)}(t) * m_2(t) \\
&= \frac{h}{T_1}\big(\delta(t) - \delta(t - T_1)\big) * m_2(t) \\
&= v\big(m_2(t) - m_2(t - T_1)\big)
\end{aligned}
$$

97

which is composed by two rectangular functions, one positive and one negative, of magnitude $a = \dfrac{v}{T_2}$ and duration $\min\{T_1, T_2\}$. Therefore the maximum value of the acceleration can be freely set by imposing

$$a = \frac{v}{T_2} = q_{max}^{(2)} \quad \rightarrow \quad T_2 = \frac{\text{v}}{q_{max}^{(2)}} = \frac{q_{max}^{(1)}}{q_{max}^{(2)}}. \tag{4.37}$$

Since the static gain of both $M_1(s)$ and $M_2(s)$ is unitary, the final value of the response of $M_1(s)\cdot M_2(s)$ to a step input of magnitude h remains h. The system output $q_2(t)$ reaches such a value with a trapezoidal velocity profile as described in Section 4.1.1, obtained by integrating $q_2^{(2)}(t)$.

The maximum acceleration of the trajectory is $q_{max}^{(2)}$, and the velocity is still limited by $q_{max}^{(1)}$. In fact, by defining for a generic function $f(t)$

$$\text{peak}\big(f(t)\big) = \max_{t \geq 0} |f(t)|$$

from (4.36) one can prove that

$$
\begin{aligned}
\text{peak}\Big(q_2^{(1)}(t)\Big) \;\leq\;& \text{peak}\Big(q_1^{(1)}(t)\Big) \cdot \int_0^\infty |m_2(\tau)| d\tau \\
\leq\;& \text{peak}\Big(q_1^{(1)}(t)\Big) = q_{max}^{(1)}
\end{aligned}
\tag{4.38}
$$

where $\int_0^\infty |m_2(\tau)| d\tau = \int_0^\infty m_2(\tau) d\tau = 1$ since $m_2(t) \geq 0$, $\forall t$. In this case, if $T_1 \geq T_2$ then the maximum velocity $q_{max}^{(1)}$ is actually reached, i.e. $\text{peak}\big(q_2^{(1)}(t)\big) = q_{max}^{(1)}$ and $q_2(t)$ is a minimum-time trajectory compliant with the given bounds $q_{max}^{(i)}$, $i = 1, 2$. Conversely, if $T_1 < T_2$ then $\text{peak}\big(q_2^{(1)}(t)\big) = \frac{|h|}{T_2} < \frac{|h|}{T_1} = q_{max}^{(1)}$, and the trajectory, that still meets the proposed constraints, is not of minimum duration. In particular, when $T_1 < T_2$, the roles of the two time constants T_i are switched, in the sense that the duration of the acceleration period is T_1 and the maximum velocity is h/T_2. In any case the total duration of the trajectory $q_2(t)$ is given by the sum of the durations of the impulse responses of $M_1(s)$ and $M_2(s)$, i.e.

$$T_{tot} = T_1 + T_2.$$

Note that the maximum velocity $q_{max}^{(1)}$ is actually reached if and only if

$$T_2 \le \frac{1}{2}T_{tot} = \frac{1}{2}(T_1 + T_2) \quad \Leftrightarrow \quad T_2 \le T_1.$$

that is if and only if the (planned) duration T_2 of the acceleration/deceleration period is not greater than half of the total duration of the trajectory.

As shown in Fig. 4-8, the second order trajectory $q_2(t)$ can be made smoother by adding a further filter $M_3(s)$ (characterized by the parameter T_3), obtaining in this way a double S velocity trajectory

$$q_3(t) = q_2(t) * m_3(t)$$

whose velocity, acceleration and jerk are respectively

$$
\begin{aligned}
q_3^{(1)}(t) &= q_2^{(1)}(t) * m_3(t) \\
q_3^{(2)}(t) &= q_2^{(2)}(t) * m_3(t) \\
q_3^{(3)}(t) &= q_2^{(3)}(t) * m_3(t).
\end{aligned}
\tag{4.39}
$$

Since $q_2^{(2)}(t)$ is composed by two rectangular functions, its derivative is a sequence of four impulsive functions of amplitude a properly shifted in time, see Fig. 4-8. Therefore, from (4.39) it descends that $q_3^{(3)}(t)$ is composed by four rectangular functions of amplitude $j = a/T_3$ and accordingly it is possible to select T_3 on the basis of the desired value of the jerk:

$$j = \frac{a}{T_3} = q_{max}^{(3)} \quad \rightarrow \quad T_3 = \frac{a}{q_{max}^{(3)}} = \frac{a}{q_{max}^{(3)}} = \frac{q_{max}^{(2)}}{q_{max}^{(3)}}. \tag{4.40}$$

Moreover, by the same argument as in (4.38) one can prove that

$$\text{peak}\left(q_3^{(2)}(t)\right) \le \text{peak}\left(q_2^{(2)}(t)\right) = q_{max}^{(2)} \tag{4.41}$$

$$\text{peak}\left(q_3^{(1)}(t)\right) \le \text{peak}\left(q_2^{(1)}(t)\right) \le \text{peak}\left(q_1^{(1)}(t)\right) = q_{max}^{(1)}. \tag{4.42}$$

In particular, if the tract with constant jerk is at most half of the acceleration/deceleration period, that is

$$T_3 \leq \frac{1}{2}(T_2 + T_3) \quad \Leftrightarrow \quad T_3 \leq T_2, \tag{4.43}$$

in (4.41) the sign equal holds true and the maximum acceleration $q_{max}^{(2)}$ is actually reached by the third order trajectory $q_3(t)$. Analogously, if the acceleration/deceleration period does not exceed half of the total duration of the trajectory, i.e.

$$T_2 + T_3 \leq \frac{1}{2}(T_1 + T_2 + T_3) \quad \Leftrightarrow \quad T_2 + T_3 \leq T_1 \tag{4.44}$$

then $\mathrm{peak}\big(q_3^{(1)}(t)\big) = \mathrm{peak}\big(q_2^{(1)}(t)\big)$ (and obviously $\mathrm{peak}\big(q_2^{(1)}(t)\big) = \mathrm{peak}\big(q_1^{(1)}(t)\big)$ since ((4.44)) implies $T_2 \leq T_1$), therefore the trajectory $q_3(t)$ reaches the maximum velocity $q_{max}^{(1)}$. If, both conditions (4.43) and (4.44) are met, the velocity and the acceleration reach the maximum values $q_{max}^{(i)}$ and $q_3(t)$ is a minimum-time double-S velocity trajectory as in Section 4.1.2. Conversely, when one (or both) of the two conditions is not true, the trajectory is compliant with the given bounds but it is not time-optimal. The procedure shown so far can be iterated by adding further filters $M_i(s)$. In the general case, the expression of the minimum-time trajectory compliant with given constraints on the first d derivatives, and therefore of order d, is

$$q_n(t) = h\,u(t) * m_1(t) * \ldots * m_{d-1}(t) * m_d(t) \tag{4.45}$$

or with a recursive formulation

$$q_d(t) = q_{d-1}(t) * m_d(t) \tag{4.46}$$

where $q_0(t) = h\,u(t)$. As already pointed out, the smoothness of the trajectory, that is the order of continuous derivative, is strictly tied to the number of filters composing the chain. If one considers d filters, the resulting trajectory will be of class $\mathcal{C}^{d-1}$. By increasing the smoothness of the trajectory, the duration augments as well. As a matter of fact the total duration of a trajectory planned by means of d dynamic

systems $M_i(s)$ is given by the sum of the lengths of the impulse response of each filter, i.e.

$$T_{tot} = T_1 + T_2 + \ldots + T_d.$$

The parameters T_i can be set with the purpose of imposing desired bounds on velocity, acceleration, jerk and higher derivatives, i.e.

$$|q_d^{(i)}(t)| \leq q_{max}^{(i)}, \quad i = 1, \ldots, d \tag{4.47}$$

by assuming

$$
\begin{aligned}
T_1 &= \frac{|h|}{q_{max}^{(1)}} \\
T_i &= \frac{q_{max}^{(i-1)}}{q_{max}^{(i)}}, \quad i = 1, \ldots, d
\end{aligned}
\tag{4.48}
$$

with the constraints

$$T_i \geq T_{i+1} + \ldots + T_d, \qquad i = 1, \ldots, d-1. \tag{4.49}$$

that guarantee that the trajectory, compliant with (4.47), is of minimum duration. Finally in lieu of implementing a proper trajectory generator on controlled system, not only the position profile of the trajectory but also the related profiles of velocity, acceleration, jerk, etc. have to be provided. The computation of the derivatives of a trajectory of generic order d, that is obtained by a cascade of d filters, is straightforward by considering the definition (4.45) and the property of convolution product (4.32). In fact,

$$
\begin{aligned}
q_d^{(1)}(t) &= q_{d-1}(t) * m_d^{(1)}(t) \\
&= q_{d-1}(t) * \frac{1}{T_d}\Big(\delta(t) - \delta(t - T_d)\Big) \\
&= \frac{1}{T_d}\Big(q_{d-1}(t) - q_{d-1}(t - T_d)\Big).
\end{aligned}
\tag{4.50}
$$
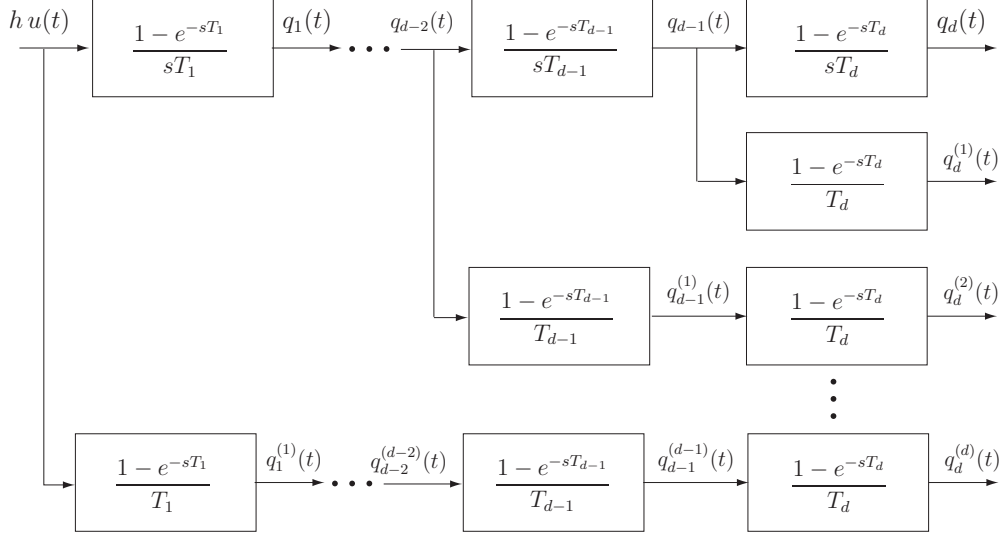
Figure 4-9: System composed by d filters for the computation of an optimal trajectory of class $\mathcal{C}^{d-1}$ and of all the derivatives of order $i = 1, \ldots, d$.

The generic derivative of i-th order, can be calculated in a recursive manner as

$$q_d^{(i)}(t) = \frac{1}{T_d} \left(q_{d-1}^{(i-1)}(t) - q_{d-1}^{(i-1)}(t - T_d) \right) \tag{4.51}$$

with $q_{d-i}^{(0)}(t) = q_{d-i}(t)$. Figure 4-9 shows the block-scheme representation of the filter for the computation of the trajectory and its derivatives, obtained by iterating and Laplace transforming (4.51). Note that the filter of Fig. 4-9 gives a closed form expression (in terms of Laplace transform) of the derivatives and does not simply provide their numerical value.

4.3.2   Filters for Trigonometric Trajectories Generation

In [12] this method is extended exploiting dynamic filters to plan motion profiles characterized by velocity, acceleration, or jerk (or higher derivatives, depending on the order of the trajectory) composed only by sinusoidal functions (see Section 4.1.3, leading to the so-called modified trapezoidal velocity trajectory, modified double-S velocity trajectory, etc., see [9]. In this case, it is sufficient to consider in the chain of averaging filters $M_i(s)$, characterized by a rectangular impulse response, a single
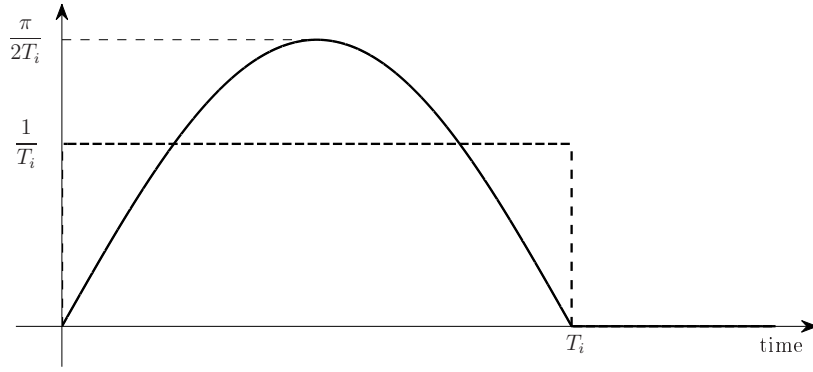
Figure 4-10: Impulse response of the filter $S_i(s)$ defined by (4.53) (solid line) compared with that of an average filter $M_i(s)$ (dashed line) characterized by the same time constant T_i.
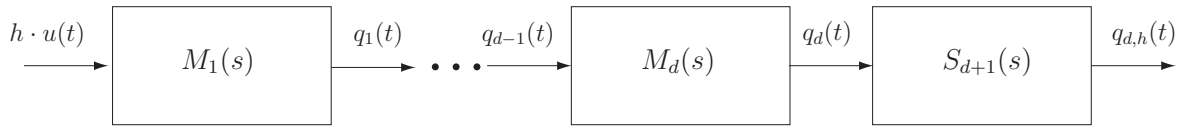
Figure 4-11: System composed by $d+1$ filters for the computation of the trajectory $q_{d,h}(t)$ of class $\mathcal{C}^{d+1}$, whose d-th derivative is only composed by sinusoidal functions.

filter whose impulse response is

$$s_i(t) = \begin{cases} \dfrac{\pi}{2T_i} \sin\left(\dfrac{\pi}{T_i}t\right) & \text{if } 0 \le t \le T_i \\[2ex] 0 & \text{otherwise} \end{cases} \tag{4.52}$$

$$= \frac{\pi}{2T_i}\left[\sin\left(\frac{\pi}{T_i}t\right)u(t) + \sin\left(\frac{\pi}{T_i}(t-T_i)\right)u(t-T_i)\right]$$

where $u(t)$ denotes again the step function, and T_i is a parameter that defines the time duration of the response, which is finite as shown in Fig. 4-10. By Laplace transforming (4.52), the transfer function of the filter can be readily obtained:

$$S_i(s) = \frac{1}{2}\left(\frac{\pi}{T_i}\right)^2 \frac{1 + e^{-sT_i}}{s^2 + \left(\dfrac{\pi}{T_i}\right)^2}. \tag{4.53}$$

Note that the system $S_i(s)$ has a unitary dc gain.

103

The generation of a trajectory $q_{d,h}(t)$ whose d-th derivative is only composed by sinusoidal functions (and therefore is of class $\mathcal{C}^{d+1}$) can be achieved by adding the "sinusoidal" filter $S_{d+1}(s)$ at the end of a chain of d filters $M_i(s)$, as shown in Fig. 4-11. With this configuration, it is possible to find the following relation between the maximum values of $q^{(d)}(t)$ and $q^{(d+1)}(t)$ and the characteristic parameter T_{d+1} of the filter:

$$q_{max}^{(d)}(t)\frac{\pi}{2T_{d+1}} = q_{max}^{(d+1)}(t).$$

As a consequence, if constraints on the d-th and $(d+1)$-th derivative are given, the time-length T_{d+1} can be computed as

$$T_{d+1} = \frac{q_{max}^{(d)}}{q_{max}^{(d+1)}}\frac{\pi}{2}. \tag{4.54}$$

Thus, for instance, for a modified trapezoidal velocity trajectory with $d = 1$ one obtains

$$T_1 = \frac{h}{v_{max}}, \quad T_2 = \frac{\pi}{2}\frac{v_{max}}{a_{max}}$$

while for a modified double-S velocity trajectory with $d = 2$

$$T_1 = \frac{h}{v_{max}}, \quad T_2 = \frac{v_{max}}{a_{max}}, \quad T_3 = \frac{\pi}{2}\frac{a_{max}}{j_{max}}$$

Note that the time constant T_{d+1} always corresponds to the sinusoidal filter.

4.3.3 Uniform B-spline Trajectory Generator

The use of dynamic filters proves to be very simple and effective in trajectory generation. In [13] the same filters of the form of (4.31) are exploited to implement a trajectory generator for uniform B-spline. As reported in Section 4.2 a uniform B-spline trajectory of degree d passing through m points can be defined as

$$q_u(t) = \sum_{j=0}^{m} \boldsymbol{p}_j \boldsymbol{B}^d(t - jT), \qquad 0 \leq t \leq mT, \tag{4.55}$$
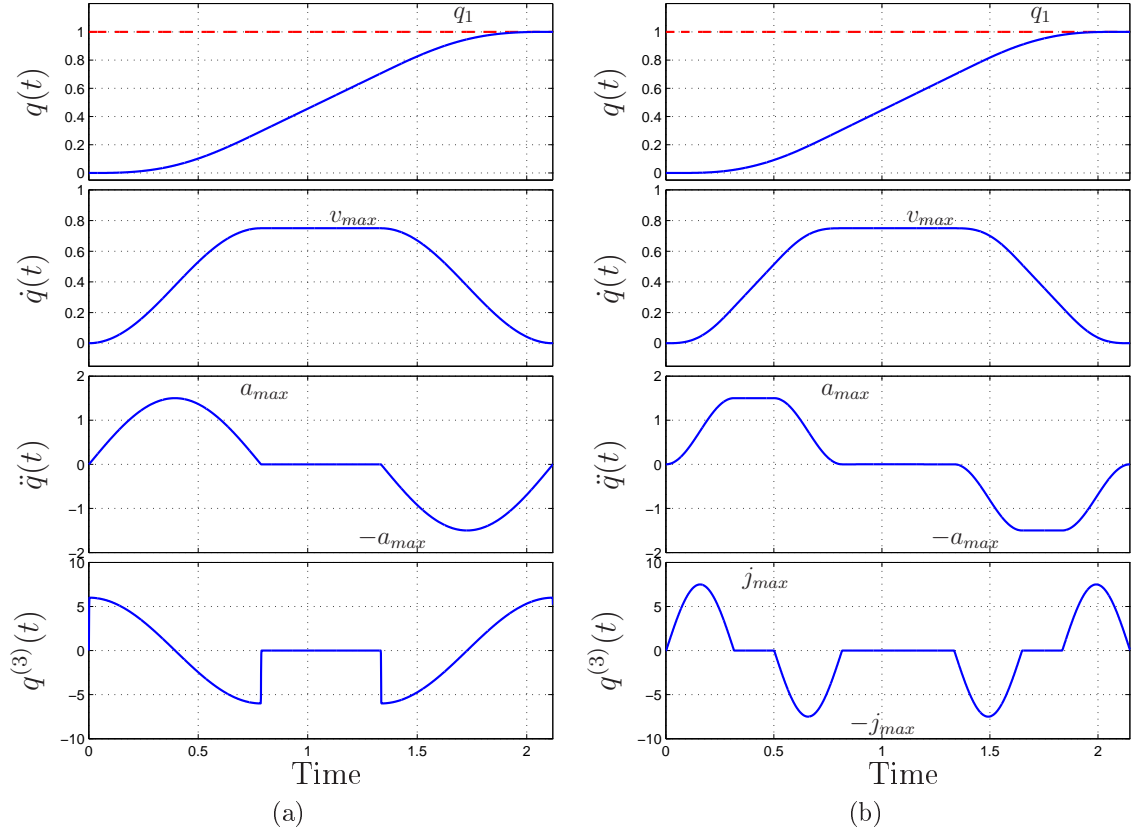
Figure 4-12: Position, velocity, acceleration and jerk of a time optimal motion from 0 to q_1 by means of modified trapezoidal velocity trajectory (a), and modified double-S velocity trajectory (a).

where $\boldsymbol{p}_j$ are the control points, T is the uniform knot span and $\boldsymbol{B}^d(t)$ is the spline basis function of degree d which is defined in a recursive manner, but also exploiting the convolution product (denoted with $*$) results equivalent to

$$
\begin{aligned}
\boldsymbol{B}^d(t) &= \frac{1}{T}\boldsymbol{B}^{d-1} * \boldsymbol{B}^0 \\
&= \underbrace{\frac{1}{T}\boldsymbol{B}^0 * \frac{1}{T}\boldsymbol{B}^0 * \ldots * \frac{1}{T}\boldsymbol{B}^0}_{d \ \text{times}} * \boldsymbol{B}^0,
\end{aligned}
\tag{4.56}
$$

with

$$
\boldsymbol{B}^0(t) = \begin{cases} 1, & \text{if } 0 \le t < T \\ 0, & \text{otherwise.} \end{cases}
$$

105

$$\underbrace{\qquad\qquad\qquad\qquad\qquad\qquad\qquad}_{d \text{ blocks}}$$
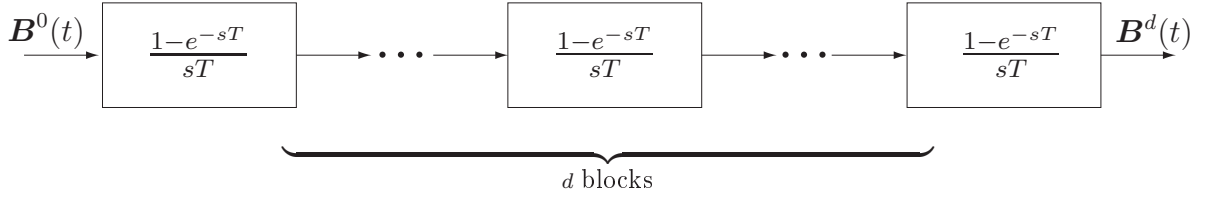
Figure 4-13: System composed by d filters for the computation of the B-spline basis function $\boldsymbol{B}^d(t)$ of degree d.

Therefore looking at the basis functions $\boldsymbol{B}^d(t)$ obtained for different values of d shown in Fig. 4-6 and analyzing the convolution product of (4.56) in a filtering perspective, it can be noted that (4.56) can be interpreted as the function $\boldsymbol{B}^0(t)$ filtered by a cascade of d filters, each one performing an averaging operation on the input signal over an interval of duration T and characterized by the transfer function

$$M(s) = \mathcal{L}\left\{\frac{1}{T}\boldsymbol{B}^0(t)\right\} = \frac{1}{T}\frac{1 - e^{-sT}}{s}, \qquad (4.57)$$

see Fig. 4-13. Moreover by Laplace transforming the general expression of the uniform B-spline (4.55) and substituting (4.56) one obtains

$$\boldsymbol{Q}_u(s) = \sum_{j=0}^{m} \mathcal{L}\left\{\boldsymbol{p}_j\boldsymbol{B}^0 * \frac{1}{T}\boldsymbol{B}^0 * \frac{1}{T}\boldsymbol{B}^0 * \ldots * \frac{1}{T}\boldsymbol{B}^0\right\} e^{-jsT}.$$

Exploiting the linearity of the above expression and the fact that $\frac{1}{T}\boldsymbol{B}^0$ is not a function of the index j, the B-spline expression becomes

$$\boldsymbol{Q}_u(s) = \left(\sum_{j=0}^{m} \mathcal{L}\left\{\boldsymbol{p}_j\boldsymbol{B}^0\right\} e^{-jsT}\right) \cdot M(s) \cdot M(s) \cdot \ldots \cdot M(s)$$

$$= \mathcal{L}\left\{\sum_{j=0}^{m} \boldsymbol{p}_j\boldsymbol{B}^0(t - jT)\right\} \cdot \underbrace{M(s) \cdot M(s) \cdot \ldots \cdot M(s)}_{p \text{ filters}}. \qquad (4.58)$$

This expression suggests that a uniform B-spline can be evaluated by feeding the cascade of d moving average filters $M(s)$, reported in Fig. 4-13, with the piecewise

constant function

$$p(t) = \sum_{j=0}^{m} \boldsymbol{p}_j \boldsymbol{B}^0(t - jT) \tag{4.59}$$

that in the generic interval $jT \leq t < (j+1)T$ assumes the constant value $\boldsymbol{p}_j$ of the j-th control point of the related analytic B-spline.

Finally, in order to find the control points which define the piecewise constant function $\boldsymbol{p}_j$, one can exploit classical techniques derived by B-spline interpolation/approximation methods.

For example, if one considers the interpolation of a set of $n+1$ points $\{\boldsymbol{q}_0, \boldsymbol{q}_1, \boldsymbol{q}_2, \ldots, \boldsymbol{q}_{n-1}, \boldsymbol{q}_n\}$ it is necessary to impose the conditions

$$q(t_i) = \boldsymbol{q}_i, \qquad i = 0, \ldots, n \tag{4.60}$$

where t_i is the time instant at which the spline $q(t)$ crosses the given point $\boldsymbol{q}_i$.

The first step consists in selecting the degree d of the spline according to the desired degree of smoothness. Strictly related to d is the choice of time instants t_i:

- if d is odd, the t_i are assumed coincident with the knots, $t_i = iT$;

- if d is even, the time instants t_i should be selected in the midpoint of each knot span, $t_i = \frac{2i+1}{2}T$.

Once the interpolation time instants t_i have been chosen, it is possible to make the system of equations (4.60) explicit with the substitution of the values of basis functions at t_i in the spline definition (4.22). In particular the values of $\boldsymbol{B}^d$ for d odd and d even, computed at points $t_i = iT$ and $t_i = \frac{2i+1}{2}T$ respectively, is independent from T because of the choice of the interpolation time instants, as a result $\boldsymbol{B}^d$ only depends on the index i, and obviously on the degree d, see [10].

Then in order to obtain a system of equations well conditioned from a mathematical point of view, it is necessary to consider symmetrical B-splines $q_s(t)$, i.e. uniform B-splines whose basis function $\beta^d(t)$ is symmetric with respect the origin. The function $\beta^d(t)$ can be deduced from $\boldsymbol{B}^d(t)$ with a simple time shift, $\beta^d(t) = \boldsymbol{B}^d \left(t + \frac{d+1}{2}T \right)$. As

a consequence symmetrical B-splines are related to standard uniform B-splines by

$$
\begin{aligned}
q_s(t) &= \sum_{j=0}^{m} \boldsymbol{p}_j \beta^d(t - jT) \\
&= \sum_{j=0}^{m} \boldsymbol{p}_j \boldsymbol{B}^d(t + \tfrac{d+1}{2}T - jT) = q_u(t + \tfrac{d+1}{2}T),
\end{aligned}
$$

that is, given the control points, uniform B-splines are equal to symmetrical B-splines delayed by $\frac{d+1}{2}T$. Obviously, the theory of Sec. 4.2 could be based on symmetrical B-splines but this would imply the presence of a temporal anticipation leading to noncausal filters for the evaluation of the B-splines.

For each point to be interpolated, with the only exception of the first and last points, the equation (4.60) becomes

$$
q_s(t_i) = \sum_{j=0}^{m} \boldsymbol{p}_j \boldsymbol{B}^d(t_i + \tfrac{d+1}{2}T - jT) = \boldsymbol{q}_i \tag{4.61}
$$

where the unknowns are the control point $\boldsymbol{p}_j$. The interpolation of the first and last points, with zero velocity and acceleration, is achieved by exploiting the characteristics of the dynamic system used to generate the spline. Since all the filters $M(s)$ have unitary static gain, the output of the filters cascade will reach and maintain the desired value $\boldsymbol{q}_0$ or $\boldsymbol{q}_n$ if the same value is applied to the input $\frac{d+1}{2}T$ seconds before. In other words, in order to smoothly start from $\boldsymbol{q}_0$ and end to $\boldsymbol{q}_n$, the first/last d control points must be equal to $\boldsymbol{q}_0/\boldsymbol{q}_n$. The $n - 1$ internal control points are then computed by solving the system of equations obtained by stacking (4.61) for $i = 1, \ldots, n - 1$ and the piecewise constant function $p(t)$ in (4.59) can be finally built by maintaining the value of each control point $\boldsymbol{p}_j$ for the entire period $jT \leq t < (j + 1)T$ by means of a zero order hold as shown in fig. 4-14.
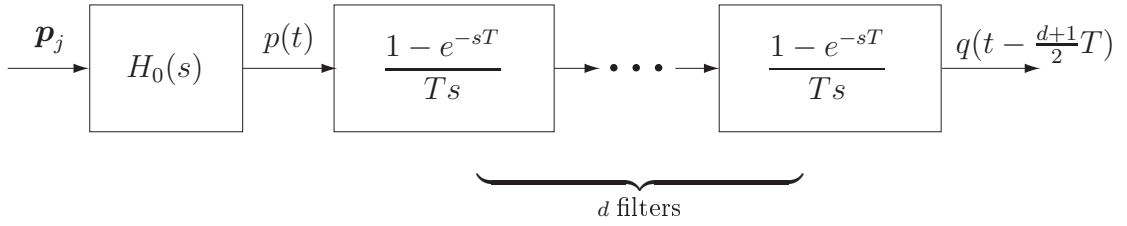
Figure 4-14: System composed by d mean filters and by a zero-order hold $H_0(s)$ for the computation of continuous-time B-spline trajectories of degree d.
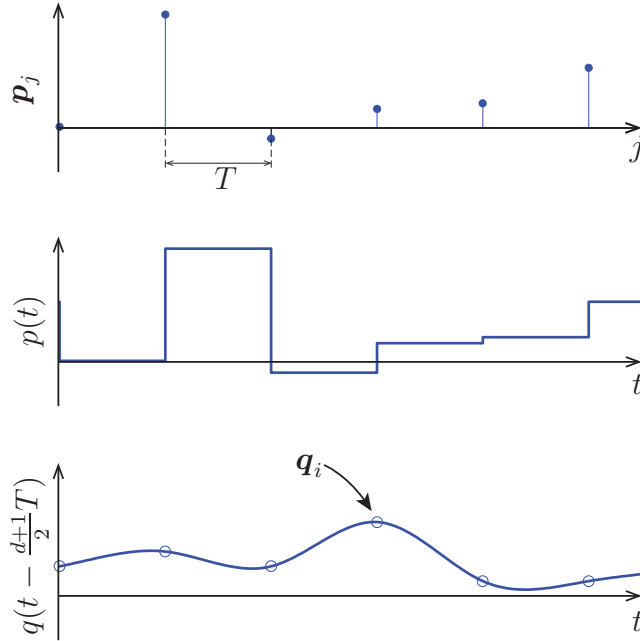
Figure 4-15: Control points sequence $\boldsymbol{p}_j$ defining a cubic B-spline and related reference trajectory $q(t - \frac{d+1}{2}T)$ with $\frac{d+1}{2} = 2$ obtained with the dynamic filter of Fig. 4-14.

4.4 Frequency Analysis of Trajectory Generators

4.4.1 Multi-Segment Polynomial Trajectories

In Section 4.3 very simple approaches have been described in order to plan some of the most common types of trajectory by means of dynamic filters. Basically all the methods rely on the implementation of a chain of a certain number of mean filters $M_i(s)$ as in (4.31) whose duration T_i has to be set in order to comply to the desired trajectory specifications. In particular in Sections 4.3.1 and 4.3.2 each T_i of the chain's filters is used as a design parameter to impose kinematic constraints on the trajectory,

109

while in Section 4.3.3 the chain is composed of identic filters of duration T, where T is the knot span of a uniform B-spline trajectory.

In addition, defining trajectories by means of filters is very useful to analyze the frequency content of a prescribed motion and therefore the effect of a given trajectory on a vibratory system. Because of the chain structure of the generators, and being the chains (mainly) composed of mean filters $M(s)$, the frequency analysis can be performed by taking into account the filter $M(s)$ at first, intended as the basic element of a trajectory generator

$$M(s) = \frac{1}{T}\frac{1 - e^{-sT}}{s} \tag{4.62}$$

In particular, assuming to have an undamped vibratory system $G(s)$ as considered in Section 1.1, it has to be noted that the implementation of the filter $M(s)$ as a command shaper assures complete vibration suppression, provided that the duration T of the filter is equal to the period of the vibration T_0 of the system $G(s)$

$$T = T_0 = \frac{2\pi}{\omega_n}, \tag{4.63}$$

where ω_n is the natural undamped frequency of the vibratory system. In lieu of the possibility to suppress vibrations by means of $M(s)$, in fig. 4-16(b) the PRV function of the mean filter is compared to a ZV IS and a ZVD IS that are standard tools for vibration suppression, as deeply discussed in Chapter 2. The reason for which this comparison is meaningful appears more clear in fig. 4-17(a) where the filter $M(s)$ is analyzed in terms of pole-zero diagram. As can be seen the effect of the filter is to provide infinite zeroes on the imaginary axis, equally spaced of $k\omega_n$, $k \in \mathbf{N}$, plus a pole in the axis origin which is cancelled by the zero associated with $k = 0$. Therefore the suppression of the vibratory mode is again due to a pole-zero cancellation as already stated in previous chapters. Also with respect to the comparison of fig. 4-16(b), the robustness of $M(s)$ is comparable to that of a ZV IS due to the single multiplicity of the zeroes of both $M(s)$ and ZV IS. Anyway the reduced distance of the zeroes of $M(s)$ makes that the overall reduction effect of the filter is greater, at least for frequency variation only (see fig. 4-17(a) and fig. 4-17(b). On the other hand
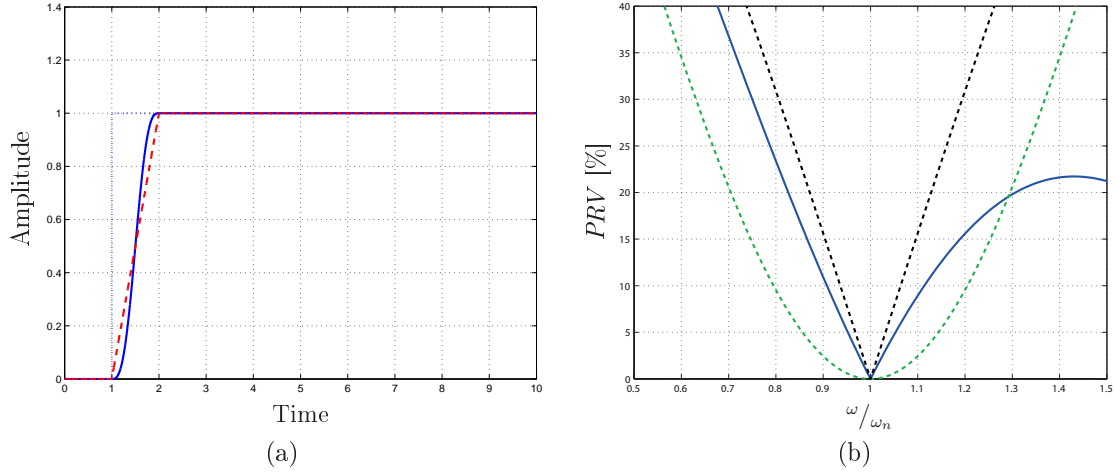
Figure 4-16: Step response of the system with $\delta = 0$ shaped by $M(s)$ (a) and PRV function of the mean filter compared to ZV IS in black dotted line and ZVD IS in green dotted line (b).

$M(s)$ lasts twice the ZV IS, being the duration of a ZV IS half period of vibration, and doesn't assure vibration suppression for system with damping $\delta \neq 0$.

Despite the consideration on $M(s)$ used as an input shaper, it is clear that the frequency analysis of a trajectory of order d defined by means of a chain of d mean filters $M_i(s)$, can be easily performed by composing the effects of the d filters. The cases of trapezoidal velocity trajectory and double-S velocity trajectory of Section 4.3.1 are straightforward, since both planners are actually composed of mean filters only. In general from (4.45) to (4.49) a class $\mathcal{C}^{d-1}$ trajectory is defined by means of d filters $M_i(s)$ where respective T_i are chosen in order to impose desired bounds on d derivatives of the trajectory

$$T_i = \frac{q_{max}^{(i-1)}}{q_{max}^{(i)}}, \quad i = 1, \dots, d,$$

resulting in a total duration of the motion

$$T_{tot} = T_1 + T_2 + \dots + T_d$$

that is the minimum time trajectory for the given kinematic bounds provided that

111
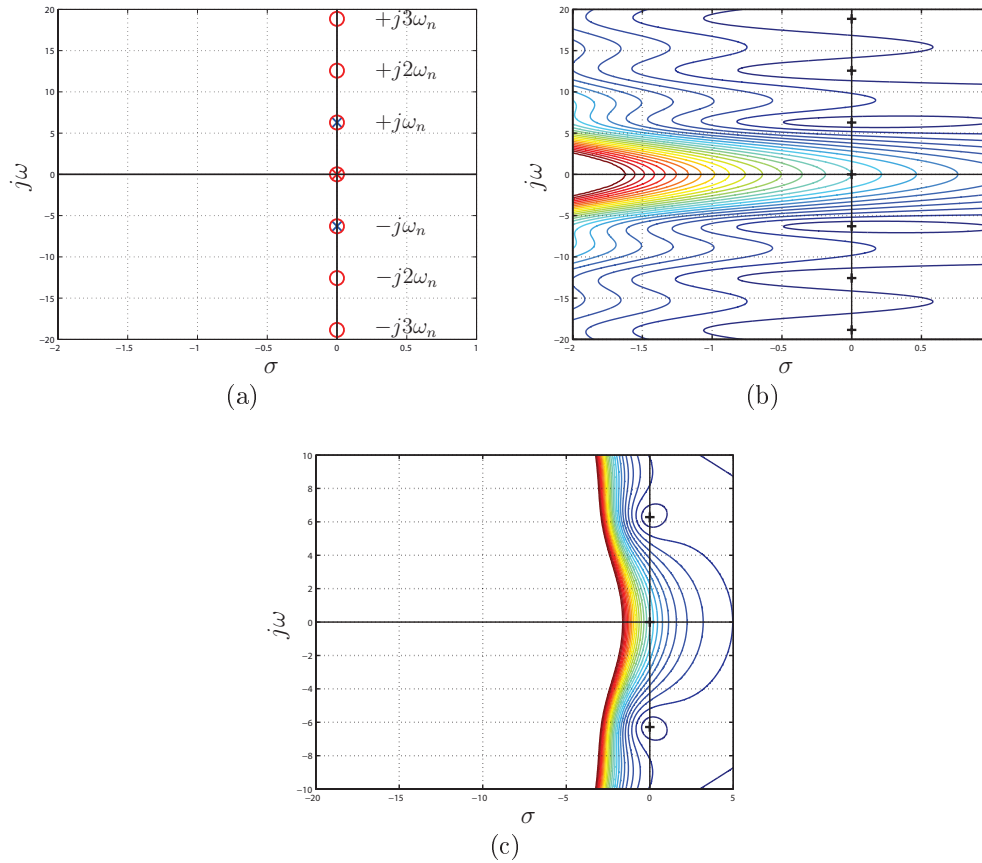
Figure 4-17: Pole-Zero diagram of the system with $\delta = 0$ shaped by the mean filter (a) and description of $M(s)$ as function of σ and $j\omega$ (b,c). In (c) the same plot of (b) is reported with full scale axis in order to better understand the behavior of the system response. In (b) and (c) the contour lines are equally spaced of 0.1 and the zeroes position is highlighted with a black cross.

the generic T_i satisfy

$$T_i \geq T_{i+1} + \ldots + T_d, \qquad i = 1, \ldots, d - 1.$$

In that case the generic trajectory planner has a transfer function of the form

$$H_d(s) = M_1(s) \cdot M_2(s) \cdot \ldots \cdot M_d(s), \tag{4.64}$$

and results quite simple to analyze by adding the contribution of each single filter. In fig. 4-18(a) the point to point motion obtained by means of a time optimal trapezoidal velocity trajectory generator $H_2(s)$ is reported for example. In particular the
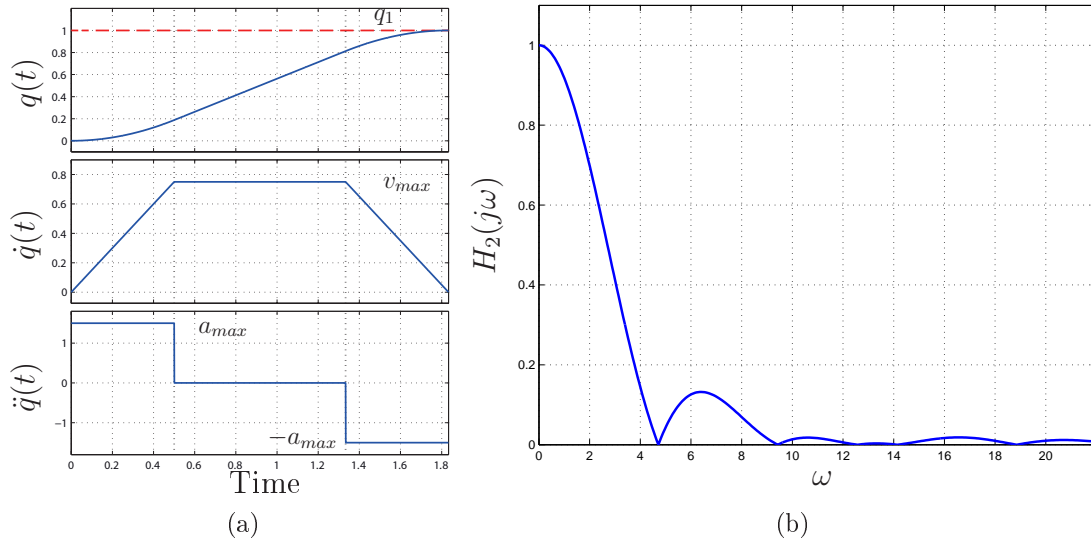
Figure 4-18: Position, velocity and acceleration of a time optimal motion from 0 to q_1 by means of trapezoidal velocity trajectory with desired bounds on velocity and acceleration. On the right the frequency response of the trajectory is reported.

generator is

$$H_2(s) = M_1(s) \cdot M_2(s),$$

where $M_1(s)$, $M_2(s)$ are mean filters as in (4.62) with

$$
\begin{aligned}
T_1 &= \frac{|h|}{v_{max}}, \\
T_2 &= \frac{v_{max}}{a_{max}},
\end{aligned}
$$

being v_{max}, a_{max} prescribed kinematic constraints for the trajectory. Also in fig. 4-18(b) the frequency content of the trajectory $q(t)$ is given by simply deriving the frequency response of the trajectory generator $H_2(j\omega)$. In addition, in fig. 4-19 the pole-zero analysis of the planner is presented, showing that the diagram of the planner $H_2(s)$ is nothing but the merge of the pole-zero diagrams of the filters $M_1(s)$, $M_2(s)$ in figs. 4-19(a) and 4-19(b) as expected. This is very convenient in terms of frequency characterization of a trajectory since it results in composition of quite simple contributions given by the generic mean filter $M_i(s)$. In particular permits to make interesting considerations with respect to the possibility of reducing or suppressing vibrations by means of such trajectories.

113
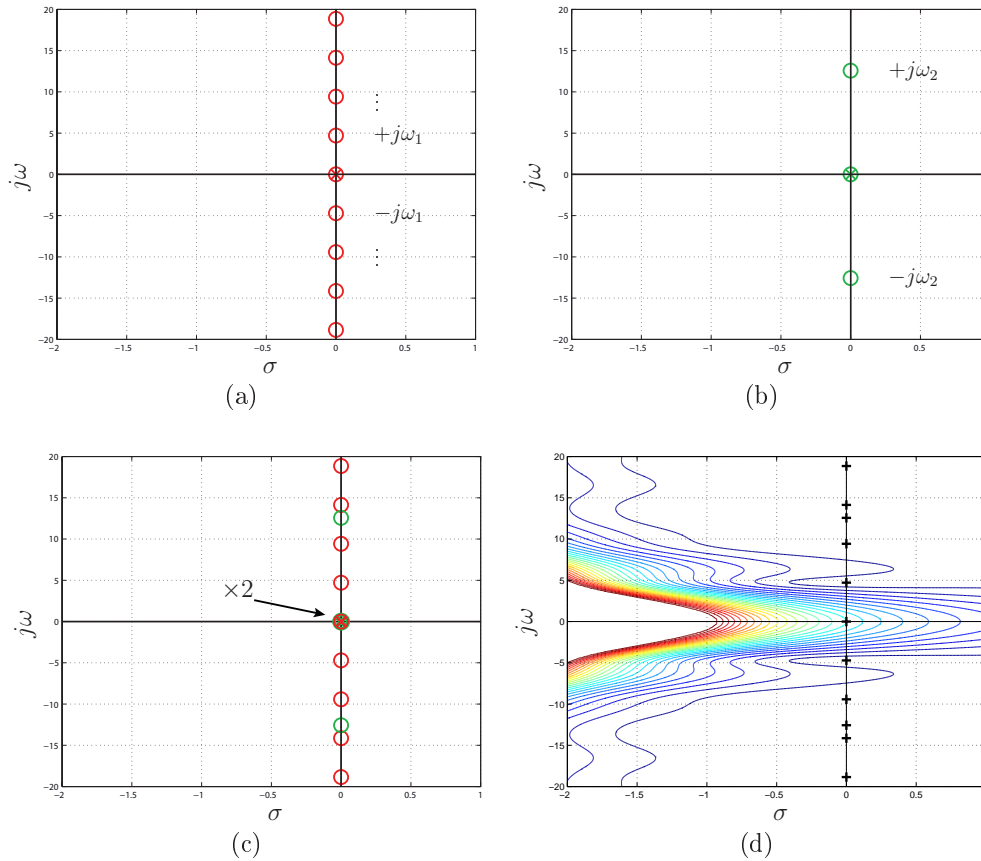
Figure 4-19: Pole-Zero diagram of a trapezoidal velocity trajectory generator $H_2(s) = M_1(s) \cdot M_2(s)$ (c): in (a) and (b) the pole-zero diagrams of respectively M_1 and M_2, being $\omega_1 = 2\pi/T_1$ and $\omega_2 = 2\pi/T_2$ are reported. In (d) the description of $H_2(s)$ as function of σ and $j\omega$ is shown, the contour lines are equally spaced of 0.1 and the zeroes position is highlighted with a black cross.

In fig. 4-20 the the time optimal trajectory in fig. 4-18 is used to command an undamped vibratory system $G(s)$ with damping $\delta = 0$ and natural frequency ω_n. As can be seen the vibration is reduced but not suppressed, according to both frequency response and pole-zero diagrams in figs. 4-20(b) and 4-20(c) that point out the fact that the cancellation of the of the vibratory component doesn't occur. As a matter of fact it is worth noting that the design method reported in Section 4.3.1 leads to define a trajectory generator for time optimal trajectories given bounds on velocity, acceleration, jerk, etc., without any particular specification on frequency.

However recalling the considerations on vibration suppression by means of a mean filter reported before, one may be interested in using one of the generator's filter $M_i(s)$
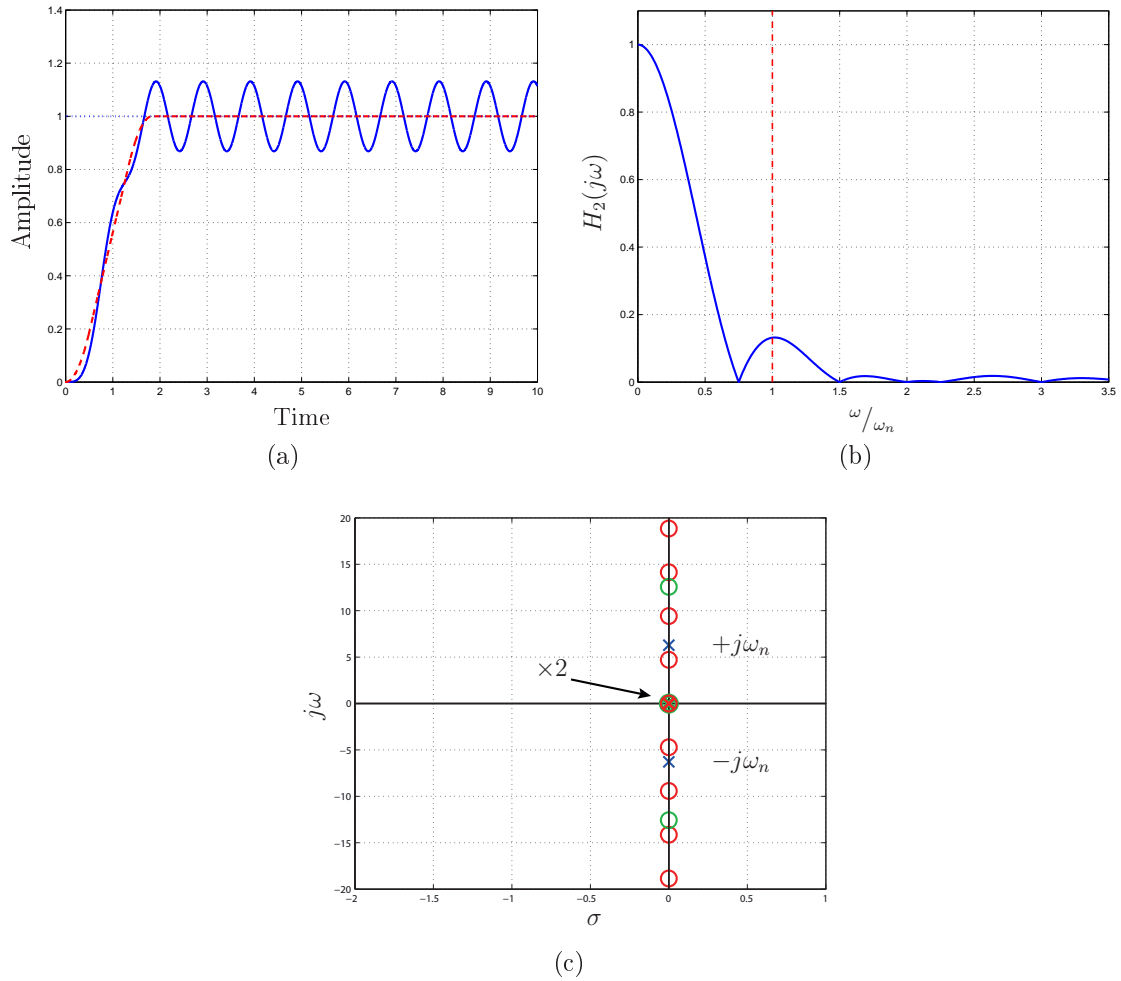
Figure 4-20: Response of the system $G(s)$ with $\delta = 0$ fed by a trapezoidal velocity trajectory generated by means of $H_2(s)$ (a) and frequency response $H_2(j\omega)$ with the vibrating frequency highlighted in red dashed line(b). In (c) the pole-zero diagram of $H_2(s)$ is reported along with the poles of the vibratory system $G(s)$ in blue.

in order to suppress vibrations, that is setting T_i equal to the period of vibration T_0 as in (4.63). With respect to the considered trapezoidal velocity trajectory for example, T_1 or T_2 must be set to T_0. In order to properly chose the which filter modify it has to be reminded that the given kinematic bounds are mandatory and also the relation for the generic T_i

$$T_i \geq T_{i+1} + \ldots + T_d, \qquad i = 1, \ldots, d-1$$

must be satisfied in any case. Therefore for a given vibratory period T_0 there could be three different situations:

1. **$\mathbf{T_0 > T_1 \geq T_2}$**

   In this case the first mean filter must be used to suppress the vibration, that is $T_1^\star = T_0$. As a consequence the velocity will be limited under the prescribed bound, namely

   $$v_{max}^\star = \frac{|h|}{T_1^\star} < v_{max}. \tag{4.65}$$

   Then in order to minimize the time duration of the trajectory the second filter must be recomputed taking into account the new velocity limit $v_{max}^\star$

   $$T_2^\star = \frac{v_{max}^\star}{a_{max}}. \tag{4.66}$$

2. **$\mathbf{T_1 > T_0 > T_2}$**

   In this case the first mean filter is defined as usual by means of the velocity limit

   $$T_1 = \frac{|h|}{v_{max}}, \tag{4.67}$$

   while the second filter must be used to suppress the vibration, that is $T_2^\star = T_0$. Therefore, being the velocity limit unaltered the acceleration will be limited under the prescribed bound, that is

   $$a_{max}^\star = \frac{v_{max}}{T_2^\star} < a_{max}. \tag{4.68}$$

3. **$\mathbf{T_1 \geq T_2 > T_0}$**

   In this case setting one of the filter's length to T_0 means shorten the time duration of M_1 or M_2 therefore exceeding the kinematic bounds. Since the trajectory must be still compliant to that bounds, the only possibility is to add a mean filter M_3 with $T_3 = T_0$. This solution lead to define a double-S trajectory with unaltered limits on velocity and acceleration and jerk limited as a consequence to

   $$j_{max} = \frac{a_{max}}{T_0}. \tag{4.69}$$

The proposed algorithm has been applied to the system in fig. 4-18 in order to sup-

press the vibration of the system $G(s)$ visible in fig. 4-20. In particular the time optimal trajectory is obtained imposing $v_{max} = 0.75$ $[rad/s]$ and $a_{max} = 1.5$ $[rad/s^2]$, thus for a step motion of 1 $[rad]$ results $T_1 = 1.33$ $[s]$ and $T_2 = 0.5$ $[s]$. The system $G(s)$ instead is characterized by a natural undamped frequency $\omega_n = 2\pi$ $[rad/s]$, therefore $T_0 = 1$ $[s]$. In this case, being $T_1 > T_0 > T_2$, the solution is to impose $T_2^\star = T_0$ that means to impose a lower acceleration bound $a_{max}^\star = 0.75$ $[rad/s^2]$.

(a)

(b)

(c)
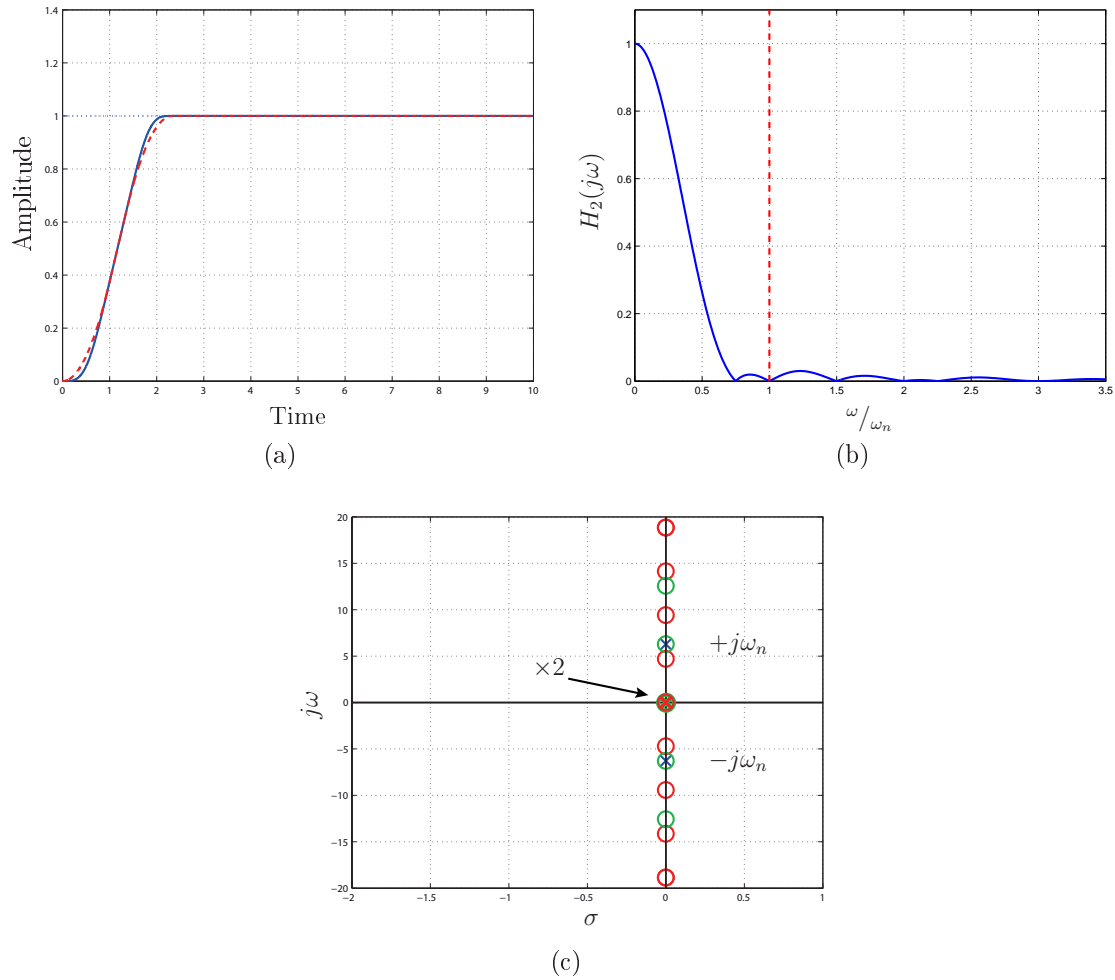
Figure 4-21: Response of the system $G(s)$ with $\delta = 0$ fed by a trapezoidal velocity trajectory generated by means of $H_2(s)$ designed for vibration suppression (a) and frequency response $H_2(j\omega)$ with the vibrating frequency highlighted in red dashed line(b). In (c) the pole-zero diagram of $H_2(s)$ is reported along with the poles of the vibratory system $G(s)$ in blue.

In fig. 4-21 is shown the effect of the modified generator, in particular it has to be noted that the poles that cause vibrations are actually cancelled by the zeroes of the

117
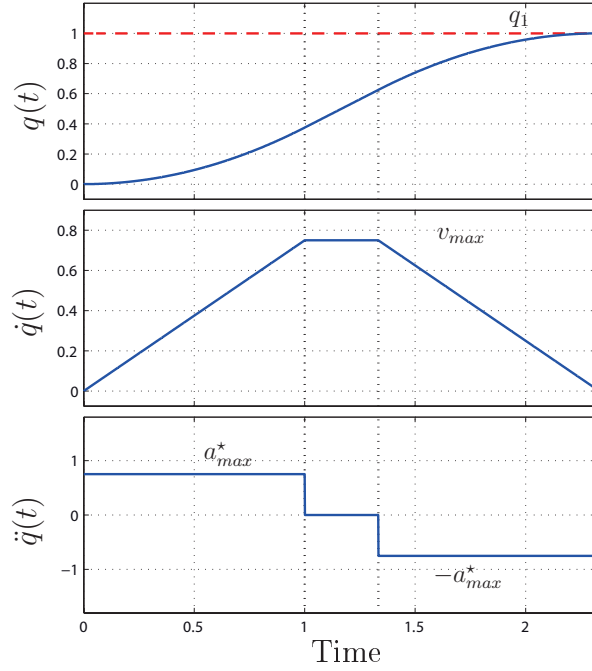
Figure 4-22: Position, velocity and acceleration of the motion from 0 to q_1 obtained by means of trapezoidal velocity trajectory designed in order to suppress a vibrating mode.

second filter (in green) whose duration T_2 has been modified. However in fig. 4-22 it can be noted the reduced limit of acceleration especially if compared to the time optimal one in fig. 4-18(a), this obviously affects the duration of the trajectory resulting longer.

The same algorithm can be easily extended for double-S velocity trajectories by considering three filters, therefore one more possible choice in terms of filter that has to be modified. The reason that lead to modify a double-S velocity trajectory is that despite the augmented smoothness and the limited jerk there is no assurance of vibration suppression because even in this case the design of the planner takes into account only kinematic constraints without caring at dynamic constraints, i.e. vibrations that has to be suppressed. For example in fig. 4-23 is shown the effect of a double-S trajectory generated by means of a filter chain $H_3(s)$ on the vibratory system $G(s)$ considered in the previous case. As can be seen the additional constraint on the jerk does not eliminate the residual vibration. This behavior is explained even more clearly in fig. 4-24 where the pole-zero diagram of the trajectory generator $H_3(s)$
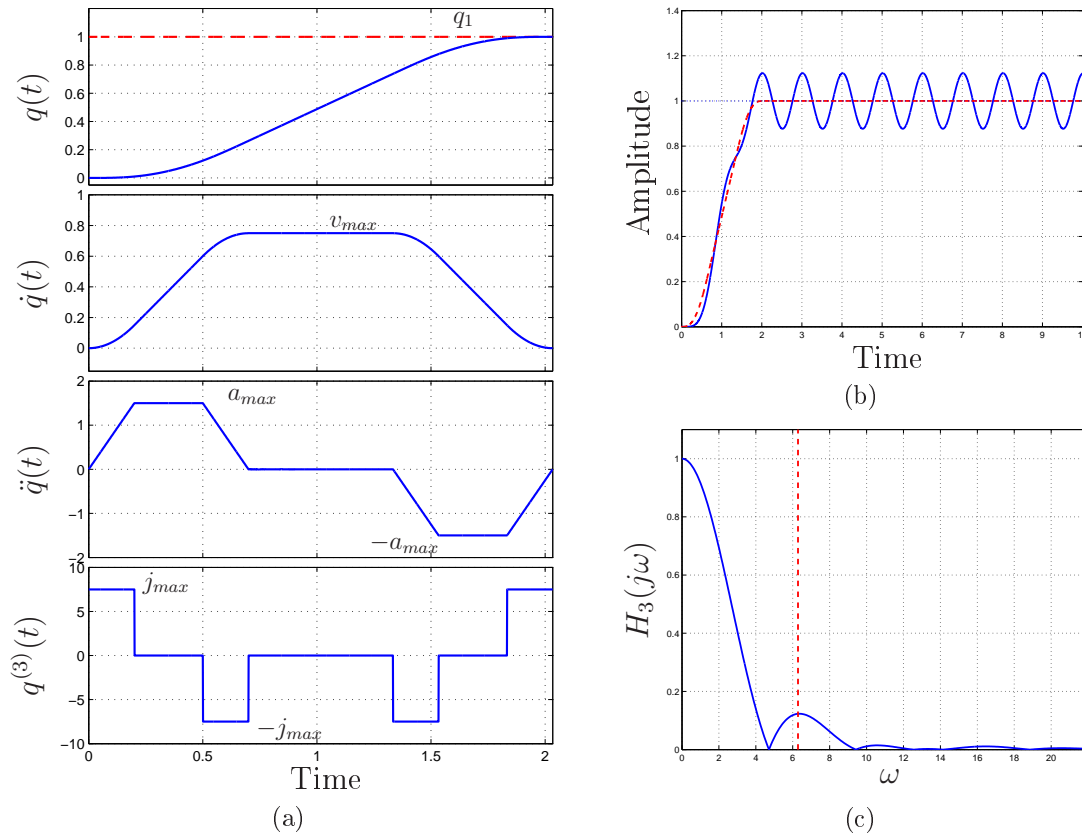
Figure 4-23: Position, velocity, acceleration and jerk of a time optimal motion from 0 to q_1 by means of double-S velocity trajectory with desired bounds on velocity, acceleration and jerk (a). On the right the response of the second order system $G(s)$ fed by $q(t)$ is shown (b) and the frequency response of the trajectory is reported below (c). In (c) the frequency of the vibration is reported in red dashed line.

reports that even in this case there is no zero able to cancel the couple of poles that cause the residual vibration.

The algorithm for a double-S generator is straightforward to the one of trapezoidal generator, it just takes into account an additional parameter T_3 but remains constrained to both kinematic bounds and minimizing time conditions as in the previous case.

1. $\mathbf{T_0 > T_1 \geq T_2 + T_3}$

   The first mean filter must be used to suppress the vibration, that is $T_1^\star = T_0$. As
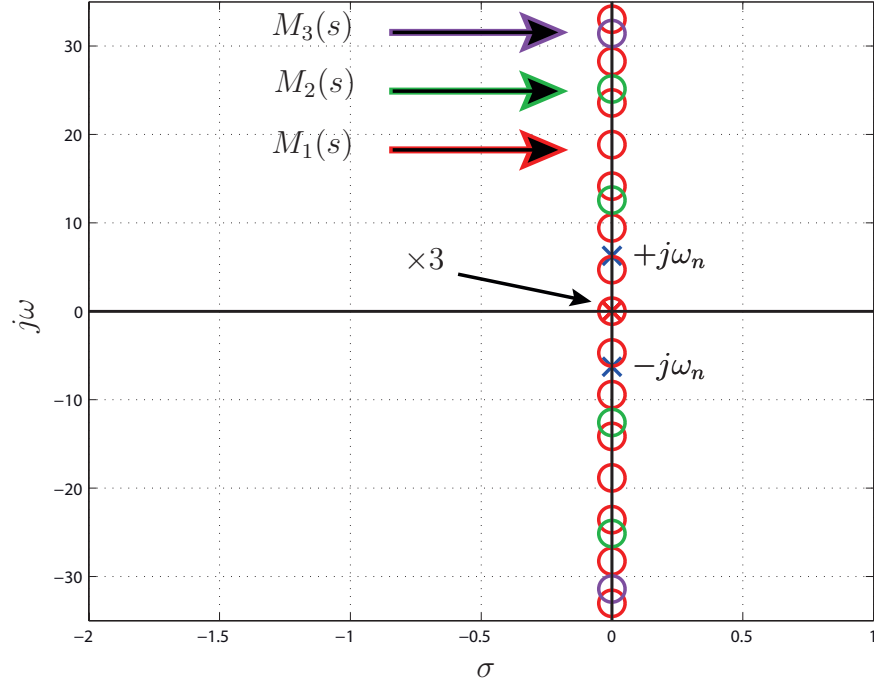
Figure 4-24: Pole-zero diagram of the double-S velocity trajectory generator $H_3(s)$. The contribution of the three filters $M_1(s)$, $M_2(s)$, $M_3(s)$ is reported respectively in red, green and purple. The poles of the vibratory system $G(s)$ is highlighted in blue.

a consequence the velocity will be limited under the prescribed bound, namely

$$v^\star_{max} = \frac{|h|}{T^\star_1} < v_{max}. \qquad (4.70)$$

Then in order to minimize the time duration of the trajectory the second filter must be recomputed taking into account the new velocity limit $v^\star_{max}$

$$T^\star_2 = \frac{v^\star_{max}}{a_{max}}. \qquad (4.71)$$

In this case since $T^\star_2 \neq T_2$ the condition $T^\star_2 \geq T_3$ must be verified in order to achieve minimum time feature. From [13] the condition holds true if

$$a_{max} \leq a_{lim} = \sqrt{v^\star_{max} j_{max}}, \qquad (4.72)$$

otherwise even the acceleration must be limited under the bound, that is

$$\hat{a}_{max} = a_{lim} < a_{max} \tag{4.73}$$

therefore T_2 and T_3 must be recomputed as

$$T_2^{\star} = \frac{v_{max}^{\star}}{\hat{a}_{max}}, \qquad T_3^{\star} = \frac{\hat{a}_{max}}{j_{max}}. \tag{4.74}$$

2. $\mathbf{T_1 > T_0 > T_2 \geq T_3}$

   In this case the first mean filter is defined as usual by means of the velocity limit

   $$T_1 = \frac{|h|}{v_{max}}, \tag{4.75}$$

   while the second filter must be used to suppress the vibration, that is $T_2^{\star} = T_0$. Therefore, being the velocity limit unaltered the acceleration will be limited under the prescribed bound, that is

   $$a_{max}^{\star} = \frac{v_{max}}{T_2^{\star}} < a_{max}. \tag{4.76}$$

   Accordingly the duration of the filter M_3 must be recomputed taking into account the new acceleration limit $a_{max}^{\star}$, that is

   $$T_3^{\star} = \frac{a_{max}^{\star}}{j_{max}}. \tag{4.77}$$

3. $\mathbf{T_2 > T_0 > T_3}$

   In this case the filters M_1 and M_2 are defined as usual by means of kinematic constraints while T_3 must be set equal to T_0. Therefore,

   $$j_{max}^{\star} = \frac{a_{max}}{T_3^{\star}} < j_{max}, \tag{4.78}$$

   being $T_3^{\star} = T_0$

121
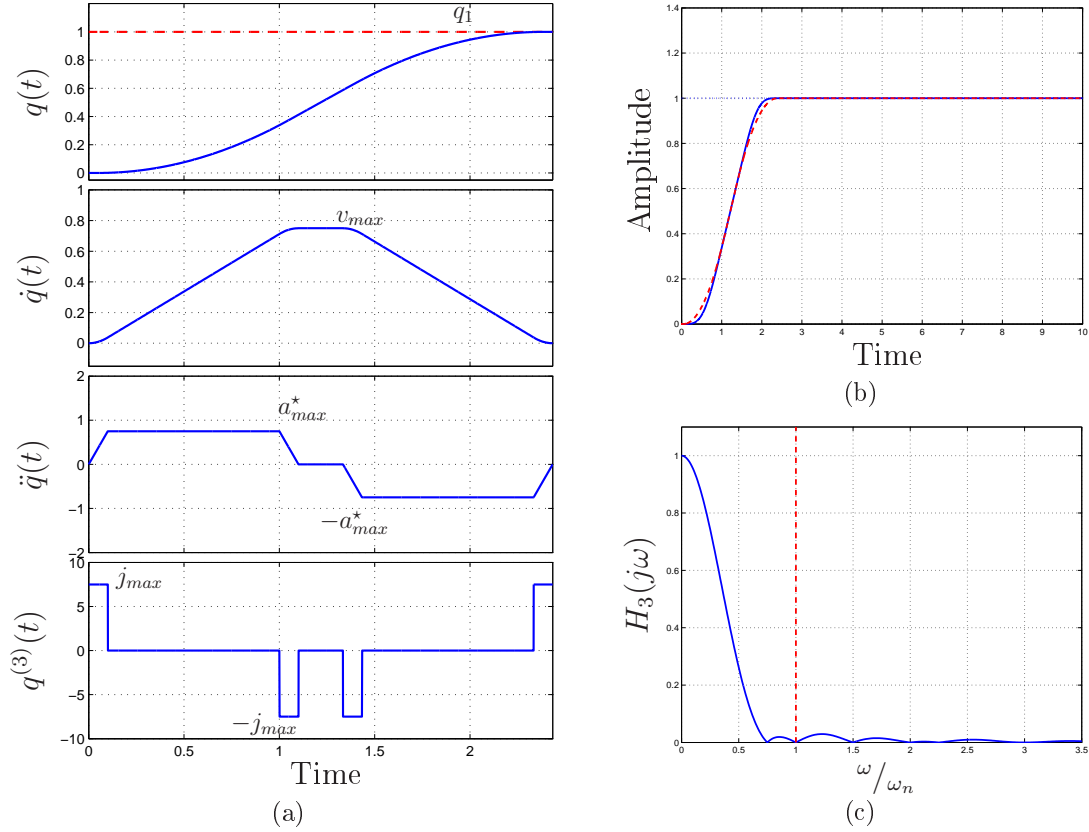
Figure 4-25: Position, velocity, acceleration and jerk of the motion from 0 to q_1 obtained by means of double-S velocity trajectory designed in order to suppress a vibrating mode (a). On the right the response of the second order system $G(s)$ fed by $q(t)$ is shown (b) and the frequency response of the trajectory is reported below (c). In (c) the frequency of the vibration is reported in red dashed line.

4. $\mathbf{T_3} > \mathbf{T_0}$

In this case in order to comply to the kinematic constraint the only possibility is to add a mean filter M_4 with $T_4 = T_0$. This solution lead to define a class $\mathcal{C}^3$ trajectory generator with unaltered limits on velocity, acceleration and jerk with the additional feature of the vibration suppression.

The proposed algorithm has been applied to the system in fig. 4-23 where the time optimal trajectory is obtained imposing $v_{max} = 0.75\ [rad/s]$, $a_{max} = 1.5\ [rad/s^2]$ and $j_{max} = 7.5\ [rad/s^3]$, thus for a step motion of 1 $[rad]$ results $T_1 = 1.33\ [s]$, $T_2 = 0.5\ [s]$ and $T_3 = 0.2\ [s]$. The system $G(s)$ instead is characterized by a natural undamped frequency $\omega_n = 2\pi\ [rad/s]$, therefore $T_0 = 1\ [s]$. In this case, being $T_1 > T_0 > T_2$,

the solution is to impose $T_2^\star = T_0$ that means to impose a lower acceleration bound $a_{max}^\star = 0.75 \ [rad/s^2]$. Accordingly T_3 has to be recomputed taking into account $a_{max}^\star$, therefore $T_3^\star = 0.1 \ [s]$. In fig. 4-25 the response of the system $G(s)$ to the trajectory provided by the modified planner is presented. As can be seen the trajectory generator designed taking care of dynamic constraints actually suppress vibrations, in particular in fig. 4-25(c) the drop of the frequency response $H_3(j\omega)$ in correspondence of the frequency of vibration ω_n denotes a proper pole-zero cancellation. On the other hand the trajectory results longer by comparing it to the one in fig. 4-23(a) since the acceleration can't reach the kinematic bound.

It has to be noted that in any case the design of the planner for vibration suppression as proposed, imply to loose the time optimality feature of the trajectory, since at least one of the derivative bounds is further limited. However allowing a slight time extension of the motion it has been proved that the trajectory generator can actually suppress vibrations. Nevertheless by means of the proposed algorithm one may obtain a time minimum trajectory generator with vibration suppression.

4.4.2   Trajectories with Sinusoidal Blends

In Section 4.3.2 has been described the method which permit to achieve a modified trapezoidal/double-S velocity trajectory generator by means of dynamic filters. That is, in order to obtain multi-segment polynomial trajectories with sinusoidal blends (i.e. described by harmonic functions in Section 4.1.3, the filter chain described in Section 4.3.1 must be modified by substituting the last mean filter with the so-called sinusoidal filter $S_i(s)$ in (4.53)

$$S_i(s) = \frac{1}{2} \left(\frac{\pi}{T_i} \right)^2 \frac{1 + e^{-sT_i}}{s^2 + \left(\frac{\pi}{T_i} \right)^2}.$$

Accordingly to the discussion in the previous section, the frequency analysis of a modified trapezoidal/double-S velocity trajectory can be performed by merging the effects of the mean filters of the chain and that of the sinusoidal filter above. In
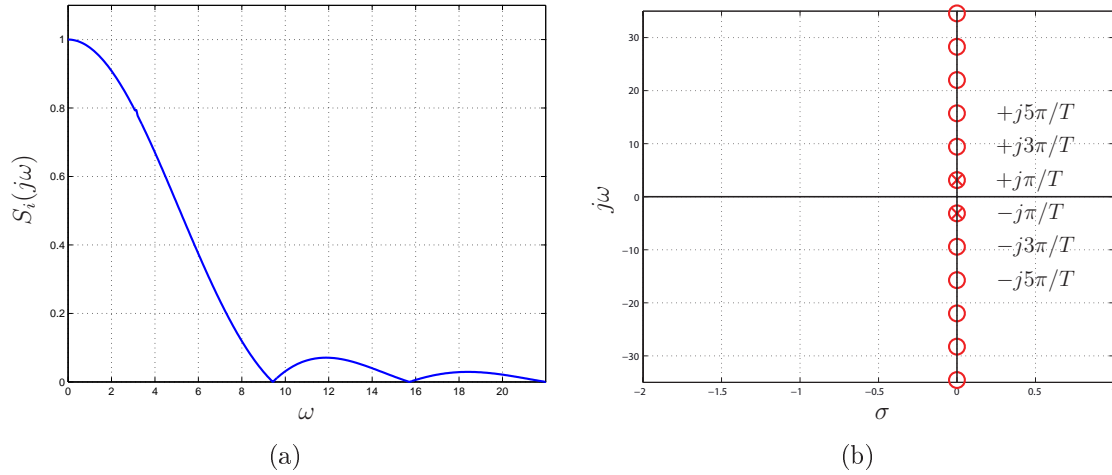
Figure 4-26: Frequency response of the sinusoidal filter $S_i(s)$ (a) and respective pole-zero diagram (b).

particular the analysis of the sinusoidal filter shows a different behavior with respect the mean filter in figs. 4-16 and 4-17. In fig. 4-26(a) the frequency response $S_i(j\omega)$ drop to zero slower than a mean filter with the same duration T. Namely it results

$$|S_i(j\omega)| = 0 \text{ if } \omega = \frac{2k+1}{2} \cdot \frac{2\pi}{T}, \text{ being } k \in \{\mathbb{N}\backslash 0\}, \tag{4.79}$$

while the mean filter is zero for $2\pi k/T$. Moreover from the pole-zero diagram in fig. 4-26(b) it is shown that the filter introduces a couple of complex conjugate poles that are cancelled by a couple of zeroes of the filter itself, enlarging the first lobe of the frequency response accordingly. Anyway the presence of infinite zeroes on the imaginary axis permit to assume the filter S_i as a candidate to suppress a vibration of an undamped system, specifically being T_0 the period of vibration, it can be proven that S_i suppress the vibration if its duration T is set to $T = 1.5T_0$.

Despite that, the use of the sinusoidal filter to suppress vibration when inserted in a trajectory generator as described in Section 4.3.2 may not be an optimal solution. In lieu of an example it can be considered the case of a modified trapezoidal trajectory with

$$\begin{cases} v_{max} = & 0.75 \ [rad/s], \\ a_{max} = & 1.5 \ [rad/s^2], \end{cases}$$

124

and a desired step motion of 1 $[rad]$, feeding a vibratory system $G(s)$ whose vibration period is $T_0 = 1$ $[s]$. From the approach in Section 4.3.2 the duration of mean filter $M_1(s)$ and that of $S_2(s)$ results results

$$\begin{cases} T_1 = & 1.33\ [s], \\ T_2 = & 0.785\ [s]. \end{cases}$$

Then by applying the proposed algorithm of Section 4.4.1 and taking into account the zeroing affect of $S_2(s)$, the duration of the sinusoidal filter has to be modified as $T_2^\star = 1.5T_0$. Unfortunately in this case $T_1 < T_2^\star$, then even T_1 has to be modified in order to respect the constraint $T_1 \geq T_2$, that is

$$T_1^\star \geq T_2^\star = 1.5\ [s],$$

therefore the total duration would be $T_1^\star + T_2^\star = 3$ $[s]$. As a matter of fact this solution it is definitely not a minimum time solution since it can be proven that a trajectory which satisfy the same constraints (both kinematic and dynamic) can be achieved by means of a modified double-S trajectory generator of shorter duration. Namely, assuming

$$\begin{cases} v_{max} = & 0.75\ [rad/s], \\ a_{max} = & 1.5\ [rad/s^2], \\ j_{max} = & 7.5\ [rad/s^2], \end{cases}$$

the duration of the filters M_1, M_2, S_3 become

$$\begin{cases} T_1 = & 1.33\ [s], \\ T_2 = & 0.5\ [s], \\ T_3 = & 0.314\ [s]. \end{cases}$$

Then by setting $T_2^\star = T_0 = 1$ the acceleration is limited to $a_{max}^\star < a_{max}$ and the duration of the sinusoidal filter must be recomputed becoming

$$T_3^\star = \frac{a_{max}^\star}{j_{max}} \frac{\pi}{2} = 0.157 \; [s].$$

Therefore the total duration of the trajectory is $T_1 + T_2^\star + T_3^\star = 2.49 \; [s]$ that is consistently shorter than the modified trapezoidal one.

4.4.3   Uniform B-Spline trajectories

In Section 4.3.3 a method for the implementation of a uniform b-spline trajectory generator based on dynamic filters is reported. The generator exploit the equivalence between a b-spline trajectory of degree d and the output of a chain of d identic mean filters of duration T, fed by a proper staircase signal built by means of the control points $\boldsymbol{p}_j$ of the desired spline trajectory. In [11] the chain of d filters has been analyzed in terms of frequency response and compared to the most common input shaping techniques, leading to a design procedure that takes into account the dynamic constraint of a given plant in order to minimize residual vibrations. In particular the analysis points out the low-pass behavior of the filter chain and a zeroing effect at frequency $\omega = 2\pi/T$ (and multiple frequencies $k\omega$, $k \in \mathbb{N}$), being T the knot span of the b-spline trajectory. Also, for growing degree d of the spline both the low-pass behavior and the zeroing effect are enhanced, making the b-spline generator even more robust of n-derivative input shapers (see Chapter 2) with respect to vibration reduction. Therefore a proper choice of the knot span T and accordingly the duration of the filters permits to greatly reduce vibrations without the addition of command shapers.

The discussion in [11] can be further extended including the considerations given in Section 4.4.1 with respect to the mean filter $M(s)$. In particular has been already stated that the mean filter can actually suppress a vibration of period $T_0 = 2\pi/\omega_n$ given that the duration of the filter $M(s)$ is set to $T = T_0$. Also, it has been shown that the frequency analysis of a trajectory generator based on a chain of dynamic filters,
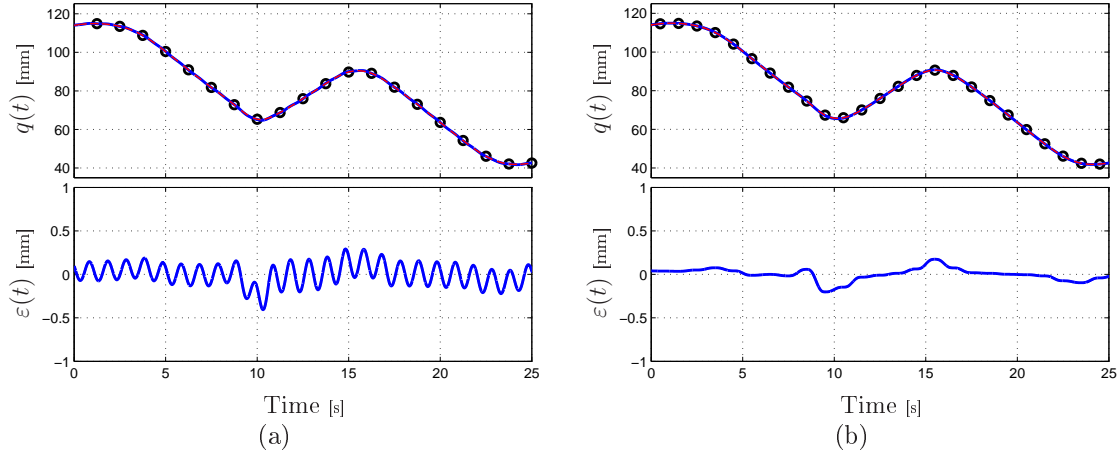
Figure 4-27: Uniform cubic b-spline trajectory applied to an undamped second order system $G(s)$ with $T_0 = 2\pi/\omega_n$. In (a) the motion law is provided by means of a filter-based generator assuming a knot span $T = 1.25T_0$. In (b) the same motion law is provided assuming $T = T_0$. Pictures below denoted with $\varepsilon(t)$, describe the error between the set-point given by the generators (red dashed line) and the actual position of the system $G(s)$ (in blue).

can be easily performed by composition of the contribution of each single element of the chain, i.e. in terms of pole-zero diagram it results the merge of the diagrams of each filter. Therefore for a b-spline generator of order d with knot span T the pole-zero diagram results equal to that of fig. 4-17(a) considering every poles/zeroes of multiplicity d. This also makes the comparison in [11] with respect to derivative-based input shapers consistent, since the effect in terms of pole-zero diagram of an n-derivative IS is to augment the multiplicity of the zeroes of a ZV IS to an order $n + 1$. In addition the vibration suppression conditions for the cascade of filters directly descend from that of the single filter $M_i(s)$, that is being $G(s)$ an undamped second order system whose period of vibration is T_0, the b-spline trajectory generator can provide a vibration-free motion if the knot span T is chosen such that $T = T_0$. However the choice of the knot span for a uniform b-spline trajectory planner has a direct influence on the dynamics of the set-point that can be provided to the plant. In particular being the knots equally spaced, the span T is usually chosen accordingly to the frequency content of the desired motion law in a sampling fashion. That is the lower is the allowed interpolation error between desired motion and spline trajectory,

127

the lower is the knot span T (which assumes the meaning of a sample time for the desired motion) and therefore the greater is the number of via-points $\boldsymbol{q}_j$. These considerations lead to define two different cases, respectively when the motion law is discretized by means of a sample time T which is longer or shorter than the period of vibration T_0.

The case $T > T_0$ is reported in fig. 4-27 for a uniform b-spline trajectory of order 3 feeding an undamped vibratory system $G(s)$. It can be noted that accordingly to what said before, even if the choice of $T > T_0$ acts as a conservative solution to reduce the amplitude of the vibrations, it doesn't assure the complete suppression because the cancellation of the poles of $G(s)$ that cause the vibration doesn't occurs. In particular the tracking error $\varepsilon(t)$ of fig. 4-27(a) highlights a residual vibration during the whole motion. In fig. 4-27(b) however, the same motion law is given by means of a generator composed of filters whose duration $T^\star = T_0$ completely suppress the vibration. It is worth noting that in general the change of the duration T must be accompanied with the recomputing of the via-points of the trajectory, in fig. 4-27(b) for example the motion law has been sampled again with the sample time $T^\star$. In this way the total number of via-points $\boldsymbol{q}_j$ has grown (up-sampling) but the resulting trajectory maintains the same characteristics in terms of kinematic constraints, i.e. velocity, acceleration, etc..

In fig. 4-28 instead the dual case is shown, that is when the spline trajectory is computed with a knot span $T < T_0$. As can be seen in fig. 4-28(a) this is an undesirable condition that may causes large vibrations. In order to suppress the vibration one has to raise the filters duration to $T^\star = T_0$, however in this case recomputing the set of via-points may not be desirable. In fact this would be a down-sampling procedure that affects the interpolation error with respect to the desired motion law, which typically grows as the sampling become less dense. Therefore when recomputing via-points is unsatisfactory the only solution is to assume an overall slow-down of the trajectory by acting only on the duration of the filters as shown in fig. 4-28(c).

128
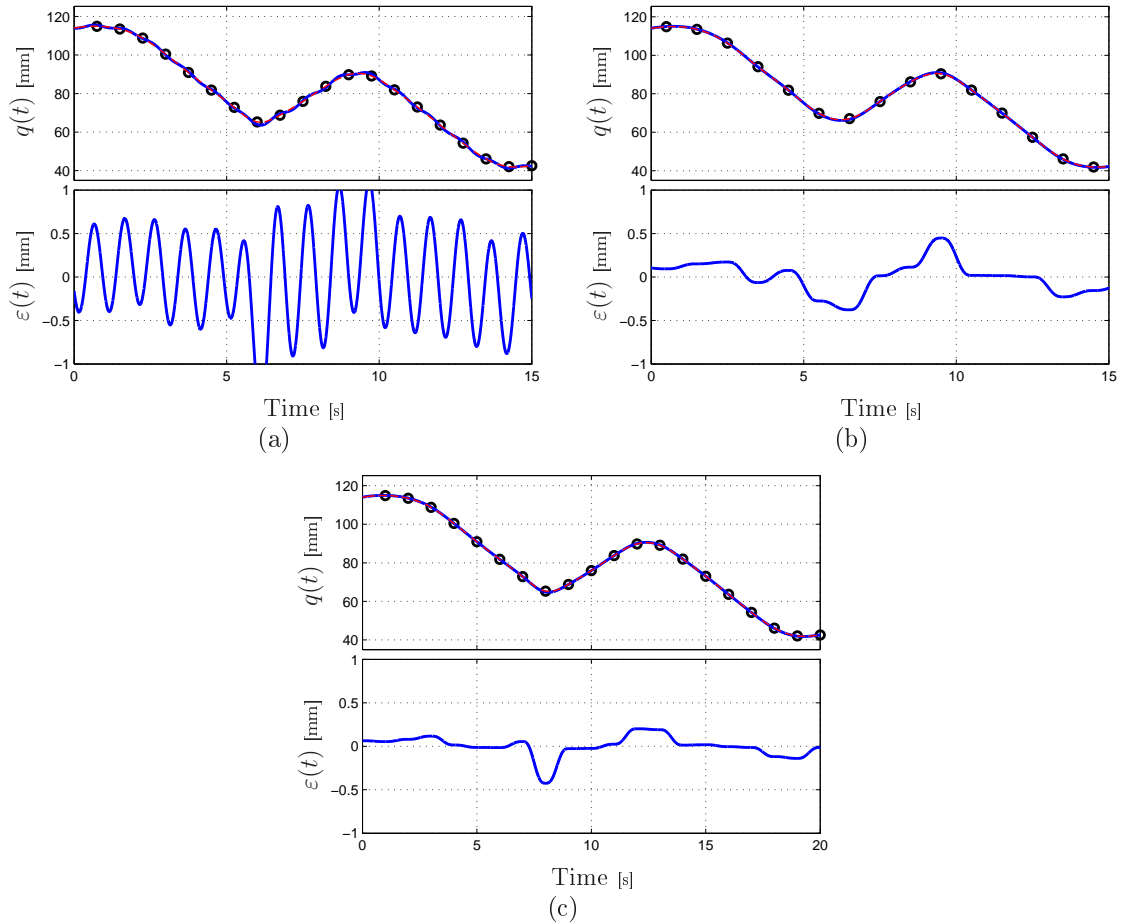
Figure 4-28: Uniform cubic b-spline trajectory applied to an undamped second order system $G(s)$ with $T_0 = 2\pi/\omega_n$. In (a) the motion law is provided by means of a filter-based generator assuming a knot span $T = 0.75T_0$. In (b) the same motion law is provided assuming $T = T_0$ and recomputing the via-points accordingly, in order to maintain the same dynamics of the trajectory. In (c) the spline trajectory is generated assuming $T = T_0$ but using the same via-points of (a) avoiding down-sampling. Pictures denoted with $\varepsilon(t)$, describe the error between the set-point given by the generators (red dashed line) and the actual position of the system $G(s)$ (in blue).

4.5   FIR Filters for Online Trajectory Generation

The expression of a generic trajectory is usually provided in the continuous-time domain by means of an analytic function of time t. On the other hand, for being used as a reference signal for a computer controlled system, it needs to be evaluated at discrete-time instants $t_k = kT_s$, being T_s the sampling period. For this reason, it is convenient to directly express the trajectory in the discrete-time domain, obtaining a system able to provide at each time instant kT_s the value $q(k)$.

4.5.1   Multi-Segment Trajectory Generator

In 4.3.1 a planner for multi-segment trajectories is obtained by connecting d filters $M_i(s)$ in a cascade configuration fed by a step function

$$\boldsymbol{Q}_d(s) = \frac{h}{s} \cdot M_1(s) \cdot M_2(s) \cdot \ldots \cdot M_d(s). \tag{4.80}$$

Starting from the above equation it is possible to deduce an equivalent discrete-time system by discretizing the filters with one of the techniques available in the literature and providing as input the sequence obtained by sampling with a period T_s the continuous step function. In particular in [13], the adoption of backward differences method leads to a discrete-time system composed by a chain of FIR filters, whose transfer function results

$$
\begin{aligned}
M_i(z) \quad &= M_i(s)\big|_{s=\frac{1-z^{-1}}{T_s}} \\
&= \frac{T_s}{T_i} \frac{1-z^{-N_i}}{1-z^{-1}} \\
&= \frac{1}{N_i} \frac{1-z^{-N_i}}{1-z^{-1}}
\end{aligned}
\tag{4.81}
$$

where

$$N_i = \frac{T_i}{T_s} \tag{4.82}$$

is the number of samples (not null) of the filter response, which is also equal to the number of elements composing the FIR filter as they appear in the equivalent
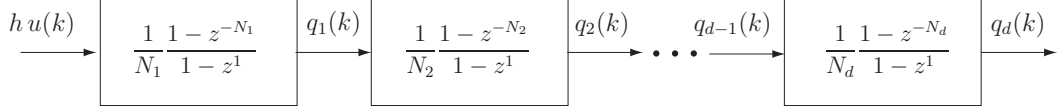
Figure 4-29: System composed by d moving average filters for the computation of an optimal trajectory of class $\mathcal{C}^{d-1}$ at discrete time-instants kTs.

(nonrecursive) formulation

$$M_i(z) = \frac{1}{N_i} + \frac{1}{N_i}z^{-1} + \frac{1}{N_i}z^{-2} + \ldots + \frac{1}{N_i}z^{-N_i-1}. \qquad (4.83)$$

Note that (4.83) is the expression of a moving average filter, which averages the last N_i samples. Finally, the expression of $Q_n(z)$ representing the discrete-time trajectory $q_n(k)$ in the Z-domain results

$$\boldsymbol{Q}_n(z) = \frac{h}{1 - z^{-1}} \cdot M_1(z) \cdot M_2(z) \cdot \ldots \cdot M_n(z) \qquad (4.84)$$

where $\dfrac{1}{1 - z^{-1}}$ is the Z-transform of

$$u(k) = \begin{cases} 1, & \text{for } k = 0, 1, 2, \ldots \\ 0, & \text{for } k < 0. \end{cases} \qquad (4.85)$$

It is worth highlighting that the temporal sequence $q_n(k) = \mathcal{Z}^{-1}Qn(z)$ only approximates the corresponding continuous-time trajectory $q_n(t)$. However, it is possible to prove that when T_s goes to zero, such an error vanishes. From a practical point of view, this means that, for sufficiently small sampling periods, the sequence $q_n(k)$ can be used in lieu of the corresponding function $q_n(t)$ without appreciable differences. The bank of d FIR filters shown in fig. 4-29, fed with sampled step functions (defining the desired final positions), can be therefore adopted to generate the trajectory of order d. Also the structure proposed in fig. 4-29 for the generation of time-optimal trajectories results very efficient from a computational point of view. In fact, the i-th

FIR filter is characterized by the differences equation

$$q_i(k) = q_i(k-1) + \frac{1}{N_i}\left(q_{i-1}(k) - q_{i-1}(k-N_i)\right), \; i = 1, \ldots, d \qquad (4.86)$$

and, for the evaluation of q_i at the i-th sampling instant, only two additions and one multiplication are necessary. Therefore the trajectory of order d requires d multiplications and $2d$ additions. It is worth nothing that the order of complexity of the chain of FIR filters and of the equivalent polynomial expression is comparable, but in case of direct evaluation of the analytic expression of the trajectory it is also necessary a search algorithm to determine which segment must be considered at a specific value of time t and a switch statement to apply a different expression for each tract. For this reason, especially for high values of the order d, the expression based on FIR filters may be preferable to the standard analytic expression of multi-segment trajectories both in terms of implementation complexity and computational costs.

4.5.2 Discrete-Time Filter for Trigonometric Blends

In Section 4.3.2 the generation of a $\mathcal{C}^{d+1}$ class trajectory with "sinusoidal" blends has been achieved by adding a proper filter $S_{d+1}(s)$ at the end of a chain of d moving average filters $M_i(s)$ as in fig. 4-11. Moreover in Section 4.5 the discretization of a multi-segment trajectory generator has been reported leading to a chain of FIR filters. Therefore in order to provide a discrete-time trigonometric trajectory generator it is necessary to discretize the sinusoidal filter $S_i(s)$ in (4.53). In [12] the discrete transfer function $S_i(z)$ of the sinusoidal filter has been computed by z-transforming the sequence obtained by sampling (4.52) with a periods T_s:

$$S_i(z) = \frac{(1 - \cos(\frac{\pi}{N_i}))(z^{-1} + z^{-(N_i+1)})}{1 - 2z^{-1}\cos(\frac{\pi}{N_i}) + z^{-2}}$$

where $N_i = T_i/T_s$ In this way, the impulse response of the discrete-time filter coincides exactly with continuous one at discrete time instants kT_s, and is therefore zero for $kT_s > T_i$. Note that, being $\cos(\frac{\pi}{N_i})$ a constant to be computed only once, the digital

132

implementation of $S_i(z)$ is computationally efficient, requiring four additions and two multiplications.

4.5.3   FIR Filters for Uniform B-spline Trajectory Generation

A unified transformation to convert analytic B-splines in the discrete domain does not exist yet. In particular, with reference to cardinal B-splines it is possible to find in the literature different techniques to obtains discrete B-splines. In general, they are defined by directly sampling analytic B-splines with Z-transform, bilinear transform, etc.

In [10] the discrete B-spline $\mathbf{q}_k$ is defined as the sequence that equals the corresponding analytic uniform B-spline $q_u(t)$ at the discrete-time instants kT_s:

$$\mathbf{q}_k = q_u(kT_s). \tag{4.87}$$

where it is assumed that $T = N T_s$, $N \in \mathbb{N}$, i.e. that the generic knot span T contains a whole number N of sampling periods. Since a B-spline is nothing but a linear combination of basis functions properly translated in time, the exact discretization of the basis function $B^d(t)$ is considered at first. In particular the discrete basis function $B_k^d = B^d(kTs)$ can be expressed as

$$B_k^d = \underbrace{\frac{1}{N}B_k^0 * \frac{1}{N}B_k^0 * \ldots * \frac{1}{N}B_k^0}_{d \text{ times}} * \mathcal{Z}^{-1}\{F_d(z^{-1})\} * B_k^0 \tag{4.88}$$

where $*$ denotes the discrete convolution product, $\mathcal{Z}$ the Z-transform,

$$B_k^0 = B^0(kT_s) = \begin{cases} 1, & \text{if } k = 0, 1, \ldots, N-1 \\ 0, & \text{otherwise.} \end{cases} \tag{4.89}$$

and $F_d(z^{-1})$ is a FIR filter defined by

$$F_d(z^{-1}) = \frac{z^{-1}Q_{d-1}(z^{-1})}{d!}, \tag{4.90}$$

$$F_1(z^{-1}) = z^{-1}$$

$$F_2(z^{-1}) = \tfrac{1}{2}z^{-1} + \tfrac{1}{2}z^{-2}$$

$$F_3(z^{-1}) = \tfrac{1}{6}z^{-1} + \tfrac{4}{6}z^{-2} + \tfrac{1}{6}z^{-3}$$

$$F_4(z^{-1}) = \tfrac{1}{24}z^{-1} + \tfrac{11}{24}z^{-2} + \tfrac{11}{24}z^{-3} + \tfrac{1}{24}z^{-4}$$

$$F_5(z^{-1}) = \tfrac{1}{24}z^{-1} + \tfrac{26}{24}z^{-2} + \tfrac{66}{24}z^{-3} + \tfrac{26}{24}z^{-4} + \tfrac{1}{24}z^{-5}$$

Table I

Expression of the filter $F_d(z^{-1})$ for different values of d.

with the polynomial

$$Q_r(z^{-1}) = c_{r,0} + c_{r,1}z^{-1} + \ldots + c_{r,r-1}z^{-(r-1)} + c_{r,r}z^{-r} \qquad (4.91)$$

whose coefficients (for $r \geq 2$) can be computed in a recursive way as

$$c_{r,0} = c_{r,r} = 1$$

$$c_{r,r-i} = c_{r-1,r-i-1} \cdot (i+1) + c_{r-1,r-i} \cdot (r-i+1)$$

with $i = 1, \ldots, \left[\frac{r}{2}\right]$, being $\left[\cdot\right]$ the integer part operator. In Tab. I the expression of the FIR filter $F_d(z^{-1})$ defined in (4.90) is reported for several values of the B-spline degree d. From (4.88) it follows that, analogously to analytic B-splines, a generic discrete basis function B_k^d of degree d can be computed by applying the sequence B_k^0 to a chain of d mean filters. In the discrete-time case, it is necessary to consider the
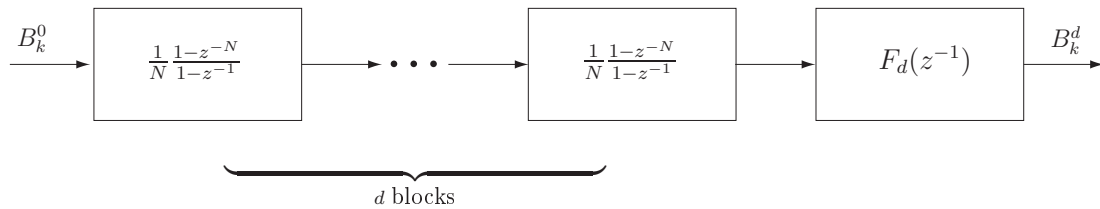
Figure 4-30: System composed by d moving average filters and by the FIR filter $F_d(z^{-1})$ defined in (4.90) for the computation of the discrete B-spline basis function B_k^d of degree d.

additional filter $F_d(z^{-1})$ as illustrated in Fig. 4-30. Therefore the discrete B-spline

$$\mathbf{q}_k = \sum_{j=0}^{m} \boldsymbol{p}_j B_{k-jN}^d \tag{4.92}$$

of degree d can be obtained as output of the dynamic system composed by a cascade of d moving average filters

$$
\begin{aligned}
M(z) &= \frac{1}{N} \frac{1 - z^{-N}}{1 - z^{-1}} \\
&= \frac{1}{N} \left(1 + z^{-1} + z^{-2} + \ldots + z^{-(N-1)} \right)
\end{aligned}
\tag{4.93}
$$

and by the additional FIR filter $F_d(z^{-1})$ feeded with the piecewise constant function

$$\boldsymbol{p}_k = \sum_{j=0}^{m} \boldsymbol{p}_j B_{k-jN}^0 \tag{4.94}$$

where $\boldsymbol{p}_j$ are the control points of the related analytic B-spline. In Fig. 4-31 the function $\boldsymbol{p}_k$ is reported along with the values of the analytic B-spline corresponding to the given control points $\boldsymbol{p}_j$ at the discrete time instants kT_s.

The procedure described so far leads to an exact discretization of the basis function of uniform B-splines of generic degree d that can be recursively defined starting from $B^0(t)$, and therefore the discrete B-spline can be obtained. However in this case it is necessary to take into account the presence of the FIR $F_d(z^{-1})$ which makes the relation more complex. On the other hand, one would expect that a discrete B-spline basis function of a given degree d could be defined as a cascade of d mean filters that receives as input the discrete-time function $B_k^0 = B^0(kT_s)$ similarly to the continuous case. This is equivalent to neglect the term $\mathcal{Z}^{-1}\left\{F_p(z^{-1})\right\}$ in (4.88) and leads to the definition of approximated discrete B-spline basis functions and approximated discrete B-splines, that do not share the same values of analytic basis functions $B^d(t)$ and analytic B-splines $\mathbf{q}_u(t)$ at discrete points kT_s but approximate such values within a prescribed tolerance that depends on N. In particular it can be proved that when N reaches an high value, the difference is considerable reduced (for

135
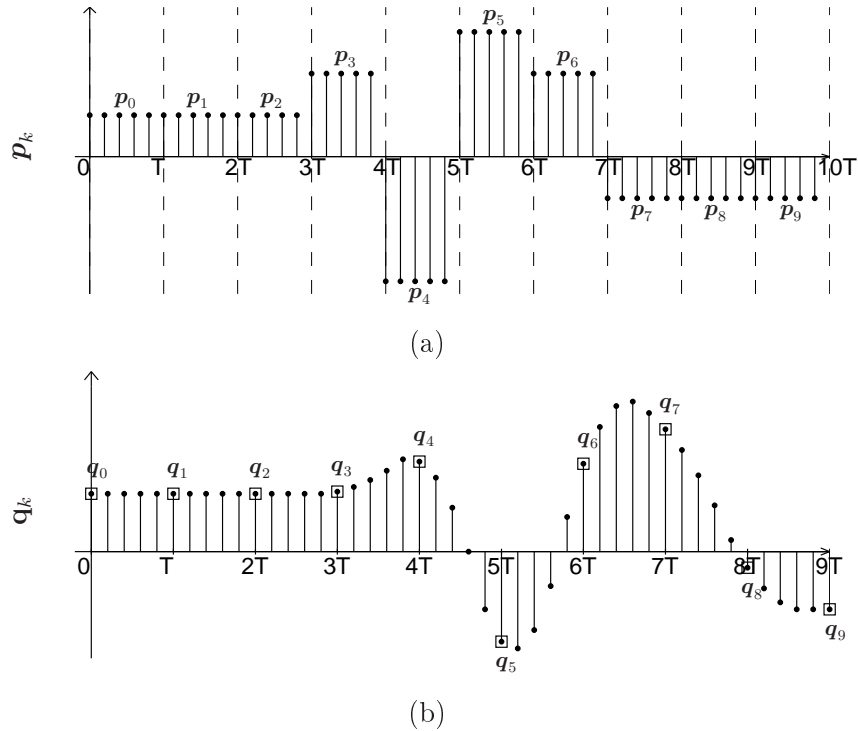
Figure 4-31: Samples of the piecewise constant function $\boldsymbol{p}_k$ (a) generating the spline profile $\mathbf{q}_k$ that interpolates the given points $\boldsymbol{q}_j$ (b).

instance for $N = 500$ the error is less than 1%) and the use of discrete B-spline basis functions with or without $F_d(z^{-1})$ is nearly the same.

Anyway, although a chain composed only by running average filters is particularly attractive (and simple), it is worth noticing that, the FIR filter $F_d(z^{-1})$ involves only a slight additional complexity. Namely this filter only depends on the last d samples of the input but relaxes constraints on N.

4.5.4 Uniform B-spline Online Trajectory Generator Based on FIR Filters

In sections 4.3.3 and 4.5 the methods for design and implementation of a uniform B-spline trajectory generator are reported showing that this kind of splines can be efficiently generated by means of a chain of linear filters properly fed with the sequence of the control points that determine the shape of the curves in the space. The trajectory generator shown in fig. 4-33(a) is composed by d moving average filters of

order N and an algorithm that transforms the desired points $\boldsymbol{q}_j$ in the set of control points $\boldsymbol{p}_j$ used for defining the sequence $\boldsymbol{p}(k)$ which is the input for the filter chain. Note that the B-spline is defined by adopting a sampling period T_s, that generally coincides with the sampling time of the overall control system, while $\boldsymbol{p}(k)$ is a piecewise constant sequence, in which the generic value $\boldsymbol{p}_j$ is maintained for $T = N \cdot Ts$ seconds. Moreover, it is worth noticing that, while the spline evaluation is performed online, its definition (i.e. the computation of the control points) is made off-line. In particular in [10] it is shown that by adopting B-splines of generic degree d, the systems to be solved for obtaining the control points will be characterized by banded matrices, whose inversion can be carried out in a very efficient way.

Anyway it is clear that such a solution can only be found once all the via-points $\boldsymbol{q}_j$ are known, i.e. the solution must be performed off-line. However, when the via-points are given progressively, it may be desirable that control points are calculated runtime by approximating, if possible, the ideal solution. To this purpose, in [14] it is demonstrated that the relationship (4.61) between control points and via-points can be seen as a dynamic relationship between via-points and control points, that in the domain of the Z-transform can be expressed as

$$\frac{P(z)}{Q(z)} = \frac{6}{z + 4 + z^{-1}} \tag{4.95}$$

for cubic B-splines, and

$$\frac{P(z)}{Q(z)} = \frac{120}{z^2 + 26z + 66 + 26z^{-1} + z^{-2}} \tag{4.96}$$

for quintic B-splines for example. Unfortunately, both filters (4.95) and (4.96) are unstable system and consequently they cannot be used for computing the sequence $\boldsymbol{p}_j$ from $\boldsymbol{q}_j$. This is a direct consequence of the fact that the interpolation procedure is a global problem that involves all the points $\boldsymbol{q}_j$. Thus in order to implement such a filter, the most straightforward method is to truncate the ideal impulse response by windowing. In other words it is possible to approximate the interpolation process by taking into account only a small set of points $\boldsymbol{q}_i$. This approach leads to a FIR filter
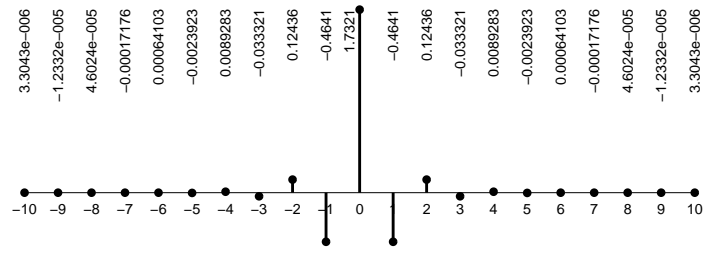
(a)
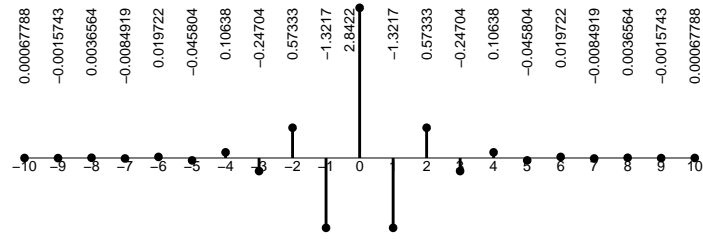
(b)

Figure 4-32: Impulse response $h(n)$ of the filter (4.95) (a) and of the filter (4.96) (b).

defined by

$$H(z) = \sum_{n=-r}^{r} h(n) \, z^{-n} \tag{4.97}$$

that approximates the impulse response of (4.95) and (4.96) within a prescribed tolerance according to the value of r. The sequences $h(n)$ for $d = 3$ and $d = 5$ are reported in Fig. 4-32 and in both cases it can be noted that the value of $h(n)$ becomes extremely small as $|n|$ grows. Namely the choice $r = 4$ for example guarantees an approximation error with respect to the exact solution of the interpolation problem, smaller than 0.5%.

Moreover, since $H(z)$ is not a causal filter, in order to practically implement the transformation between via points and control points it is necessary to introduce a delay equal to r which makes the filter feasible, that is

$$H'(z) = z^{-r} \, H(z) = \sum_{n=0}^{2r} h(n-r) \, z^{-n}. \tag{4.98}$$

138

By means of $H'(z)$ it is possible to replace the off-line interpolation leading to a complete on-line trajectory generator that assume an arbitrarily small interpolation error. The chain is then composed by two main elements a FIR filter $H''^r_d(z)$ of order $2r+1$ that computes the control points from desired via-points and a cascade of d moving average filters. The former element is computed with a sample time T, multiple of the basic sample period Ts $(T = N \cdot T_s)$, that represents the time distance among the points to be interpolated/approximated. The average filters are implemented with a period T_s, and they have an impulse response of length equal to T, being of order N. Between the two elements, it is necessary a rate transition from T to T_s, that maintains the value $\boldsymbol{p}_j$ for T seconds, see fig. 4-33(b).

$\{\boldsymbol{q}_j\}$ → Interpolation/approximation problem solver → $\{\boldsymbol{p}_j\}$ → Sequencer → $\boldsymbol{p}_k$ → $\dfrac{1}{N}\dfrac{1-z^{-N}}{1-z^{-1}}$ → $\cdots\cdots$ → $\dfrac{1}{N}\dfrac{1-z^{-N}}{1-z^{-1}}$ → $\boldsymbol{q}_{ak}$ → $\boxed{F_d(z^{-1})}$ → $\boldsymbol{q}_k$

$\underbrace{}_{d \text{ blocks}}$

(a)

On-line (T) $\quad$ On-line (T_s)

$\boldsymbol{q}_j$ → $H''_3(z)$ → $\boldsymbol{p}_j$ → Rate transition → $\boldsymbol{p}_k$ → $\dfrac{1}{N}\dfrac{1-z^{-N}}{1-z^{-1}}$ → $\dfrac{1}{N}\dfrac{1-z^{-N}}{1-z^{-1}}$ → $\dfrac{1}{N}\dfrac{1-z^{-N}}{1-z^{-1}}$ → $\boldsymbol{q}_k$

(b)
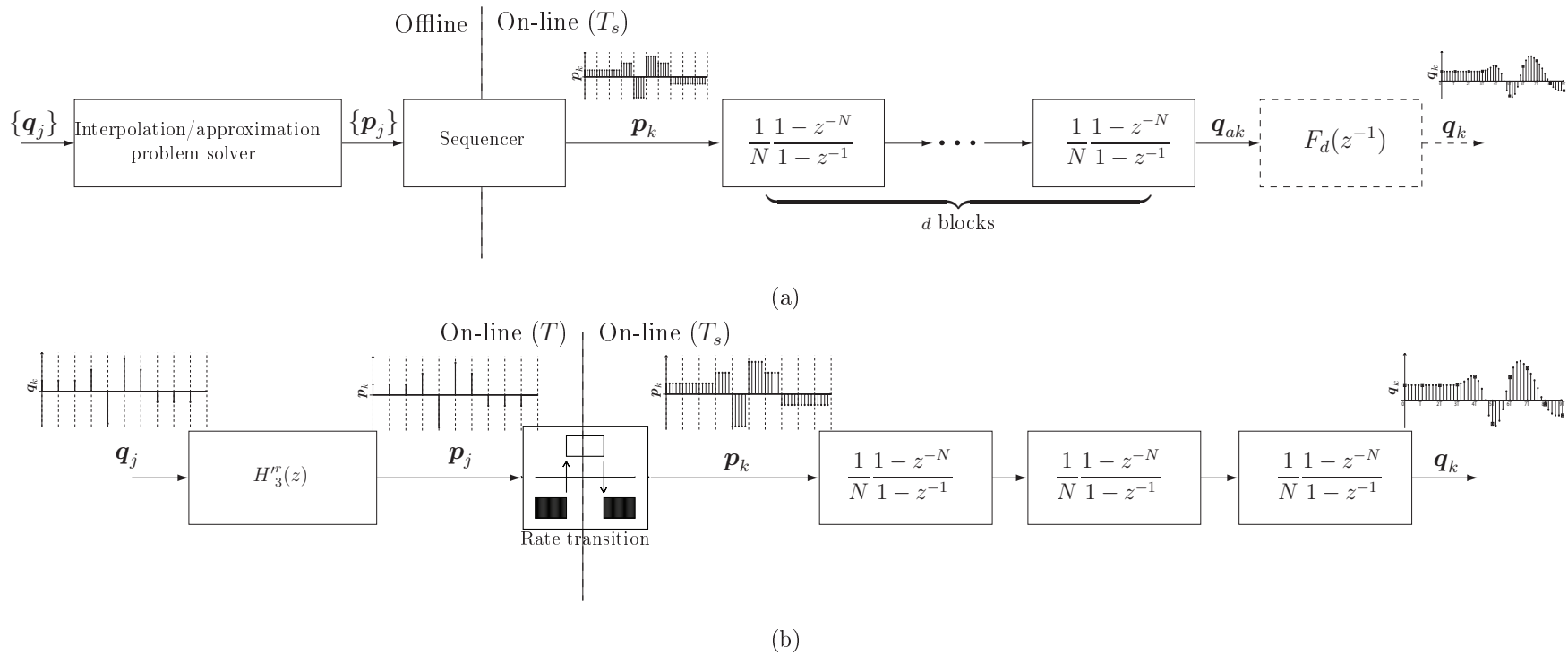
Figure 4-33: Overall structure of the filter for B-spline trajectories planning. In (a) is shown the solution with off-line interpolation as reported in Section 4.5, while in (b) is the full on-line trajectory generator which implements the filter $H'(z)$ for approximated interpolation solution, in particular the case of an on-line cubic spline trajectory generator is shown.

Chapter 5

Optimal Trajectories
for Vibration Reduction
Based on Exponential Filters

5.1   Filter for Exponential Jerk Trajectory

In Section 4.4.1 the considerations upon the frequency analysis of multi-segment polynomial trajectory generators based on dynamic filters leaded to a technique for the optimal selection of the parameters of a standard d-order trajectory, when dynamic constraints are taken into account aside from kinematic ones. In particular for a third order trajectory generated by means of three linear filters

$$M_i(s) = \frac{1 - e^{-sT_i}}{sT_i},$$

as shown in fig. 5-1, the parameters of the trajectory generator (i.e. time duration of the filters T_i) are chosen such that

$$T_1 = \frac{|h|}{v_{max}}, \quad T_2 = \frac{v_{max}}{a_{max}} \tag{5.1}$$

$$r(t) \xrightarrow{\quad} \boxed{\dfrac{1 - e^{-sT_1}}{sT_1}} \xrightarrow{q_1(t)} \boxed{\dfrac{1 - e^{-sT_2}}{sT_2}} \xrightarrow{q_2(t)} \boxed{\dfrac{1 - e^{-sT_3}}{sT_3}} \xrightarrow{q_3(t)}$$
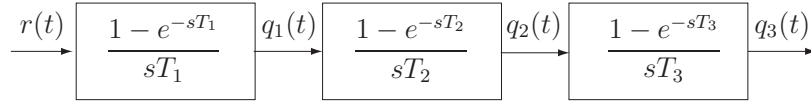
Figure 5-1: Structure of a standard third order trajectory generator.

guarantee that the trajectory from q_0 to q_1 ($h = q_1 - q_0$) complies with the velocity limit v_{max} and the acceleration limit a_{max}, and the choice

$$T_3 = \frac{2\pi}{\omega_n} \tag{5.2}$$

assures that the frequency content of the trajectory is able to cancel the residual vibration when the trajectory is applied to an undamped resonant system characterized by natural undamped frequency ω_n and $\delta = 0$.

Unfortunately, if the damping coefficient is not zero, the effectiveness of the filter output (and therefore of standard constant jerk trajectories) in vibration suppression considerably decreases. In fig. 5-2 the tracking errors of a resonant system with $\delta = 0.0083$ and $\delta = 0.083$ to a standard third order trajectory are compared. Note that if δ grows, when the motion stops (that is for $t \geq T_{tot}$), the peak value of the oscillations of the mechanical system accordingly increases. Moreover, also very small values of δ cause vibrations. The effects of damping are analyzed in fig. 5-3, where PRV, the percent residual vibration, is shown as a function of δ. The increasing of vibration's amplitude is consequence of the fact that in the design of the filter $M_3(s)$ the damping coefficient is not considered. The only way to take into account δ is in the selection of the time constant T_3, and therefore the duration of the constant jerk segment, which can be assumed as

$$T_3 = \frac{2\pi}{\omega_n \sqrt{1 - \delta^2}}.$$

Unfortunately this choice mitigates but does not solve the problem, as shown in fig. 5-3.

In order to suppress vibrations in systems whose damping is not negligible, in [7] the use of a nonconstant limited jerk profile is proposed. In particular, a dynamic filter

142
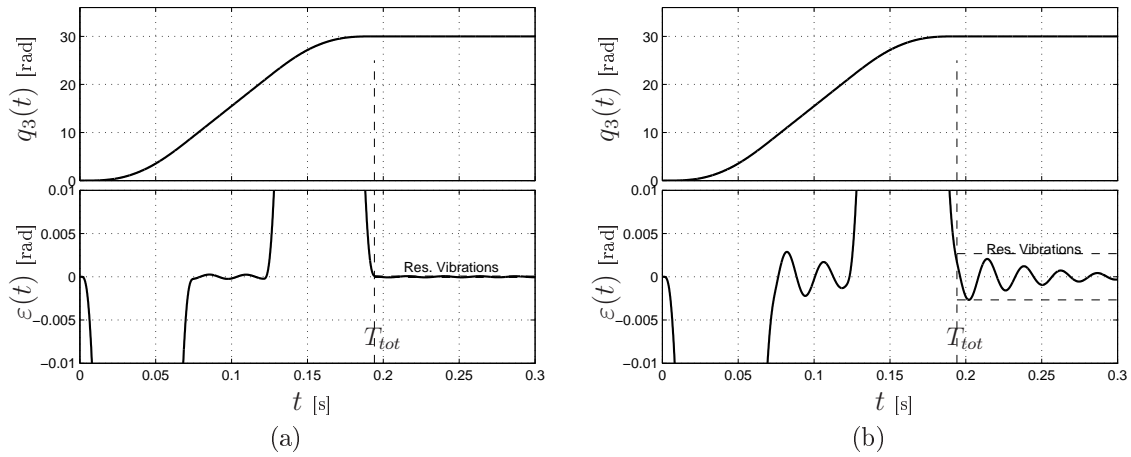
Figure 5-2: Residual vibration due to a third order trajectory $q_3(t)$ with $h = 30$ rad, $v_{max} = 250$ rad/s, $a_{max} = 5000$ rad/s^2, applied to a second order system with $\omega_n = 260.43$ rad/s and $\delta = 0.0083$ (a) and $\delta = 0.083$ (b).
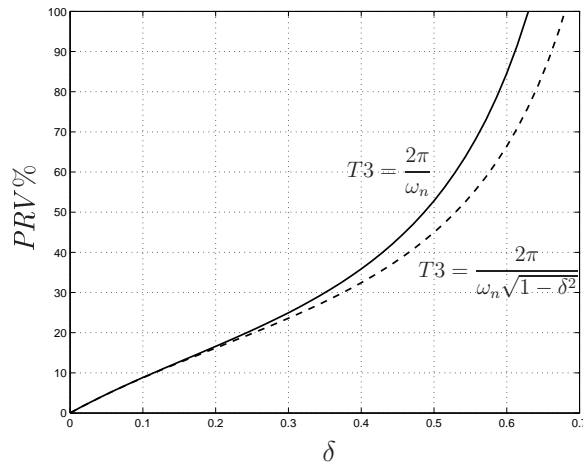
Figure 5-3: Percent residual vibration as a function of damping coefficient δ of a second order filter system whose input is filtered by $M_3(s)$.

to be applied to second order trajectories is devised. The filter produces asymmetric jerk segments, characterized by a linear decrease, as shown in fig. 5-4. The slope of these segments is computed by solving an optimization problem aiming at minimizing the residual vibration. This approach seems very promising as shown in fig. 5-5, where the same conditions of fig. 5-2 are considered: in both cases the residual vibrations are completely suppressed.

However, it is worth noticing that some weak points still exist in this technique:

- A closed-form solution for the computation of the filter parameters is not avail-

143
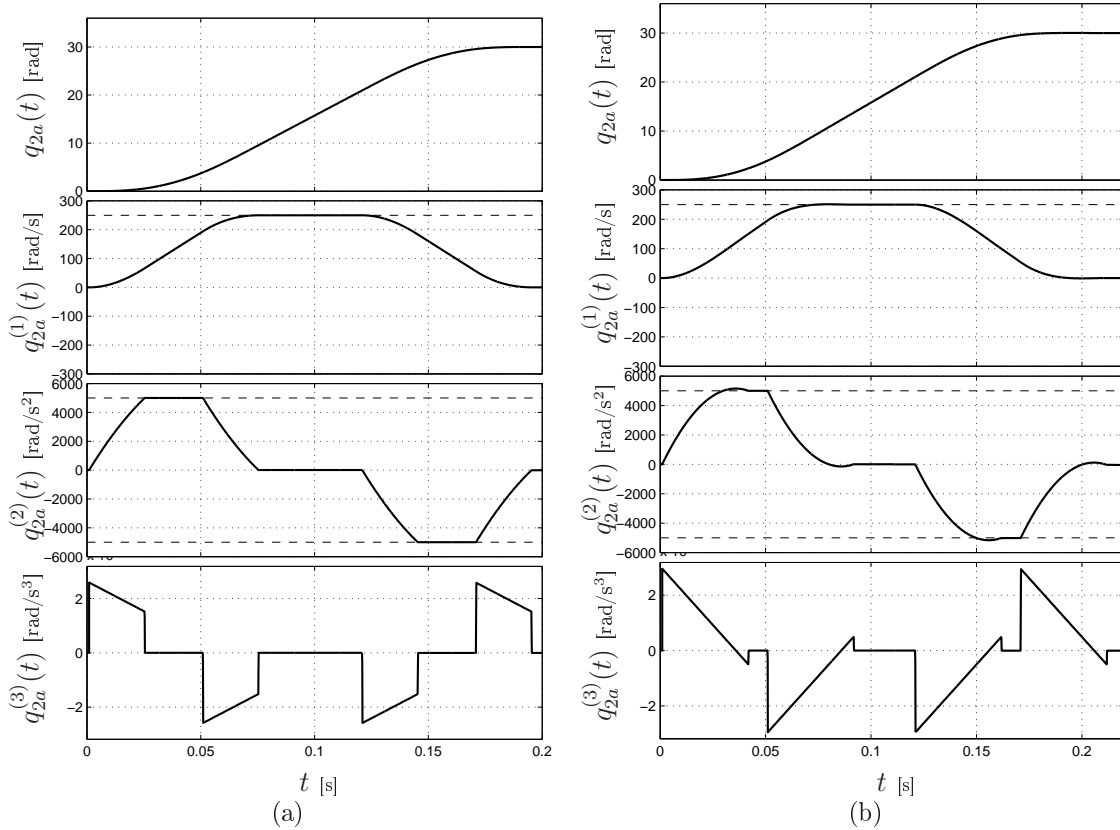
Figure 5-4: Asymmetric jerk trajectory $q_{2,a}$ for $h = 30$ rad, $v_{max} = 250$ rad/s, $a_{max} = 5000$ rad/s^2, and $\delta = 0.083$ (a) and $\delta = 0.45$ (b).

able and the numerical approximation provided in the paper is valid only for δ sufficiently close to 0. For instance, if $\delta = 0.45$ the trajectory does not cancel residual vibrations, as shown in fig. 5-6.

• For high values of δ, it may happens that the sign of jerk changes within the same segment. As a consequence the acceleration profiles exhibits undesirable overshoots, see fig. 5-4(b).

In order to avoid the above mentioned problems, a shaping technique based on exponential functions has been proposed in [15]. Given a second order trajectory $q_2(t)$, obtained for instance with the cascade of two filters $M_1(s) \cdot M_2(s)$, a multi-segment trajectory with jerk segments defined by exponential functions can be obtained by

144
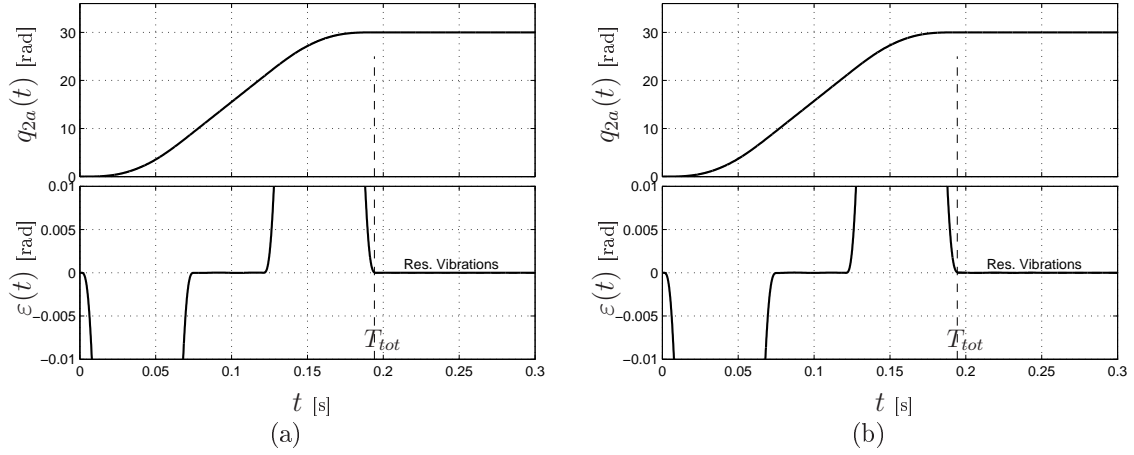
Figure 5-5: Residual vibration due to a third order trajectory with asymmetric jerk $q_{2,a}(t)$ under the same conditions of fig. 5-2.
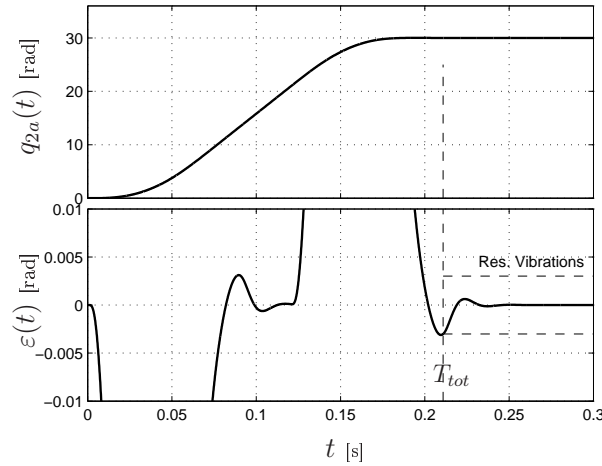
Figure 5-6: Residual vibration due to a third order trajectory with asymmetric jerk $q_{2,a}(t)$ when the value $\delta = 0.45$ is considered.

adding in the chain the filter

$$F_{exp}(s) = \frac{\alpha}{e^{\alpha T_J} - 1} \frac{1 - e^{\alpha T_J} e^{-T_J s}}{s - \alpha} \qquad (5.3)$$

where α and T_j are proper parameters that determines the decay rate and the time duration of impulses composing the jerk profile. As a matter of fact, the impulse response of $F_{exp}(s)$, shown in fig. 5-7, is

$$f_{exp}(t) = \frac{\alpha}{e^{\alpha T_J} - 1} e^{\alpha t} \, m(t), \quad m(t) = \begin{cases} 1, & 0 \leq t \leq T_J \\ 0, & \text{otherwise} \end{cases} \, .$$

145
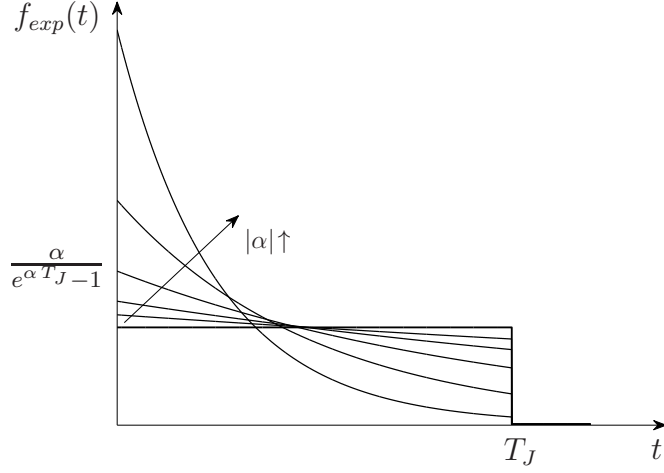
Figure 5-7: Impulse response of filter $F_{exp}(s)$ for negative values of parameter α.

Therefore when applied to the trajectory $q_2(t)$ characterized by a piece-wise constant acceleration, the filter transforms the jerk signal composed by impulsive function $\pm a_{max} \delta(t - t_i)$ in a sequence of exponential segments, see fig. 5-8. Note that the maximum value of the jerk can be computed as $j_{max} = a_{max} \frac{\alpha}{e^{\alpha T_J} - 1}$.

The filter $F_{exp}(s)$, which does not modify the limit values of velocity and acceleration of the original trajectory $q_2(t)$, can be profitably applied to suppress residual vibrations in those resonant systems that are characterized by significant damping coefficient in lieu of standard third order trajectories with limited, but constant, jerk.

Theorem 1. *The filter $F_{exp}(s)$ in (5.3) guarantees the complete residual vibration suppression for a vibratory systems $G(s)$ described by (1.3) in Section 1.1 fed by step inputs if*

$$\alpha = -\delta \, \omega_n \tag{5.4}$$

$$T_J = k \, \frac{2\pi}{\omega_n \sqrt{1 - \delta^2}} \qquad\qquad k = 1, 2, \dots \tag{5.5}$$

Proof. When a step input filtered by $F_{exp}(s)$ is applied to the system (1.3), the tracking error between the load position and the motor position can be computed as

$$E(s) = \frac{-s^2}{s^2 + 2\delta\omega_n s + \omega_n^2} \cdot F_{exp}(s) \cdot \frac{1}{s}. \tag{5.6}$$

146
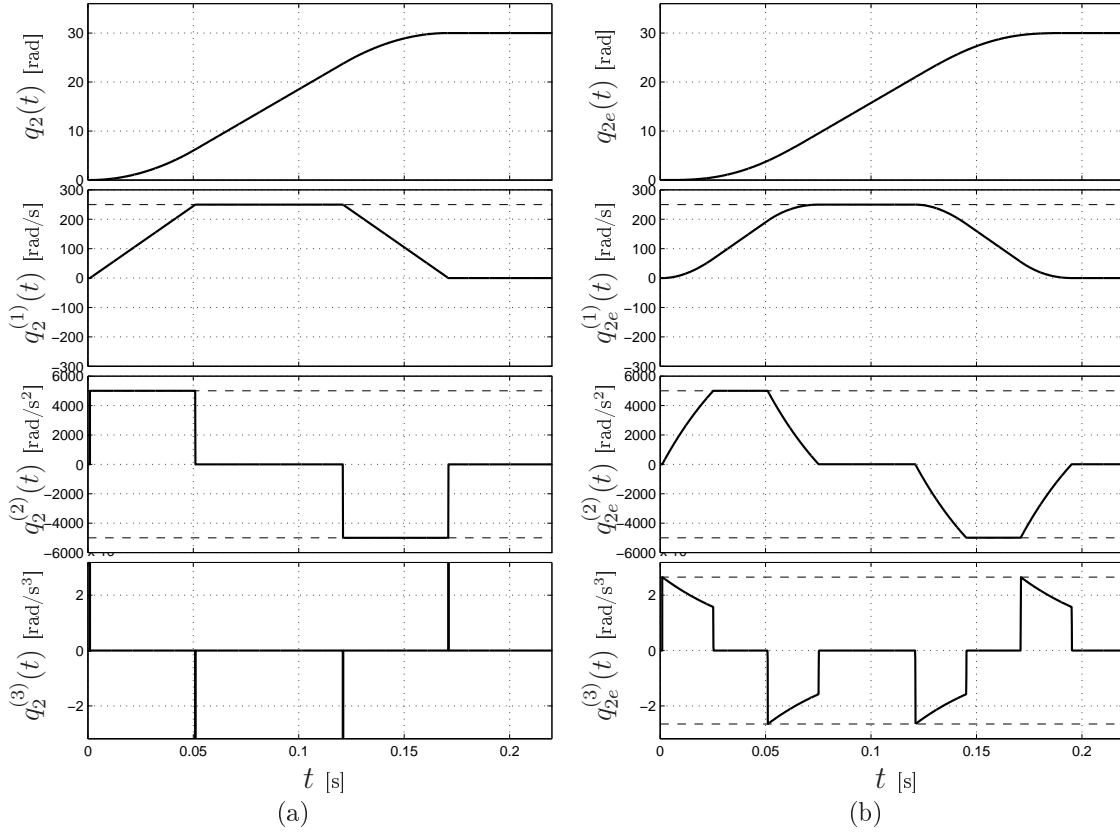
Figure 5-8: Second order trajectory $q_2(t)$ with $h = 30$ rad, $v_{max} = 250$ rad/s, $a_{max} = 5000$ rad/s^2, and corresponding exponential jerk trajectory $q_{2,e}$ for $\omega_n = 260.43$ rad/s and $\delta = 0.083$ (b).

By inverse Laplace transforming $E(s)$ and assuming $t \geq T_J$, the analytic expression of residual vibrations descends:

$$\varepsilon(t) = A \left[\alpha e^{-\delta \omega_n t} \left(\cos(\Omega t) - \cos(\Omega(t - T_J)) e^{(\delta \omega_n + \alpha) T_J} \right) \right.$$
$$\left. - B e^{-\delta \omega_n t} \left(\sin(\Omega t) - \sin(\Omega(t - T_J)) e^{(\delta \omega_n + \alpha) T_J} \right) \right]$$

with

$$A = \frac{\alpha}{(e^{\alpha T_J} - 1)(\alpha^2 + 2\delta \omega_n \alpha + \omega_n^2)}, \tag{5.7}$$
$$B = \frac{\alpha \omega_n \delta + \omega_n^2}{\omega_n \sqrt{1 - \delta^2}},$$
$$\Omega = \omega_n \sqrt{1 - \delta^2}.$$

147

Therefore, in order to assure that $\varepsilon(t) = 0$, $\forall\, t \geq T_J$ it is sufficient that

$$\delta\omega_n + \alpha = 0 \quad \Leftrightarrow \quad \alpha = -\delta\omega_n$$

$$\Omega\, T_J = 2\pi\, k \quad \Leftrightarrow \quad T_J = k\,\frac{2\pi}{\Omega} = k\frac{2\pi}{\omega_n\sqrt{1-\delta^2}}, \quad k = 1, 2, \dots$$

$\square$

Note that $F_{exp}(s)$ is a generalization of a standard filters with rectangular impulse response, which produce piecewise constant jerk profiles. As a matter of fact, when $\delta = 0$ and consequently $\alpha = 0$, the straightforward application of the l'Hôpital's rule leads to

$$\lim_{\alpha \to 0} \frac{\alpha}{e^{\alpha\, T_J} - 1} = \frac{1}{T_J}$$

and therefore

$$\lim_{\delta \to 0} F_{exp}(s) = \lim_{\alpha \to 0} \frac{\alpha}{e^{\alpha\, T_J} - 1}\, \frac{1 - e^{\alpha\, T_J}\, e^{-T_J\, s}}{s - \alpha} = \frac{1}{T_J}\frac{1 - e^{-s T_J}}{s}.$$

Differently from asymmetric jerk trajectories, whose ability to cancel vibrations for systems with $\delta = 0$ leaded to define a proper design algorithm in Section 4.4.1, the parameters of $F_{exp}(s)$ that assure the complete vibrations cancellations are easily calculable in the whole range of $\delta \in [0, 1[$, and the problems tied to changes in the jerk sign are never present.

Theorem 2. *Third order trajectories with the jerk profile composed by exponential segments satisfying* (5.4) *and* (5.5) *guarantee that no residual vibrations are present in the resonant system* (1.3).

Proof. Third order trajectories with exponential jerk, whose analytical expression is reported in Chapter 4, can be obtained by filtering a step signal of amplitude h (where h is the desired displacement) with the cascade of linear filters $M_1(s) \cdot M_2(s) \cdot F_{exp}(s)$. Therefore, when the trajectory is applied to the system G(s), the tracking error
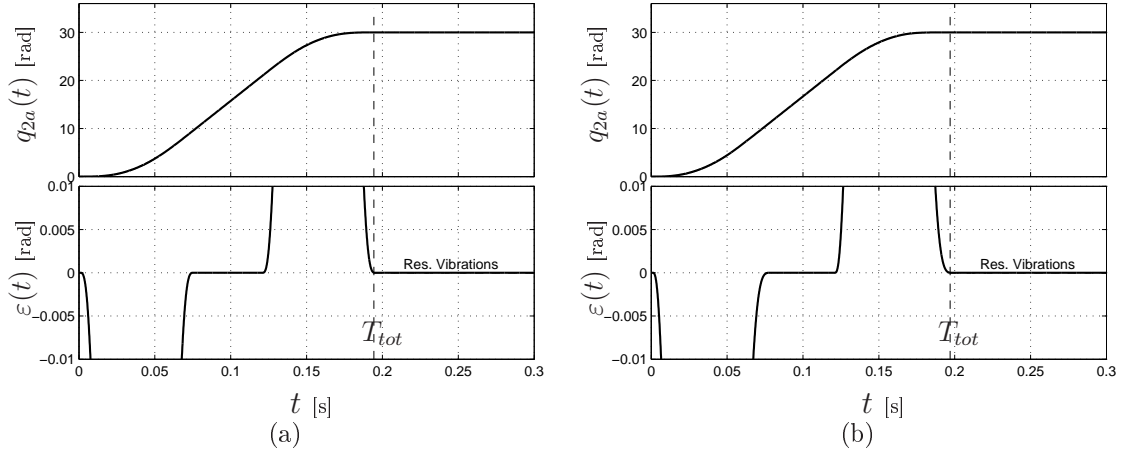
Figure 5-9: Residual vibrations due to a third order trajectory with exponential jerk $q_{2,e}(t)$ under the same conditions of fig. 5-2, but with $\delta = 0.083$ (a) and $\delta = 0.45$ (b).

between the load position and the motor position is given by

$$
\begin{aligned}
E_{q_{2e}}(s) &= \frac{-s^2}{s^2 + 2\delta\omega_n s + \omega_n^2} \cdot \left(M_1(s) \cdot M_2(s) \cdot F_{exp}(s) \cdot \frac{h}{s} \right) \\
&= h \cdot M_1(s) \cdot M_2(s) \cdot \left(\frac{-s^2}{s^2 + 2\delta\omega_n s + \omega_n^2} \cdot F_{exp}(s) \cdot \frac{1}{s} \right) \\
&= h \cdot M_1(s) \cdot M_2(s) \cdot E(s)
\end{aligned}
\tag{5.8}
$$

where $E_{q_{2e}}(s)$ is the Laplace transform of the tracking error to an exponential jerk trajectory, and $E(s)$ is the transform of the error $\varepsilon(t)$ to a step input, considered in (5.6). If the conditions (5.4) and (5.5) are met, $e(t) \neq 0$ only for $t \leq T_J$ and, because the filters $M_1(s)$ and $M_2(s)$ are characterized by a finite length impulse response of duration T_1 and T_2 respectively, from (5.8) it follows that $e_{q_{2e}}(t) \neq 0$ for $t \leq T_1 + T_2 + T_J$ and $e_{q_3}(t) = 0$ otherwise. This means that after the end of the reference trajectory (whose duration is $T_{tot} = T_1 + T_2 + T_J$) residual vibrations are completely cancelled. $\qquad \square$

In fig. 5-9 the tracking errors obtained with exponential jerk trajectories are shown by considering resonant systems with quite different damping coefficients, i.e. $\delta = 0.083$ (a) and $\delta = 0.45$ (b). In both cases residual vibrations are completely suppressed.

149

5.2 Sensitivity to Errors in Parameters Definition

Since the identification of the optimal values of the filter parameters does not require an explicit knowledge of the damping coefficient and of the natural frequency of the plant, the robustness of $F_{exp}(s)$ is evaluated first by considering errors in σ and T_J with respect to their nominal values, while the sensitivity with respect to changes in δ and ω_n will be analyzed in Sec. 5.4 in order to compare different types of solutions to the problem of vibrations suppressions. In fig. 5-10 the percent residual vibration $PRV\%$ due to errors in the estimation of the parameters α and T_J are reported for different values of the damping coefficient and natural frequency of the plant. In particular the ranges $[\hat{\alpha}/2, 2\hat{\alpha}]$ and $[\hat{T}_J/2, 2\hat{T}_J]$ about the nominal values $(\hat{\delta}, \hat{T}_J)$ are considered. From the figure, it is possible to conclude that

- the nominal value of the natural frequency of the plant does not influence the robustness of the filter $F_{exp}(s)$ while the damping coefficient does;

- the choice of T_J is definitely more critical than the choice of α;

- an underestimation of T_J leads to large oscillations; conversely, a value of T_J higher than the nominal one produce limited vibrations especially for high damping coefficients.

5.2.1 Sensitivity to Unmodeled Dynamics of the Plant

According to Theorem 1 the filter $F_{exp}(s)$ in (5.3) and consequently the exponential-jerk trajectory obtained when the filter is applied to a second order trajectory $q_2(t)$, like in fig. 5-8, guarantees a complete cancellation of the vibrations if the plant can be modelled as a second order system such as (1.3). However, typical industrial plants include additional dynamics that may modify the effects of the proposed filter. If the model of the plant includes additional stable dynamics $\Delta G(s)$, e.g.

$$G_P(s) = G(s)\,\Delta G(s), \qquad (5.9)$$

150
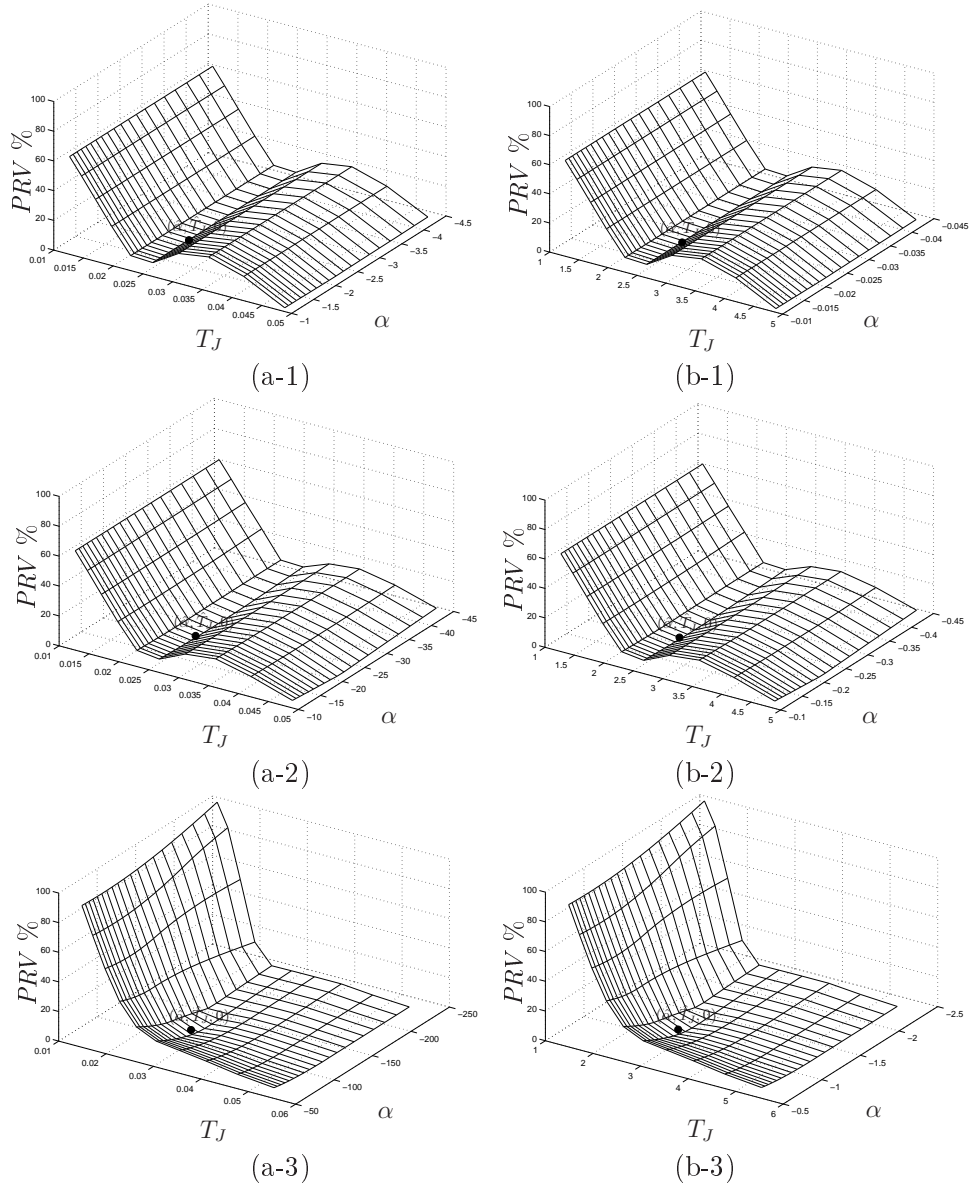
Figure 5-10: Sensitivity of $F_{exp}(s)$ to changes in σ and T_J for different values of δ and ω_n of the plant: $\delta = 0.0083$ (1), $\delta = 0.083$ (2) and $\delta = 0.45$ (3); $\omega_n = 260.53$ rad/s (a) and $\omega_n = 2.6053$ rad/s (b).
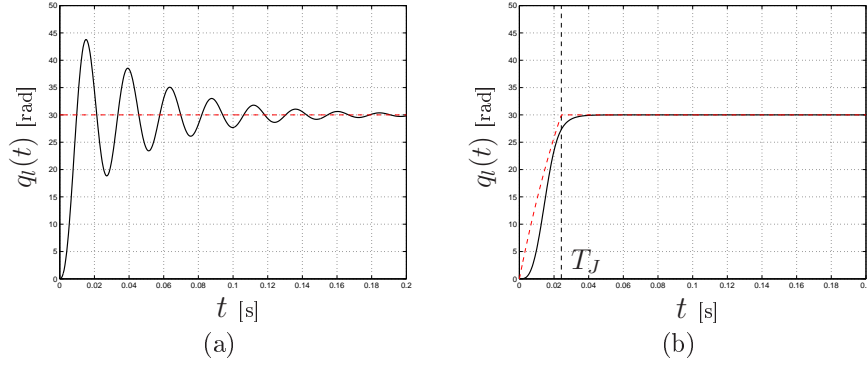
Figure 5-11: Response of a resonant system with an additional real pole, $G_P(s) = G(s) \frac{1}{\tau s + 1}$ with $\omega_n = 260.43$ rad/s, $\delta = 0.0083$ and $\tau = 0.0046$s, forced by a step input of amplitude $h = 30$ rad (a) and a step input filtered by the filter $F_{exp}(s)$ (b).

it is possible to show that the properties of $F_{exp}(s)$ remain unaltered. As a matter of fact, because of the linearity the response of the system (5.9) to a filtered step input is

$$Q_l(s) = G_P(s) \, F_{exp}(s) \frac{1}{s} = \Delta G(s) \left(G(s) \, F_{exp}(s) \frac{1}{s} \right).$$

Therefore, the ideal response obtained with the nominal model $G(s)$ which, according to Theorem 1, does not have residual vibration, is simply filtered by $\Delta G(s)$. Note that the dynamics $\Delta G(s)$ will introduces additional modes in the response, but cannot excite again the resonant mode of $G(s)$ damped by the filter $F_{exp}(s)$.

In particular, if $\Delta G(s)$ represents a dynamics faster than the nominal model $G(s)$ and completely damped, for instance a real pole with time-constant $\tau = \frac{1}{10} \frac{1}{\delta \omega_n}$, the response of the system to a step input without and with the filter $F_{exp}(s)$ is the one shown in fig. 5-11: the presence of the additional pole involves an increased duration of the response that in the nominal case reaches the steady-state condition in T_J seconds, but the residual vibration is completely suppressed.

Also, if the convergency rate of the additional pole is comparable with the rate of the undamped (complex) poles that characterize $G(s)$ the result is similar, that is the use of F_{exp} cancel the oscillations that otherwise will affect the response. See fig. 5-12 where the unmodeled dynamics $\Delta G(s) = \frac{1}{\tau s + 1}$ with $\tau = \frac{1}{\delta \omega_n}$ has been considered.

In case of systems with multiple vibratory modes, a single filter $F_{exp}(s)$ is only able to cancel the oscillations due to a specific mode. As a consequence, the use of a

152
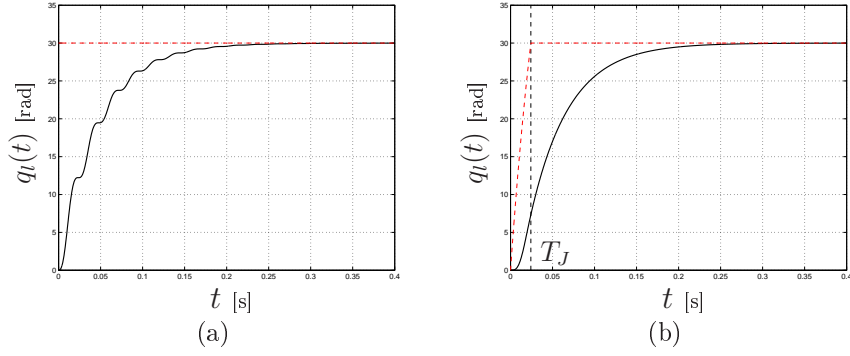
Figure 5-12: Response of a resonant system with an additional real pole, $G_P(s) = G(s) \frac{1}{\tau s + 1}$ with $\omega_n = 260.43$ rad/s, $\delta = 0.0083$ and $\tau = 0.046$s, forced by a step input of amplitude $h = 30$ rad (a) and a step input filtered by the filter $F_{exp}(s)$ (b).
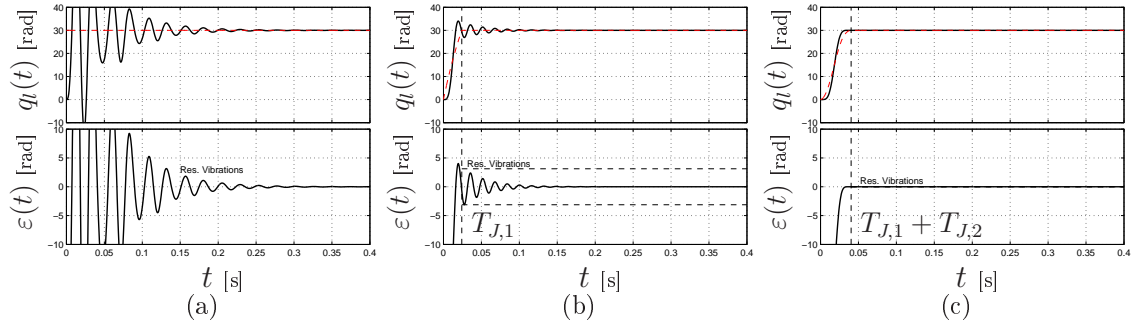
Figure 5-13: Response of a resonant system with 2 vibrational modes characterized by $\omega_{n,1} = 260.43$ rad/s, $\omega_{n,2} = 389.2971$ rad/s and $\delta = 0.0083$ forced by a step input of amplitude $h = 30$ rad (a), a step input filtered by the filter $F_{exp}(s)$ designed to take into account ω_1 (b) and a step input filtered by two filters $F_{exp}(s)$ which consider both ω_1 and ω_2 (c).
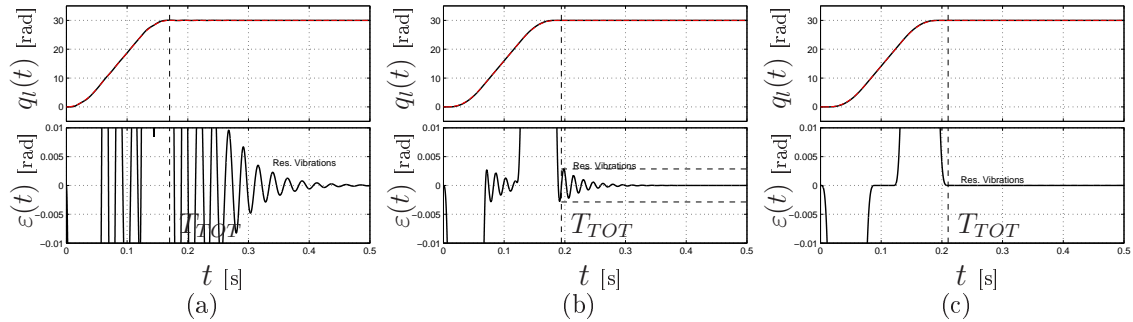
Figure 5-14: Response of a resonant system with 2 vibrational modes characterized by $\omega_{n,1} = 260.43$ rad/s, $\omega_{n,2} = 389.2971$ rad/s and $\delta = 0.0083$ forced by a second order trajectory $q_2(t)$ with $h = 30$ rad, $v_{max} = 250$ rad/s, $a_{max} = 5000$ rad/s^2 (a), an exponential jerk trajectory $q_{2,e}(t)$ taking into account ω_1 (b) and the trajectory $q_{2,2e}(t)$ of fig. 5-15 which considers both ω_1 and ω_2 (c).

153

filter $F_{exp}(s)$ does not guarantee the complete residual vibration suppression but it is necessary to consider the cascade of two or more filters, each one related to a specific mode. In fig. 5-13 the step response of a plant characterized by two modes with the same damping coefficient δ but different natural frequencies $\omega_{n,1}$ and $\omega_{n,2}$, with $\omega_{n,2} = \frac{1}{2}\omega_{n,1}$ without and with filtering action is shown. A single filter $F_{J,1}(s)$ considerably reduces residual vibration but does not cancel all the oscillations. Therefore, a second filter $F_{J,2}(s)$ is necessary to completely suppresses undesired vibrations with the consequent increase of the delay caused by the filters. If the two filters are not applied to a step signal but to a second order trajectory $q_2(t)$, like in fig. 5-14, the capability of suppressing residual vibrations can be merged with the compliance to kinematic constraints but in this case the final trajectory is not characterized by a jerk profile composed by tracts of exponential function, see fig. 5-15.
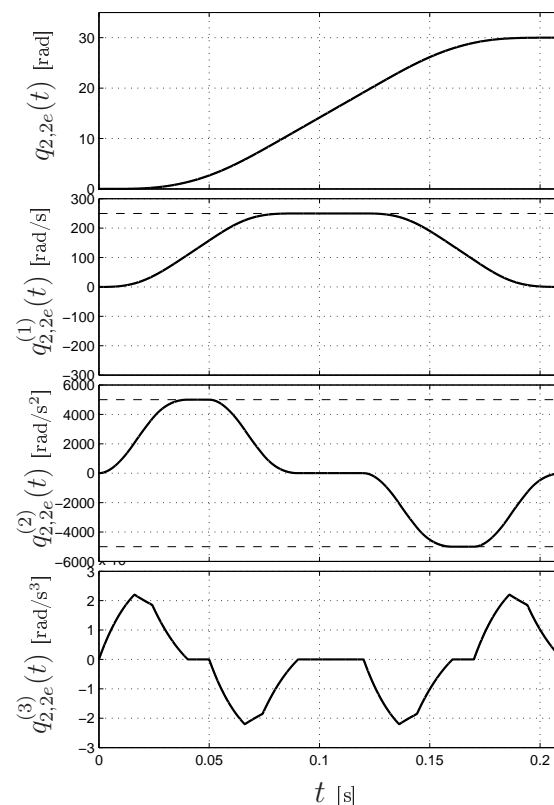
Figure 5-15: Profiles of the trajectory $q_{2,2e}(t)$ obtained by applying to the trajectory $q_2(t)$ of fig. 5-8(a) two exponential filters with $\omega_{n,1} = 260.43$ rad/s, $\omega_{n,2} = 389.2971$ rad/s and $\delta = 0.083$ (b).
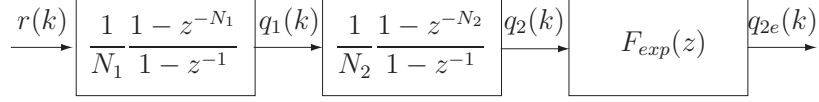
Figure 5-16: Structure of the discrete-time filter for exponential jerk generation.

5.3 Digital Implementation of the Exponential Filter

Since the generation of exponential jerk trajectories is based on the dynamic filters fed by step functions, i.e.

$$Q_{2e}(s) = M_1(s) \cdot M_2(s) \cdot F_{exp}(s) \cdot \frac{h}{s}$$

it can be easily performed online by modifying the input signal. However, the practical use of the proposed filter requires its transformation in the discrete time domain (T_s denotes the sampling period) because trajectory planning is generally performed by digital controllers. This conversion can be obtained with two main techniques, being the impulse response of $F_{exp}(s)$ of finite length:

1. it is possible to obtain the coefficients of a FIR filter by sampling the impulse response $f_{exp}(t)$ with period T_s;

2. it is possible to deduce the IIR transfer function corresponding to $F_{exp}(s)$ by means of usual discretization techniques.

In order to obtain a closed form expression of $F_{exp}(z)$ the second approach has been preferred. By Z-transforming the filter $F_{exp}(s)$ given in (5.3) and imposing a unitary static gain, the following expression descends

$$F_{exp}(z) = \frac{1 - e^{\alpha T_s}}{1 - e^{\alpha T_s} e^{\alpha N_J}} \frac{1 - e^{\alpha T_s} e^{\alpha N_J} z^{-N_J}}{1 - e^{\alpha T_s} z^{-1}} \tag{5.10}$$

where $N_J = \text{round}(T_J/T_s)$. In fig. 5-16 the complete structure of the discrete-time filter for online generating exponential jerk trajectories is shown. Note that in order to guarantee that the sequence of values of the discrete time-trajectory coincides with the continuous-time profile at sampling times, its expression should be obtained by

155

Z-transforming the overall chain of continuous filters with a step input, i.e. $Q_{2e}(z) = \mathcal{Z}\{Q_{2e}(s)\}$. Therefore, the following expression can be deduced

$$Q_{2e}(z) = \frac{h}{1 - z^{-1}} \cdot M_1(z) \cdot M_2(z) \cdot F_{exp}(z) \cdot F'(z) \qquad (5.11)$$

where $F'(z)$ is a FIR filter with unitary static gain, whose expression is

$$F'(z) = f_0 \, z^{-1} + f_1 \, z^{-2} + f_2 \, z^{-3} \qquad (5.12)$$

being

$$f_0 = \frac{-2 + 2e^\rho - 2\rho - \rho^2}{2(e^\rho - 1)\rho^2}$$
$$f_1 = \frac{4 - 4e^\rho + 2\rho + 2\rho e^\rho - \rho^2 + \rho^2 e^\rho}{2(e^\rho - 1)\rho^2}$$
$$f_2 = \frac{-2 + 2e^\rho - 2\rho e^\rho + \rho^2 e^\rho}{2(e^\rho - 1)\rho^2}$$

and $\rho = \alpha T_s$. By comparing (5.11) with the discrete-time generator of fig. 5-16, it comes out that the difference between the two output sequences is only caused by the filter $F'(z)$, whose main effect consists in a time delay of two sampling intervals[1]. By neglecting this filter, a time anticipation is therefore introduced in the generator, as shown in fig. 5-17, where the step response of the continuous-time filter and the sequences obtained with the exact discretization and with the approximated generator of fig. 5-16 are reported. In order to emphasize the approximation error the sampling period has been intentionally assumed very large ($T_s = 0.1$ s). In this way it is possible to appreciate that, besides the time anticipation, the discrete-time filter provides an excellent approximation of the desired trajectory. Obviously, when the sampling period decreases, the difference between $q_{2e}(t)$ and the approximated $q_{2e}(k)$

---

[1]Since the sampling frequency ω_s is generally chosen by assuming that $\omega_s \geq 10\omega_n$, the parameter $\rho = -\delta\omega_n \frac{2\pi}{\omega_s}$ results quite small in magnitude, i.e. $-0.6283 \leq \rho \leq 0$. As a consequence, the range of variation of the coefficients defining $F'(z)$ is rather limited ($0.1412 \leq f_0 \leq 0.1667$, $0.6666 \leq f_1 \leq 0.6656$, $0.1667 \leq f_2 \leq 0.1932$). Moreover, f_1 is considerably higher than other coefficients and therefore a rough approximations of $F'(z)$ can be obtained by neglecting f_0 and f_2, and assuming that that $F'(z) \approx z^{-2}$.
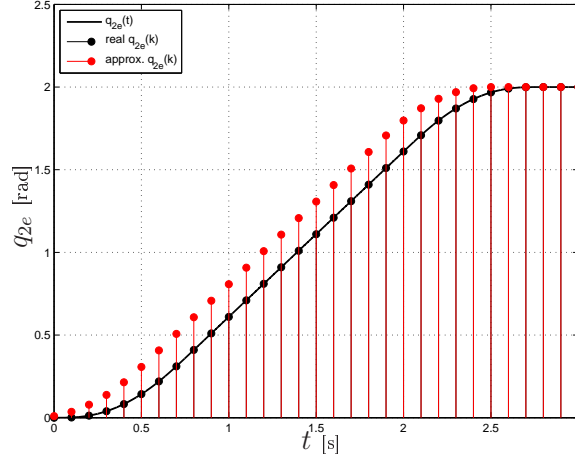
Figure 5-17: Comparison between the trajectories produced by exponential jerk trajectory filters defined in the continuous- and discrete-time domain with $T_1 = 1\,\mathrm{s}$, $T_2 = 0.6\,\mathrm{s}$ ($N_i = \mathrm{ceil}(T_i/Ts)$), $T_J = 0.2\,\mathrm{s}$ and $\alpha = -3$.

tends to vanish.

A last remark concerns the computation complexity of the proposed trajectory generator. As illustrated in Tab. I, where the difference equations of the trajectory generator shown in fig. 5-16 are reported, at each sampling time the computation of the output of the the cascade of filters requires a total of 6 additions and 5 multiplications. If the filter $F'(z)$ is considered, 2 more additions and 3 multiplications must be performed. Moreover three memory areas are necessary, in order to store the last N_1 values of $q_1(k)$, the last N_2 values of $q_2(k)$ and the last N_J values of $q_{2e}(k)$. Note that the trajectory generation based on the cascade of dynamic filters is considerably more efficient than the direct calculation of the closed form equations of the

Table I

Difference equations corresponding to the trajectory generator of fig. 5-16. The values of the constant parameters a_i are:
$a_1 = \frac{1}{N_1}$, $a_2 = \frac{1}{N_2}$, $a_3 = e^{\alpha\,T_s}$, $a_4 = \frac{1 - e^{\alpha\,T_s}}{1 - e^{\alpha\,T_s}\,e^{\alpha\,N_J}}$, $a_5 = e^{\alpha\,T_s}\,e^{\alpha\,N_J}$.

$$q_1(k) = q_1(k) + a_1\Big(r(k) - r(k - N_1)\Big)$$
$$q_2(k) = q_2(k) + a_2\Big(q_1(k) - q_1(k - N_2)\Big)$$
$$q_{2e}(k) = a_3\,q_{2e}(k) + a_4\Big(q_2(k) - a_5\,q_2(k - N_J)\Big)$$

157
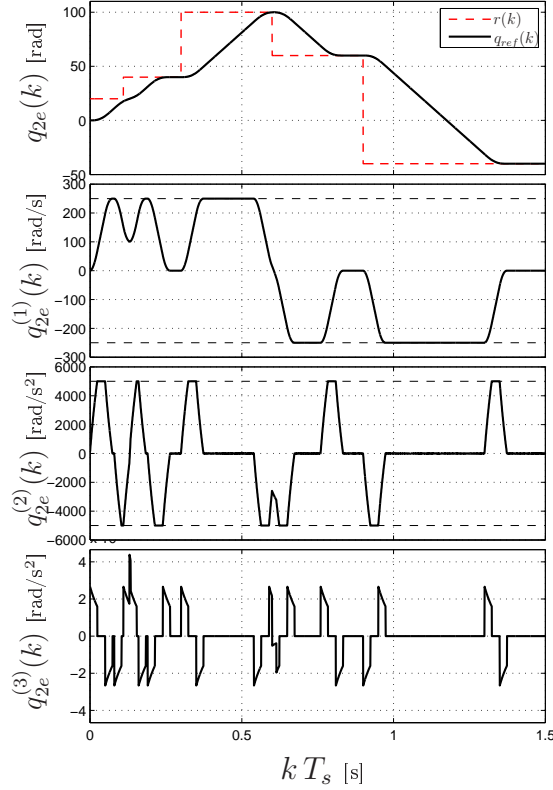
Figure 5-18: Complex motion profile $q_{2e}(k)$ with $v_{max} = 250$ rad/s, $a_{max} = 5000$ rad/s^2, $\omega_n = 260.43$ rad/s and $\delta = 0.083$, obtained by applying to the system in fig. 5-16 a reference signal $r(k)$ composed by several step functions applied at generic time instants.

trajectory, which, besides a larger number of additions and multiplications, requires 2 divisions and the computation of an exponential function depending on t.

When a reference signal $r(k)$ composed by several step functions starting at generic time instants is applied to the trajectory generator of fig. 5-16, the profiles shown in fig. 5-17 are obtained. If the time-instants in which a new trajectory is triggered comply with the conditions reported in [13] a complex motion profile $q_{2e}(t)$ that meets velocity and acceleration constraints and cancels residual vibrations is obtained. Note that in this case the jerk profiles is no longer composed by tracts defined by an exponential function because of overlaps between adjacent jerk impulses. However, the capability of suppressing vibrations remain unaltered. See fig. 5-19 where the residual vibrations obtained with a second order trajectory $q_2(k)$ and with $q_{2e}(k)$ are compared.
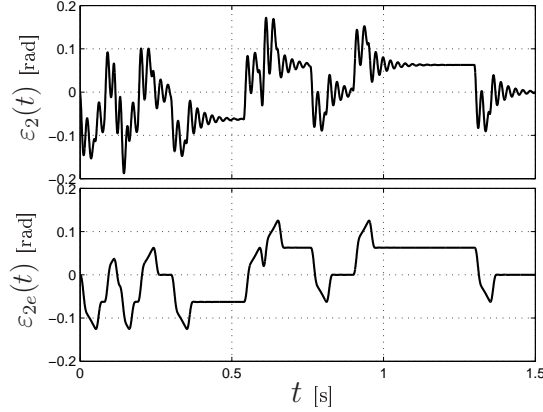
Figure 5-19: Comparison between the residual vibration caused by the application to a resonant system $G(s)$ of a second order trajectory $q_2(k)$ ($\varepsilon_2(t)$) and the corresponding exponential jerk trajectory $q_{2e}(k)$ shown in fig. 5-18 ($\varepsilon_{2e}(t)$).

5.4 Comparative Analysis with Alternative Techniques for Vibration Suppression

As mentioned in the introduction, the main techniques for complete residual vibration suppression based on a proper filtering of the reference signal are input shaping and inversion of the plant dynamics. A first important difference between these techniques and the proposed filter $F_{exp}(s)$ is that they do not increase the smoothness, i.e. the order of continuous derivatives, of the filtered input. They are generally applied to reference trajectories with bounded velocity and acceleration and therefore at least $\mathcal{C}^1$, that is with continuous first-order derivative, and provide as output a trajectory of the same class in case of input shapers or even of lower class if filters based on system inversion are applied. In fig. 5-20 the reference signals obtained by filtering the second order trajectory $q_2(t)$ with a ZVD input shaper and with a system-inversion-based filter are shown. Note that the trajectory $q_{2,\mathrm{zvd}}(t)$ remains $\mathcal{C}^1$, i.e. with discontinuous acceleration, and is compliant with the desired bounds imposed to the original trajectory $q_2(t)$. The trajectory $q_{2,\mathrm{inv}}(t)$ filtered by the inverse dynamics of the plant becomes $\mathcal{C}^0$, because some discontinuities appears in the velocity profile. Moreover the bounds on the trajectory derivatives are not met anymore, see the acceleration profile of $q_{2,\mathrm{inv}}(t)$. This behavior of the system-inversion-based filter

159
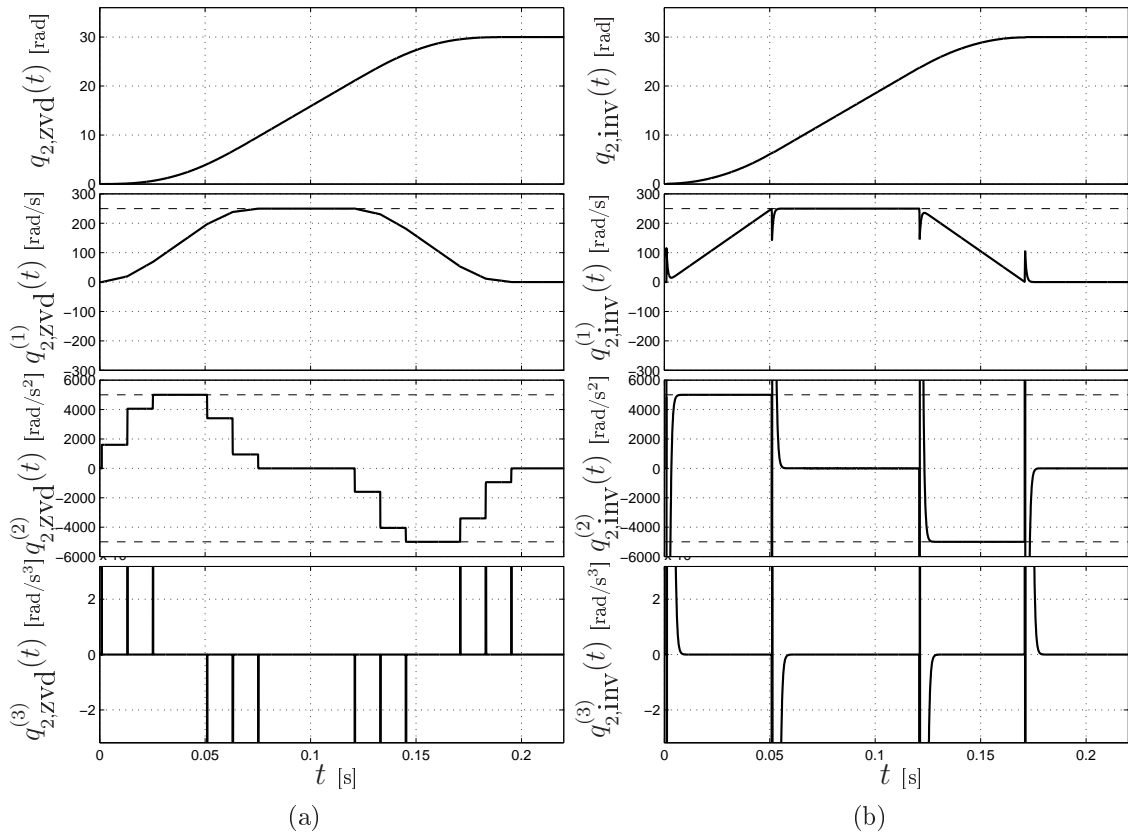
Figure 5-20: Reference signals obtained by filtering the second order trajectory $q_2(t)$ of fig. 5-8(a) with a ZVD input shaper (a) and with the inverse dynamics of the plant (b).

can be rather troublesome, since as shown in fig. 1-1 the system $G(s)$ that causes vibrations models only the load and the elastic transmission of a more complex system which includes also the actuator, supposed to be able to perfectly track the reference trajectory $q_{ref}(t)$. Therefore the reference scheme of a standard motion system with elastic linkage results as in fig. 5-21. Unfortunately, any kind of actuation system is characterized by physical limitations on velocity and acceleration and if these bounds are not met the trajectory becomes unfeasible. Moreover, the requirement of perfect
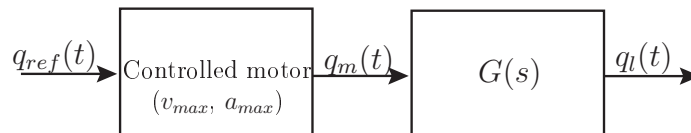
Figure 5-21: Complete model of a motion system with elastic linkage.

160

tracking relates the smoothness of the reference trajectory, supposed $\mathcal{C}^p$, with the relative degree r of the linear time-invariant system describing the actuation system [30], i.e

$$p \geq r - 1.$$

As a consequence, in case of an electric actuator, with $r = 3$, the reference position for the motor[2] must be at least $\mathcal{C}^2$. This implies that if an input shaping filter is used for vibrations suppression, the second order trajectory $q_2(t)$ is not sufficient but a $\mathcal{C}^2$ function is required. With an inverse dynamics filter a $\mathcal{C}^3$ trajectory must be used. Conversely, the proposed filter $F_{exp}(s)$, that increases the smoothness of the input trajectory, needs a simple $\mathcal{C}^1$ function, like the function $q_2(t)$ which leads to the exponential jerk trajectory of fig. 5-8.

From a functional point of view, input shapers, system-inversion-based filter and the proposed filter $F_{exp}(s)$ guarantee the complete vibrations suppression in nominal conditions. However as already pointed out in previous chapters, one of the most important features for a command shaper is the robustness with respect to errors in model parameters, i.e. δ and ω_n in of the considered plant. Accordingly to the discussion about the other techniques, the robustness of the proposed exponential filter is investigated by means of the analysis of the transfer function $F_{exp}(s)$.

In particular, assuming to have a vibratory system $G(s)$ as considered in Section

---

[2]Note the the transfer function of a standard DC motor is

$$G_a(s) = \frac{Q_m(s)}{V(s)} = \frac{K_i}{L_a J_m s^3 + (R_a J_m + B_m L_a)s^2 + (K_b K_i + R_a B_m)s}$$

where K_i is the torque constant, K_b the back-emf constant, R_a the armature resistance, L_a the armature inductance, J_m the rotor inertia, B_m the viscous-friction coefficient and $V(s)$ denotes the Laplace transform of the input voltage [54]. A feed-forward control that in nominal case assures perfect tracking is

$$V_{ff}(s) = G_a^{-1}(s)Q_{ref}(s) = \left(\frac{L_a J_m}{K_i}s^3 + \frac{R_a J_m + B_m L_a}{K_i}s^2 + \frac{K_b K_i + R_a B_m}{K_i}s \right) Q_{ref}(s)$$

which corresponds to

$$v_{ff}(t) = \frac{L_a J_m}{K_i}q_{ref}^{(3)}(t) + \frac{R_a J_m + B_m L_a}{K_i}q_{ref}^{(2)}(t) + \frac{K_b K_i + R_a B_m}{K_i}q_{ref}^{(1)}(t).$$

The control action $v_{ff}(t)$ is feasible, that is $v_{ff}(t) < \infty$, only if $q_{ref}^{(3)}(t)$ is limited and accordingly the reference trajectory $q_{ref}(t) \in \mathcal{C}^2$.
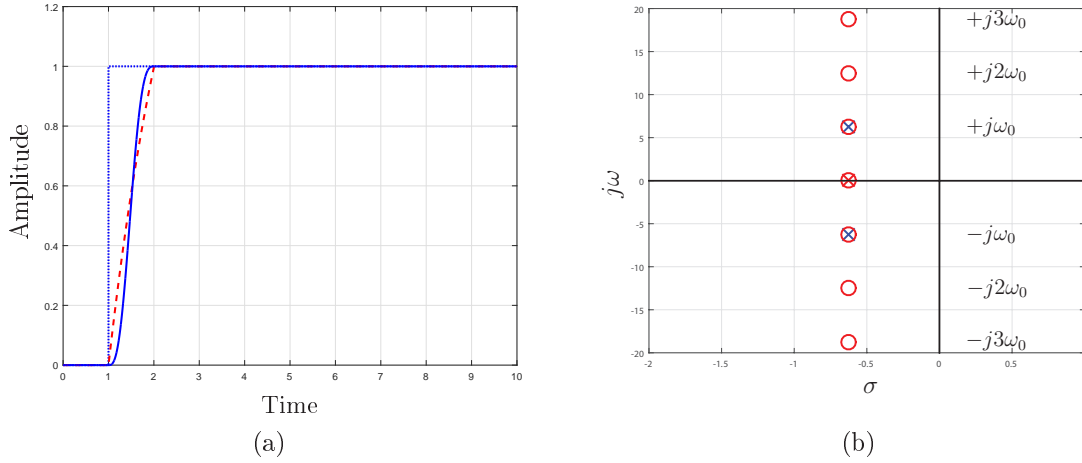
Figure 5-22: Step response (a) and Pole-Zero diagram (b) of the system with $\delta = 0.1$ shaped by $F_{exp}(s)$.

1.1, the exponential filter assures complete vibration suppression, provided that the conditions in (5.4) and (5.5) are satisfied. In fig. 5-22 the vibration-free step response of a second order system with natural frequency ω_n and damping $\delta = 0.1$ is reported along with the pole-zero diagram of the shaped system $F_{exp}(s) \cdot G(s)$, demonstrating that the vibration is suppressed since the zeroes of the exponential filter actually cancel the poles of the system $G(s)$ that cause vibrations. In addition it has to be noted that the effect of the filter is to provide infinite zeroes located on a line parallel the imaginary axis, plus a pole on the real axis which is cancelled by the zero associated with the multiplicity $k = 0$. Recalling the pole-zero diagram of the mean filter $M(s)$ in fig. 4-17 it is clear that the two transfer functions differs only by a frequency translation that depends on the value of the damping δ. Therefore the exponential filter can be considered the frequency translated version of a mean filter, in particular $F_{exp}(s)$ preserves the frequency behavior of $M(s)$ (i.e. frequency response) and permit to exploit it in the whole decaying sinusoidal domain, that is with $\delta \neq 0$.

This consideration is not so surprising since has been already demonstrated that the exponential filter $F_{exp}(s)$ is a generalization of standard filters with rectangular impulse response, which produce piecewise constant jerk profiles. Namely in fig. 5-7 it is shown that the impulse response $f_{exp}(t)$ varies accordingly to $|\alpha|$, and the

162

exponential-like shape degenerates into a rectangular impulse of length T_J for $|\alpha| = 0$. Moreover, being $\alpha = -\delta \omega_n$ and known that for a typical second order system the characteristic complex conjugate couple of poles is lying on a vertical line intersecting the real axis in $\sigma = -\delta \omega_n$, it is straightforward to assume the decay rate α as the required frequency translation needed to suppress a damped vibration by means of a mean filter $M(s)$. In fact, being

$$M_J(s) = \frac{1}{T_J} \frac{1 - e^{-sT_J}}{s},$$

and $\alpha = -\delta \omega_n$ the desired frequency translation, results

$$M_J(s - \alpha) = \frac{1}{T_J} \frac{1 - e^{-sT_J} e^{\alpha T_J}}{s - \alpha} = AF_{exp}(s),$$

where A takes into account the fact that the proposed exponential filter has unitary static gain.

Finally this discussion permits to highlight a strong connection between the design procedure of the exponential filter and input shapers. In section 2.5 has been addressed that the effect of $\delta \neq 0$ in the design of IS result in a frequency translation of the transfer function for the undamped case. In particular in equations from (2.42) to (2.47) it is shown that the parameter K defined in (2.3) takes into account the value of the damping δ providing the shift of the zeroes of the IS. In a similar way for the exponential filter, the translation of α in the above equation, enrich the numerator of $M_J(s)$ of the term

$$e^{\alpha T_J} = e^{-\frac{2\pi\delta}{\sqrt{1-\delta^2}}}.$$

By recalling from (2.3)

$$K = e^{-\frac{\pi\delta}{\sqrt{1-\delta^2}}},$$

it turns out that the analogy is evident.

In order to compare the exponential filter to the other techniques for vibration suppression, in fig. 5-23 the analysis of $F_{exp}(s)$ on the complex plane is reported along

163
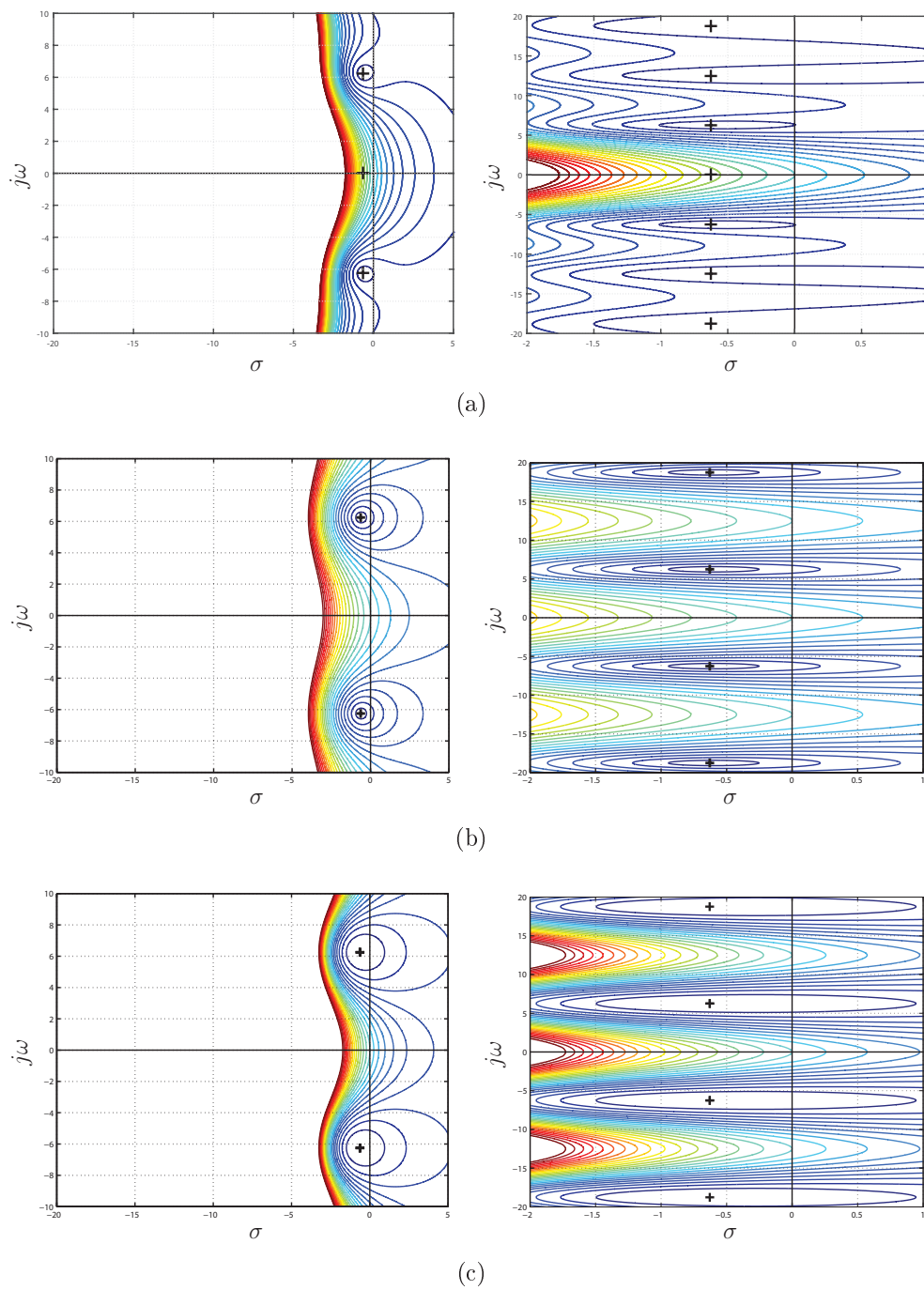
Figure 5-23: Comparison of transfer function description on the complex plane of respectively exponential filter $F_{exp}(s)$ (a), ZV IS (b) and ZVD IS (c). On the right the diagrams are reported with equal scale to the one of fig. 5-22 in order to better understand the behavior of the system response. The contour lines are equally spaced of 0.1 and the zeroes position is highlighted with a black cross
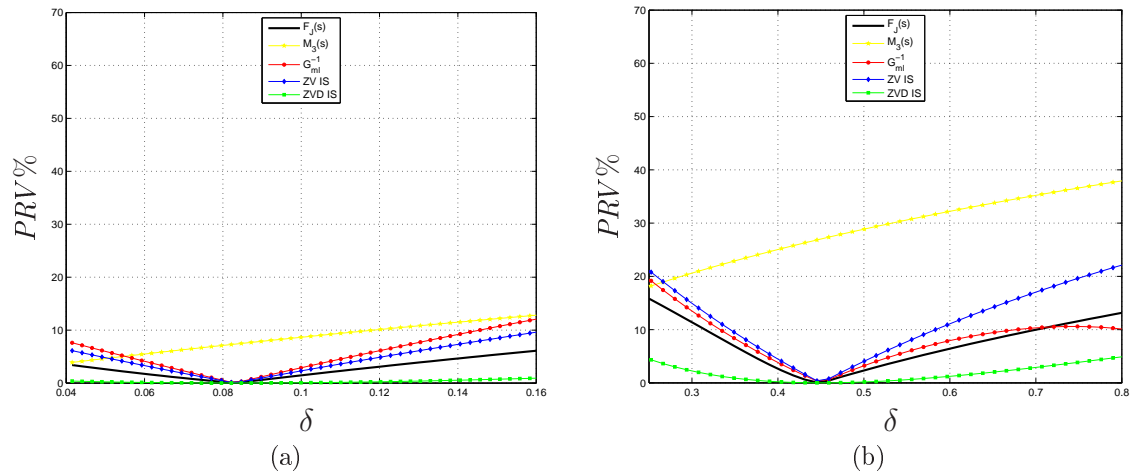
Figure 5-24: Percent residual vibration as a function of the damping coefficient δ about the nominal value $\hat{\delta} = 0.081$ (a) and $\hat{\delta} = 0.45$ (b).

with that of ZV IS and ZVD IS. As already noticed from the PRV function of the mean filter in fig. 4-16 the robustness of the proposed filter $F_{exp}(s)$ is at an intermediate value between ZV and ZVD input shapers. This is due to two main aspects, on the one hand the multiplicity of the zeroes is one, like ZV IS, on the other hand the reduced distance between the zeroes of $F_{exp}(s)$ has a grater overall filtering effect. In particular it can be noted that for frequencies higher than the nominal one, the response of the exponential filter is considerably lower than that of IS. That is for example in lieu of an approximate design solution, one may profitably takes into account an approach based on underestimating the frequency parameter, while in case of IS this assumption can't be considered since the response of IS is always symmetric to the zeroes.

Also to the aim of comparing all the mentioned different approaches in vibration suppression, an extensive simulation activity has been carried out in order to evaluate the percent residual vibration of system $G(s)$ as a function of the errors in the estimation of its parameters, when applying different techniques. In particular since the inverse-dynamics filter requires a continuous input function, the comparative analysis has been conducted by using the trajectory $q_2(t)$ as test function in lieu of the standard step signal. By means of extensive simulations, the curves reported in fig. 5-24 and fig. 5-25 have been obtained. For the sake of clarity, the variations of parameters

165
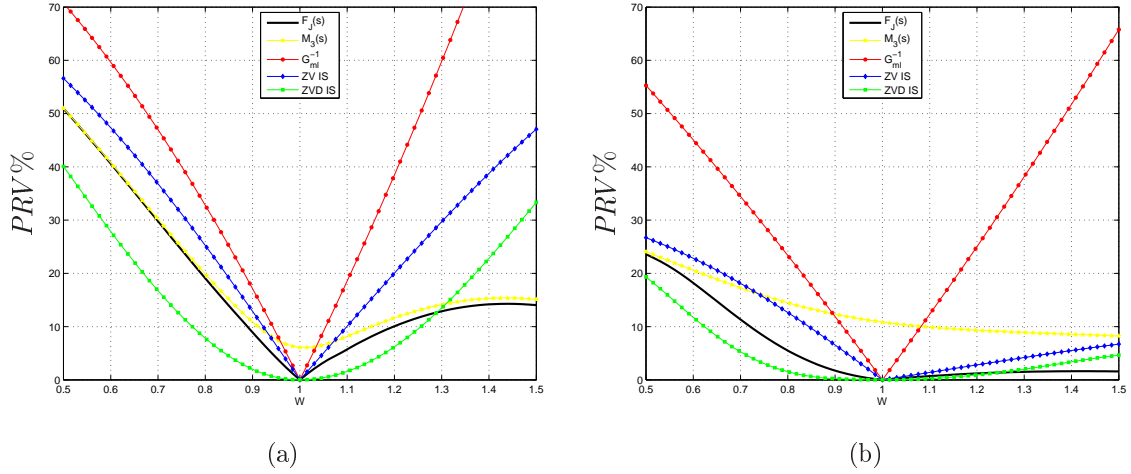
Figure 5-25: Percent residual vibration as a function of the ratio $\omega_n/\hat{\omega}_n$, where ω_n is the actual natural frequency of $G(s)$ and $\hat{\omega}_n$ is the nominal value used to define the filter, for $\delta = 0.081$ (a) and $\delta = 0.45$ (b).

δ and ω_n with respect to their nominal values are considered separately. In fig. 5-24 the percent residual vibration is shown as a function of δ. Since the nominal value $\hat{\delta}$ influences the results, two different values have been considered in order to show the behavior of the different filters for small and large damping coefficients ($\hat{\delta} = 0.081$ and $\hat{\delta} = 0.45$ respectively). For the natural frequency, the nominal value $\hat{\omega}_n = 260.53$ rad/s has been assumed, but it is worth noticing that the percent residual vibration does not depends on this particular value.

The relationship between actual value of natural frequency and percent residual vibration is shown in fig. 5-25, where the ratio $\omega_n/\hat{\omega}_n$ has been considered. Also in this case two different values of δ have been taken into account.

These curves highlight that the proposed filter $F_{exp}(s)$ is characterized by an intermediate robustness between ZV and ZVD input shapers, and results much more robust than system-inversion-based filters. Moreover, for high values of ω_n, $F_{exp}(s)$ offers the best performances, see fig. 5-25. As already discussed in Chapter 4, the filter $M_3(s)$ that produces constant jerk trajectories, provides similar results for small values of δ (see fig. 5-25(a)), but cannot completely suppress residual vibrations.

Finally, a fair comparison between these methods requires also an estimation of the time-delay that the filters introduce and of the consequent increase of the motion

166

duration. With this respect, it is well-known that an higher robustness of Input Shapers is obtained by increasing the number of impulses that form the shapers and accordingly the delay introduced in the motion generation.

System-inversion-based filters do not cause any delay in the reference signal tracking. However, the need for smoother trajectories implies higher durations of the motion with respect to lower order trajectories, the bounds on velocity, acceleration, and higher derivatives being equal. Input shapers, like ZV and ZVD filters, introduce in the system time-delays similar to that caused by the $F_{exp}(s)$ filter; in particular the additional delays are $T_J/2$ for ZV and T_J for ZVD, but also in this case the need for higher order input trajectories with respect to the filter $F_{exp}(s)$ may increase the total duration of the motion.

5.5 Experimental Validation of the Exponential Filter

In order to experimentally test the proposed method the setup of fig. 5-26 has been arranged. This simple system is characterized by a linear motor, LinMot PS01-37x120, whose slider is connected to an inertial load by means an elastic transmission obtained with a coil spring. The load is placed on a liner guide in order to guarantee the axial alignment with the motor slider and to reduce static friction. The control system is based on the servo controller LinMot E2010-VF that performs the basic current control, while the position control (based on a PID controller and a feedforward action) has been implemented on a standard PC with a Pentium IV 3 GHz processor and 1 GB of RAM, equipped with a Sensoray 626 data acquisition board, used to both communicate with the servo controller and acquire the sensors signals. The position of the motor is measured by an incremental encoder with a resolution of $1\mu m$ integrated in the stator, and the monitoring of vibrations is obtained via a load cell connected between the slider and the elastic transmission. As a matter of fact, the force f_k exerted by the spring is proportional to the error ε between motor position

167
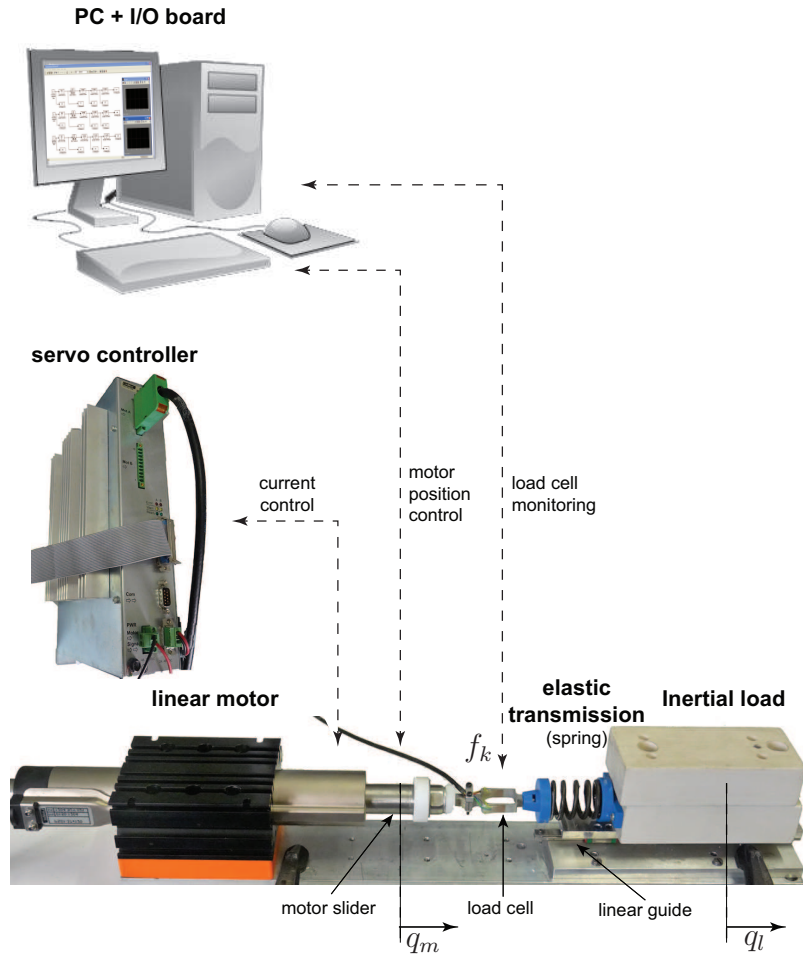
Figure 5-26: Experimental setup.

and load position, and, if the inherent damping of the transmission is considered, like in fig. 1-1, force f_k is simply a scaled, low-pass filtered version of ε.

The real-time operating system RTAI-Linux on a Debian SID distribution with Linux kernel 2.6.17.11 and RTAI 3.4 allows the position controller to run with a sampling period $T_s = 500 \mu s$. For the design of the control scheme and of trajectory generator, the MatLab/Simulink/RealTime Workshop environment has been used.

In Tab. II the main characteristics[3] of the mechanical system are reported. The value of the internal damping b_t is unknown, but it can be easily deduced from the parameters α and T_J of the filter $F_{exp}(s)$. The value of these parameters is obtained as described in Sec. 5.2 but the oscillation is induced by physically blocking the mo-

---

[3]The symbols refer to the model of fig. 1-1(b).

Table II

Motion system parameters.

Parameter	Symbol	Value	Unit
Slider mass	J_m	0.599	kg
Load mass	J_l	0.623	kg
Spring stiffness	k_t	6490	N m

tor slider and applying an initial deformation to the spring. In fig. 5-27, the force $f_k(t)$ recorded during an experiment is shown together with the force of the identified system characterized by $\hat{\delta} = 0.0246$ and $\hat{\omega}_n = 101.3724$ rad/s, which correspond to $\hat{\alpha} = -2.4958$ and $\hat{T}_J = 0.0620$ s (indeed, several tests have been performed and the mean value of the parameters has been assumed). Note that the value of ω_n found in the experiments is consistent with the theoretical value $\sqrt{k_t/J_l} = 102.0653$ rad/s. The main difference between the responses of real and ideal system lies in the manner in which the oscillation vanishes, see fig. 5-27 for $t \geq 0.9$ s: the model's output goes to zero asymptotically while the real system suddenly stops probably because of the (unmodeled) static friction. Moreover, besides the vibratory dynamics $G_{ml}(s)$ the model of the real system should include the poles of the controlled actuator, but since the control feedback has been designed with a very high bandwidth these poles have been neglected. As a matter of fact, as already noted in Sec. 5.2.1 unmodeled poles faster than the mechanical dynamics that induces vibrations do not modify significantly the results of the application of the filter $F_{exp}(s)$ and of the exponential jerk trajectories.

In fig. 5-28, the response of the system to second-order trajectory $q_2(t)$ used as basic motion profiles is reported. This trajectory, characterized by a total displacement h of 30 mm, has been obtained by means of the two filters of fig. 5-16 with $N_i = T_i/T_s$, $i = 1, 2$, being $T_2 = 1.5\,\hat{T}_J = 0.0930$ s and $T_1 = 2\,T_2 = 0.1860$ s. With these parameters, the maximum velocity and the maximum acceleration are $v_{max} = 0.1613$ m/s and $a_{max} = 1.7343$ m/s^2 respectively. Obviously the behavior of the system at the end of motion (highlighted in the plots with the white background) is very similar to that of the uncontrolled system of fig. 5-27.

When the filter $F_{exp}(z)$ is added and the exponential jerk trajectory is applied to
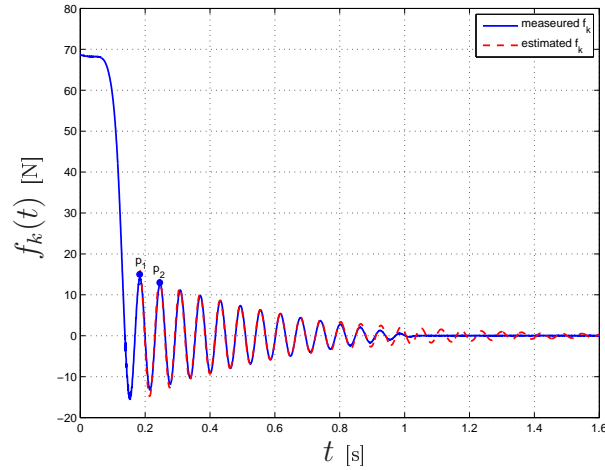
Figure 5-27: Oscillations of the system of fig. 5-26 used for the identification of the parameters of filter $F_{exp}(s)$.
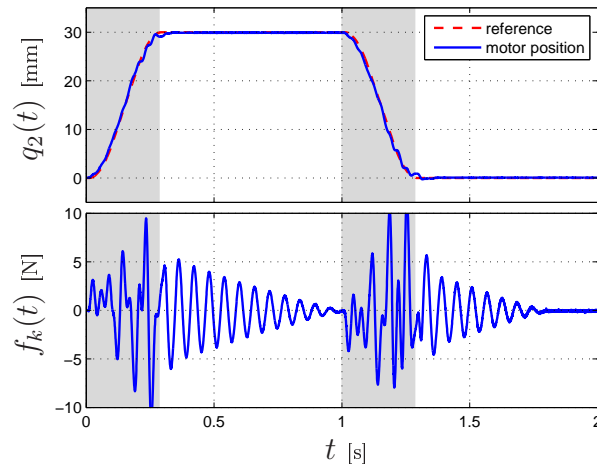
Figure 5-28: Residual vibrations induced in the system of fig. 5-26 by the application of a second order trajectory $q_2(t)$.

the resonant system, the residual vibration is considerably reduced, see fig. 5-29(a). However, it is not completely cancelled. Note that the residual vibration seems not due to additional unmodelled (linear) dynamics of the plant since its period is exactly $\hat{T}_J$. Instead, the cause must be probably sought in nonlinear phenomena (i.e. the static and Coulomb friction on the motor slider) and external disturbances (such as the cogging which is present in the linear motor) affecting the system. These effects are probably not completely compensated by the motor controller and the actuator does not behaves like an ideal position source.

In order to evaluate the benefits of the proposed method in real applications, its
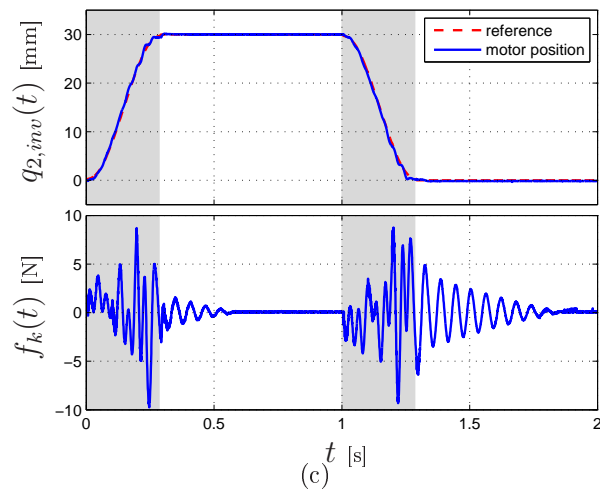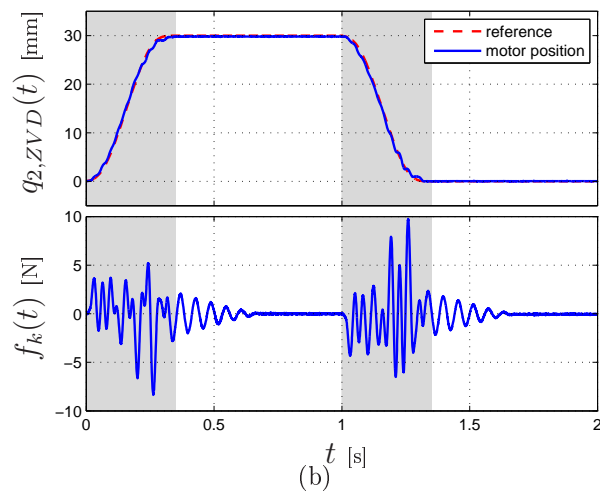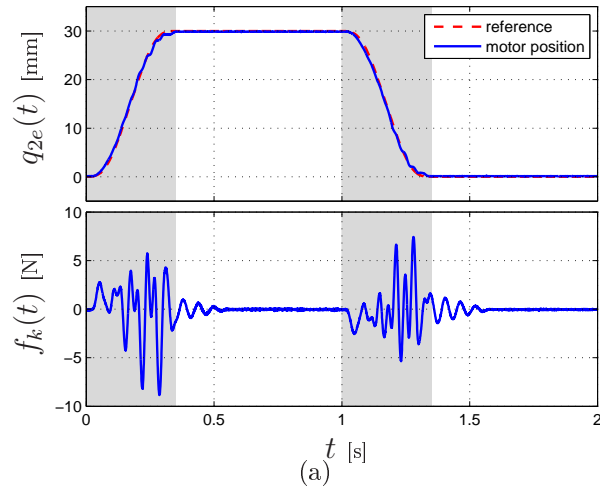
Figure 5-29: Comparison between residual vibrations induced in the system of fig. 5-26 by the application of an exponential jerk trajectory (a), a second order trajectory filtered by a ZVD input shaper (b) and a second order trajectory filtered by the system inverse dynamics (c).
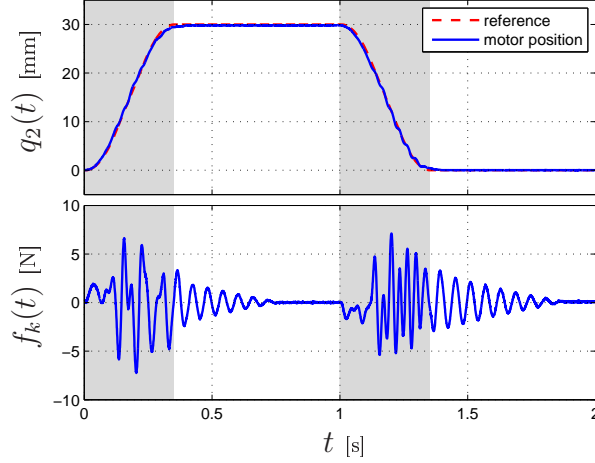
Figure 5-30: Residual vibrations induced in the system of fig. 5-26 by the application of a second order trajectory $q_2(t)$ with $T_2 = 0.1137$s.

behavior has been compared with those of the alternative approaches mentioned in Section 5.4, which should lead to a complete cancellation of residual vibrations. In particular, in fig. 5-29(b) the response of the experimental setup to the trajectory $q_2(t)$ filtered by a ZVD input shaper is shown, and in fig. 5-29(c) the result with the inverse dynamics filter is reported. The actual capabilities of the exponential jerk trajectory and of the input shaper in vibrations suppression are comparable, while the filter based on the dynamics inversion shows a lower robustness with respect to the above mentioned non-idealities: the level of vibrations decreases with respect to those obtained with the direct application of $q_2(t)$ only for a positive displacement of the motor, while it remains practically unchanged if the motion occurs along the negative direction. Note that several tests have been performed but the result was always the same.

Note that the vibrations reduction shown in fig. 5-29 with respect to fig. 5-28 is marginally caused by the increase of the time-duration of the trajectory because of the additional filters. As a matter of fact, both for exponential jerk trajectory and for the input shaper filtered trajectory the duration of the motion is $T_{tot} = T_1 + T_2 + \hat{T}_J = 0.3410$ s. Therefore, in order to perform a more precise comparison, a second-order trajectory $q_2(t)$ with the same total duration (that is $T_2 = 0.1137$ s $T_1 = 2\,T_2$ and $T_{tot} = T_1 + T_2 = 0.3410$ s) has been applied to the mechanical system. The result,
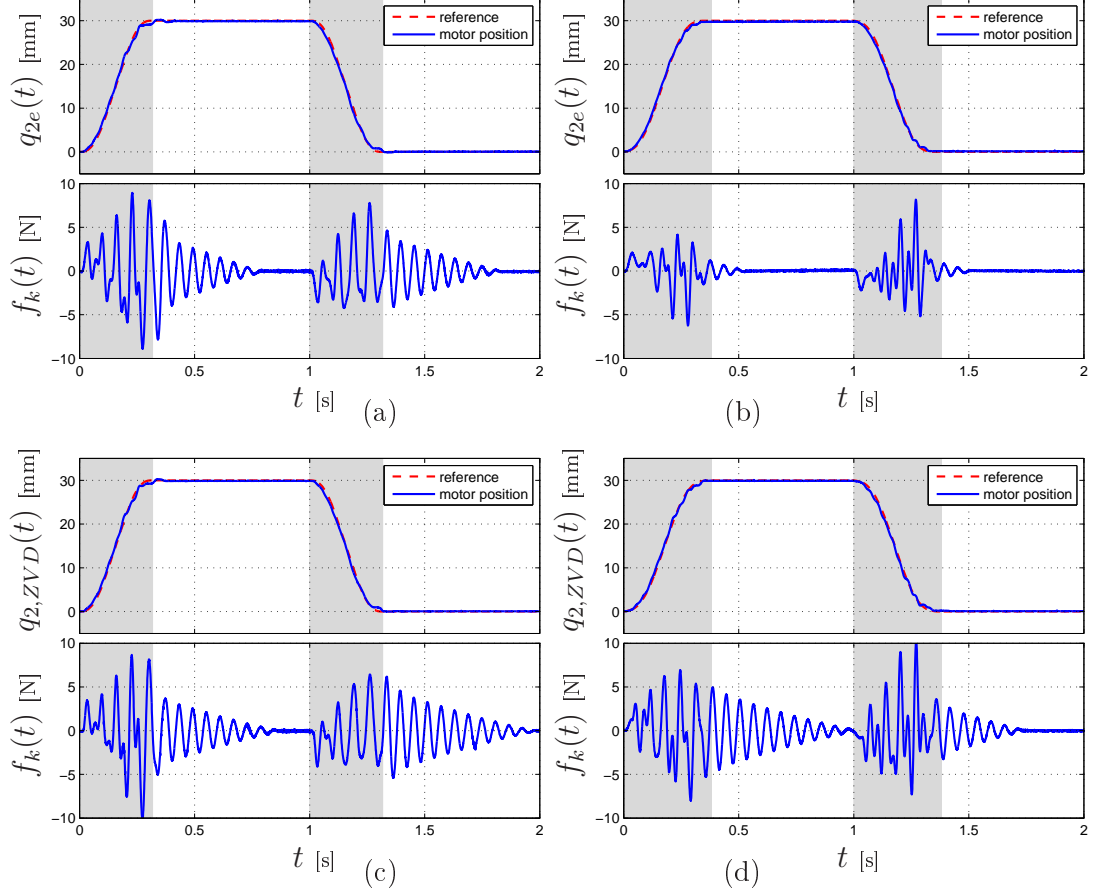
Figure 5-31: Residual vibrations induced in the system of Fig. by an exponential jerk trajectory with $T_J = 0.5\hat{T}_J$ (a) and $T_J = 1.5\hat{T}_J$ (b), and by a second order trajectory filtered by a ZVD input shaper with $T_J = 0.5\hat{T}_J$ (c) and $T_J = 1.5\hat{T}_J$ (d).

illustrated in fig. 5-30, confirms that the reduction of the residual vibration obtained with a simple time-scaling is rather limited if compared with the proposed approach, for equal time duration of the overall trajectory.

Finally, the robustness of the filter F_{exp} with respect to errors in the parameter T_J has been experimentally tested. In fig. 5-31(a) and fig. 5-31(b) the responses of the system to the exponential jerk trajectory computed with the parameter T_J equal to $0.5\hat{T}_J$ and $1.5\hat{T}_J$ are reported, and confirm that an underestimation of T_J makes the filter F_{exp} less effective while an overestimation of T_J lead to small residual vibrations. Conversely, with ZVD input shapers only the nominal values of the parameters produce good performances. In fact, both underestimation and overestimation of T_J cause large residual vibrations, see fig. 5-31(c) and (d). Note that in the test reported in

173

fig. 5-31(b) the residual vibration is even smaller than the vibration obtained with the nominal value of parameter T_J and shown in fig. 5-29(a). This is probably due to the fact that the higher duration of the trajectory, i.e. $T_{tot} = T_1 + T_2 + 1.5\hat{T}_J = 0.3808\,\text{s}$, with respect to the nominal trajectory, for which $T_{tot} = 0.3410\,\text{s}$, mitigates the above mentioned non-ideal phenomena, like friction and cogging, and allows the motor to better track the given profile $q_{ref}(t)$.

5.6 Feedforward Control of an Elastic Joint for Vibrations Suppression

In the previous Sections it has been shown that the use of exponential jerk trajectories, which can be efficiently generated by filtering standard trapezoidal trajectories, allows to reduce considerably the vibrations level in motion systems with elastic transmission. In particular a dynamic filter $F_{exp}(s)$ has been defined and characterized both analytically and experimentally. In order to further exploit the capability of the exponential filter, in [18] has been proposed as a feedforward controller for Variable Stiffness Actuators (VSAs).

VSAs are trend topic in robotics since two decades ago. The development of service robots close cooperating with humans has driven the designers towards novel mechanical solutions aiming at increasing the mechanical compliance and reducing the apparent inertia of robot manipulators [20]. Unfortunately, an high level of mechanical compliance deteriorates the performance of the plant, in particular with respect to precision. For this reason, in order to solve simultaneously safety and performance issues, VSAs, which introduce a mechanical compliance in the joint actuation that can be altered via control action, have been proposed [23, 110, 104, 22]. Unfortunately, the performance of Variable Stiffness Joints (VSJ) robots are still far from those of standard rigid joints manipulators, because of the high order nonlinear dynamics of the system, due to the additional stiffness variation mechanism, and the strongly nonlinear characteristics of VSAs. Moreover, a major problem of VSAs is the

very low intrinsic damping that usually characterizes this type of devices, which may cause vibrations and undesired oscillations, [3]. Accordingly, injecting damping into the system is one of the main control goal in this field. Several control approaches for VSJ robots are presented in the literature. While many controllers are conceived for single-joint systems (see [103, 3] among many others), the multi-joint case is treated less frequently. A feedback linearization algorithm is designed and validated in simulations in [69]. A state feedback controller aiming at obtaining the desired level of damping is presented in [76], while, more recently, in [77] a backstepping approach has been proposed in order to manage the complexity of a VSA system.

The choice of a feed-forward control for VSAs is motivated by a twofold reason:

- the goal of the control is to cancel the oscillations that affect point-to-point motions of the robot joints, connected to the motors by the (variable stiffness) elastic transmissions with low damping, while static performances, in terms of precision, are not addressed;

- the proposed open-loop control does not alter the stiffness seen at the link side, while a closed-loop control does it [3].

Note that, in the literature a number of feedforward controller has been applied to robotic system with elastic elements. In [5, 59, 65] the command shaping technique has been used for robots with flexible links in order to reduce vibrations. The same goal has been achieved for robot manipulators with elastic joints, in [52], where an input shaping techniques is combined with an iterative learning mechanism that updates the parameter of a Zero Vibration (ZV) input shaper in order to take into account nonlinear and time-varying characteristics of the plant.

The control of a single robotic joint with elastic transmission, like the one depicted in fig. 5-32, can be easily performed by considering only variables at the motor side. It is well known, see e.g. [27], that, in absence of gravity, a PD control based on motor's position q_m and velocity $\dot{q}_m$ is stable for any positive value of the proportional and derivative gains. Therefore, it is possible to obtain a controlled system that in principle is arbitrarily fast and precise. Unfortunately, even if the motor is able to
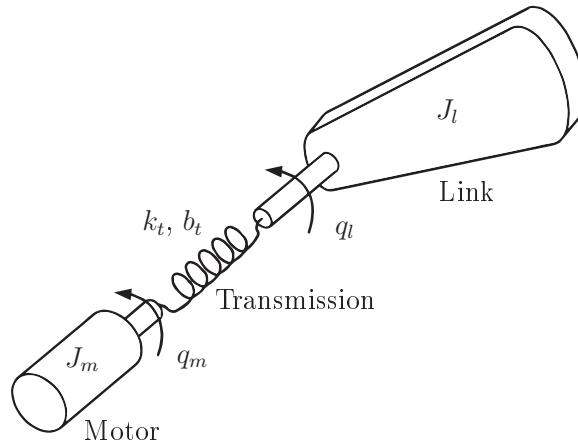
Figure 5-32: Structure of a robotic joint with elastic transmission.

track the desired reference signal $q_{ref}(t)$ with small errors (and therefore it is possible to assume $q_m(t) \approx q_{ref}(t)$) the link position may be affected by undesired oscillations and vibrations. As a matter of fact, the relationship between the motor position and the link position can be modelled as a typical second order system $G(s)$ like the one in (1.3). Thus the use of the exponential filter $F_{exp}(s)$ in (5.3) as a command shaper for the controlled motor has been already proven to be a simple and effective way to reduce/suppress the oscillation. This consideration allow to generalize the results in previous Sections to any type of Single Input Single Output (SISO) Linear Time-Invariant (LTI) system, characterized by one or more oscillating dynamical modes. Therefore, given a dynamic system modelled as

$$G(s) = \frac{N(s)}{D(s)(s^2 + 2\delta\omega_n s + \omega_n^2)}$$

where $N(s)$ and $D(s)$ are generic polynomial ($D(s)$ Hurwitz), it is possible to show that the contribution to the response of the oscillating mode characterized by (δ, ω_n) can be completely nullified T_J seconds after the application of the input signal by inserting between the input and the system a properly tuned filter $F_{exp}(s)$.

176

5.7 Feedforward Control of MIMO LTI Systems for Residual Vibration Suppression

The extension of the results for SISO systems to Multiple Input Multiple Output (MIMO) systems is straightforward. As a matter of fact, for MIMO LTI systems, usually modelled in the state space domain as

$$
\begin{cases}
\dot{x} & = \boldsymbol{A}x + \boldsymbol{B}u \\
y & = \boldsymbol{C}x + \boldsymbol{D}u
\end{cases}
\tag{5.13}
$$

where $x \in \mathcal{R}^n$ is the state vector, $u \in \mathcal{R}^r$ is the input vector, $y \in \mathcal{R}^m$ is the output vector, and $\{\boldsymbol{A}, \boldsymbol{B}, \boldsymbol{C}, \boldsymbol{D}\}$ are matrices of appropriate dimensions, it is possible to deduce the transfer matrix, i.e. the matrix of the transfer function between the r inputs and the m outputs,

$$
\boldsymbol{H}(s) = \frac{\boldsymbol{C}\,\mathbf{Adj}(s\boldsymbol{I}_n - \boldsymbol{A})\boldsymbol{B} + |s\boldsymbol{I}_n - \boldsymbol{A}|\,\boldsymbol{D}}{|s\boldsymbol{I}_n - \boldsymbol{A}|}
\tag{5.14}
$$

where $\mathbf{Adj}(\boldsymbol{X})$ is the adjoint matrix associated with $\boldsymbol{X}$ and $|\boldsymbol{X}|$ denotes the determinant of $\boldsymbol{X}$. The term $|s\boldsymbol{I}_n - \boldsymbol{A}|$ is an n-th polynomial, whose roots are the poles[4] of the transfer functions that compose $\boldsymbol{H}(s)$. Note that, if no cancellations occur between the numerator and the denominator of these transfer functions, they share the same poles. Therefore, in order to suppress the effects of a poorly damped mode (δ, ω_n) on the outputs, it is necessary to insert a filter $F_{exp}(s)$ before each of the r inputs.

5.8 Feedforward Control of Robotic Manipulators with Elastic Joints

In order to apply the technique proposed in Section 5.1 to a robotic system accordingly to the MIMO case extension in Section 5.7, it is necessary to consider the complete

---

[4]As well-known, if no cancellations occur the poles coincide with the eigenvalues of matrix $\boldsymbol{A}$.

model of the manipulator. The reduced model[5] of a visco-elastic joints robot is

$$\boldsymbol{M}(\boldsymbol{q}_l)\ddot{\boldsymbol{q}}_l + \boldsymbol{C}(\boldsymbol{q}_l, \dot{\boldsymbol{q}}_l)\,\dot{\boldsymbol{q}}_l + \boldsymbol{g}(\boldsymbol{q}_l) + \boldsymbol{K}_t \cdot (\boldsymbol{q}_l - \boldsymbol{q}_m)$$
$$+ \boldsymbol{B}_t \cdot (\dot{\boldsymbol{q}}_l - \dot{\boldsymbol{q}}_m) = 0 \qquad (5.15)$$

where $\boldsymbol{M}(\boldsymbol{q}_l)$, and $\boldsymbol{C}(\boldsymbol{q}_l, \dot{\boldsymbol{q}}_l)$ are the inertia and centrifugal/Coriolis forces matrices, $\boldsymbol{g}(\boldsymbol{q}_l)$ represents the gravity term, $\boldsymbol{K}_t = \mathrm{diag}\{k_{ti}\}$, $\boldsymbol{B}_t = \mathrm{diag}\{b_{ti}\}$ are the matrices of the transmission stiffness and viscous friction, $\boldsymbol{q}_l$ and $\boldsymbol{q}_m$ denote the vector of the joint positions at the link side and at the motor side, respectively [28]. Note that the motors' dynamics that usually accompanies (5.15) has been neglected since, according to a standard decentralized control of robot manipulators, it is assumed that the motors behave like ideal position sources able to impose any desired configuration $\boldsymbol{q}_m$.

The model of VSJ robots can be ideally obtained from (5.15) by assuming that the stiffness matrix is not a constant but a function of time, i.e.

$$\boldsymbol{K}_t = \boldsymbol{K}_t(t).$$

The stiffness modification is generally obtained with extra command inputs to the robot system that allow to change each joint stiffness independently, i.e.

$$k_{ti} = k_{ti}(s_i)$$

where s_i denotes the activation signal of the stiffness of the i-th joint. Therefore, it is possible to rewrite the transmission stiffness matrix as $\boldsymbol{K}_t = \boldsymbol{K}_t(s)$. In many cases, in particular when the variable stiffness mechanism is obtained with a couple of antagonistic actuators (like in the experiments proposed in this paper) [69], the elastic torque not only depends on the external signal $s(t)$ but is a nonlinear function of the motors displacement. As a consequence, the general expression of the elastic

---

[5]This model is based on the assumption that the angular kinetic energy of the motors is only due to their own spinning [99].

transmission torque should be $\boldsymbol{\tau}_{\mathrm{el}} = \boldsymbol{\tau}_{\mathrm{el}}(\boldsymbol{q}_l - \boldsymbol{q}_m, s)$ where $\boldsymbol{\tau}_{\mathrm{el}}(\Delta q, \cdot)$ denotes a vectorial nonlinear function whose elements are odd strictly monotonically increasing functions of Δq and $\boldsymbol{\tau}_{\mathrm{el}}(0, \cdot) = 0$. Finally, it is worth noticing that often the variable stiffness mechanism makes also the damping torques not constant but variable as a function of the time. Therefore, a quite general expression that describes the dynamics of VSJ robots is

$$
\boldsymbol{M}(\boldsymbol{q}_l)\ddot{\boldsymbol{q}}_l + \boldsymbol{C}(\boldsymbol{q}_l, \dot{\boldsymbol{q}}_l)\,\dot{\boldsymbol{q}}_l + \boldsymbol{g}(\boldsymbol{q}_l) + \boldsymbol{\tau}_{el}(\boldsymbol{q}_l - \boldsymbol{q}_m, s)
$$
$$
+ \boldsymbol{\tau}_{\mathrm{damp}}(\dot{\boldsymbol{q}}_l - \dot{\boldsymbol{q}}_m, s) = 0 \qquad (5.16)
$$

where, similarly to $\boldsymbol{\tau}_{\mathrm{el}}$, $\boldsymbol{\tau}_{\mathrm{damp}}(\Delta\dot{q}, \cdot)$ denotes a vectorial nonlinear function whose elements are odd strictly monotonically increasing functions of $\Delta\dot{q}$ and $\boldsymbol{\tau}_{\mathrm{damp}}(0, \cdot) = 0$.

5.8.1 Linearized Model of a VSJ Robot and Feed-Forward Design

In order to find the parameters of the proposed filter for feed-forward control for a given value $s = s^{\star}$, it is necessary to linearize (5.16) around the desired equilibrium state $(q_l, \dot{q}_l) = (\boldsymbol{q}_l^{\star}, 0)$ with $q_l^{\star}$ related to the equilibrium input $(q_m, \dot{q}_m) = (\boldsymbol{q}_m^{\star}, 0)$ by

$$
\boldsymbol{g}(\boldsymbol{q}_l^{\star}) + \boldsymbol{\tau}_{\mathrm{el}}(\boldsymbol{q}_l^{\star} - \boldsymbol{q}_m^{\star}) = 0. \qquad (5.17)
$$

Note that, for the sake of clarity, since the input s is supposed to be a constant the dependance of $\boldsymbol{\tau}_{\mathrm{el}}$ and $\boldsymbol{\tau}_{\mathrm{damp}}$ on it has been omitted. The approximation of (5.16) by Taylor series expansion up to the first order provides the following expression

$$
\boldsymbol{M}(\boldsymbol{q}_l^{\star})\Delta\ddot{\boldsymbol{q}}_l + \boldsymbol{g}(\boldsymbol{q}_l^{\star}) + \left.\frac{\partial \boldsymbol{g}(\boldsymbol{q}_l)}{\partial \boldsymbol{q}_l}\right|_{\boldsymbol{q}_l = \boldsymbol{q}_l^{\star}} \Delta\boldsymbol{q}_l + \boldsymbol{\tau}_{\mathrm{el}}(\boldsymbol{q}_l^{\star} - \boldsymbol{q}_m^{\star})
$$
$$
+ \left.\frac{\partial \boldsymbol{\tau}_{\mathrm{el}}(\Delta q)}{\partial \Delta q}\right|_{\Delta q = \boldsymbol{q}_l^{\star} - \boldsymbol{q}_m^{\star}} (\Delta\boldsymbol{q}_l - \Delta\boldsymbol{q}_m) + \left.\frac{\partial \boldsymbol{\tau}_{\mathrm{damp}}(\Delta\dot{q})}{\partial \Delta\dot{q}}\right|_{\Delta\dot{q} = 0} (\Delta\dot{\boldsymbol{q}}_l - \Delta\dot{\boldsymbol{q}}_m) = 0 \qquad (5.18)
$$

where $\Delta\boldsymbol{q}_l = \boldsymbol{q}_l - \boldsymbol{q}_l^{\star}$, $\Delta\boldsymbol{q}_m = \boldsymbol{q}_m - \boldsymbol{q}_m^{\star}$, etc. represent small variations with respect to the corresponding equilibrium values. Note that centrifugal/Coriolis terms, that

179

are quadratic with respect to the velocity, disappear in the linearized model. By substituting (5.17) in (5.18) and denoting

$$\boldsymbol{G}^{\star} = \left.\frac{\partial \boldsymbol{g}(\boldsymbol{q}_l)}{\partial \boldsymbol{q}_l}\right|_{\boldsymbol{q}_l = \boldsymbol{q}_l^{\star}}$$

$$\boldsymbol{K}_t^{\star} = \left.\frac{\partial \boldsymbol{\tau}_{\mathrm{el}}(\Delta q)}{\partial \Delta q}\right|_{\Delta q = \boldsymbol{q}_l^{\star} - \boldsymbol{q}_m^{\star}}$$

$$\boldsymbol{B}_t^{\star} = \left.\frac{\partial \boldsymbol{\tau}_{\mathrm{damp}}(\Delta \dot{q})}{\partial \Delta \dot{q}}\right|_{\Delta \dot{q} = 0}$$

the expression of the linearized model becomes

$$\boldsymbol{M}(\boldsymbol{q}_l^{\star})\Delta \ddot{\boldsymbol{q}}_l + \boldsymbol{G}^{\star}\Delta \boldsymbol{q}_l + \boldsymbol{K}_t^{\star}(\Delta \boldsymbol{q}_l - \Delta \boldsymbol{q}_m) + \boldsymbol{B}_t^{\star}(\Delta \dot{\boldsymbol{q}}_l - \Delta \dot{\boldsymbol{q}}_m) = 0 \tag{5.19}$$

which can be rewritten in the state-space form such as (5.13) with

$$\boldsymbol{A} = \begin{bmatrix} \boldsymbol{0}_n & \boldsymbol{I}_n \\ -\boldsymbol{M}^{-1}(\boldsymbol{q}_l^{\star})\boldsymbol{K}_t^{\star} - \boldsymbol{M}^{-1}(\boldsymbol{q}_l^{\star})\boldsymbol{G}^{\star} & -\boldsymbol{M}^{-1}(\boldsymbol{q}_l^{\star})\boldsymbol{B}_t^{\star} \end{bmatrix}$$

$$\boldsymbol{B} = \begin{bmatrix} \boldsymbol{0}_n & \boldsymbol{0}_n \\ \boldsymbol{M}^{-1}(\boldsymbol{q}_l^{\star})\boldsymbol{K}_t^{\star} & \boldsymbol{M}^{-1}(\boldsymbol{q}_l^{\star})\boldsymbol{B}_t^{\star} \end{bmatrix}$$

where the state and input vector are $x = \begin{bmatrix} \Delta \boldsymbol{q}_l \\ \Delta \dot{\boldsymbol{q}}_l \end{bmatrix}$ and $u = \begin{bmatrix} \Delta \boldsymbol{q}_m \\ \Delta \dot{\boldsymbol{q}}_m \end{bmatrix}$ respectively. By analyzing the eigenvalues of the matrix $\boldsymbol{A}$ it is possible to find the values of the resonant modes that affect the robotic plant. A n degrees-of-freedom robot manipulator with undamped or poorly damped elastic joints will be characterized by n pairs of complex conjugate eigenvalues with (δ_i, ω_{ni}), $i = 1, \ldots, n$. In order to suppress the oscillations at a constant configuration $\boldsymbol{q}_l^{\star}$ it is sufficient to filter the reference signals of the motors, and consequently the motor positions $q_m(t)$ supposed to be equal to $q_{ref}(t)$, with a chain of filters $F_{exp_i}(s)$, one for each mode of the system.

5.9 Experimental Results

The method described in previous sections has been tested on a real soft robotic arm build with QBMove - Maker Pro VSAs by QBRobotics [81]. These actuators implement the concept of variable stiffness servo motors, i.e. motor units that include also (position) sensing and control system allowing the user to command both the position and the stiffness of the output shaft with an external signal. For these reason, these actuators are very suitable for rapid prototyping robots with variable stiffness joints [22]. QBMove VSAs are provided with an easy to use Matlab/Simulink toolbox that can runs without particular restriction even on standard operating system and communicates with the actuators via USB. In the experiments reported in this section Matlab ran with a fixed step size $T_s = 2$ ms. For this reason, the filter $F_{exp}(s)$ has been discretized according to the techniques reported in Section 5.3.

The mechanical structure of these VSAs is based on an antagonistic configurations with two servomotors connected to the output shaft by tendons that are fixed to springs. The working principle is quite simple: the shaft position is the mean of the servos position so it is due to the concordant motion of the servo motors, while the stiffness grows as the displacement between the servos increases. Therefore, when the user specifies a give shaft position q_l and a stiffness preset s, these values, related to the motor position by

$$q_l = \frac{q_{m,1} + q_{m,2}}{2}, \quad s = \frac{q_{m,1} - q_{m,2}}{2},$$

are translated by the QBMove controller in the motor positions $q_{m,1}$ and $q_{m,2}$, that are actuated by the two servomotors. As a consequence, a feedforward controller that filters the inputs q_l and s is actually placed before the motor position $q_{m,1}$ and $q_{m,2}$, as supposed in Sec. 5.8.
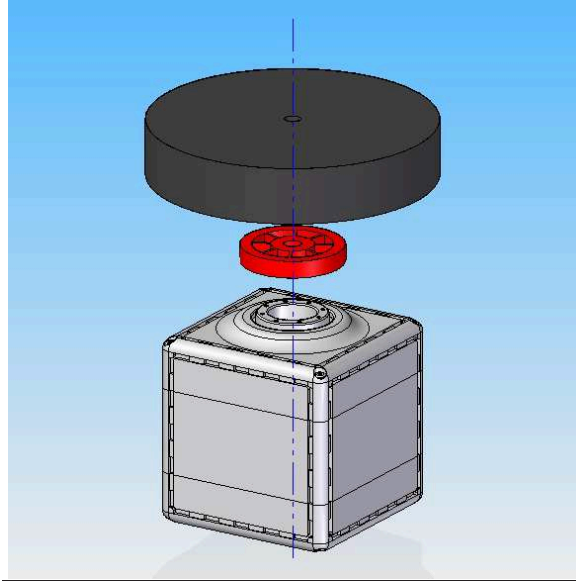
Parameter	Value	Unit
Peak (Maximum) Torque	1.5	Nm
Maximum Speed	9.5	rad/s
Maximum Stiffness	13	Nm/rad
Minimum Stiffness	0.5	Nm/rad

Figure 5-33: CAD view of the setup for parameters evaluation and main data of the servomotor.

5.9.1 Characterization of a Single Actuator

In order to test the proposed method, an intensive experimental analysis on a single actuator has been carried out to estimate the parameters α and T_J which characterize the filter $F_{exp}(s)$. In order to better appreciate the oscillations due to the elastic transmission, a known inertial load represented by an iron disk of diameter 10 cm and weight 1 kg has been attached to the actuator shaft, as shown in fig. 5-34. Then a step of 45° have been commanded to the actuator with a fixed stiffness preset value and the response has been evaluated.

Several tests has been performed with various stiffness values in order to analyze different step responses. As can be seen from the responses of fig. 5-34, the system behaves like a second order system. This means that the dominant dynamics is the mechanical dynamics of the inertia with the elastic transmission, while the dynamics of the two servo motors inside the actuators can be neglected. For each stiffness
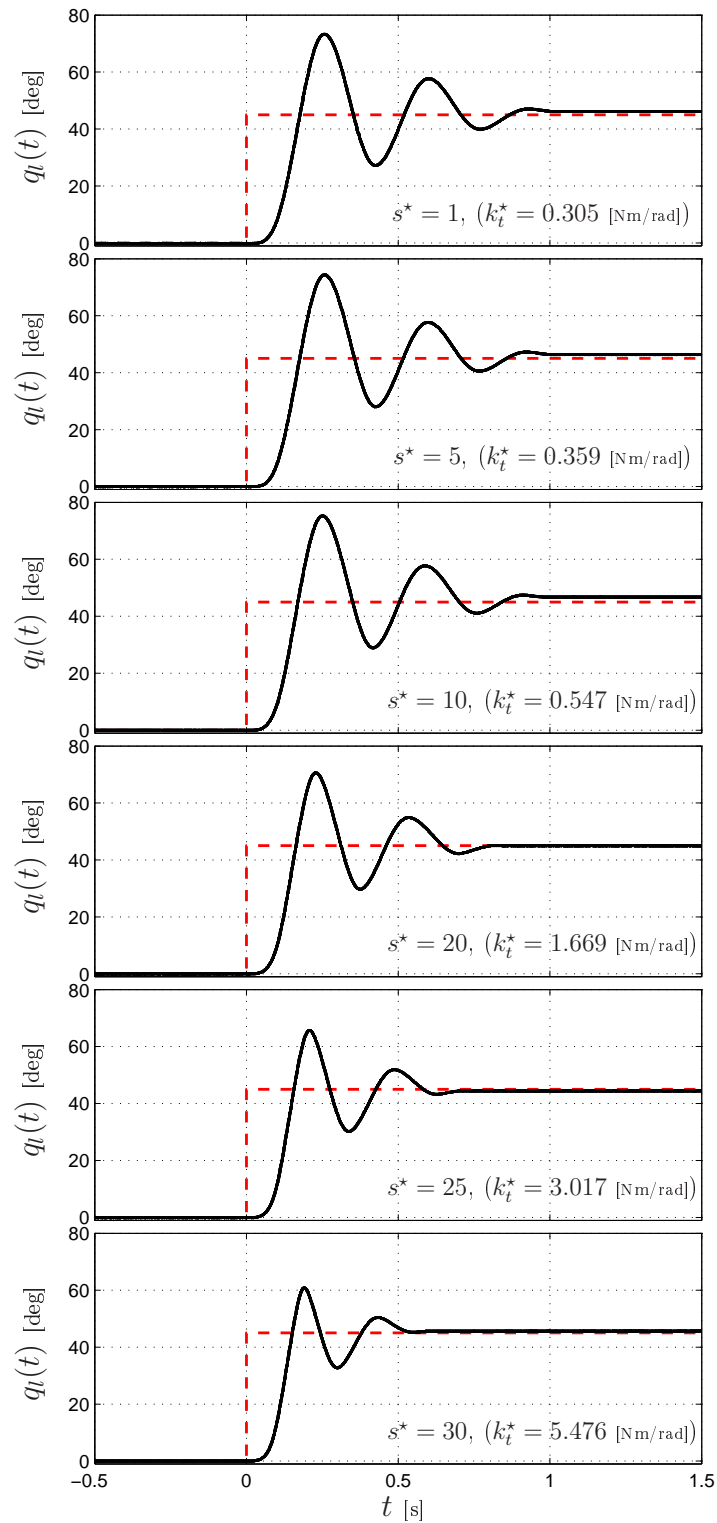
Figure 5-34: Step response $q_l(t)$ of the servomotor with an inertial load with different stiffness values $k_t^\star$. In red the step set-point of 45° is reported.
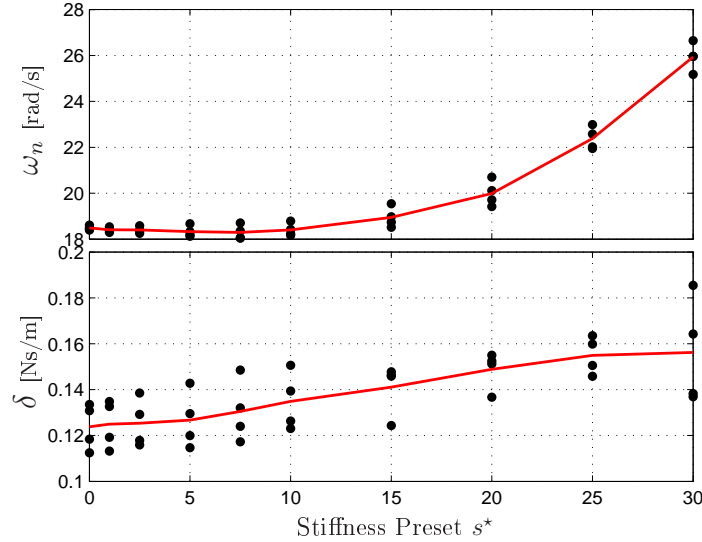
Figure 5-35: Estimated parameters ω_n (a) and δ (b) for different values of stiffness presets $s^\star$. Different equilibrium points have been considered.

preset $s^\star$, and therefore for each values of the stiffness $k_t^\star$, the values of the damping coefficient δ and natural frequency ω_n of the system have been determined, and are reported in fig. 5-35. It is worth noticing that, as expected, ω_n increases as the stiffness grows but it is also visible a slight increase of δ, due to friction effects of the particular transmission of the QBMove. Since J_l is known, from δ and ω_n it is possible to immediately deduce the values of the stiffness and damping $(k_t^\star, b_t^\star)$ about the equilibrium point.

In a first stage of this experimental activity, the proposed feedforward control based on the exponential filter $F_{exp}(s)$ has been applied to a single actuator and its performance have been compared with those of ZVD Input Shapers, that are the most widespread filtering methods for residual vibration suppression, see [95, 86, 106]. In order to appreciate the effectiveness of the proposed method, only very low stiffness values have been considered as they represent a more challenging situation in terms of vibrations. With the parameters derived by means of the procedure described above, the appropriate parameters of the exponential and ZVD filters have been derived for every stiffness preset that has been considered. Then a filtered step input has been provided to the actuator. The obtained results are shown in fig. 5-36: the performances of the two methods in terms of residual vibration reduction and time

184
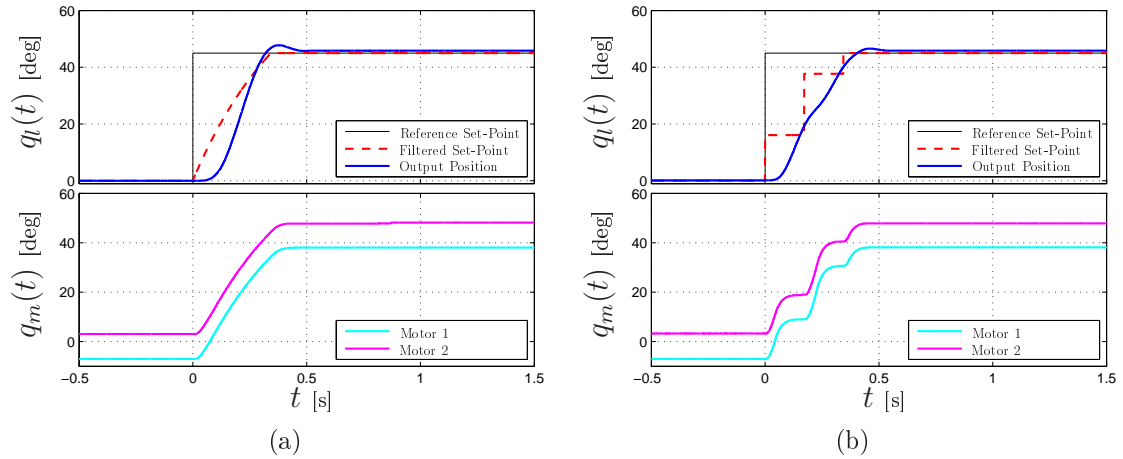
Figure 5-36: Response of the system with stiffness preset $s^\star = 5$ to a step input of 45°, shaped by exponential jerk filter (a) and ZVD input shaper (b).

duration of the motion are similar and in general very good. However, it is interesting to notice the difference between the motions $q_{m,1}(t)$ and $q_{m,2}(t)$ performed by the two servo motors. While the motors with the ZVD input shaper are fed by several steps, exponential filter provide a smoother trajectory that can be easily tracked.

5.9.2 Application of the feed-forward control to a planar robot

The proposed technique has been applied to the 3-dofs planar robotic arm made of QBmove VSAs shown in fig. 5-37. For our purpose the arm has been controlled only in position without caring about orientation, therefore the discussion refers only to the first two joints. The actuator parameters $(k_t^\star, b_t^\star)$ derived in previous section for a given stiffness preset $s^\star$ have been used to determine the values (δ_i, ω_{ni}) of the two vibratory modes that characterize the robot model, linearized about the desired final configuration. From these values the parameters of two exponential filters, which are arranged in a cascade configuration on the reference inputs of the motor, are obtained, see fig. 5-38. Also in this case the behavior obtained with the proposed exponential filter is compared with the those obtained with ZVD Input Shapers.

In the test shown in fig. 5-39, only the first joint is moved, according to a step signal of 30°. In this case the preset stiffness signal has been set to 5. Despite the large variations, the filters, designed for linear systems, are able to cancel the oscillation
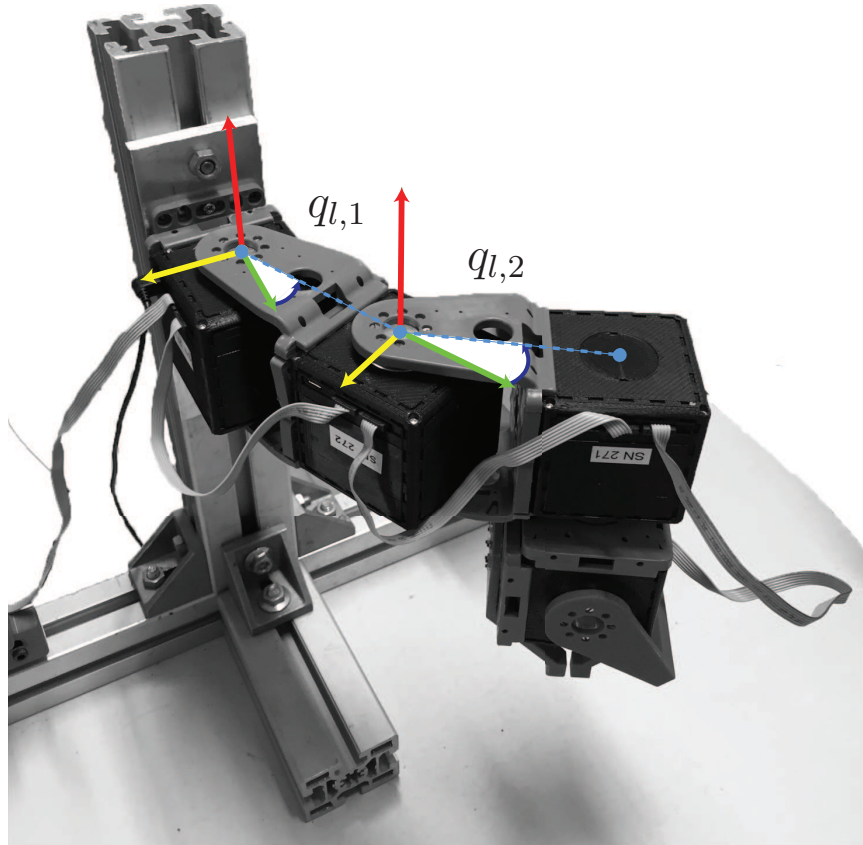
Figure 5-37: Picture of the 3-dofs robotic arm made of QBmove VSAs.
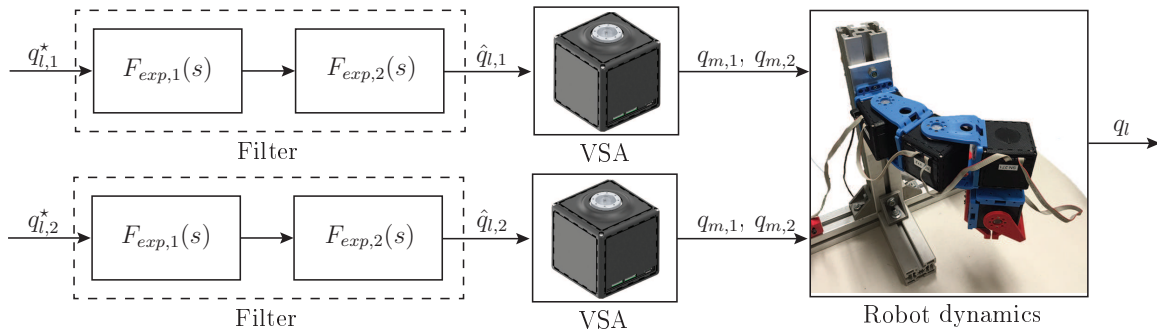
Figure 5-38: Block-scheme representation of the feedforward control.

on the first joint and also to avoid the mutual influence with the second joint, see fig. 5-39(b). In fig. 5-40 a simultaneous motion of 30° is required to both joints. It is quite evident that the proposed method eliminates residual vibrations. Moreover, it guarantees a smoother motion with respect to the ZVD input shaping technique with the same time performance. In both the experiments it is evident a noticeable position error due to the fact that feedforward control is not able to compensate for friction

effects (the gravity does not affect the system which move on the horizontal plane). Anyway, the fact that even without filters the static error is comparable proves that this problem is not related to the specific trajectory generation, but rather to the small value of the stiffness.

In fig. 5-41 the same experiment of fig. 5-40 but with an higher value of the stiffness ($s^\star = 30$) is shown. The conclusions do not change with respect to the previous test, that is the use of exponential filters on the reference inputs cancels the oscillations on the joints positions. In this case, the static precision slightly improves, because of the higher stiffness.
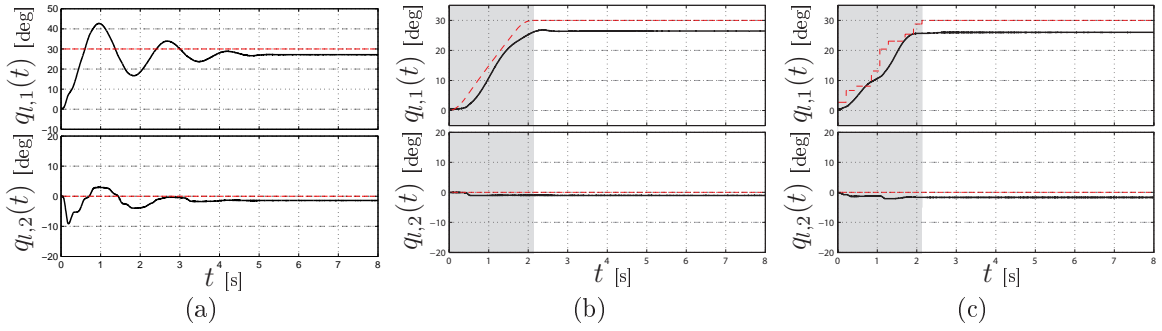
Figure 5-39: Response of the actuators ($q_{l,2}(t)$ and $q_{l,2}(t)$) that compose the 2-dofs robotic arm to a step input trajectory with a stiffness preset $s^\star = 5$. In dashed red the actual trajectory is reported. fig. 5-39(a) is a pure step, fig. 5-39(b) is an exponential filtered step, fig. 5-39(c) is a ZVD shaped input.
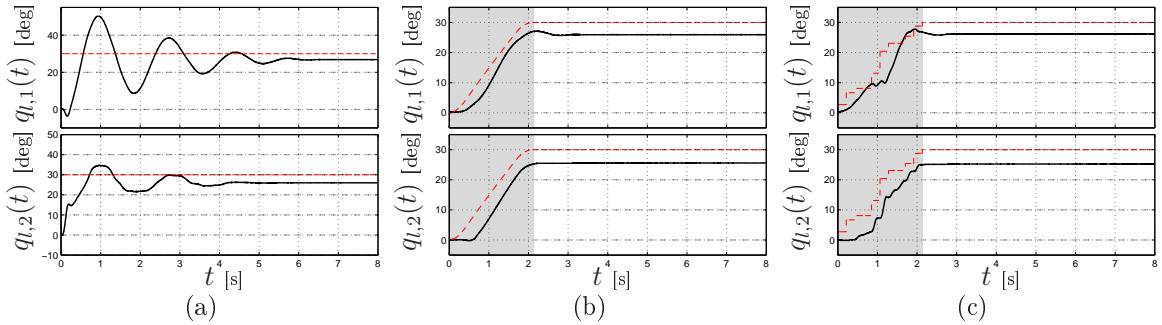
Figure 5-40: Response of the actuators ($q_{l,1}(t)$ and $q_{l,2}(t)$) that compose the 2-dofs robotic arm to a step input trajectory with a stiffness preset $s^\star = 5$. In dashed red the actual trajectory is reported. fig. 5-40(a) is a pure step, fig. 5-40(b) is an exponential filtered step, fig. 5-40(c) is a ZVD shaped input.
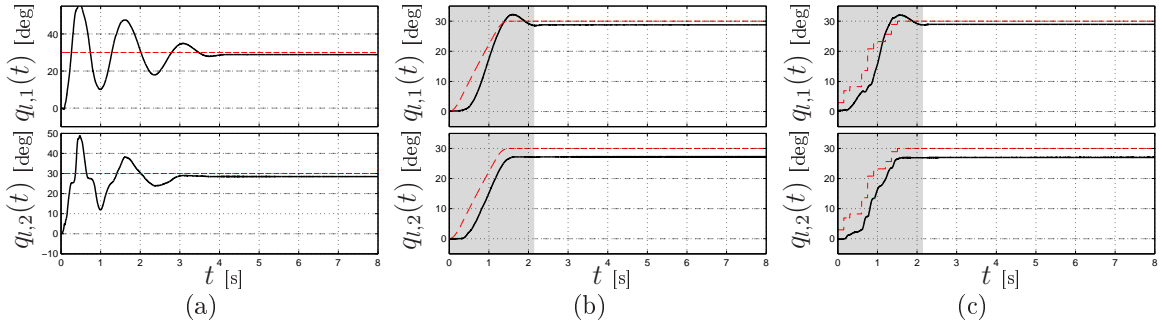
Figure 5-41: Response of the actuators ($q_{l,1}(t)$ and $q_{l,2}(t)$) that compose the 2-dofs robotic arm to a step input trajectory with a stiffness preset $s^\star = 30$. In dashed red the actual trajectory is reported. fig. 5-41(a) is a pure step, fig. 5-41(b) is an exponential filtered step, fig. 5-41(c) is a ZVD shaped input.

Chapter 6

A Repetitive Control Scheme
for Industrial Robots
Based on B-Spline Trajectories

6.1   Motivations

In practical applications, desired tasks are often repetitive or cyclic in nature. This is particularly true in industrial robotics and in automatic machines, where many tasks simply imply the continuous repetition of a given motion. From a control point of view, it is therefore required to track and/or reject a periodic exogenous signal that can be considered known since it refers to planned trajectories or disturbances whose cycle time is easily measurable or known in advance. In order to improve the tracking accuracy, Repetitive Control (RC) represents a simple and effective method, since it aims at cancelling tracking errors over repetitions by learning from previous iterations. RC was first developed by Inoue et al. [45, 44] to improve the control of the power supply in a proton synchrotron accelerator, but soon was applied to many other different systems. Many surveys, see e.g. [25], [109], report the successful use of RC in a number of applications, such as high accuracy trajectory tracking of servomechanism, torque vibration suppression in motors, noise cancellation in power

supply, industrial robotics, and so on. The theoretical foundation of the RC is due to the internal model principle (IMP) [35] which states that to track or reject a certain signal without steady-state error, the signal can be regarded as the output of an autonomous generator that is inside the control system. The IMP with the well known fact that any periodic signal with period T can be generated by a time-delay positive feedback system with an appropriate initial function, are the basis of a Repetitive Controller.

Stabilizability of a RC system is not a trivial problem due to the presence of a time-delay in the positive feedback loop. In order to address this issue, several solutions have been presented providing necessary and/or sufficient conditions for stability and error convergence to zero.

In [17, 16], a novel repetitive control scheme is presented. The scheme is based on a proper modification of the reference trajectory for the plant, which is supposed to be already controlled. A similar idea has been already proposed in the continuous-time domain in [37], where a two-degree-of-freedom local control, and a plug-in type RC is used to update the reference trajectory. The novelty of this case consists in assuming that the reference trajectories are defined by spline functions, which are de-facto the standard tool used in the industrial field for planning complex motions interpolating a set of given via-points [9]. Thanks to the possibility of generating B-spline trajectories by means of dynamic filters as reported in Chapter 4, the trajectory planner has been inserted in an external feedback control loop that modifies in real-time the control points of the B-spline curve so that the tracking error at the desired via-points converges to zero. The proposed control scheme has been directly developed in the discrete time-domain, and is characterized by a very low computational complexity. Moreover, the application of this control scheme is independent by the particular control law of the plant, which is seen as a servo-system able to track a spline curve.

6.2 B-spline Curves and B-spline Filters for Set-point Generation

In a number of practical applications the reference signal for dynamical systems is defined by using spline functions that interpolate a set of desired via-points $\boldsymbol{q}_j$, $j = 0, \ldots, n - 1$ at time instants t_j. By assuming a B-spline form of the trajectory, as reported in Section 4.2 results

$$q(t) = \sum_{j=0}^{n-1} \boldsymbol{p}_j \, B_j^d(t), \qquad t_0 \leq t \leq t_{n-1} \tag{6.1}$$

where $B_j^d(t)$ is a B-spline basis function of degree d, the control points $\boldsymbol{p}_j$ must be computed by imposing interpolation conditions on the given data points $\boldsymbol{q}_j$, see [9]. Note that, as shown in fig. 6-1, the control points alone determine the geometric shape of the B-spline curve, which represent a sort of smooth approximation of the so-called control polygon.

6.2.1 B-spline Evaluation

In order to evaluate the spline (6.1) for a given value $t \in [t_0, t_{n-1}]$ it is necessary to compute the basis functions $B_j^d(t)$ via numerical procedures, which are usually based on recursion. As described in Section 4.3.3 if uniform B-splines are considered, i.e. B-splines characterized by an equally-spaced distribution of the knots t_j i.e. $t_{j+1} - t_j = T \; j = 0, \ldots n - 2$, the generation of the trajectory can be obtained by means of a chain of d dynamic filters defined as

$$M(s) = \frac{1 - e^{-sT}}{Ts}$$

fed by the staircase signal $p(t)$ obtained by maintaining the value of each control point $\boldsymbol{p}_j$ for the entire period $jT \leq t < (j + 1)T$. See the scheme of fig. 6-2 and the signals shown in fig. 4-15, where the generation of a cubic B-spline is considered. Note that $p(t)$ is obtained by applying a zero-order hold to the train of impulses of
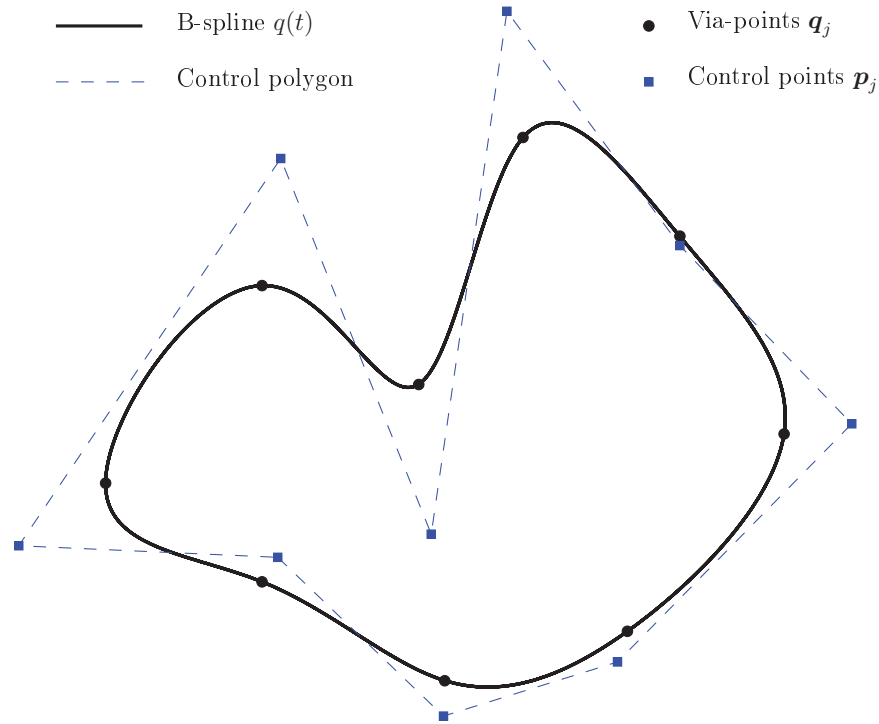
Figure 6-1: Two-dimensional B-spline trajectory interpolating a set of via-points $\boldsymbol{q}_i^\star$.
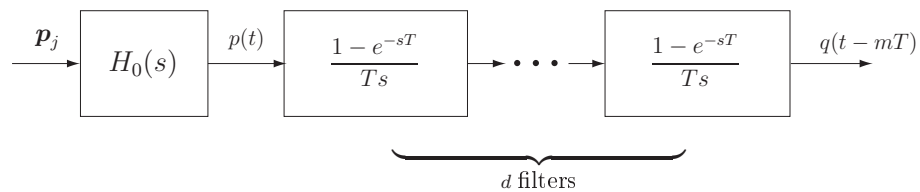
Figure 6-2: System composed by d mean filters and by a zero-order hold $H_0(s)$ for the computation of continuous-time B-spline trajectories of degree d.

amplitude $\boldsymbol{p}_j$. Moreover, it is worth noticing that the output trajectory is delayed with respect to the application of control points of mT seconds, where $m = \frac{d+1}{2}$. For computer controlled systems equipped with digital controllers with sampling period T_s, the B-spline reference trajectory must be computed at time-instants kT_s. It is therefore necessary to discretize the filter of fig. 6-2. By Z-transforming the chain of d filters $M(s)$ with a zero-order hold the system of fig. 6-3 is obtained, where $F_d(z^{-1})$ is a FIR filter defined by

$$F_d(z^{-1}) = \frac{z^{-1}Q_{d-1}(z^{-1})}{d!}, \tag{6.2}$$
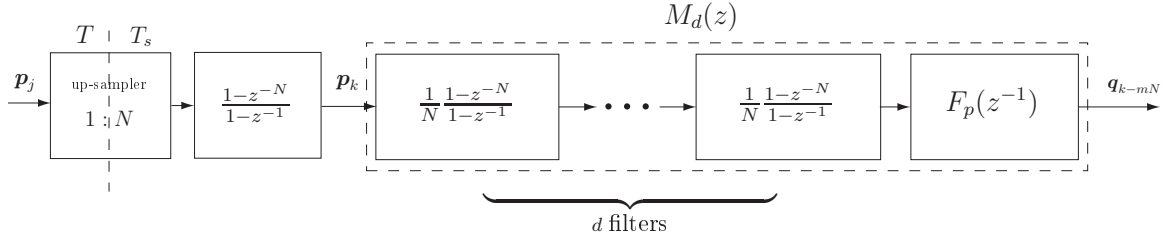
Figure 6-3: System $M_d(z)$ composed by d moving average filters and by the FIR filter $F_d(z^{-1})$ defined in (6.2) for the generation of discrete-time B-spline trajectories of degree d.

as reported in Section 4.5. The samples of the B-spline sequence are then generated by the filter denoted by $M_d(z)$ and coincide with the value of the continuous-time trajectory at time instants kT, i.e $\boldsymbol{q}_k = q(kT)$, see fig. 6-4.

6.2.2 Control Points Computation

The control points $\boldsymbol{p}_j$ are computed by imposing the interpolation conditions on the via-points at the time-instants defined by knots which for uniform B-spline are multiple of the fundamental period T, i.e.

$$q(jT) = \boldsymbol{q}_j, \qquad j = 0, \ldots, n - 1. \tag{6.3}$$

As well-known the definition of the interpolating B-spline is a global problem, that can be performed only when the entire set of via-points is provided. However, it is possible to approximate this global mapping between via-points and control points within a smaller set of data, see Section 4.5.4. The system $H(z)$ is a FIR filter that approximates the relation between via-points and control points assuming to treat the interpolation problem as a dynamic relationship between via-points and control points, i.e.

$$\frac{P(z)}{Q(z)} = \frac{6}{z + 4 + z^{-1}} \tag{6.4}$$

193
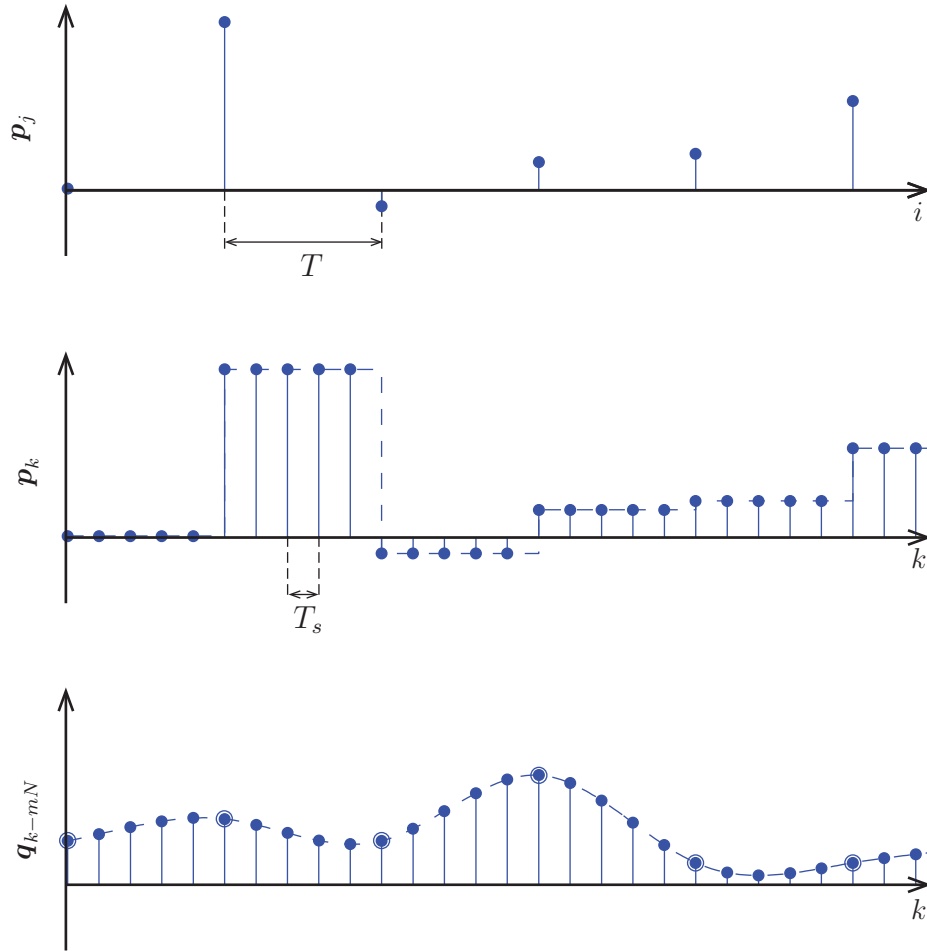
Figure 6-4: Control points sequence $\boldsymbol{p}_j$ defining a cubic B-spline and related reference trajectory $\boldsymbol{q}_{k-mN}$ with $m = 2$ obtained with the dynamic filter of fig. 6-3.

for a cubic B-spline. This approach leads to a FIR filter defined by

$$H(z) = \sum_{n=-r}^{r} h(n) \ z^{-n} \tag{6.5}$$

that approximates the interpolation problem within a prescribed tolerance according to the value of r. The coefficients $h(n)$ for $d = 3$ can be computed as

$$h(n) = \frac{1 - \alpha}{1 + \alpha} \alpha^{|n|}$$

where $\alpha = -2 + \sqrt{3}$ is the stable pole of (6.4). The sequence $h(n)$ is shown in fig. 4-32. Note that the value of $h(n)$ becomes extremely small as $|n|$ grows (for more details

194
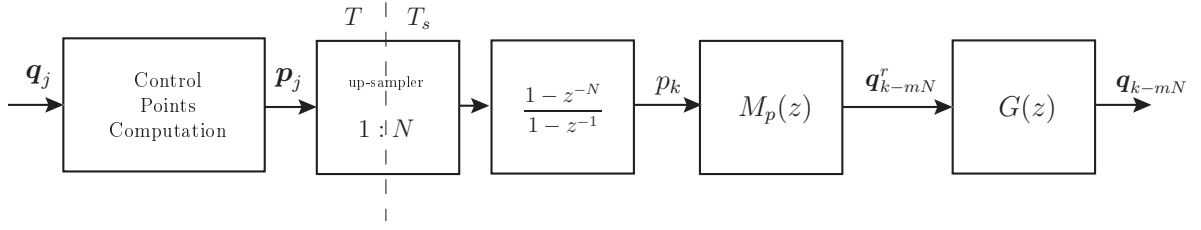
Figure 6-5: Set-point definition by means of B-spline filter for a (controlled) discrete-time system $G(z)$.

see [14]).

In the scheme of fig. 6-7, the filter $H(z)$ is used to transform the interpolation errors $\tilde{q}_j$ in an error in the control points position $\tilde{p}_j$. Since $H(z)$ is not a causal filter, it is necessary to introduce a delay equal to r to make it feasible, that is

$$H'(z) = z^{-r} H(z) = \sum_{n=0}^{2r} h(n-r) \, z^{-n}. \tag{6.6}$$

The reference trajectory generated by the discrete B-spline filter is then provided to the plant, as illustrated in fig. 6-5. Since this scheme has a standard cascade structure without control actions but with the only purpose of generating arbitrarily complex trajectories for the plant $G(z)$, the capabilities of $G(z)$ to track such a kind of signals are implicitly assumed. Therefore, the system $G(z)$ is assumed to be a controlled plant, with a standard closed-loop structure, whose frequency response is characterized by a typical low-pass behavior with a static gain as close as possible to the unity. In order to follow the input signal accurately, the bandwidth of system must be large enough [67], and in particular larger than the maximum spectral components of the input. In case of uniform B-splines generated by the linear filter $M^d(z)$, the spectrum of the resulting trajectories can be determined by analyzing the frequency response of $M^d(z)$. In particular the magnitude of $M_p(e^{j\omega T_s})$ is

$$|M_p(e^{j\omega T_s})| = \left|F_p(e^{-j\omega})\right| \cdot \left|\frac{\mathrm{sinc}\left(\frac{\omega}{\omega_0}\right)}{\mathrm{sinc}\left(\frac{\omega}{\omega_s}\right)}\right|^d, \quad \omega \le \frac{\omega_s}{2}$$

195
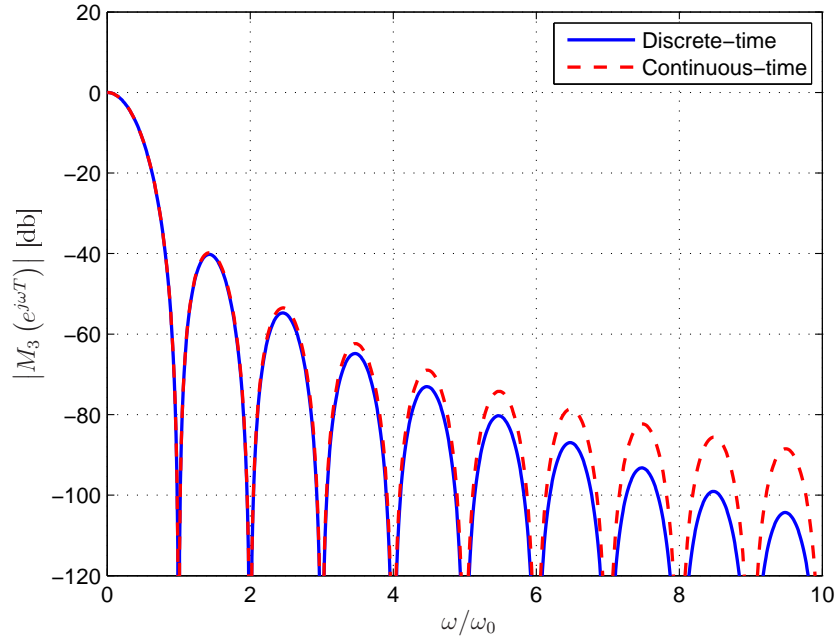
Figure 6-6: Magnitude of the frequency response of the B-spline filter $M_p(z)$ for $p = 3$ (and $N = 25$) compared with the frequency response of the continuous-time generator $M^d(s)$.

where $\text{sinc}(\cdot)$ denotes the normalized sinc function defined as $\text{sinc}(x) = \frac{\sin(\pi x)}{\pi x}$ and $\omega_0 = \frac{2\pi}{T}$, $\omega_s = \frac{2\pi}{T_s}$. The FIR filter $F_p(e^{-j\omega})$ has a standard low-pass behavior, therefore $|M^d(e^{j\omega T_s})|$ is a low-pass filter as well, and its magnitude decreases rather quickly as ω grows, especially for high values of p. In fig. 6-6, the frequency response of the cubic $(p = 3)$ B-spline filter is reported. Obviously, the frequency response of $M_p(z)$ is a good approximation of that of the continuous time generator (the approximation level depends on the ratio N between T and T_s). Fig. 6-6 highlights that spectrum components of the reference trajectory $q^r(t - mT)$ at the output of this filter are significant only in the frequency range $[0, \omega_0]$, while the reduction of the components for $\omega > \omega_0$ is at least of two order of magnitude (-40 db). From common practice, it is known that in order to obtain good tracking performances, the controlled plant $G(z)$ must have a cutoff frequency $\omega_c \gg \omega_0$ (typical values are $\omega_c \geq \alpha\omega_0$, with $\alpha = 5 \div 10$). Consequently, since the sampling frequency ω_s is chosen as $\omega_s \geq \beta\omega_c$ with $\beta = 5 \div 10$, the minimum value of N may range between 25 and 100.

Unfortunately, even if the considerations on $G(z)$ above mentioned are verified, that is

$$G(e^{j\omega T_s}) \approx 1 \text{ for } \omega \leq \frac{2\pi}{T} \ll \omega_c \tag{6.7}$$

the tracking error $e = q - \boldsymbol{q}^r$ between plant output and reference B-spline trajectory can be not negligible, because $G(e^{j\omega T})$ is equal to one only approximatively and may be affected by external disturbances.
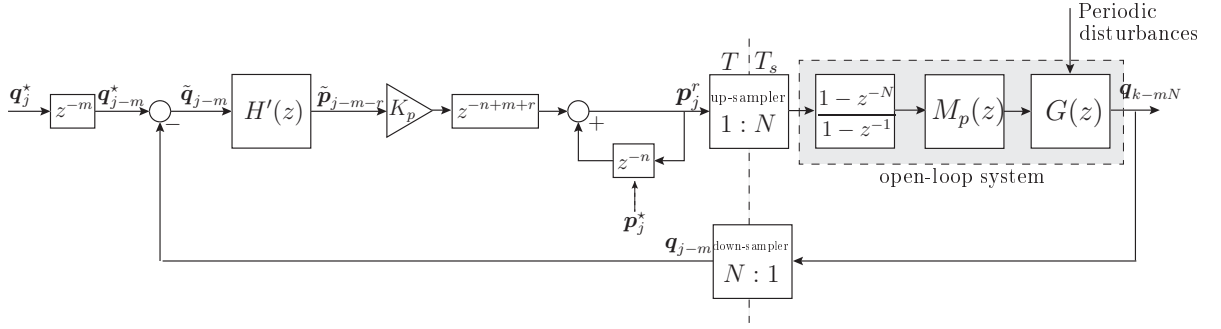
Figure 6-7: Discrete-time repetitive control scheme based on discrete-time B-spline filter.

6.3   Repetitive Control Scheme Based on Discrete-Time B-spline Filter Generator

We assume here that the tasks to be performed are cyclic, and therefore that the trajectories to be tracked are repetitive. Moreover, we assume that also "external" disturbances have the same property, i.e. that there might be either external loads or unmodeled dynamics depending on the current state of the system. In figs. 6-8 and 6-9 is depicted the typical situation of a robot tracking a given trajectory $\boldsymbol{q}^\star(t)$ which interpolates a set of desired via-points $\boldsymbol{q}_j^\star$. Being the robot subject to a certain tracking error, the actual robot position $\boldsymbol{q}(t)$ doesn't match the given trajectory, thus the desired via-points. In this case, it is possible to implement a procedure for modifying the reference signal in order to guarantee that the interpolation error at

197
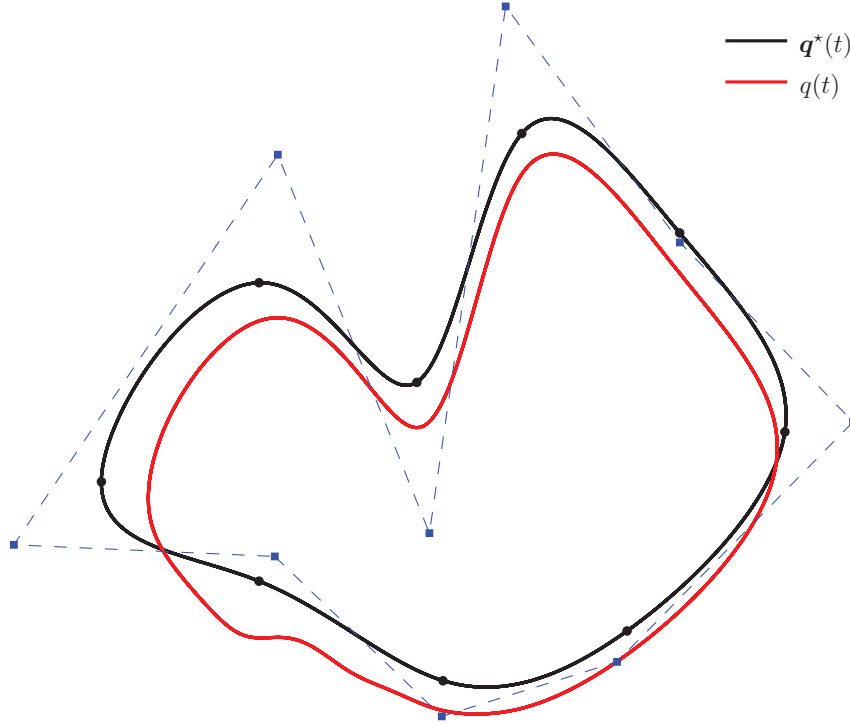
Figure 6-8: Two-dimensional B-spline trajectory interpolating a set of via-points $\boldsymbol{q}_j^\star$.

the given via-points $\boldsymbol{q}_j^\star$ asymptotically vanishes as highlighted in fig. 6-9.

The scheme of fig. 6-7 shows the mechanism for B-spline modification based on the RC approach. In this scheme, both the trajectory generator and the plant $G(z)$ are inserted in a discrete-time control loop that, on the basis of the interpolation error $\tilde{\boldsymbol{q}}_j = \boldsymbol{q}_j^\star - \boldsymbol{q}_j$, modifies in real-time the control points sequence (denoted by $\boldsymbol{p}_j^r$) from the initial value $\boldsymbol{p}_j^\star$. It is a typical dual rate system with the feedback loop running at a sampling time T considerably higher than the period T_s of the trajectory generator and of the controlled plant $G(z)$.

The sequence $\tilde{\boldsymbol{p}}_j$ multiplied by the constant K_p, assumed to be equal to one, and properly delayed in time is provided to the filter

$$\frac{1}{1 + z^{-n}} \tag{6.8}$$

used to compute the reference sequence of points $\boldsymbol{p}_j^r$ for the discrete-time interpolator based on B-splines and the controlled plant. Note that the initial value of the output
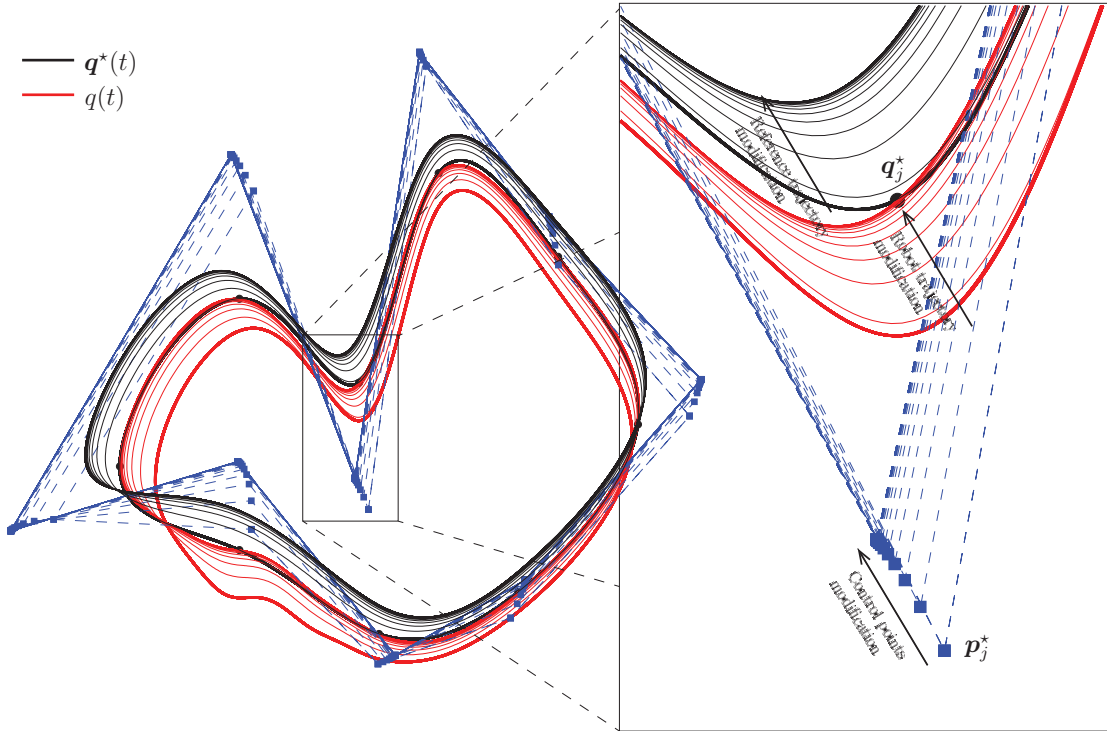
Figure 6-9: Two-dimensional B-spline trajectory interpolating a set of via-points $\boldsymbol{q}_j^\star$.

of filter in (6.8) has been set to $\boldsymbol{p}_j^\star$, that is the sequence of the control points defining the ideal trajectory.

Theorem 1. *The control scheme of fig. 6-7, subject to periodic disturbances, guarantees that the interpolation error $\tilde{\boldsymbol{q}}_j = \boldsymbol{q}_j^\star - \boldsymbol{q}_j$ between the desired via-points and the plant output at time $t_j = jT = kNT_s$ asymptotically converges to zero provided that the plant $G(z)$ meets the trajectory tracking condition (6.7).*

Proof. According to the theory of discrete-time repetitive control [105], that exploits the internal model principle [35], the presence in the control loop of the transfer function (6.8) assures asymptotic perfect tracking of a periodic signal with period n (in this case the sequence of desired via points $\boldsymbol{q}_j^\star$) if the stability of the whole system is assured.

Because of the structure of the control scheme, the stability analysis of the system at the slow sampling rate (T) can be deduced by neutralizing the effects of up-sampler and down-sampler. By considering the cascade of the filter $H(z)$ and of the system

with period T_s composed by plant and trajectory generator, as shown in fig. 6-10(a), it is possible to simplify the scheme by means of some formal manipulations:

- Since the controlled plant $G(z)$ is supposed to have a standard low-pass structure, in a worst case perspective, in lieu of the transfer function $G(z)$ the (constant) complex number

$$G_{\mathrm{wc}} = \max_{\omega \leq \omega_0} |G(e^{j\omega T_s})| \; \mathrm{e}^{\displaystyle j \min_{\omega \leq \omega_0}\{\arg G(e^{j\omega T_s})\}}$$

  can be considered in order to take into account the maximum gain variation and the maximum (negative) phase displacement caused by $G(z)$. The use of the B-spline filter allows to restrict the range of variation of ω to the interval $[0, \omega_0]$ because, as already noted, the reference signal for the plant can be considered null outside this interval. In this way, the block describing the plant and the down-sampler can be exchanged, as shown in fig. 6-10(b).

- the filter $H(z)$ which approximates the relation between via-points $\boldsymbol{q}_j^{\star}$ and control points $\hat{\boldsymbol{p}}_j^{\star}$ is followed by the B-Spline generator which, fed by the control points $\hat{\boldsymbol{p}}_j^{\star}$, provides at knots jT the desired via-points $\hat{\boldsymbol{q}}_{j-m}^{\star}$ delayed of mT instants[1]. As consequence this cascade can be reduced to a simple time-delay z^{-m}, as shown in fig. 6-10(c).

Finally, the scheme of fig. 6-7 can be reduced to the one shown in fig. 6-11, that runs with a sampling period T. It is a quite standard repetitive control scheme whose stability can be inferred by analyzing its characteristic equation

$$1 + \frac{z^{-n}}{1 - z^{-n}} K_p\, G_{\mathrm{wc}} = 0. \tag{6.9}$$

By following the approach proposed in [102], it is possible to see that the asymptotic stability of (6.9) is equivalent to the stability of the feedback system with loop-transfer

---

[1]Note that $\hat{\boldsymbol{p}}_j^{\star}$, and consequently $\hat{\boldsymbol{q}}_{j-m}^{\star}$, is only an approximation of the real value $\boldsymbol{p}_j^{\star}$, because of the filter $H(z)$. However, the level of the approximation can be arbitrarily improved by assuming larger values of r. If the interpolation of n via-points with B-spline trajectory of degree p is considered, the optimal (highest) value of r is $r = n - m$, being $m = \frac{p+1}{2}$.
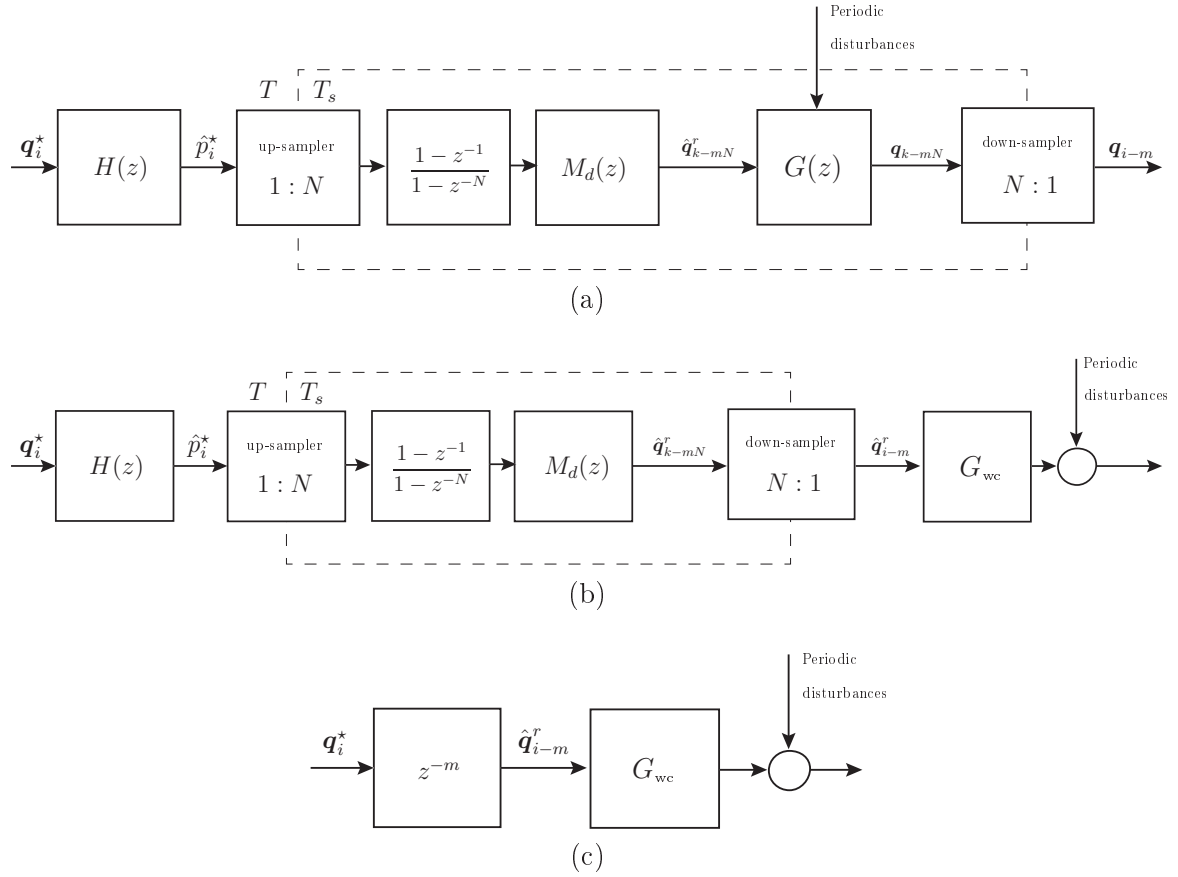
Figure 6-10: Model reduction of the discrete-time repetitive control scheme based on B-spline filter.

function

$$L(z) = z^{-n}(K_p G_{\mathrm{wc}} - 1).$$

Therefore, by applying the Nyquist criterion it descends that all the poles of (6.9) are within the unit circle if and only if the polar plot of $L(e^{j\omega T})$ for $-\frac{\pi}{T} \leq \omega \leq \frac{\pi}{T}$ does not encircle or touch the critical points -1. This can be assured by imposing that

$$||K_p G_{\mathrm{wc}} - 1|| < 1. \tag{6.10}$$

Being $K_p \leq 1$ (usually $K_p = 1$), the stability condition (6.10) holds if condition (6.7) is met (in this case $G_{\mathrm{wc}} \approx 1$). $\qquad \square$
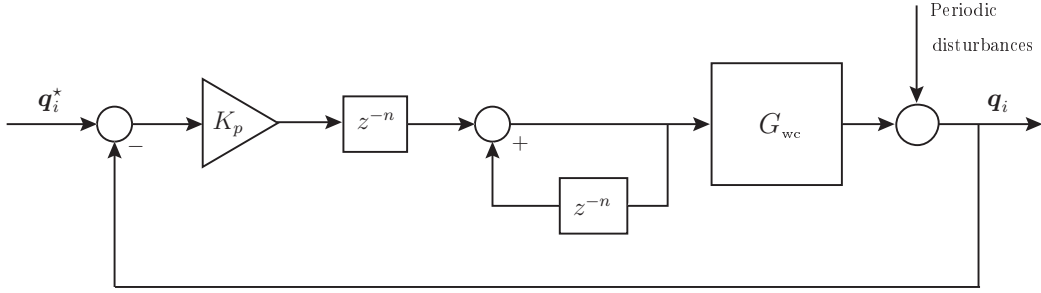
Figure 6-11: Discrete-time repetitive control scheme with sampling period T obtained from the dual-rate scheme of fig. 6-7 based on discrete-time B-spline filter.

Note that from (6.7) results

$$K_p < \frac{2\cos\left(\min_{\omega \leq \omega_0}\{\arg G(e^{j\omega T_s})\}\right)}{\max_{\omega \leq \omega_0}|G(e^{j\omega T_s})|}. \tag{6.11}$$

Thus, in case of ideal systems, the complex number $G_{\mathrm{wc}} = 1$ then suitable values for the gain are $K_p \in]0,2[$. As a matter of fact real plants doesn't assure null tracking error presenting static gain just close to unity, therefore one may consider $\max_{\omega \leq \omega_0}|G(e^{j\omega T_s})| < 1$, and then values $K_p > 2$ may be acceptable. In this case however, the argument of the plant plays a key role since it can be shown that for increasing values of the argument, the maximum value allowed for K_p decreases. At least for $\arg G(e^{j\omega T_s}) = \frac{\pi}{2}$, K_p collapses to zero therefore the system with RC becomes unstable.

6.4 Experimental analysis on a single actuator

In order to experimentally test the proposed method the setup of Fig. 6-12 has been arranged. This system reproduces the typical behavior of a robotic joint without the risk of structural damages even if instability conditions occur, and is the ideal tool for analyzing limits and performances of the proposed approach.

The test bed is characterized by two linear motors, LinMot PS01-37x120, rigidly connected along the axis of motion. Linear motor A is controlled by means of a position controller properly set up to track a desired periodic motion defined by a uniform B-spline trajectory. On the other side, the linear motor B, equipped with
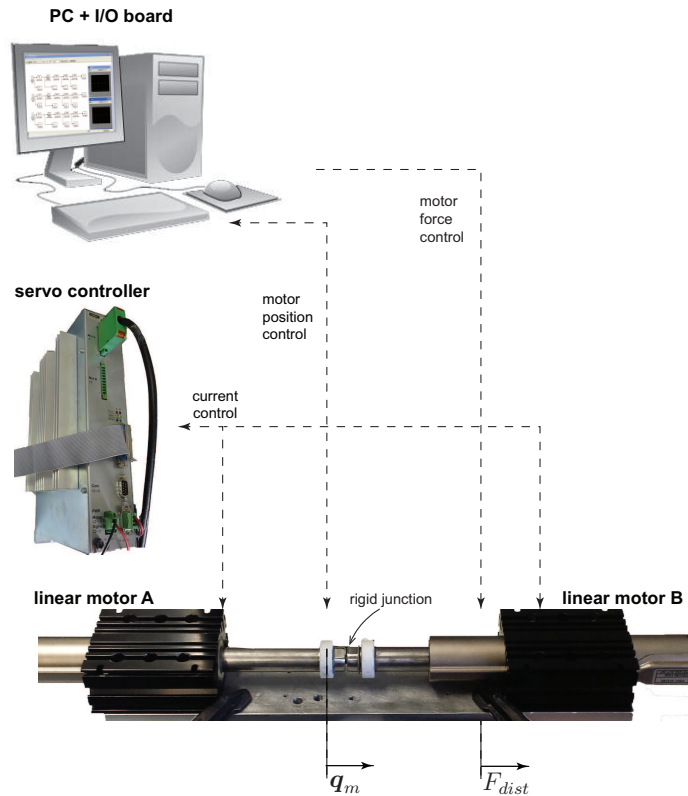
Figure 6-12: Experimental setup.

a force/current controller, is used to generate an external periodic disturbance that emulates a mechanical load connected to the actuator A or the inertial coupling that exists among different axes of a robot manipulator. In particular, in the experiments the simple relation

$$F_{dist} = -k\, q_m(t) - c\, \dot{q}_m(t)$$

that reproduces a spring-damper system has been assumed, with the parameters $k = 500$ [N m] and $c = 100$ [N m s^{-1}]. The control system is based on the servo controller LinMot E2010-VF that performs the basic current control, while the position control (based on a standard velocity/position cascade control scheme) and the force control have been implemented on a standard PC with a Pentium IV 3 GHz processor and 1 GB of RAM equipped with a Sensoray 626 data acquisition board, used to communicate with the servo controller. The position of the motor is measured by an incremental encoder with a resolution of $1\mu m$ integrated in the stator. The real-time operating system RTAI-Linux on a Debian SID distribution with Linux
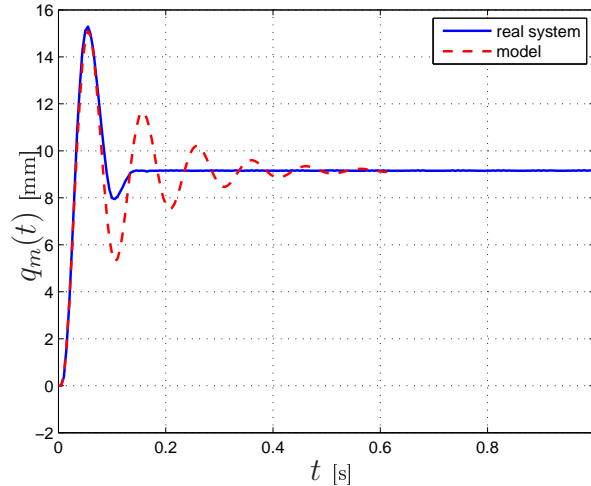
Figure 6-13: Response of the servo system of fig. 6-12 to a step input of amplitude 10mm.

kernel 2.6.17.11 and RTAI 3.4 allows the position controller to run with a sampling period $T_s = 500\mu s$. For the design of the control scheme and of trajectory generator, the MatLab/Simulink/RealTime Workshop environment has been used.

In order to better highlight the behavior of the RC mechanism, the integral control term which is present in the position control loop of the actuator has been disabled. The response of the plant to a step input of amplitude 10 mm is shown in fig. 6-13 where it is compared with that of a model based on a second order system characterized by a static gain of 0.915 and a natural frequency $\omega_n = 63$ rad/s. Note that the real system is affected by not negligible nonlinear phenomena due to the very high level of static and coulomb friction.

In order to test the performances of the system with the RC scheme, a trajectory passing through $n = 20$ via-points is considered. Once that the shape of the B-spline trajectory and its control-points, which depend only on the given via-points, have been fixed, the only parameters of the trajectory generator that can be changed are the knot span T (and accordingly the total duration of the trajectory) and the order d of the spline. In fig. 6-14, the behavior of the system with and without RC modification of the trajectory is shown, along with the interpolation errors $\tilde{\boldsymbol{q}}_j$, for different values of the degree d. When the RC is not activated the tracking error,
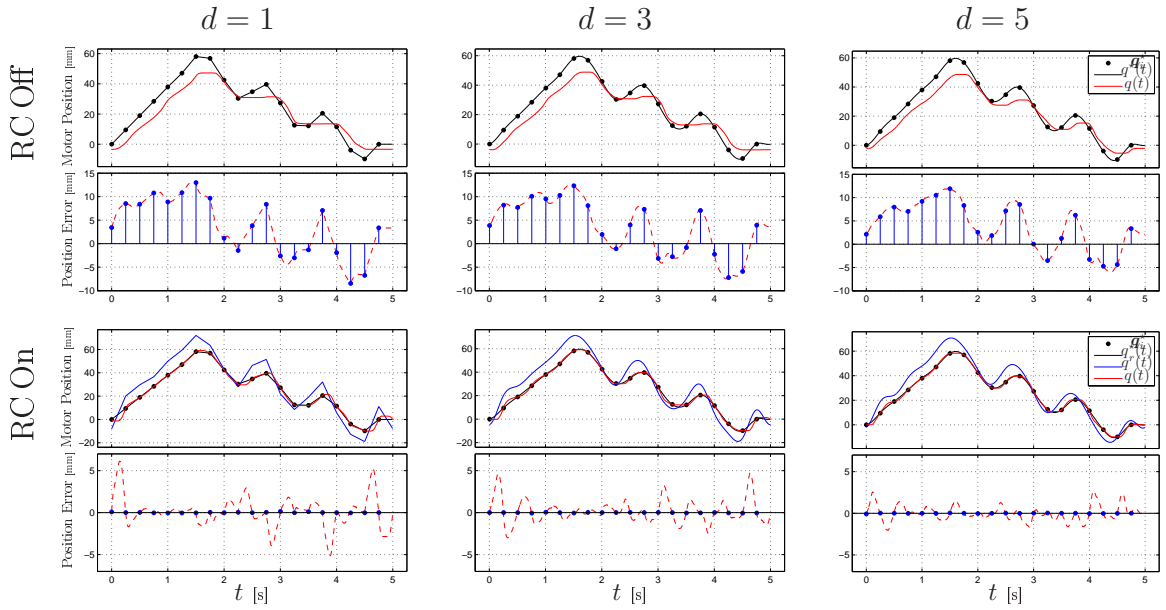
Figure 6-14: Reference trajectory and actual position of the motor A and related interpolation error $\tilde{\boldsymbol{q}}_j$ without and with RC mechanism as a function of d ($T = 0.25$ s).

intentionally quite large due to the noticeable external disturbance, seems to be not influenced by d. On the contrary, when the RC is activated (after 15 cycles), even if the interpolation error $\tilde{\boldsymbol{q}}_j$ at sampling time jT is negligible, during the inter-samples the tracking error is strongly affected by d. The same conclusions can be deduced from the results illustrated in fig. 6-15, where the tracking errors obtained with the RC for different values of T and d are shown. It has to be noted that in these experiments the gain K_p has been maintained equal to one, therefore the stability of the overall control system only depends on T, as stated in Section 6.3. In fact the system is stable until ω_0 is smaller than the cutoff frequency of the plant ($\omega_c \approx \omega_n = 63$ rad/s). But when $T = 0.05$ s and accordingly $\omega_0 = 125.6637$ rad/s overcomes ω_c the control system becomes unstable, independently of d. Also by analyzing fig. 6-15, it is clear that the amplitude of the inter-sample oscillation depends on d, and in particular it decreases as d grows. This appear reasonable, since practical experience suggests that smoother reference signals, represented by B-spline of higher degree d, are usually better tracked by physical plants.

Finally, the role played by the gain K_p has been investigated. As a matter of fact,
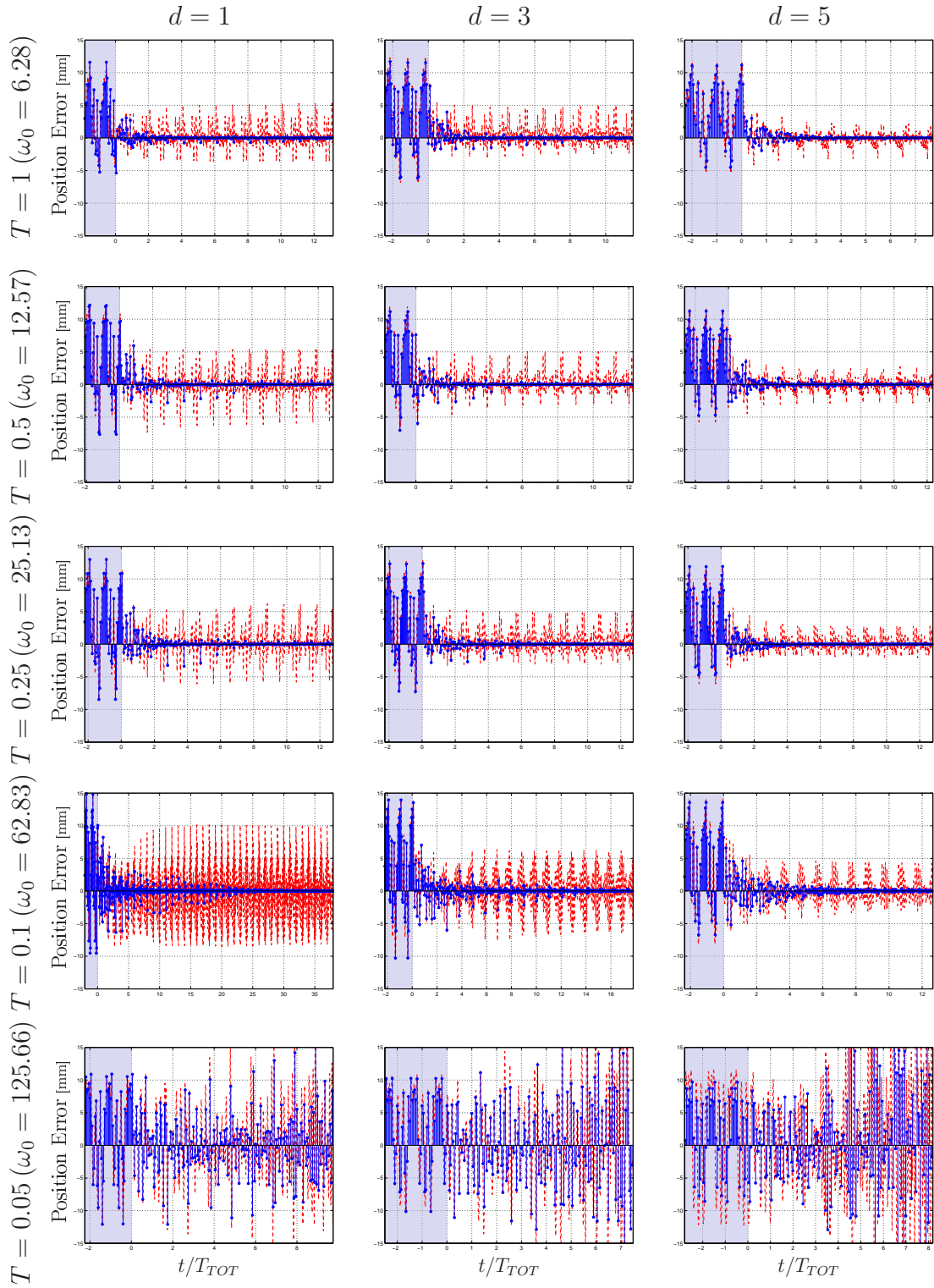
Figure 6-15: Interpolation error $\tilde{\boldsymbol{q}}_j$ at sampling instants jT as a function of d and T. On the x-axis, t/T_{TOT}, being $T_{TOT} = nT$ the total duration of the desired spline trajectory, represents the number of iterations.

206
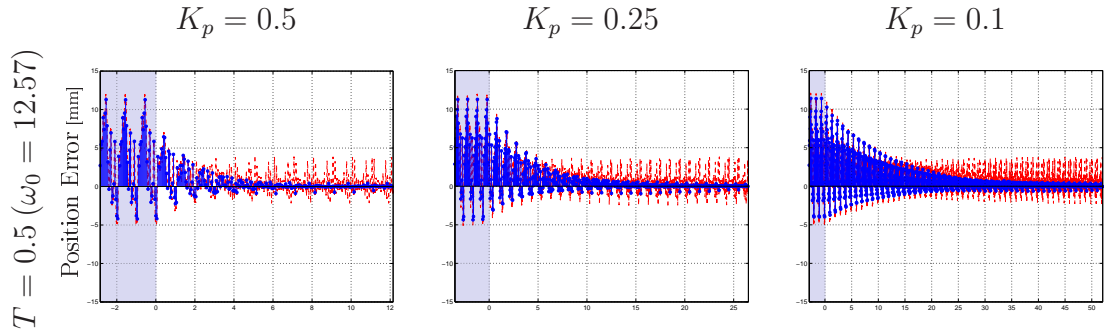
Figure 6-16: Interpolation error $\tilde{\boldsymbol{q}}_j$ at sampling instants jT as a function of K_p. On the x-axis, t/T_{TOT}, being $T_{TOT} = nT$ the total duration of the desired spline trajectory, represents the number of iterations.

despite the effect on the rate of convergency of the error $\tilde{\boldsymbol{q}}_j$ which is visible in fig. 6-16, K_p has a role even on the stability of the system as stated in Section 6.3. In fig. 6-17 the experiments which denoted stable conditions in fig. 6-15 has been tested with different values of K_p, showing that the system remains stable even with $K_p = 2$. This can be explained by recalling that the static gain of the experimental system is 0.915, therefore $K_p = 2$ still verifies the stability condition in (6.10), while $K_p = 2.5$ leads to instability. On the contrary the case with $T = 0.05$, which was unstable with $K_p = 1$, can be stabilized only with very low values of K_p as reported in fig. 6-18.
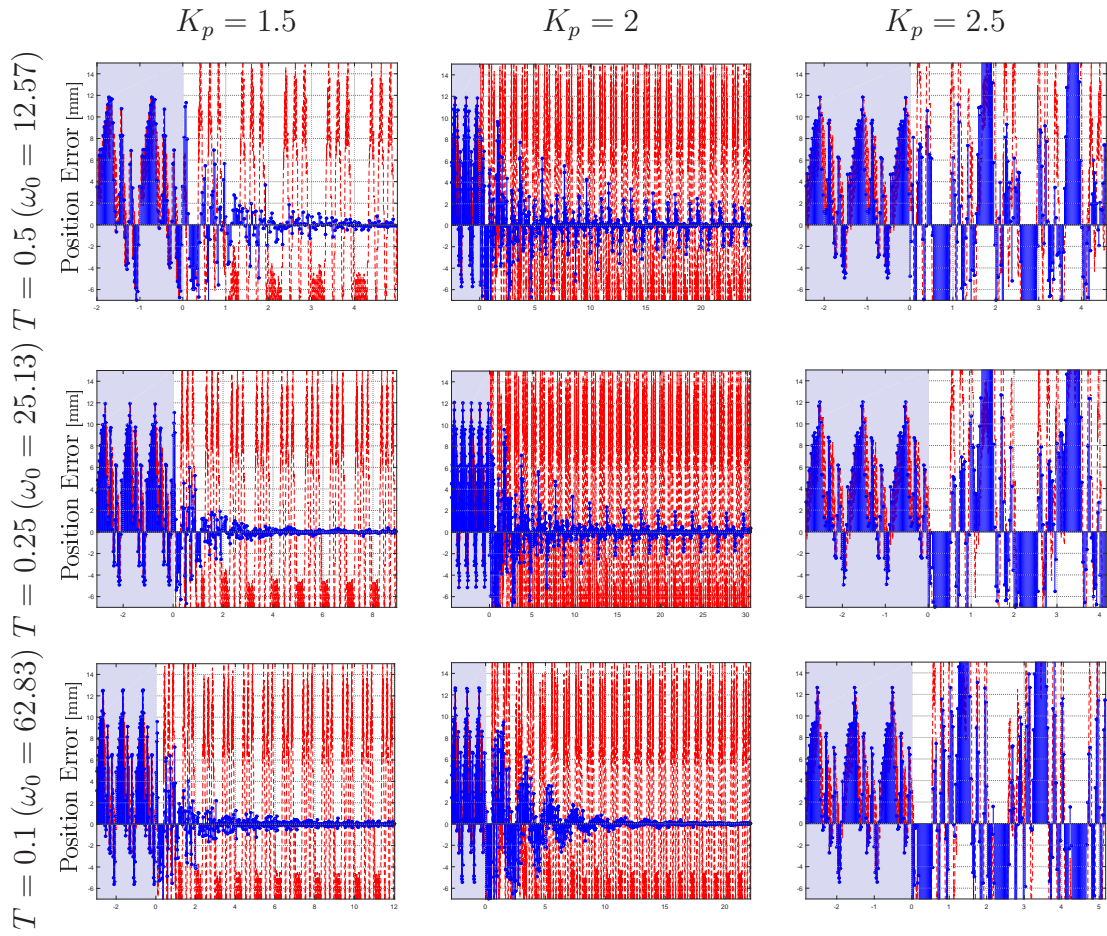
Figure 6-17: Interpolation error $\tilde{\boldsymbol{q}}_j$ at sampling instants jT as a function of K_p and T. On the x-axis, t/T_{TOT}, being $T_{TOT} = nT$ the total duration of the desired spline trajectory, represents the number of iterations.
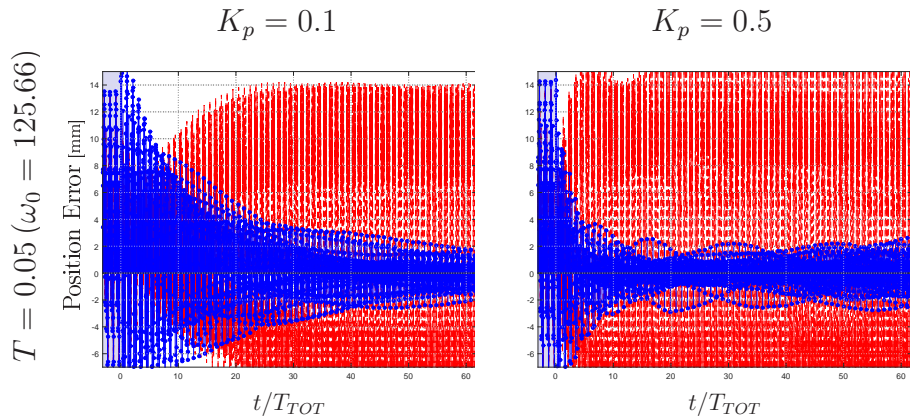
Figure 6-18: Interpolation error $\tilde{\boldsymbol{q}}_j$ at sampling instants jT as a function of K_p for system close to instability. On the x-axis, t/T_{TOT}, being $T_{TOT} = nT$ the total duration of the desired spline trajectory, represents the number of iterations.

6.5 Application of the RC scheme to a Comau Smart5 Six industrial manipulator

In a real scenario involving an industrial manipulator, like the Comau Smart5 Six, the proposed control can be used according two different schemes and purposes:

a) the iterative modification of the robot trajectories defined in the joint-space is obtained on the basis of the measurements provided by the proprioceptive sensors of the robot, i.e. motors encoders;

b) the robot trajectories are directly defined in the workspace and are modified on the basis of an external sensor that detect the position of the end-effector in the 3-D space, i.e. a RGB-D camera [38].

In the case a) the goal of the repetitive control is improving the robot precision by compensating the errors that the internal controller of the robot is not able to correct, while in case b) the external sensor allows the compensation of errors that are not sensed by the motors encoders, e.g. position errors due to the elasticity of the transmission chain.

6.5.1 Scenario a

In order to experimentally evaluate the proposed method the setup of Fig. 6-19 has been arranged. The system is composed of a COMAU Smart5 Six industrial robotic
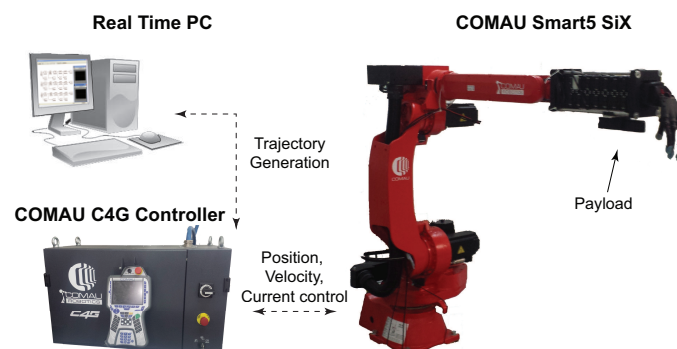
Figure 6-19: Experimental setup.

arm, a COMAU C4G Controller and a standard PC with an Intel Core 2 Duo 2.4 GHz processor and 1 GB of RAM. The COMAU Smart5 Six is a 6 DOF robot with anthropomorphic structure, with a payload of 6 Kg. The robot is driven by the COMAU C4G Controller that performs both the position/velocity control (adaptive control) and the power stage management with current control of each joint. The C4G Controller also implements a software option called "C4G OPEN" that allows the integration of the robot control unit with the external personal computer, in order to develop complex control systems at high hierarchical level. The C4G Open architecture is based on a real time communication on Ethernet network between the controller and the real time PC. In particular the PC runs on the real-time operating system RTAI-Linux on a Ubuntu NATTY distribution with Linux kernel 2.6.38.8 and RTAI 3.9 that allows the trajectory generator to run with a sampling period $T_s = 1ms$. For the design of the control scheme and of trajectory generator, the MatLab/Simulink RealTime Workshop environment has been used.
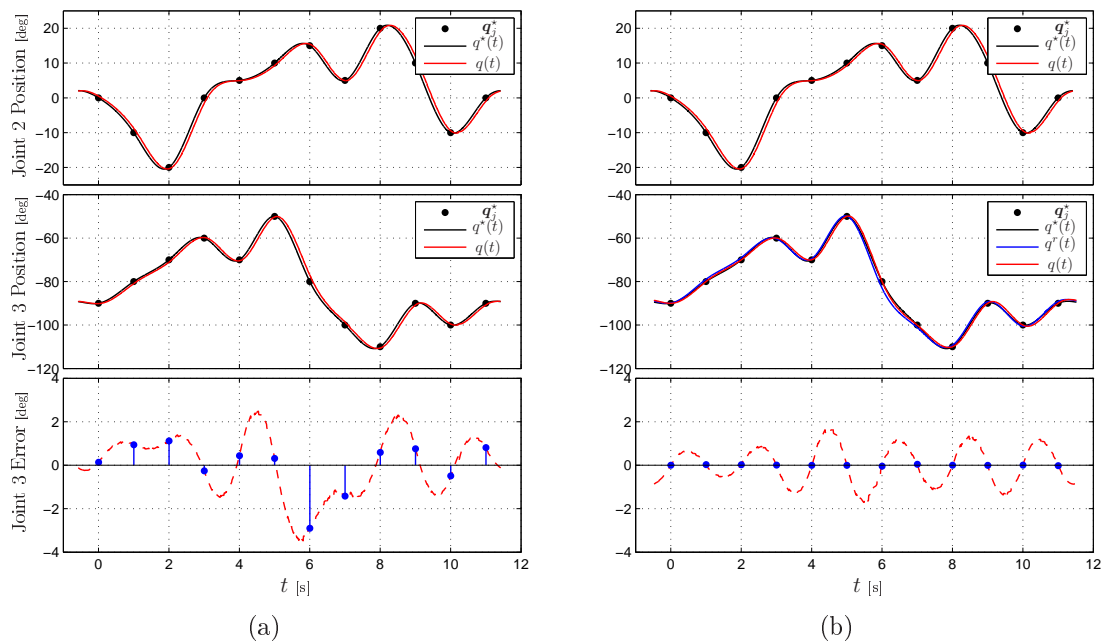
Figure 6-20: Tracking performance of the system due to the factory controller without RC (a) and with RC controller activated (b). In the middle, the modified reference trajectory $q^r(t)$ for the third joint is reported in blue, as a result of the implementation of the RC controller.
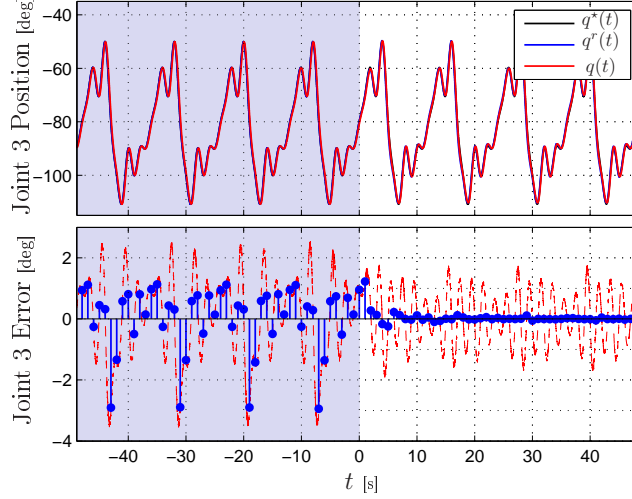
Figure 6-21: Response of the system at the activation of the Repetitive Control ($t = 0$). Errors at sampling instants T are highlighted in blue.

For sake of simplicity, the RC of Fig. 6-7 has been implemented on the third joint only, while the second joint has been actuated in order to disturb the third joint because of the dynamic coupling. Obviously, both joints are required to track two different cyclic spline trajectories with the same period. In particular, each trajectory interpolates 12 via-points $\boldsymbol{q}_i^\star$ with uniform knot span $T = 1s$. In Fig. 6-20(a) the performance of the system is shown. As can be seen, the third joint is affected by a quite evident tracking error, due to both the second joint movement and a 3 Kg payload represented by the UBHand IV robotic hand [64]. It is worth noting that the tracking error is relevant even in correspondence of the points $\boldsymbol{q}_i^\star$ that define the spline trajectory.

In Fig. 6-21 the tracking performance of the third joint is presented when the RC is switched on. It can be noted that the error decreases in overall terms, but mainly, in correspondence of the points $\boldsymbol{q}_i^\star$ the decay is drastic and occurs in a few cycles.

In Fig. 6-20(b) a detail of the trajectory tracking with RC (after 5 cycles) is shown: in this case the reference trajectory $q^r(t)$ is different from the theoretical spline $q^\star(t)$, as it is modified by the controller in order to suppress tracking error at instants T. By comparing Fig. 6-20(a) and Fig. 6-20(b) the reduction of the tracking error is evident, particularly in correspondence of the points $\boldsymbol{q}_i^\star$.

211
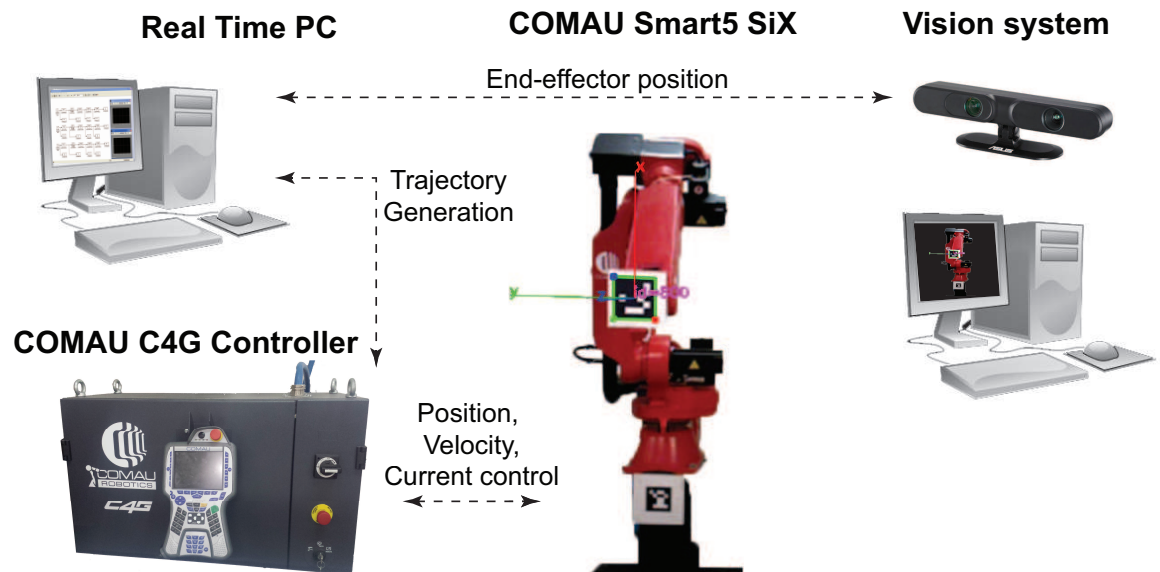
Figure 6-22: Experimental setup based on a Comau Robot with an external RGB-D sensor.

6.5.2 Scenario b

In a number of practical applications the motion of the robot is defined with respect to its workspace rather than to the joint space. In this case, cyclic motions could be affected by errors that come from either external loads or unmodeled dynamics. Sometimes also the kinematic inversion could be a source of errors due to parameters variation and numerical roundings. In this scenario, RC can be effectively used to nullify the position tracking error of the end-effector that is required to cross a number of via-points, usually used for defining complex motions. Furthermore, if a precise position measurement in the workspace is available, like a vision system, errors due to uncertainties on the displacement between robot and the surroundings can be cancelled.

In this experiment, the robot with the control architecture shown in fig. 6-22 has been equipped with an external sensor, that is a simple vision system, based on ASUS Xtion PRO Live RGB-D camera, which detects the position of a marker located at the robot end-effector. For the sake of simplicity, the desired path has been defined by means of 60 via-points $q_i^\star$ disposed on $y - z$ plane and the robot is moved with a fixed orientation. In fig. 6-23 the view of the camera, which is disposed in front of the
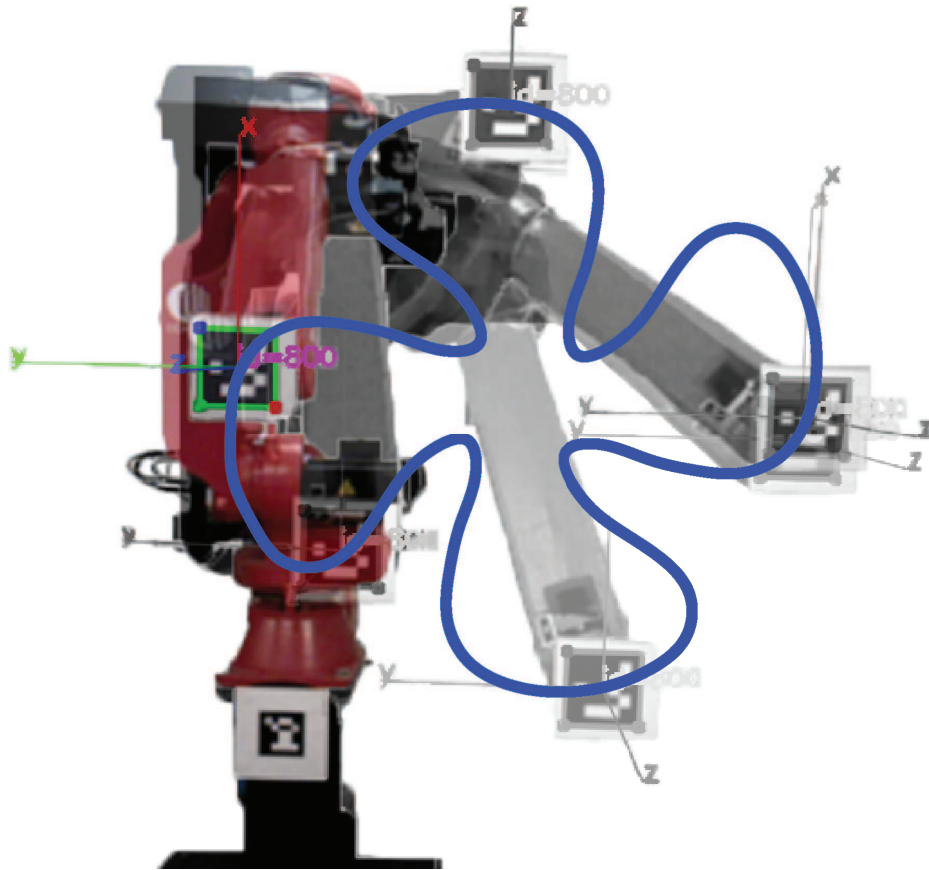
Figure 6-23: Overposed snapshots of the camera view of the comau. The desired trajectory is reported in blue.

robot, and the desired trajectory are reported. The image elaboration system runs on a dedicated standard desktop PC running Ubuntu Operating System and provides position of the marker with respect to the camera framework within a resolution of about 1 mm. Note that the precision of the camera, which is a low cost devices, is lower than the precision of the industrial robot (whose repeatability is 0.05 mm) but the proposed experiment is only a proof of concept aiming at demonstrating how real applications can benefit from the RC scheme. The desired trajectory is defined in the camera space and the (large) initial tracking error, shown in fig. 6-24(a) for the y-axis, is probably due to a misalignment between robot and camera and to a non-perfect calibration of the camera. In any case, whatever the cause of the tracking error is, the position feedback directly provided in the workspace is able to asymptotically cancel the error between via-points and end-effector position, as shown in fig. 6-24(b)

for the y-axis. In fig. 6-25 the workspace trajectory of the robot $q(t)$ along with the modified reference trajectory $q^r(t)$ are shown. The tracking error decay as a function of time is reported in fig. 6-26. Despite the noise, due to the position estimation with the camera, the repetitive control scheme is able to considerably reduce the errors between via-points and geometric path.

(a)   (b)
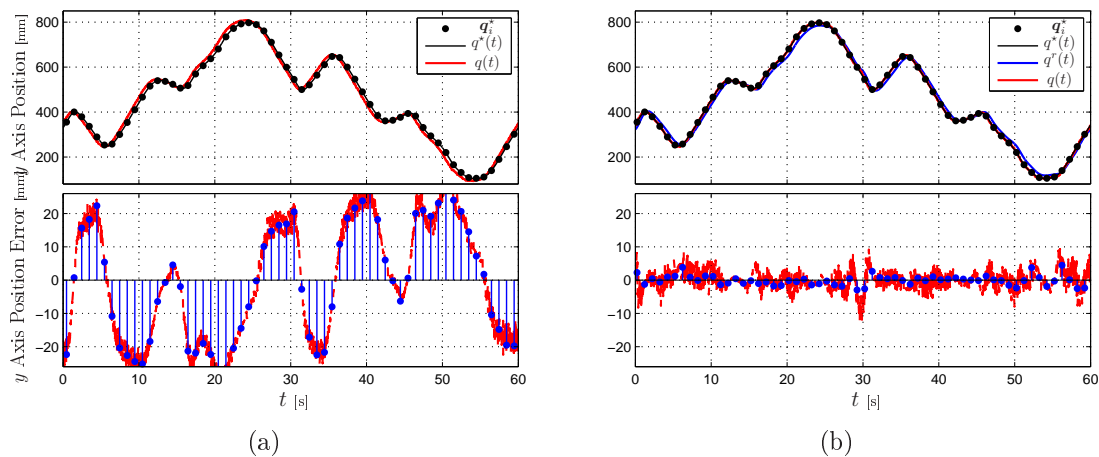
Figure 6-24: Tracking performance of the system due to the factory controller without RC (a) and with RC controller activated (b). In the middle, the modified reference trajectory $q^r(t)$ for the y coordinate is reported in blue, as a result of the implementation of the RC controller.
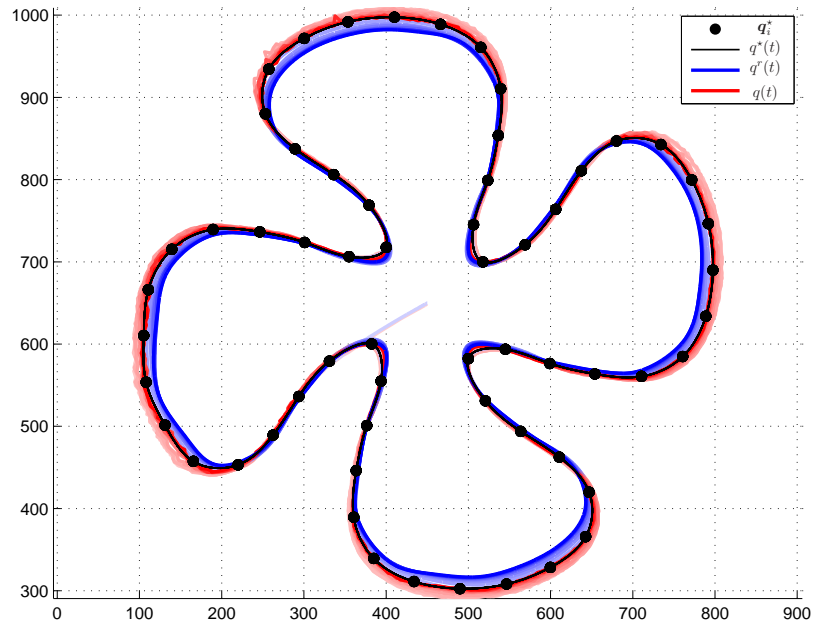
Figure 6-25: $y - z$ planar view of the tracking performance of the system with RC controller activated. The modified reference trajectory $q^r(t)$ is reported in blue, as a result of the implementation of the RC controller, while the actual trajectory of the end-effector is in red. Colors are reported with increasing intensity as the time goes on.
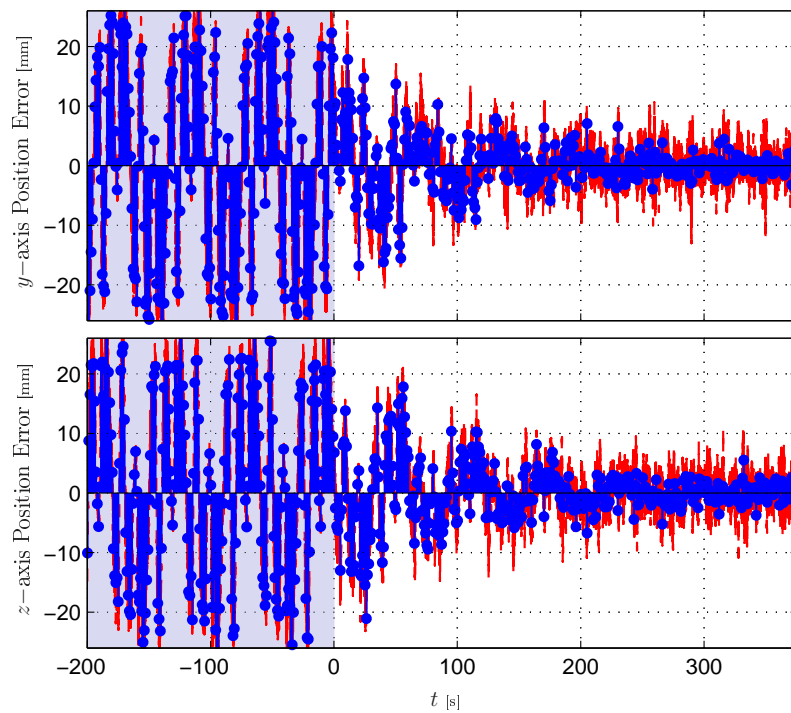
Figure 6-26: Error decay in the y and z directions after the activation of the RC mechanism ($t = 0$).

6.6   Conclusions

In [17, 16], motion planning and reactive control have been integrated in order to obtain a perfect tracking of a desired set of via-points. By considering tasks performed cyclically, which are quite common in the industrial and robotics field, a trajectory generation based on B-spline has been enhanced with a RC-type mechanism that modifies in real-time the control points defining the spline in order to nullify the tracking error at the desired points. The effectiveness of the proposed approach has been demonstrated both analytically and experimentally. In particular, tests performed on an industrial manipulator have shown that this scheme can be used to enhance the performance of the original position controller of the robot. Finally, the proposed approach could be used to refine the computation of the control points for a given motion trajectory in order to compensate for cyclic disturbances that characterize the plant. After an initial "training" the modified control points $\boldsymbol{p}_i^r$ that take into account the dynamic behavior of the plant could be used without the adaptation mechanism in lieu of the theoretical values $\boldsymbol{p}_i^\star$.

Chapter 7

Conclusions

In this thesis the most widely used techniques for planning trajectories in industrial field have been revised in order to meet specific dynamic requirements of a given plant, and two novel trajectory generators based on dynamic filters have been developed and implemented.

In the first part of the thesis, besides the conventional description, all the mentioned methods have been deeply analyzed in terms of their respective transfer functions within a filter-based framework. As a matter of fact, traditional techniques for vibration suppression address the problem of residual vibrations under different points of view: input shapers are defined by means of the impulse response of the system (i.e. time domain), traditional filters relates to the frequency response of the system, techniques based on system inversion mainly focus on the transfer function of the modelled plant (i.e. poles/zeroes content) and analytic trajectory planning is usually performed in order to comply with kinematic constraints of the actuators, providing a certain level of smoothness.

As a result it has been demonstrated how different techniques such as input shaping and analytic trajectory planning for example, are actually closely related if treated as dynamic filters. Therefore the design procedure of a trajectory planner for vibration reduction can benefit from a unified framework, which allows to properly compare and chose the optimal solution for any need. In particular the analysis performed in this thesis permits to uniquely characterize the two fundamental parameters for a

generic command shaper:

- **Effectiveness**, which is related to the ability of the considered method to perform a proper cancellation of the pair of complex conjugate poles which cause the vibrations, under nominal conditions of the characteristic parameters of the plant. Note that the possibility to cancel vibrations needs to be accompanied by a proper design techniques, that is a direct definition of the cancelling zeroes.

- **Robustness**, which is the effect of the given technique when a parameters mismatch occurs between modelled and real plant, and relates to the overall response of the filtering method in the proximity of the nominal conditions. In particular the robustness is affected by both the overall content in terms of those poles/zeroes which are not involved in the cancellation, and the eventual augmented multiplicity of the cancelling zeroes.

Moreover the description by means of dynamic filters allows to easily analyze each method using well known control systems techniques, in order to achieve significant features such as time delay, sensitivity and smoothness of the resulting trajectory.

In addition, the use of a common framework to describe various techniques allows not only to make bridges between those methods but also to merge valuable features. For example, in Chapter 4 commonly used trajectories defined by means of analytic functions and compliant to kinematic bounds have been described as filter chains. On the other hand the filter-based analysis applied on standard tools for vibration suppression, such as input shapers, led to define precise conditions for achieving vibration-free motion in Chapter 2. Then, techniques proposed in both Chapters 4 and 5 can be seen as methods for planning optimal trajectories which comply to hybrid constraints, that is both kinematics and dynamics.

With respect to analytic trajectory also, the use of dynamic filters results very convenient in terms of implementation and integration in more complex systems. In particular the repetitive control scheme proposed in Chapter 6 demonstrates that the

integration of widespread techniques for trajectory generation into a reactive feedback system for perfect tracking can be easily achieved thanks to the definition of an on-line trajectory generator based on discrete time filters.

Appendix A

Development of an Optoelectronic 6-axis Force/Torque Sensor for Robotic Applications

A.1 Introduction

Nowadays, one of the most challenging goals in robotics is the development of autonomous devices able to interact with dynamic environments and cooperate with humans in every-day life. Either in a domestic or an industrial environment, a robot must be able to sense what surrounds it in order to operate safely and autonomously. For this reason, robots are equipped with many sensors in order to achieve a reasonable autonomy level for performing several tasks in unstructured environments. In particular, the availability of Force/Torque (F/T) sensors is a common requirement in robotic systems designed for interacting with unknown environments and with humans, and are also useful for the manipulation of uncertain objects, allowing the online adaptability of the robot to the real characteristics and conditions of the object, environment or person.

Commercial F/T sensors are mostly based on strain-gauges. The motivation behind this fact can be ascribed to the reliability of this solution, to the wide literature
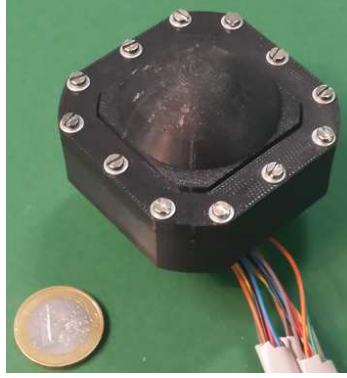
Figure A-1: A prototype of the optoelectronic 6-axis Force/Torque sensor.

about the optimization of this sensing principle [19, 98], to the relatively simple numerical methods for the estimation of strain in multi-axis F/T sensors [57] and to the large stiffness of the sensor that does not introduce destabilizing effects when applied on conventional industrial manipulators. As a consequence, this technological solution has been used in a wide number of different robotic applications, e.g. in [97] where a 4-axis strain-gauge sensor has been developed for measuring interaction forces in haptic devices or in [51] where a 6-axis F/T sensor has been embedded in an intelligent robotic foot.

Focusing on grasping and manipulation tasks, the sense of touch is essential to proper manipulation of objects. Indeed, the huge amount of work in tactile sensing literature is justified by the importance of having a proper sensing of the contact forces exerted during manipulations. A recent and complete review on tactile sensor technologies and features is reported e.g. in [26]. Despite this, a relatively limited number of commercial tactile sensors are currently available, mainly due to high manufacturing complexity and cost. Even if many different design solutions have been proposed and several physical transduction principles have been exploited, the design of reliable and accurate tactile sensors has proven to be very hard, then the use of F/T sensors as intrinsic tactile sensors [21] has been investigated because of the simplicity of the device (if compared to tactile sensors). In this scenario, the adoption of optical-based F/T sensors may introduce several advantages, as shown by the many different implementations proposed in literature. While strain-gauge based F/T sen-

sors measure the strain induced on the mechanical structure by the an external force and/or torque, optoelectronic sensors exploit the scattering or the reflection of a light beam emitted by a source and received by suitable detectors to directly measure the deformation of a compliant structure or the relative displacement between elastically coupled elements caused by the external force and/or torque. The applications of optoelectronic-based force sensors range from conventional mono-axial measurements, like in [73] where discrete optoelectronic components are used to measure the forces in a tendon based transmission system, to 6-axis F/T sensors, as in [56] where the authors adopt optoelectronic devices mounted on a compliant structure to measure human-robot interaction forces. The research carried out by Hirose and Yoneda [40] in the field of optical F/T sensors is particularly noticeable: they implemented an optical 6-axis F/T sensor adopting a 2-axis photosensor for measuring the deformation caused by the external load on a compliant structure. In the field of tactile sensors, a quite common optical technology is based on Fibre Bragg Gratings (FBG), exploiting the relationship between the variations of the FBG wavelength and the external force applied to the FBG [39]. Other optoelectronic solutions are based on CCD or CMOS camera to acquire the deformation of a surface caused by external force [46]. Both these solutions are quite expensive and introduce serious design problems if their integration in complex robotic structures like anthropomorphic hands and robotic arms is considered. In [31] and [36] the light beam of a Light Emitting Diode (LED) is scattered by a silicon dome and a urethane foam cavity respectively: the compression of the dome or the cavity due to applying an external force, causes a scattered energy density variation that is detected by several PhotoDetectors (PDs). In [29] another interesting example of optical tactile sensors based on a matrix of LED/PD couples covered by a deformable elastic layer can be found. This sensor exploits both the cavity scattering principle mentioned before and taxel-based reconstruction typical of CMOS sensors. In [101] an example of tactile/force sensor exploiting the reflection of the light cone emitted by an LED on a silicon rubber dome is reported. The measuring principle of this sensor is based on the measurement of the radiation intensity spatial distribution variation after the light reflection on the deformable dome above

223

the optical components caused by the deformation of the dome itself under the effect of the external contact force.

The main advantages of optical F/T sensors with respect to the ones based on strain-gauges are: the easier assembly procedure; the adaptability to mechanical structures characterized by limited stiffness; the simpler conditioning electronics; the intrinsic robustness with respect to electromagnetic noise; the possibility of integrating a large number of sensing elements on the same device, e.g. in CCD and CMOS sensors; the reduced cost of the sensing devices. On the other hand, strain-gauge based F/T sensors ensure better reliability and sensitivity.

In [72] is reported the development of a 6-axis F/T sensor [1] based on the optical reflection concept mentioned above. Due to the already mentioned advantages, this solution allows to obtain an easily scalable and low-cost F/T sensor, suitable also to be used as an intrinsic tactile sensor. Moreover, because of the adoption of optical components, the proposed sensor requires an extremely simple conditioning electronics. Finally, with a proper exploitation of the light reflection, the sensor design can be significantly simplified since all the required electronic components can be allocated in a single Printed Circuit Board (PCB), making it easier the sensor integration into complex robotic structures such as robotic hands.

A.2   Sensor Concept and Mathematical Modeling

The basic working principle of the proposed sensor is based on the modulation of the current flowing through a PD caused by the power variation of the received light generated by an infrared source such as an LED. The light power modulation is mainly due to variations both of the angle of view and of the length of the optical path [50]. The sensor is composed by an LED, a certain number of PDs arranged on the same plane (mounted on the PCB) and a Reflective Surface (RS), e.g. a mirror, located above the PCB. The frame supporting the PCB and the one supporting the RS are mechanically connected by a compliant structure that allows the relative motion of

---

[1] Patented [63].
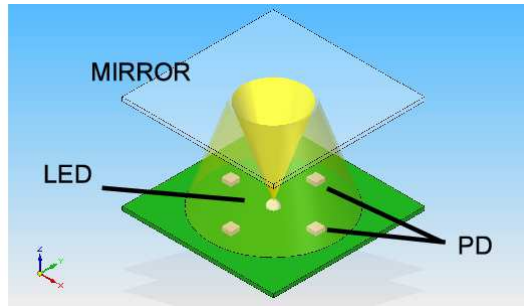
(a) Rest position.
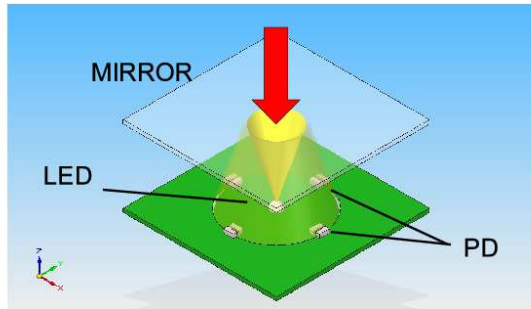
(b) Pure translation.
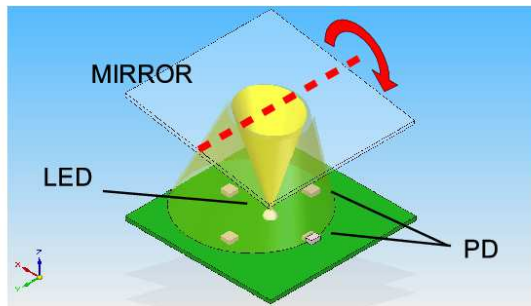
(c) Pure rotation.

Figure A-2: Reflection of an ideal light cone under the action of a moving mirror.

the RS with respect to the PCB under the effect of an external force. As seen in the case of tactile sensors, the applied force can be reconstructed by measuring the motion of the RS on which the light reflection or scattering occurs. In this case, the RS is not deformable as in [29], but it can move if an external force is applied thanks to a suitably designed compliant structure. Therefore, the basic idea is use the light intensity measured by the PDs to reconstruct the position and orientation of the RS and, as a consequence, the applied force and torque.

Figure A-2 reports a schematic view of the basic elements that compose the pro-
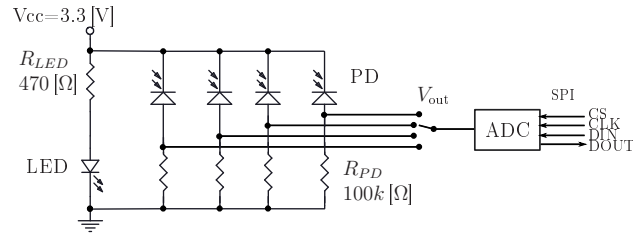
Figure A-3: Simplified measuring circuit of the PCB with one LED and four PDs.

posed sensor: one LED is mounted in the center of a square PCB, and 4 PDs are symmetrically arranged around the LED at a proper distance. In front of the PCB, a rigid RS deviates the light coming from the LED back to the PDs. The PCB with the optoelectronic components is fixed to a base frame, while the RS is connected to the base frame by means of a suspension system that allows the mirror to change its relative position and orientation with respect to the PCB. A schematic view of the reflected light behavior when basic movements (translation or rotation) are applied to the RS is shown in fig. A-2. From this figure it is possible to see that each basic RS movement causes a variation of both the light path length and the reflection angle. Since the light reflection is invariant with respect both to RS translations along directions tangent to the RS itself (up to the dimension of the RS) and rotations around the RS normal axis, it is clear that the device shown in fig. A-2 is sensible only to translations normal to the RS, and rotations around RS tangent axes. Then, three parameters describing the actual RS configuration (1 translation and two rotations) can be estimated by using a minimum number of three PDs. In our implementation, four PDs have been used to introduce a certain redundancy in the measure, fact that can improve the quality of the measure itself from the point of view of the precision and noise rejection, reducing also the issues related to the non-ideal component assembly. The PD photocurrents can be then simply measured by means of proper resistors and directly acquired by an Analog-to-Digital Converter (ADC) as shown in fig. A-3.

226
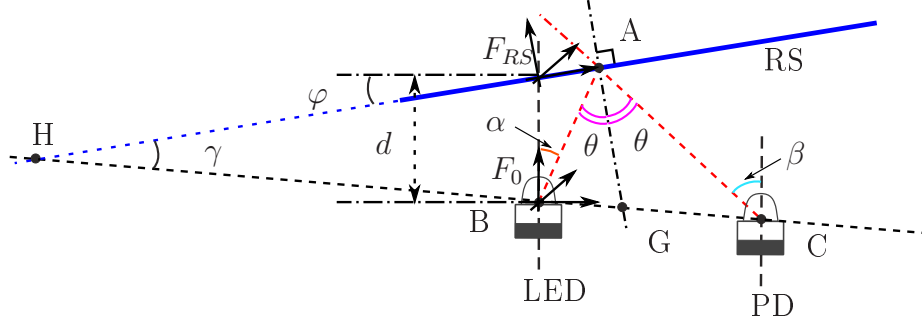
Figure A-4: Interaction between the optoelectronic components.

A.2.1 Theoretical Model of the LED-PD Interaction

With the aim of collecting useful information for the sensor design, a mathematical model describing how the light propagates from the LED to the PD under the action of the moving RS has been developed. To derive the theoretical model, let us firstly recall the basic working principle of the device by means of the simplified representation of a LED-PD interaction reported fig. A-4. In this scheme, the LED and the PD are supposed to be mounted on parallel planes, such that their optical axes are parallel and lie on the same plane. This assumption is made because in the practical implementation of the device, the optical axes of the optoelectronic components are normal to the PCB, but the height of the LED and the PD are different. In fig. A-4, α represents the angle between the LED optical axis and the segment denoting the light path, while β represents the angle between the PD optical axis and the light path. From this scheme, it is clear that α and β depend on the reflection angle θ, that in turn depends on the RS orientation φ and distance d. Moreover, also the length l of the light path changes with the RS orientation and distance. In this conditions, a certain amount of light emitted by the LED reaches the PD and it is proportionally converted into an electrical current, that considering the others as constant parameters, can be expressed as a function of α and β, i.e. $I_p(\alpha, \beta)$ (also referred to as photocurrent). When the RS orientation φ and its distance d experience a variation with respect to their initial values, the light path changes and a different amount of light power will be sensed by the PD, and then a photocurrent variation occurs. The radiant intensity pattern of the LED $\mathcal{L}(\cdot)$ and the responsivity pattern of the PD

227

$\mathcal{R}(\cdot)$ are available from the data-sheets of the components. According to the general theory on the interaction between the optoelectronic components [50], given the LED radiant intensity $\mathfrak{I}(I_{\text{LED}})$ as a function of the LED bias current I_{LED}, the radiant intensity pattern of the LED, evaluated in α (denoted as $\mathcal{L}(\alpha)$) and the responsivity pattern of the PD, evaluated in β (denoted as $\mathcal{R}(\beta)$, the intensity that irradiates the PD, $\mathfrak{I}_r$, is:

$$\mathfrak{I}_r = \mathfrak{I}(I_{\text{LED}}) \, \mathcal{L}(\alpha) \, \mathbb{R}\{R\} \, \mathcal{R}(\beta) \qquad [\text{mW/sr}] \tag{A.1}$$

where $\mathbb{R}\{R\}$ is the real part of the reflectivity R of the mirror, that is determined by the angle of incidence of the ray with respect to the normal of the mirror (θ in fig. A-4) and the complex refractive indices of air (n_1) and the RS (n_2):

$$R = (R_S + R_P)/2$$

$$R_S = \left| \frac{n_1 \cos(\theta) - n_2 \sqrt{1 - (\frac{n_1}{n_2} \sin(\theta))^2}}{n_1 \cos(\theta) + n_2 \sqrt{1 - (\frac{n_1}{n_2} \sin(\theta))^2}} \right|^2$$

$$R_P = \left| \frac{n_1 \sqrt{1 - (\frac{n_1}{n_2} \sin(\theta))^2} - n_2 \cos(\theta)}{n_1 \sqrt{1 - (\frac{n_1}{n_2} \sin(\theta))^2} + n_2 \cos(\theta)} \right|^2$$

The relation between the LED radiant intensity and current $\mathfrak{I}(I_{\text{LED}})$ can be derived from the component datasheet. As a simplifying assumption, we assume this relation is almost linear

$$\mathfrak{I}(I_{\text{LED}}) = K_{\text{LED}} \, I_{\text{LED}} \tag{A.2}$$

where K_{LED} is a proper constant (this assumption holds for the selected device in a wide range of the current I_{LED}). The problem is then to define the relation between, on one side, the orientation φ and the distance d of the RS and, on the other side, the angles α, β, θ and the light path length l. By simple geometrical relations it follows

that (a detailed analysis is reported in [72]):

$$\alpha = \text{acos}\frac{(\overline{BA})_z}{BA}, \ \beta = \text{acos}\frac{(\overline{CA})_z}{CA}, \tag{A.3}$$

$$\theta = \text{acos}\left(a_{RS}^T \overrightarrow{BA}\right), \ l = BA + CA \tag{A.4}$$

where a_{RS} is the unit vector orthogonal to the RS plane, the position of a point with respect to the origin of the reference system is denoted by capitol letter, e.g. A, $\overline{AB} = A - B$ denotes the segment connecting A and B, $AB = ||\overline{AB}||$ is the length of $\overline{AB}$, $\overrightarrow{AB} = \overline{AB}/AB$ is the unit vector denoting the direction of $\overline{AB}$ pointing from A to B and the subscript $_z$ denotes the z-coordinate of the relative vector.

The PD output photocurrent I_p is then computed as a function of the spectral flux density $\mathcal{E}_e$, that is the power incident on the PD surface (in mW/cm^2)

$$I_p = f(\mathcal{E}_e, V_{PD}) \tag{A.5}$$

where V_{PD} is the voltage drop across the PD and the function $f(\cdot, \cdot)$ is reported on the PD datasheet. Since in the proposed implementation the PD works far from the saturation region, eq. (A.5) can be approximated as

$$I_p = K_{\text{PD}} \mathcal{E}_e \tag{A.6}$$

where K_{PD} is a proper constant. It is worth noticing that while eq. (A.1) expresses the LED radiant intensity in mW/sr, in eq. (A.6) the light power density in mW/cm^2 is considered. This implies a conversion from the PD surface to the LED solid angle (i.e. the solid angle delimited by the cone with vertex in the LED center and as base the PD sensitive area), that involves the path length l. To perform this conversion, the PD sensible area is firstly supposed to be normal to the light path direction ($\overline{AC}$ segment) and with circular shape. Then, the radius r of the PD area, i.e. the solid angle aperture, is simply $r = \sqrt{\mathbf{A}_{PD}/\pi}$, where $\mathbf{A}_{PD}$ is the PD sensitive area, while the radius R of the sphere centered on the LED and containing the LED solid angle is $R = \sqrt{l^2 + r^2}$. The the LED solid angle ω can be then computed from the ratio

between the area $\mathbf{A}_z = 2\,\pi\,R(R-l)$ of the sphere portion bounded by the PD sensitive area and the whole sphere area

$$\omega = \frac{4\,\pi\,\mathbf{A}_z}{4\,\pi\,R^2} = \frac{8\,\pi^2\,R(R-l)}{4\,\pi\,R^2} = 2\,\pi\,\left(1 - \frac{1}{\sqrt{1+(r/l)^2}}\right) \qquad (\text{A.7})$$

The power incident on the PD surface can be then obtained from the LED radiant intensity

$$\mathcal{E}_e = \frac{\mathbf{A}_{PD}}{\omega}\mathfrak{I}_r \cos\beta \qquad [\text{mW/cm}^2] \qquad (\text{A.8})$$

where the term $\cos\beta$ takes into account the reduction of the PD area due to the angle between the light path direction and the PD surface itself. It is also implicitly assumed that the LED radiant intensity pattern $\mathcal{L}(\cdot)$ and the PD responsivity pattern $\mathcal{R}(\cdot)$ present constant values, corresponding to the ones evaluated in α and β respectively (i.e. along the light path ABC), within the solid angle ω. From (A.7) and (A.8) it can be noted that the light power $\mathcal{E}_e$ incident on the PD is related to the light path length l by an inverse-square relation. Finally, the photocurrent I_p can be simply measured by means of a resistor, as shown in fig. A-3, converting the photocurrent into an output voltage, the ADC then converts it into a digital signal that is transmitted through the digital bus.

Summarizing, the mathematical model of the LED-PD interaction is described by eq. (A.1), (A.3), (A.6) and (A.8). The numerical evaluation of this model has been developed taking as basic components an infrared LED with a narrow viewing angle and with a typical peak wavelength of 860 nm (Osram SFH4451), and as PD a silicon NPN phototransistor (Osram SFH3010) with a maximum peak sensitivity at 860 nm wavelength. The LED radiant intensity pattern $\mathcal{L}(\cdot)$ and the PD responsivity pattern $\mathcal{R}(\cdot)$ have been derived by cubic interpolation of a suitable point set taken from the datasheet of the devices, while the parameters of the selected optoelectronic components are reported in Tab. I. Considering a LED-PD couple arranged on a printed circuit board at a distance of 6 mm, fig. A-5 reports the PD output voltage for different values of the distance and orientation of the RS. The plot reports a limited range of d and φ variations because to reduce at most as possible the overall
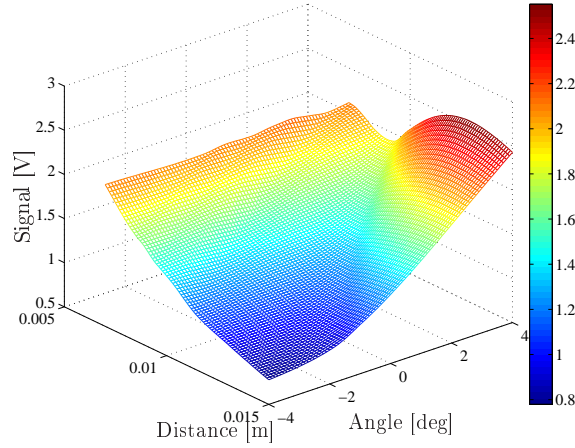
Figure A-5: Theoretical Output voltage as a function of angle and distance of the RS.

device dimensions, these parameters should be as small as possible. This figure shows a quite complex behavior of the PD output voltage modulated by the RS motion. Indeed, it is clear from the previous analysis that the RS distance and orientation affects the angles α, β, θ and the light path length l in a quite complex and non-linear way. The selection of a LED with narrow viewing angle avoids that the PD is illuminated by direct light from the LED (without being reflected first). Moreover, a narrow viewing angle is crucial to boost the effect of the α and β variations on the output voltage, providing a good sensitivity also on very small angular and linear displacements, as shown in fig. A-5. Moreover, due to the amplitude of the output voltage variation, this signal can be directly digitalized without introducing any signal amplifier, allowing a significant simplification of the sensor conditioning electronics.

Table I
LED and PD Parameters.

Description	Symbol	Value	Unit
PD Sensitive Area	$\mathbf{A}_{PD}$	0.04	mm^2
PD Sensitivity	K_{PD}	280	μA cm^2 mW^{-1}
LED Radiant Intensity	K_{LED}	600	mW sr^{-1} A^{-1}

(a) Model vs. Experiment comparison.

(b) Relative Model Error.
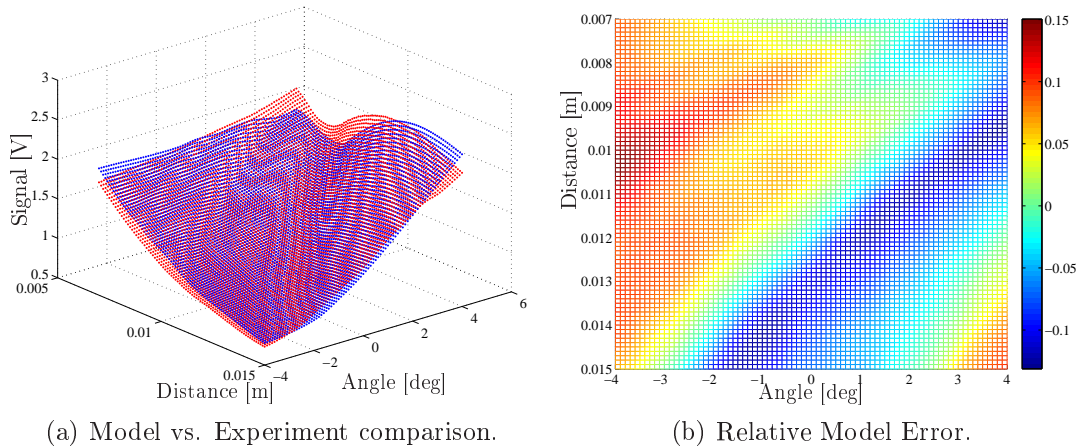
Figure A-6: Comparison between the theoretical model (blue) and experimental data (red).

A.2.2 Theoretical Model Validation

The results of the model presented in the previous section have been compared with experimental data acquired from a purposely developed setup, in which the position of the RS (both translations and rotations) with respect to the optoelectronic components can be accurately measured. Some of the results are shown in fig. A-6.

The experimental setup is composed by three linear motors LinMot P01-23Sx80 (see fig. A-7) driven by two servo controllers LinMot E210-VF (each servo controller can drive up to two linear motors). The control system is based on a standard PC with Pentium IV 3GHz processor, equipped with a Sensoray 626 data acquisition board used both to communicate with the servo controllers and to acquire the PD output signal. Each motor is provided with an integrated linear position encoder with a resolution of $1\,\mu$m. The RTAI-Linux realtime operating system has been used for controlling the system, while the MatLab/Simulink/RealTime Workshop environment has been used for the development of the control scheme and as user interface. The linear motors are driven by a low-level control system that allows precise regulation of the motor slider positions compensating for the friction, motor cogging and external disturbance forces [68]. Figure A-7(a) shows the top view of this experimental setup, in which the upper cover has been removed to allows a better vision of the internal structure, whereas fig. A-7(b) provides a better view of the

232

(a) Top view of the experimental setup. (b) Lateral view of the experimental setup.
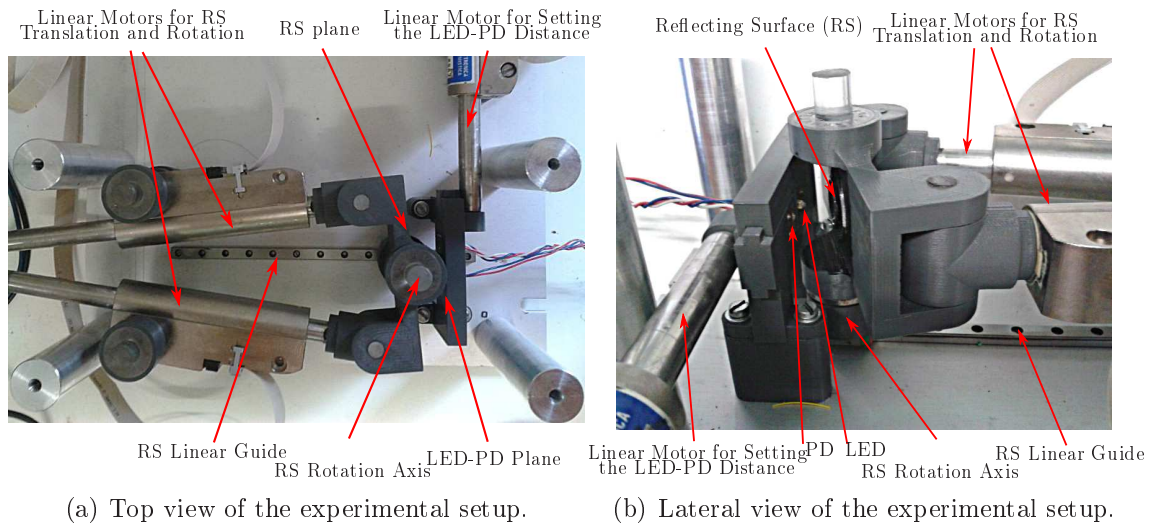
Figure A-7: Experimental setup (without upper cover) for the validation of the LED-PD theoretical interaction model.

LED, PD and RS arrangement. In this experimental setup, the RS is mounted on a planar element (RS plane) that can slide along a linear guide aligned with the LED optical axis, moreover the rotation of the RS plane along an axis orthogonal to the linear guide is allowed. The RS is moved by two linear motors, and its linear and angular displacements are reconstructed by means of the linear motor integrated encoders. The LED is mounted on a fixed element, while the PD is mounted on a sliding element whose position is controlled by the third linear motor. This allows to evaluate also the theoretical model for different values of the LED-PD distance, but for the sake of brevity the discussion reported in this paper is restricted to the case of minimum LED-PD distance compatible with the device implementation (3 mm) for achieving the minimum overall device dimension. As shown in fig. A-6(b) where the colormap representation of the relative error is reported, the maximum error between the model and the experimental data is about 10% over the whole range under investigation. Anyway, these results are quite satisfactory since they allow to investigate in advance, by exploiting the developed theoretical model described in Section A.2.1, the design and the characteristics of the device taking into consideration the optoelectronic component parameters, their arrangement and the RS range of motion. In fig. A-8 the combined output voltage sensitivity (normalized within the
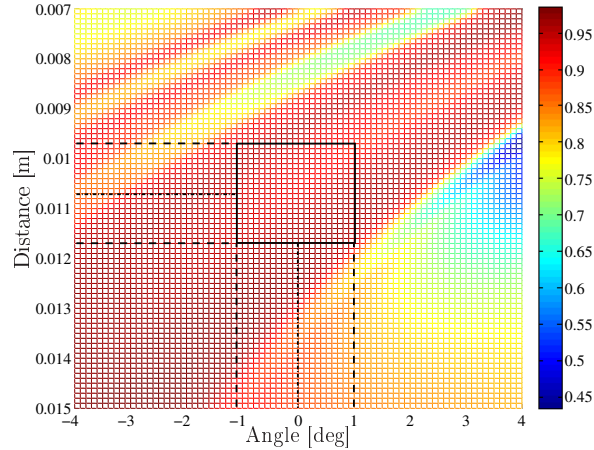
Figure A-8: Evaluation of the normalized output voltage combined sensitivity with respect to both linear and angular RS displacement.

range [0, 1]) with respect to both the linear and angular RS displacement is reported: the higher the combined sensitivity is, the higher is the output voltage variation in case of both the linear and angular RS motions, while a lower combined sensitivity means that the output voltage is less sensitive with respect to that motions or is sensitive to one motion type only (linear or angular). For symmetry reasons, and since more than one PD will be mounted on the same PCB, we are interested in the investigation of an angular working range centered on 0 deg (the RS is parallel to the PCB in rest conditions), then fig. A-8 suggests the selection of a working range for the proposed device of [-1, +1] deg and [0.0097, 0.0117] mm, resulting in a distance between the RS and the LED center in rest conditions of 10.7 mm. In this working range, the output voltage combined sensitivity is almost homogeneous at the maximum value, as shown in fig. A-8, and the model error is also limited to about 5%, as reported in fig. A-6(b).

Aiming at measuring the distance and the orientation of the RS with respect to the LED-PD plane, the experimental setup shown in fig. A-7 has been modified as reported in the CAD drawing fig. A-9(a), where the element supporting the LED and the PD has been replaced with the one shown in fig. A-9(b) (the linear motor for adjusting the LED-PD distance is not used anymore). In this device two pairs of PDs are symmetrically arranged with respect to the LED, reproducing the LED-

234

(a) CAD of the experimental setup.

(b) Detail of the replaceable element with the LED-PD PCB and cover mask.
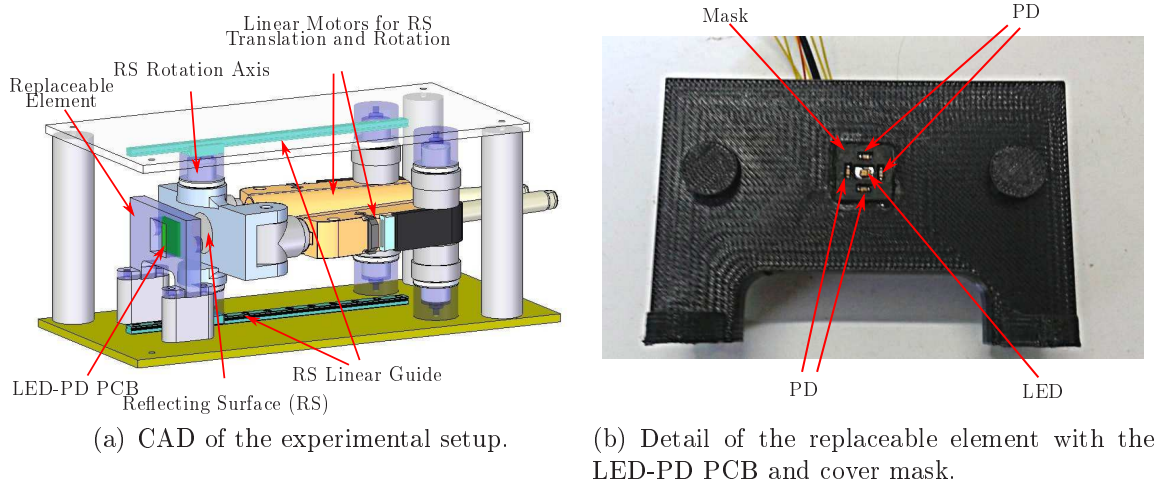
Figure A-9: Experimental setup for the evaluation of the RS distance and orientation.
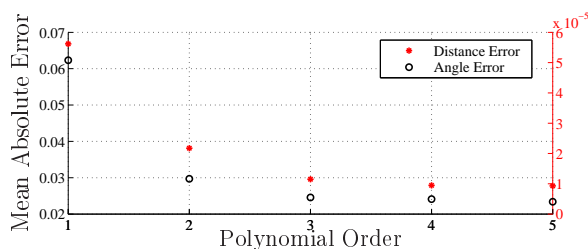
Figure A-10: Mean absolute error vs. Polynomial interpolation order.

PD arrangement shown in fig. A-2, and a mask for reducing the effects of spurious reflections on the PD output voltages has been mounted over the PCB. Since in the experimental setup the RS can be rotated along one axis only, the output voltages of only two PDs (over the available four) will be used for reconstructing the RS position and orientation. In particular, the output voltage of the two PDs arranged along the direction normal to the RS rotation axis are used for this purpose. Although the obtained characteristic is strongly nonlinear, it is interesting to investigate the usage of a polynomial map of the output characteristic, at least in a region surrounding the center of the working range (angle = 0 deg, distance 10.7 mm), for the reconstruction of the PDs and both the linear and angular RS displacements. This will allow the adoption of a quite simple estimation procedure for reconstructing the RS motion by means of the device output voltage. The mapping between the PD output voltages and the RS position and orientation is then achieved by the following polynomial

(a) Linear displacement. (b) Angular displacement.
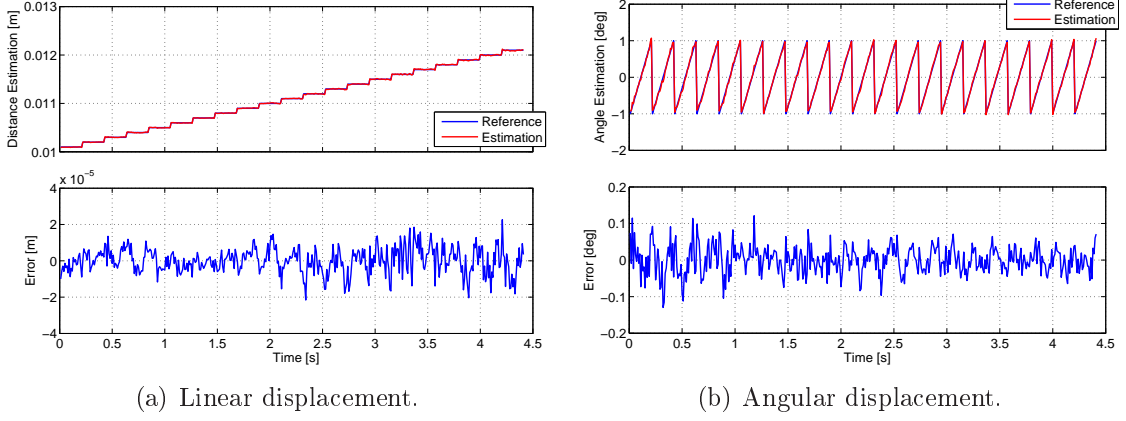
Figure A-11: Reconstruction of linear and angular displacement using a LED and two PDs.

interpolation:

$$\begin{bmatrix} d \\ \varphi \end{bmatrix} = M\,v \tag{A.9}$$

where

$$v = \begin{bmatrix} v_1^n & v_2^n & v_1^{n-1} & v_2^{n-1} & \cdots & v_1 & v_2 & 1 & 1 \end{bmatrix}^T$$

is the vector of the output voltages of the two PDs, v_1 and v_2 respectively, and the corresponding powers up to the order n (the two ones at the end of the vector are used to remove the output voltage offset), and M is the calibration matrix that can be derived from experiments as

$$M = \Lambda\,\Sigma^+ \tag{A.10}$$

where Σ^+ denotes the pseudoinverse of matrix Σ and

$$\Lambda = \begin{bmatrix} d_1 & d_2 & \cdots & d_i & \cdots & d_m \\ \varphi_1 & \varphi_2 & \cdots & \varphi_i & \cdots & \varphi_m \end{bmatrix}$$
$$\Sigma = \begin{bmatrix} v_1 & v_2 & \cdots & v_i & \cdots & v_m \end{bmatrix}$$

are the matrices of the m experimental measures of the RS position and orientation and of the PD output voltages. Figure A-10 reports the mean absolute error in the estimation of the RS position and orientation from the PD output voltages over the

236

whole set of experimental measures for different order of the polynomial map: it can be noted that no significant improvement is obtained with an order greater than three, then this order is selected as a valid trade-off between estimation error and computational complexity. The results reported in fig. A-11 show that, within the selected working range, this device allows to reconstruct the RS distance and the orientation with an estimation error less than the 10% of the measurement.

A.3   Sensor Prototype

The basic element for building up the proposed 6-axis F/T sensor is a PCB with a LED mounted in its center and four PDs symmetrically arranged around it on a circle of radius 3 mm. In the implemented device, the PCB is a 10×10 mm electronic board (1 cm^2). Furthermore, to measure forces and torques along the three axes with a proper redundancy, 3 of these basic elements have been placed on three faces of a cube. Despite three of these PCBs mounted on non parallel planes are sufficient to discriminate all the components of forces and torques along the 6-axis, this PCBs arrangement intuitively allows to achieve the maximum sensitivity and decoupling of the measurements.   A prototype of the sensor is shown in fig. A-12 and fig. A-13. Note that the geometry of the sensor and the placement of the PCB may vary depending on the specific application for which the sensor is designed. A specific mask with suitable hollows has been designed in order to avoid cross-disturbances (light reflections) between the three boards, as also detailed in fig. A-9(b). The relative motion of the RS with respect to the PCBs is achieved by means of a compliant frame, whose design is detailed in Section A.3.1, connecting the internal part of the sensor (where the PCBs are fixed) to the external contact surface, the cover (where the RSs are attached). The compliant frame deforms in an elastic way when a contact force is applied to the external contact surface. Note that, by a suitable design of these elastic elements, the sensor working ranges (in the force domain) can be freely adjusted according to the application requirements.   The conditioning electronics is extremely simple, as the circuit schematic in fig. A-3 shows. This aspect is quite
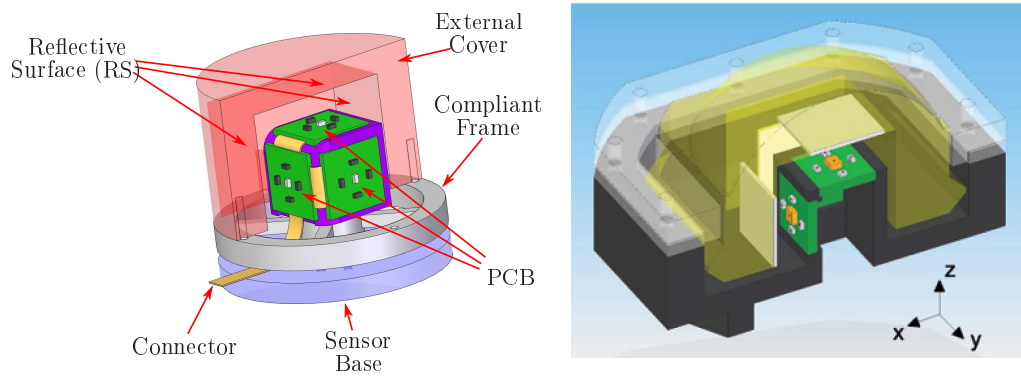
Figure A-12: Conceptual design of the sensor prototype.
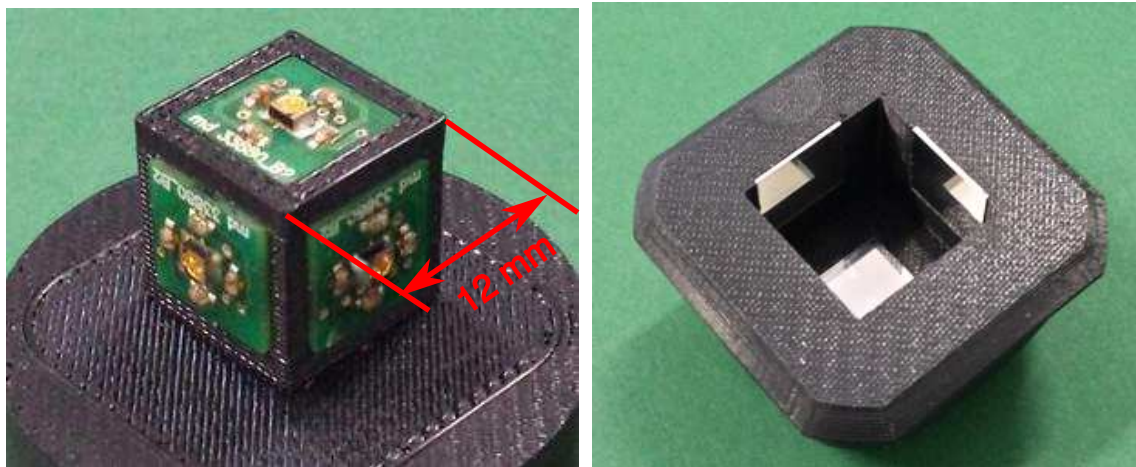
Figure A-13: Internal view of the sensor: the cube with the three PCBs and the cover with the RS.

important because it allows a simple integration of the sensor in mechanically complex structure, since the whole circuit in fig. A-3 can be implemented in the same PCB where the LED and the PDs are hosted. The three PCB shown in fig. A-13 are then connected through the SPI digital bus to a microcontroller board located into the sensor base that elaborates the PDs output signals to perform noise filtering and providing the force estimation on the base of the calibration data (the calibration procedure is described in Section A.4). The microcontroller is then able to transmit the estimated forces and torques via digital bus using different protocol and bus types: the CAN bus and CanOpen protocol have been adopted for the developed sensor prototype.

The external surface of the sensor, in this specific prototype, is a spherical cap

with radius $R = 44$ mm. This particular design has been developed since the sensor is going to be placed on the fingertips of an underwater three-fingered robot gripper, [8], and both the dimension and some of the design choices (e.g. the o-rings for water insulation as reported in A.5) derive from this specific application. In particular, the overall dimension of the sensor could be drastically reduced for other types of applications.

A.3.1   Compliant Frame Design

Figure A-14(a) shows the structure of the compliant frame used for connecting the contact surface, and then the RS rigidly connected to it, to the base frame of the sensor where the PCB with the LEDs and the PDs are located. In particular, the compliant frame is composed by an inner frame, rigidly connected to the sensor base, an outer frame connected to the contact surface and a set of flexible links (three in the specific case) that connect the inner and the outer frames. Suitable elements to limit the maximum deformation and to avoid damage to the deformable structure itself can also be added to the compliant frame, but this issue is not addressed here to simplify the discussion. It the following analysis, it is supposed that only the links are deformed by the effects of the external force, while both the inner and the outer frames are treated as rigid bodies. Moreover, all the links are considered equal (with the same physical dimension and material) to achieve a symmetric deformation of the compliant frame. Figure A-14(a) reports also the reference frame of the sensor base, of each link of compliant frame and the one of the contact surface.

According with the Timoshenko beam theory, the stiffness of each link can be

239

expressed as [75]

$$K_L = \begin{bmatrix} \frac{AE}{L} & 0 & 0 & 0 & 0 & 0 \\ 0 & \frac{12EI_z}{L^3} & 0 & 0 & 0 & \frac{6EI_z}{L^2} \\ 0 & 0 & \frac{12EI_y}{L^3} & 0 & -\frac{6EI_y}{L^2} & 0 \\ 0 & 0 & 0 & \frac{GJ}{L} & 0 & 0 \\ 0 & 0 & -\frac{6EI_y}{L^2} & 0 & \frac{4EI_y}{L} & 0 \\ 0 & \frac{6EI_z}{L^2} & 0 & 0 & 0 & \frac{4EI_z}{L} \end{bmatrix} \qquad (A.11)$$

where E and G are the modulus of elasticity (Young modulus) and the shear modulus respectively, that are equal for all the links, L, I_y, I_z, A and J are the length, the area moment of inertia about the y- and z-axis, the cross section area and the torsion constant (polar moment of inertia) of the i-th link respectively. The matrix K_L represents the stiffness of a 6-dimensional spring that allows to compute the force/torque vector $w = [f^T,\ m^T]^T$ generated at the link reference frame when the cross section in the yz-plane experiences a displacement $p = [\delta x^T, \delta\gamma^T]$ (translations and rotations) with respect to the other link end. To clarify the proposed analysis, it is important to introduce the dependence of the terms in eq. (A.11) from the physical dimensions of the links. fig. A-14 shows the simplified structure of a link together with the position of the reference frame used to define the link's stiffness matrix (A.11). With reference to fig. A-14(b), the particular geometry of the links allows the computation of the parameters appearing in (A.11) in a very straightforward way:

$$A = a\,b, \quad I_y = \frac{1}{12}\,a^3\,b, \quad I_z = \frac{1}{12}\,a\,b^3, \quad J = I_y + I_z$$

The subscript $_L$ means that this stiffness matrix is defined with respect to a reference frame attached at one link end and with the x-axis along the link length and the y- and z-axis normal to the lateral surface, as shown in fig. A-14(b). A suitable change of coordinates is used to represent the stiffness matrix of each link in the reference frame of the contact surface. It is supposed that the contact surface reference frame F_e is translated along the z-axis by p_z with respect to the base reference frame F_0, while
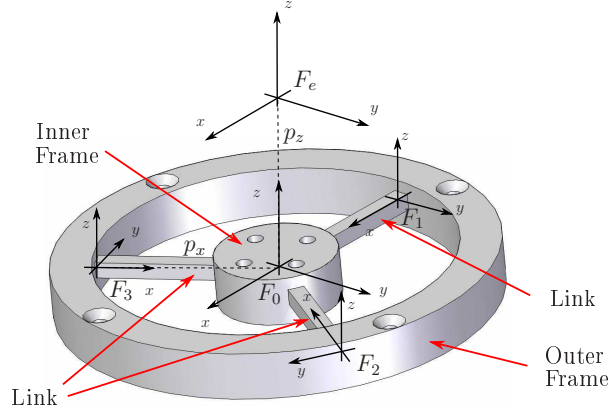
(a) Sketch of the compliant frame and related reference systems.
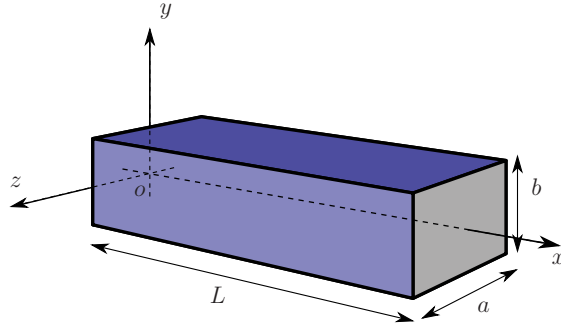
(b) 3D view of the link.

Figure A-14: Detailed view of the compliant frame and of the links.

the reference frame attached to each link F_i, $i = 1, \cdots, k$, where k is the number of links, are rotated along the z-axis by $\phi_i = -2\,(i-1)\pi/k$ and then translated along the x-axis by $-p_x$. So the homogeneous transformation matrix ${}^eT_0$ expressing the position of F_0 with respect to F_e is

$$
{}^eT_0 = \begin{bmatrix} 1 & 0 & 0 & 0 \\ 0 & 1 & 0 & 0 \\ 0 & 0 & 1 & -p_z \\ 0 & 0 & 0 & 1 \end{bmatrix}
\tag{A.12}
$$

while ${}^0T_i$ expressing the position of F_i with respect to F_0 is

$$
{}^0T_i = \begin{bmatrix} \cos\phi_i & -\sin\phi_i & 0 & -p_x \\ \sin\phi_i & \cos\phi_i & 0 & 0 \\ 0 & 0 & 1 & 0 \\ 0 & 0 & 0 & 1 \end{bmatrix}
\tag{A.13}
$$

It is important to say that this coordinate transformation is performed by means of the velocity transformation matrix ^eG_i and the force/torque transformation matrix $^eG_i^T$ [83]. Recalling the general form of homogeneous transformations

$$^bT_a = \begin{bmatrix} ^bR_a & ^ap_{ab} \\ 0 & 1 \end{bmatrix}, \quad ^ap_{ab} = \begin{bmatrix} p_x & p_y & p_z & 1 \end{bmatrix}^T,$$

$$^aP_{ab} = \begin{bmatrix} 0 & -p_z & p_y \\ p_z & 0 & -p_x \\ -p_y & p_x & 0 \end{bmatrix}$$

where ^bR_a and ^bp_a are respectively the rotation matrix and the origin translation between F_a and F_b, it results

$$^eG_i = \begin{bmatrix} ^eR_i & -^eR_i\,^iP_{ie} \\ 0 & ^eR_i \end{bmatrix}$$

Then the stiffness matrix K_e seen from the (external) contact surface can be computed as the sum of each link stiffness expressed in the frame F_e:

$$K_e = \sum_{i=1}^{k} {}^eG_i^T\, K_L\, {}^eG_i \tag{A.14}$$

In the same way, it is possible to define the compliance matrix as $C_e = K_e^{-1}$ that maps the force applied to the contact surface into its displacement.

The compliant frame design problem is now to select the link parameters a, b, L (within a suitable range compatible with the implementation of the device) and the the link number k in such a way to obtain the desired stiffness along the different directions according to the application requirements and taking into account the maximum displacement range discussed in Section A.2.2. The parameters of the compliant frame used in the experiments here reported can be found in Tab. II: note that these parameters have been selected to obtain a compliant frame with similar linear stiffness and similar torsional stiffness along all the directions for sensor testing purposed, but are not selected according to any particular applications.

Table II
Compliant frame parameters.

Description	Symbol	Value	Unit
ABS Young Modulus	E	2900	MPa
ABS Shear Modulus	G	1050	MPa
Link Thickness	a	1.5	mm
Link Width	b	4.8	mm
Link Length	L	16.5	mm
Link x-axis Offset	p_x	21.5	mm
Number of Links	k	4	
Surface z-axis Offset	p_z	20	mm

A.4 Calibration and Characterization

A.4.1 Sensor Calibration

The calibration procedure has been performed by using as reference sensor an ATI Gamma SI-130-10 F/T sensor. The developed sensor prototype has been mechanically connected to the reference ATI sensor in such a way that, apart form a suitable changes in the reference frame and in the point where the force is applied, the sensor are subject to the same forces and torques. Then a variable load in terms of both forces and torques has been applied to the sensor prototype and the data from both sensors have been acquired. As mentioned in Section A.2.2, being the compliant frame working within the elastic regime, it can be assumed that a linear function exists between the applied force/torque vector $w = [f^T, \ m^T]^T$ and RS displacement. Then, similarly to what is described is Section A.2.2, the mapping between the PD output voltages and the applied force and torque can be done by polynomial interpolation as

$$w = \mathbf{C} \, v \tag{A.15}$$

where

$$v = \begin{bmatrix} v_1^n & \cdots & v_{12}^n & \cdots & v_1 & \cdots & v_{12} & 1 & \cdots & 1 \end{bmatrix}^T$$

is the vector of the sensor output voltages (12 PD output voltages), and the corresponding powers up to the order n (the 12 ones at the end of the vector are used to

remove the output voltage offset), and $\mathbf{C}$ is the calibration matrix that can be derived from experiments as

$$\mathbf{C} = \Omega \, \Sigma^+ \tag{A.16}$$

where Σ^+ denotes the pseudoinverse of the matrix Σ and

$$\Omega = \left[\begin{array}{cccccc} w_1 & w_2 & \cdots & w_i & \cdots & w_m \end{array} \right]$$
$$\Sigma = \left[\begin{array}{cccccc} v_1 & v_2 & \cdots & v_i & \cdots & v_m \end{array} \right]$$

are the matrices of the m experimental measures of the external forces/torques applied to the optoelectronic sensor and of the PD output voltages respectively. For the derivation of the calibration matrix, the force and torque components are acquired by the reference sensor and preliminary converted to the optoelectronic sensor reference frame by means of a suitable transformation matrix. As described in Section A.2.2, a 3rd-order interpolation polynomial has been adopted for deriving the external force/torque vector from the sensor output signals.

Because of the specific mechanical design[2], the operating range of the sensor is $[-50 \div 50]$ N along the linear axes, while torques are limited to $[-1 \div 1]$ Nm about the rotational axes. fig. A-15 shows a test in which forces are measured by the reference sensor and by the proposed optoelectronic sensor after calibration; force and torque estimation errors are reported as well.

A.4.2 Cross Coupling Analysis

The analysis of the cross coupling error is usually performed to verify the properties of strain-gauge based F/T sensors, especially in case of mechanically decoupled sensors [98, 58, 111], and it can be considered as an index of the sensor quality. According to the definition given in [49], the cross coupling error is defined as the ratio of unfavorable signals to the intended one at a given output of the sensor according to pure force components. In the case of the proposed sensor, since we are not interested

---

[2]As already mentioned, the mechanical and elastic parts of the sensor can be tailored for specific applications, and therefore different performances can be achieved if desired.

(a) Force Reconstruction.

(b) Torque Reconstruction.
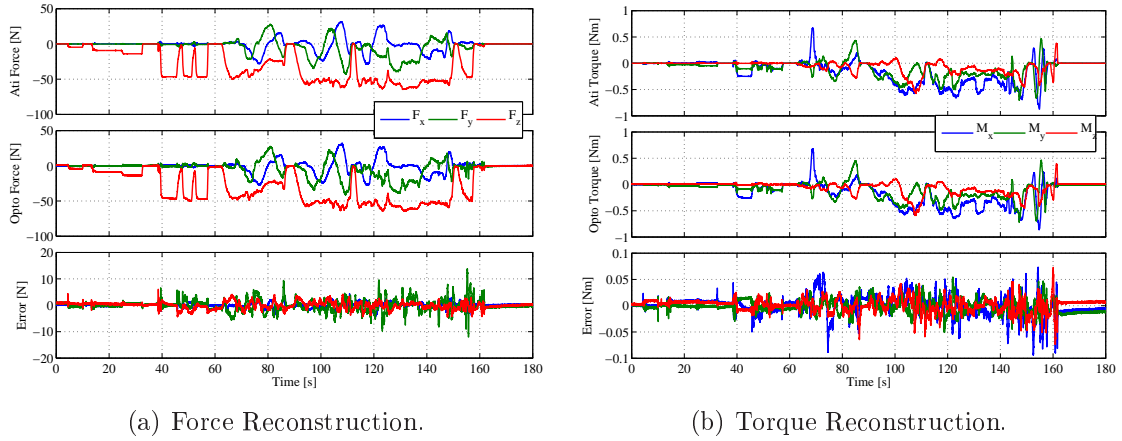
Figure A-15: Performance of the optoelectronic F/T sensor: Force and Torque reconstruction.

in measuring the strain induced on the mechanical structure and since there are several output signals that are expected to change when a pure force component is applied to the sensor, the analysis of the cross coupling error is performed by taking into account the output voltages variations of the PD conditioning circuit when a pure force or torque is applied along the sensor reference axes. Assuming that the PCBs are mounted orthogonally to the sensor reference axes, due to the structure of the proposed measuring circuit, a pure force component along a reference axis will produce, in ideal conditions, a variation of the PD output voltages in the PCB orthogonal to the force direction only, while a pure torque component will produce a variation of the PD output voltages in the PCBs that are parallel to the torque direction only. Any deviation from this expected behavior can be ascribed to misalignment between the reference axes and the PCBs (and the RS), defects in the PCB assembly that cause deviation of the LED and PD optical axes with respect to the PCB plane or to spurious light reflections.

The cross coupling error has been then evaluated by considering the maximum load (50 N force or 1 Nm torque) along the sensor reference axes and the corresponding PD output voltage variations. The cross coupling errors c_i are defined in this case as the ratio between the absolute value of each PD output variation, denoted as $|\Delta V_i|$,

and the maximum one, denoted as $|\Delta V_i|_{\max}$, i.e.

$$c_i = \frac{|\Delta V_i|}{|\Delta V_i|_{\max}} \tag{A.17}$$

In Tab. III the cross coupling errors evaluated on the experimented sensor prototype are reported: note that the PDs numbered from 1 to 4 are mounted on the PCB orthogonal to the x axis, the ones numbered from 5 to 8 are mounted on the PCB orthogonal to the y axis and the ones numbered from 9 to 12 are mounted on the PCB orthogonal to the z axis. From these results it can be stated that, even if a considerable coupling error exists, probably due to the aforementioned defects in the sensor implementation, the variation of the output signals are consistent with the expected behavior.

Table III
The cross coupling errors evaluated on the experimented sensor prototype.

c_i	$F_x = 50\,\mathrm{N}$	$F_y = 50\,\mathrm{N}$	$F_z = 50\,\mathrm{N}$	$M_x = 1\,\mathrm{Nm}$	$M_y = 1\,\mathrm{Nm}$	$M_z = 1\,\mathrm{Nm}$
c_1	0.996	0.324	0.109	0.211	1	0.990
c_2	1	0.215	0.080	0.129	0.772	0.872
c_3	0.993	0.199	0.170	0.132	0.951	0.940
c_4	0.884	0.235	0.122	0.190	0.698	0.761
c_5	0.141	1	0.059	0.901	0.054	0.847
c_6	0.120	0.971	0.166	0.764	0.184	0.798
c_7	0.195	0.899	0.098	1	0.045	0.604
c_8	0.208	0.910	0.119	0.655	0.101	1
c_9	0.210	0.351	0.891	0.689	0.804	0.129
c_{10}	0.207	0.103	0.989	0.872	0.922	0.032
c_{11}	0.181	0.099	0.889	0.541	0.799	0.007
c_{12}	0.190	0.177	1	0.967	0.985	0.150

A.4.3   Characterization as Intrinsic Tactile Sensor

Among the variety of possible F/T sensor applications, several authors reported how to use them in robotics as intrinsic tactile sensors, i.e. for the computation of the contact point between e.g. the fingers of a robot hand and the grasped object, see [21, 82, 24, 61]. Considering an "hard finger" contact hypothesis (i.e. only forces and

not torques can be applied at the contact point), the use of the proposed device as an intrinsic tactile sensor has been investigated. As described e.g. in [21], in case of a sensor with spherical surface (with radius r) the position p_c of the contact point can be obtained from the force f and torque m measured by the F/T sensor from

$$
\begin{aligned}
\lambda &= -\frac{1}{\|f\|}\sqrt{r^2 - \frac{\|f \times m\|^2}{\|f\|^4}} \\
r_0 &= \frac{f \times m}{\|f\|^2} \\
p_c &= r_0 + \lambda f
\end{aligned}
$$

These equations admit up to two possible solutions (the intersection of a line with a spherical surface), then the right solution can be selected assuming that the contact force can only push on the sensor external surface. Some experimental tests are reported in fig. A-16, where the measured forces and the corresponding contact point position on the sensor surface are represented by blue lines and red dots respectively. In this tests, the estimated $[x, y, z]$ coordinates have been computed as $[-2.4, -1.7, 43.9]$ mm, $[-5.1, -10.5, 42.4]$ mm, $[-10.6, -7.2, 42.1]$ mm and $[13.6, -0.6, 41.8]$ mm. For the sake of comparison, in fig. A-16 also the forces measured by the ATI reference sensor and the corresponding contact point positions are reported with green lines and black dots respectively. These results allow to state that the proposed optoelectronic device can be used as intrinsic tactile sensor.

A.4.4   Slip Detection

A slip detection algorithm exploiting the information gathered from the proposed optoelectronic sensor has been implemented and experimentally tested. Figure A-17 shows the experimental setup composed by two linear motors LinMot-37x160: the first motor (Motor 1) is mounted with its motion axis aligned with the sensor z-axis and is used to hold an object against the optoelectronic sensor by means of a rounded tip (to simulate the contact between the object and a second fingertip); the second motor (Motor 2) is positioned perpendicularly to Motor 1 and is equipped with a
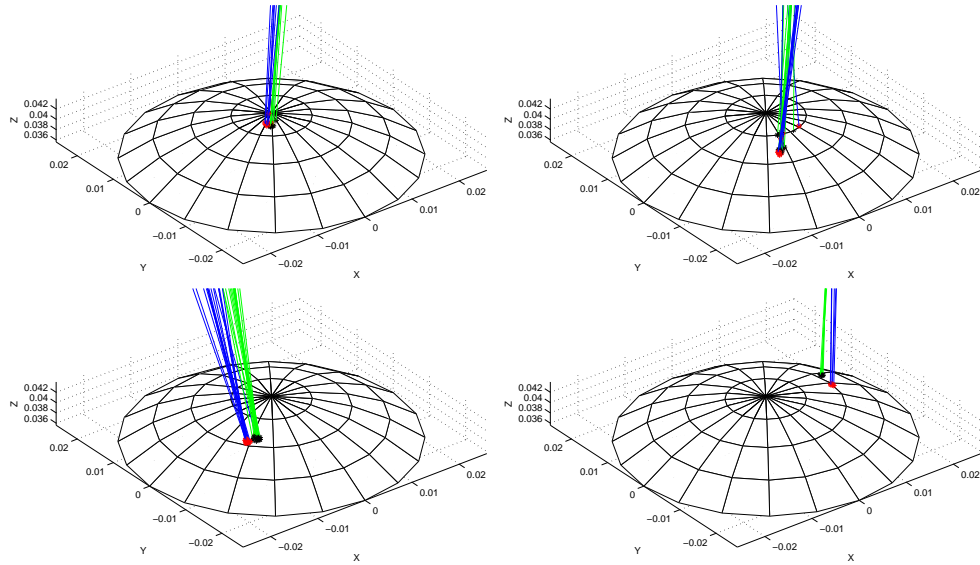
Figure A-16: Contact point reconstruction tests: force directions (blue lines) and contact point positions (red dots) measured by the optoelectronics F/T sensor; for comparison, force directions (green lines) and contact point positions (black dots) measured by the reference ATI sensor.

precision load cell. Motor 2 is used both to apply to the object a tangential force and to measure the object displacement during slip by means of the integrated encoder.

Figures A-18 and A-19 show the typical behavior of the object in case of slow and fast increasing of the tangential force respectively. In particular, referring to fig. A-18(a), the tangential force is slowly increased and the measured motion of the object is mostly due to the elastic deformation of the sensor and of the silicon rubber on the contact surface during the first part of the experiment, while in the second part of the experiment (at about 65 s) it is possible to see that the object speed suddenly increases when the tangential force reach a certain threshold. This event shows that the object slip occurs, fact that can also be noted from the FFT analysis of the tangential force signal. In this tests, the FFT has been performed considering $N = 256$ samples each iteration, that considering a sensor sampling frequency of 100 Hz, results in a fundamental FFT frequency of 0.39 Hz. It is possible to note from the blue plot in Fig.A-18(a) reporting the second harmonic of tangential force signal, that its value is quite small during the hold phase, while a peak emerges when the object start to slip. As also widely reported in literature [41], this information can be extracted
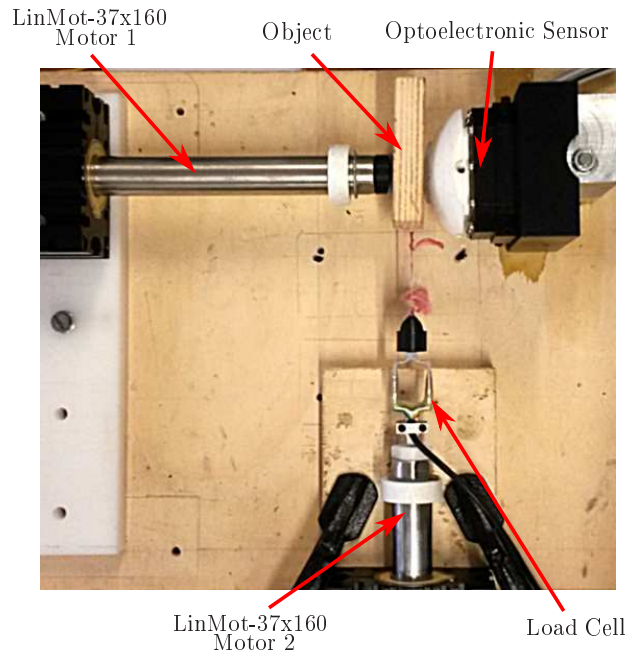
Figure A-17: Laboratory setup for calibration and experimental validation.

from the sensor measure and can be used for object slip detection and prevention. A zoom over the region where the slip occurs is reported in fig. A-18(b). As a possible implementation of the slipping detection algorithm, a suitable threshold it has been assumed: beyond this PSD threshold the slipping compensation should be activated increasing the normal force used to hold the object to increase the friction force. In fig. A-18(b) the time instants at which the identification occurs are highlighted by red circles: this points are in the proximity of the change of slope of the plots of the object position, which clearly indicates that the object is slipping. To test the algorithm under different conditions, the test has been executed with different tangential force variation rates. Figure A-19 reports the test results in case of a fast tangential force variation: in fig. A-19(a) the whole experiment is reported, whereas in fig. A-19(b) the region over the object slipping and the instant in which the PSD threshold is exceeded are shown.
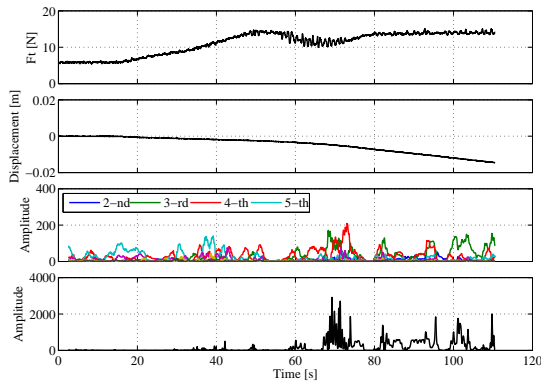
(a) Slow tangential force variation. From top to bottom: tangential force, object displacement, harmonics amplitude, product between the second and the third harmonic.
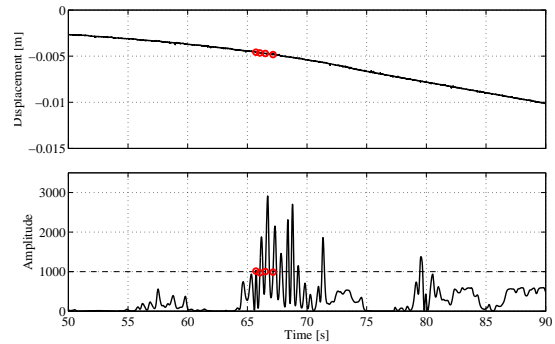
(b) Detail of the slippage test. Top: object displacement; bottom: product between the second and the third harmonic. The dashed line shows the slip detection threshold, the red circles highlight when the PSD exceeds the threshold.

Figure A-18: Slippage detection algorithm: slow tangential force variation.
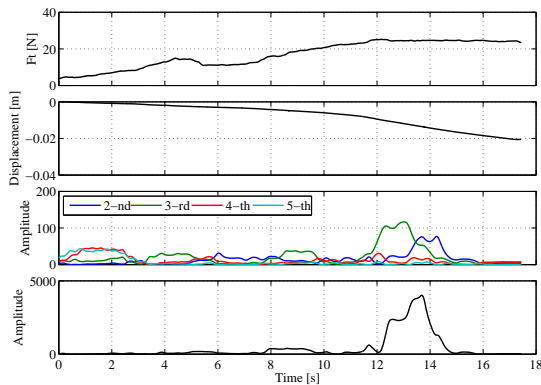
(a) Slow tangential force variation. From top to bottom: tangential force, object displacement, harmonics amplitude, product between the second and the third harmonic.
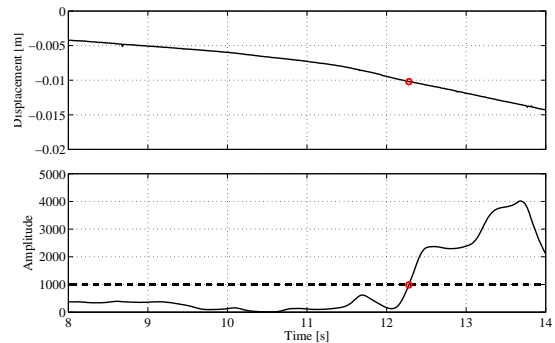
(b) Detail of the slippage test. Top: object displacement; bottom: product between the second and the third harmonic. The dashed line shows the slip detection threshold, the red circles highlight when the PSD exceeds the threshold.

Figure A-19: Slippage detection algorithm: fast tangential force variation.

A.5 Waterproof Prototype for Underwater Robotics
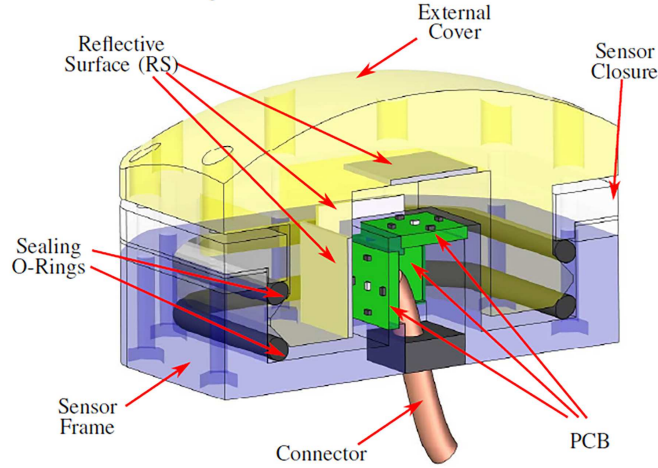
Figure A-20: A prototype of the sealed optoelectronic 6-axis Force/Torque sensor and internal design of the sensor.

As already mentioned in Section A.3, one of the key features of this sensor is the possibility to easily adapt the mechanical design to the specific use, provided that the geometrical constraints of photo-components and reflective surfaces are satisfied. In fig. A-12 two different implementations are shown, in particular it can be noted that they differ from the top cover and the compliant frame design. While the top cover has no influence on the sensor performances, the compliant frame has direct influence on the measurement range. Moreover it is a crucial section of the sensor when the insulation of the sensor from the environment is compulsory. This is the case addressed in [62, 70, 71] in which the 6-axis F/T sensor is exploited as an intrinsic tactile sensor for underwater applications.

In this particular version of the sensor the relative motion of the RS and the PCBs is achieved by exploiting the o-ring seals compliance, that elastically deform when an external force is applied to the external cover of the sensor, but also guarantee the sensor sealing as can be seen in fig. A-20.
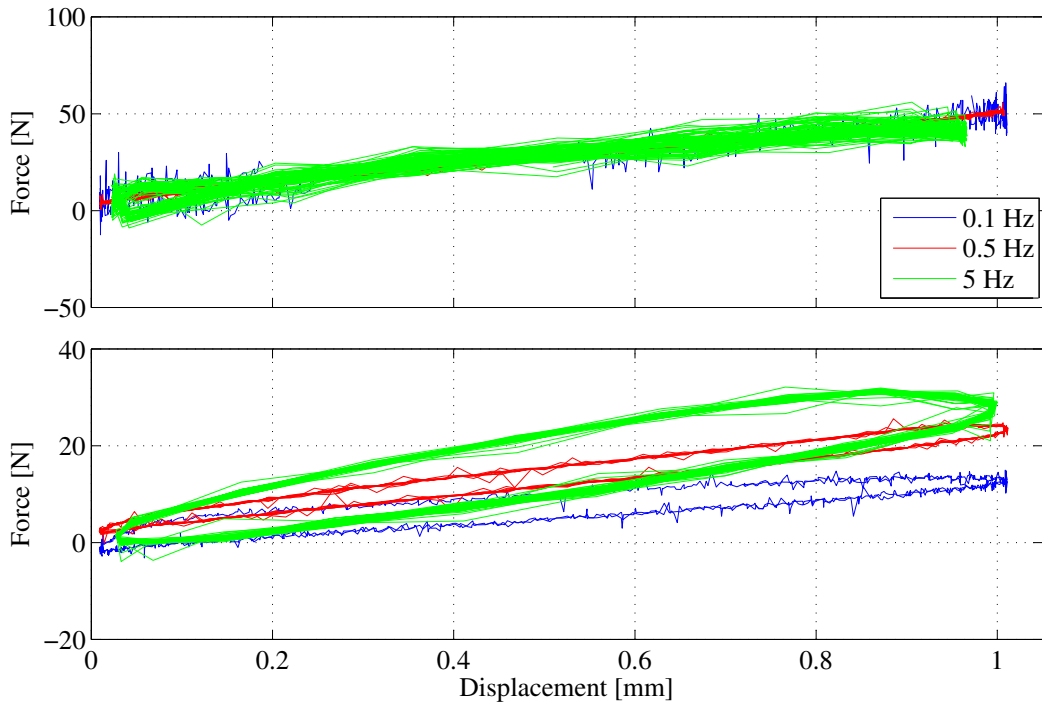
Figure A-21: Displacement/force characteristic of silicon rubber (top) and fluorocarbon rubber (bottom) o-rings for different compression rates.

A.5.1   Characterization of O-ring Materials

The characteristics of two different o-ring materials have been evaluated by means of suitable experiments to find which material is better suited for our application. In these experiments, silicon rubber and fluorocarbon rubber o-rings have been compared by applying a sinusoidal compression with frequency range from 0.1 to 5 Hz and measuring the corresponding reaction force. The o-rings have the same dimensions in both the cases, with a thickness of 3.53 mm and an internal diameter of 47.62 mm, and both the materials present an hardness of 70 Shore A. The results reported in fig. A-21 shows that, while silicon rubber presents a quite linear response within the displacement and frequency range of our interest, fluorocarbon rubber presents a large hysteresis for high value of the compression rate. Since we are interested in a implementing a sensor whit an as wider as possible constant frequency response, the silicon o-rings are more suitable for the implementation of the proposed sensor.
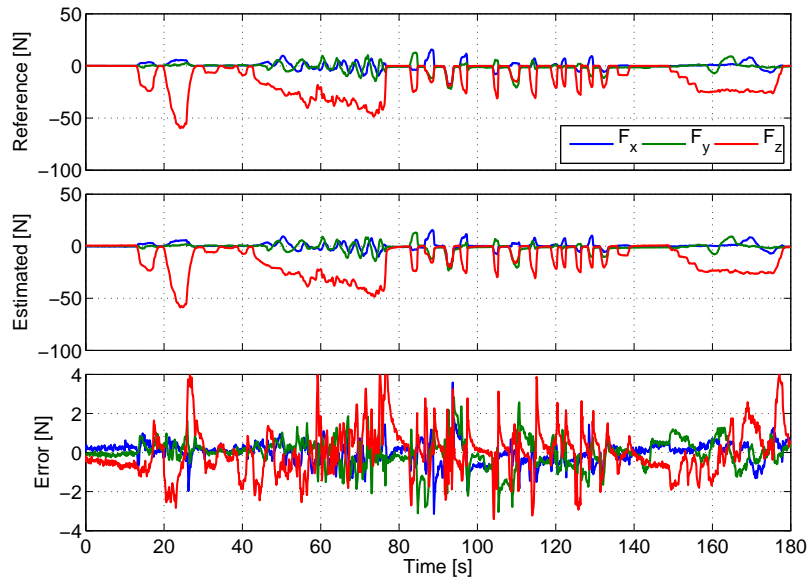
Figure A-22: Force reconstruction after calibration.

A.5.2 Calibration of the Waterproof Sensor

For the calibration and the experimental characterization of the sensor, the same setup of fig. A-17 has been used and the same procedure of Section A.4 has been followed. fig. A-22 shows a test in which forces are measured by the reference sensor and by the new sensor after calibration, and the difference among them. From the plots, and in particular from the plot of the difference, it can be noticed that there are some "peaks" when the applied force has a sudden change. These peaks are due to the different elastic properties of the two sensors (the o-rings have a more evident visco-elastic behaviour).

A.5.3 Dynamic Performance of the Sensor

In order to fully characterize from a static and dynamic point of view the sensor, other experiments have been performed. In particular, the sensor has been installed on the setup of fig. A-23 in order to apply precise axial forces (z direction).

For example, fig. A-24 shows a test in which a sinusoidal force with constant frequency (0.1 Hz) and increasing amplitude is applied by the motor along the z axis. It is possible to see an increasing error when the force gradient becomes larger and larger. As a matter of fact, because of the visco-elastic properties of the rubber used to

253
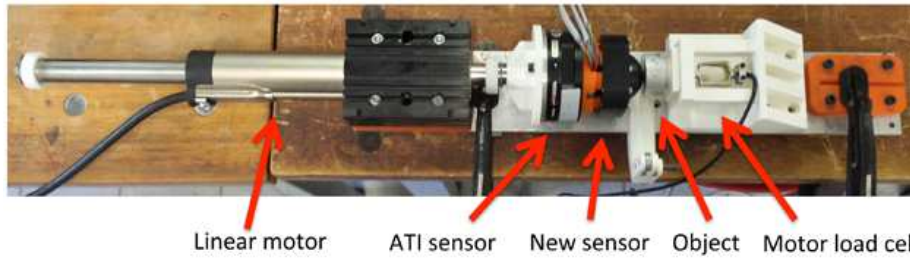
Figure A-23: Laboratory setup for calibration and experimental validation.
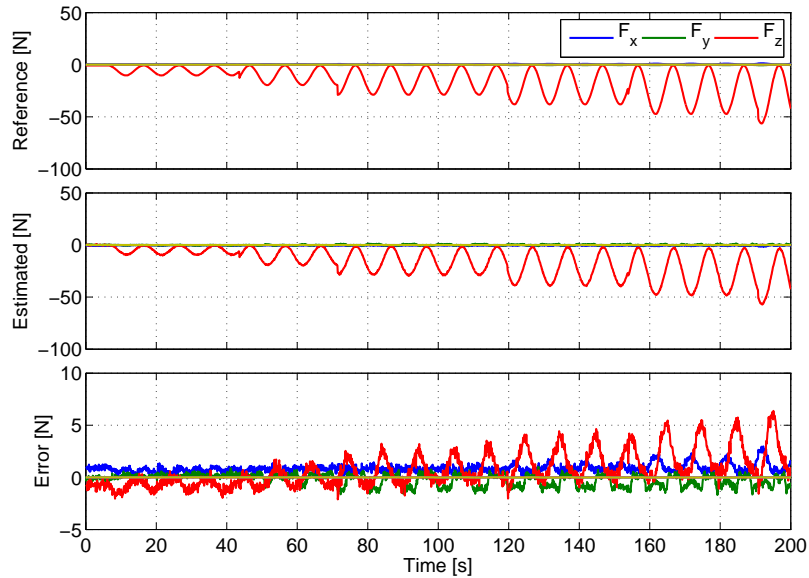
Figure A-24: Application of a sinusoidal force signal with increasing amplitude at 0.1 Hz.

seal the optical sensor, this is 'slower' than the reference sensor in recovering the unloaded position. This effect is more evident in fig. A-25 where a 20 N sinusoidal force is applied at increasing frequencies, from 0.01 to 3 Hz. The error increases with the frequency of the input signal.

However, it has to be pointed out that this effect is not due to some intrinsic limitations of the basic principle of the sensor, but rather to the particular mechanical design employing rubber sealing. To verify this fact, the force/displacement response of the sensor without and with o-ring sealing has been measured and analyzed. In fig. A-26 it is clear that the introduction of the sealing elements reduce the frequency range of the sensor, reducing in this way also the sensitivity of the sensor. Then, in particular in case frequency based detection techniques are used, the effect of the sealing material needs to be considered during the calibration of the system for a

proper identification of the slip events. It also possible to see that no significant difference exists in the sensor response in case of rubber or silicon sealing.
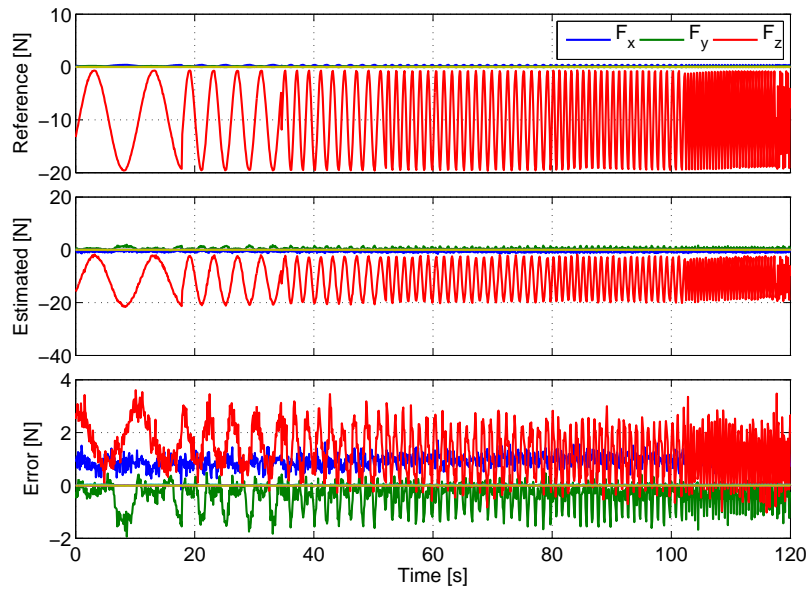
Figure A-25: Application of a sinusoidal force signal (20 N) at increasing frequencies.
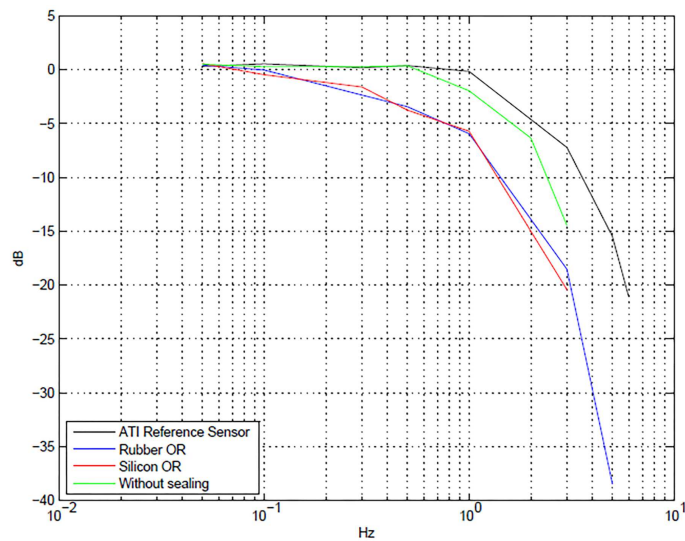
Figure A-26: Frequency response of the sensor with respect to the ATI reference sensor, without sealing and with sealing.
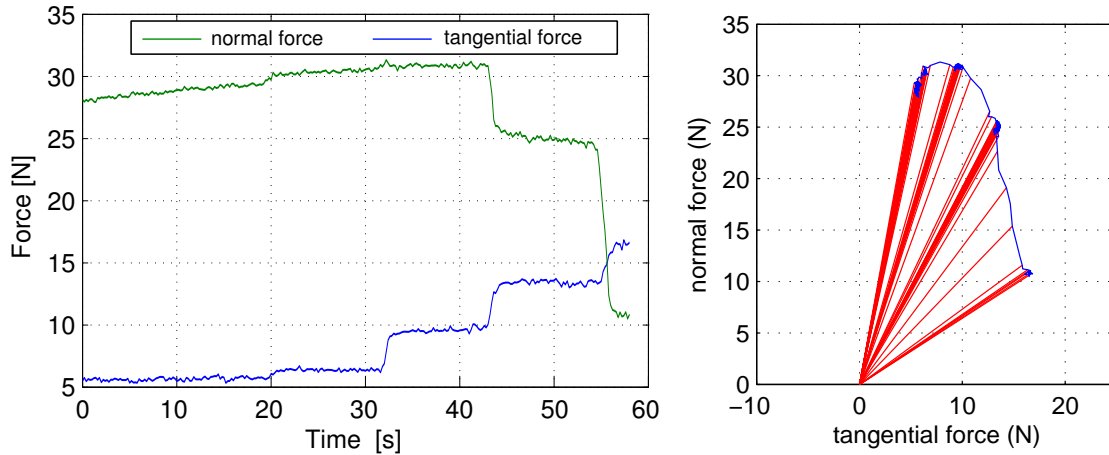
Figure A-27: Measurement of the normal and tangential forces.

A.5.4 Evaluation of the Friction Coefficient

Another experiment is reported in and fig. A-27, where a constant force along the z direction is applied to an object. On the object, an external increasing force is applied as well (by means of some weights) and therefore the sensor measures both the normal (z axis) and tangential ($x-y$ plane) forces (f_n, f_t). In the experiment, the object was covered by a silicon rubber to increase friction (the surface of the sensor, built with 3D printing technology, has a very low friction coefficient), and the applied tangential forces were $f_t = 3, 8, 13, 18$ N, while the normal force was $f_n = 30$ N. Notice that with the load of $f_t = 13$ N, the object starts to slide. The decrease of the normal force f_n when the tangential component is $f_t = 13$ N is due to the non negligible deformation of the silicon rubber covering the object. This type of experiment allows also to estimate the friction coefficient $\mu = f_t/f_n$ and to implement some control strategies in order to avoid slippage of the object.

A.5.5 Tactile Sensing Test

Finally the sensor has been characterized as intrinsic tactile sensor following the procedure in Section A.4.3 Typical results are reported in fig. A-28, where the applied forces are shown as lines and the contact points are measured on the surface of the sensor. In this test, three forces are applied at three different points, whose $[x, y, z]$ coordinates have been computed as $[1.2,\ 2.1,\ 21.1]$ mm, $[-1.4,\ 10.7,\ 18.1]$ mm and
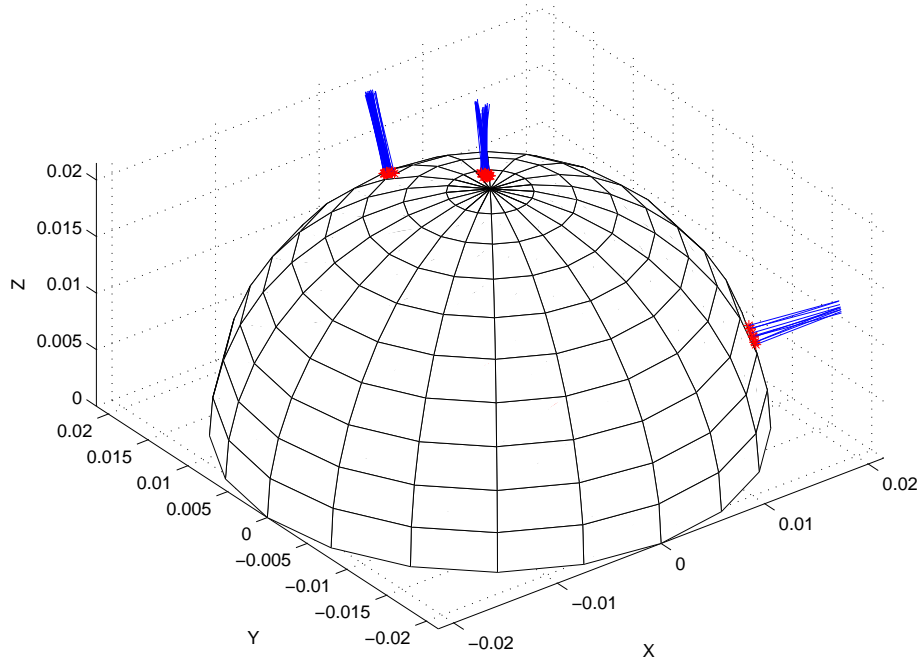
Figure A-28: Measurement of the applied forces and of the contact point.

[17.6, −7.8, 5.4] mm, corresponding to radii of 21.2, 21.1 and 20.0 mm respectively (the radius of the spherical surface is 21.5 mm).

A.6   Conclusions

Thanks to the adoption of discrete optoelectronic components, the proposed sensor is characterized by a low-cost and a simple and reliable implementation. As additional remarkable advantages, the compact and customizable electronics of the implemented sensor allow an easy mechanical and electronic integration into relatively complex robotic systems. As a preliminary evaluation of the sensor characteristics, several experiments have been performed to validate the mathematical model of the device. These experiments confirmed that the mathematical model of the sensor can be used for selecting a suitable device working range. The reported experiments show satisfactory performance of the proposed device not only for the estimation the applied force and torque, but also for detecting the contact point location and object slip. This result allows to state that the proposed device can be used as an 'intrinsic tactile' sensor.

257

Moreover the same device has been exploited in order to be integrated in a three-fingered gripper for underwater applications. A different mechanical configuration of the compliant frame has been developed by means of o-rings seals, in order to achieve a waterproof sensor. An extensive experimental activity has been carried out in order to both characterize different elastic materials and analyze their effects on the sensor's performances. Despite the limited dynamic range due to the o-rings based sealing, the experimental results confirm the satisfactory benchmarks of the original sensor even for the waterproof version.

Appendix B

List of Personal Pubblications

Here follows the list of achievements arising from the research activities reported in this thesis.

B.1 Publications in Journals

1. G. Palli, L. Moriello, U. Scarcia, C. Melchiorri, **"*Development of an Optoelectronic 6-axis Force/Torque Sensor for Robotic Applications*"**, Sensors & Actuators A: Physical, Volume 220, Page(s) 333 to 346, December 2014

2. L. Biagiotti, C. Melchiorri, L. Moriello, **"*Optimal Trajectories for Vibration Reduction Based on Exponential Filters*"**, IEEE Transactions on Control Systems Technology, in press, 2015

B.2 Publications in Conferences

1. C. Melchiorri, L. Moriello, G. Palli, U. Scarcia, **"*A New Force/Torque Sensor for Robotic Applications Based on Optoelectronic Components*"**, IEEE International Conference on Robotics and Automation, Hong Kong, China, May 31 - June 7, 2014

2. G. Palli, L. Moriello, U. Scarcia, C. Melchiorri, **"An Intrinsic Tactile Sensor for Underwater Robotics"**, 19th IFAC World Congress, Cape Town, South Africa, August 24-29, 2014

3. G. Palli, L. Moriello, C. Melchiorri, **"The Effects of Sealing in 6-axis Force/Torque Sensors for Underwater Applications"**, Fifteenth International Conference on Computer Aided Systems Theory, Workshop on Marine Sensors and Manipulators, La Palma de Gran Canaria, Spain, February 11-13, 2015

4. G. Palli, L. Moriello, C. Melchiorri, **"Performance and Sealing Material Evaluation in 6-axis Force-Torque Sensors for Underwater Robotics"**, IFAC Workshop on Navigation, Guidance and Control of Underwater Vehicles NGCUV'2015, Girona, Spain, April 28-30, 2015

5. G. Palli, L. Moriello, C. Melchiorri, **"On the Bandwidth of 6-axis Force/Torque Sensors for Underwater Applications"**, MTS/IEEE Oceans series of Conferences OCEANS'15, Genova, Italy, May 18-21 ,2015

6. L. Biagiotti, C. Melchiorri, L. Moriello, **"A Repetitive Control Scheme Based on B-Spline Trajectories Modification for Robotic Manipulators"**, 11th IFAC Symposium on Robot Control, Salvador, Brasil, August 26-28, 2015

7. L. Biagiotti, C. Melchiorri, L. Moriello, **"A Repetitive Control Scheme for Industrial Robots Based on B-Spline Trajectories"**, IEEE/RSJ International Conference on Intelligent Robots and Systems, Hamburg, Germany, September 28 - October 02, 2015

8. L. Biagiotti, L. Moriello, C. Melchiorri, **"Feedforward Control of Variable Stiffness Joints Robots for Vibration Suppression"**, submitted to IEEE/RSJ International Conference on Intelligent Robots and Systems, Daejeon, Korea, 2016

B.3 Patents

1. G. Palli, C. Melchiorri, L. Moriello, U. Scarcia, "*Optoelectronic System for the Measurement of Position and Orientation*", Italian Patent n. 0001420480, January 2016.

Bibliography

[1] M. Ahmad, F. Misran, M. Ramli, and R. Raja Ismail, "Experimental investigations of low pass filter techniques for sway control of a gantry crane system," in *Electronic Computer Technology (ICECT), 2010 International Conference on*, May 2010, pp. 1–4.

[2] M. Ahmad, R. Raja Ismail, M. Ramli, A. Nasir, and N. Hambali, "Feed-forward techniques for sway suppression in a double-pendulum-type overhead crane," in *Computer Technology and Development, 2009. ICCTD '09. International Conference on*, vol. 1, Nov 2009, pp. 173–178.

[3] A. Albu-Schäffer, S. Wolf, O. Eiberger, S. Haddadin, F. Petit, and M. Chalon, "Dynamic modelling and control of variable stiffness actuators," in *Robotics and Automation (ICRA), 2010 IEEE International Conference on*, May 2010, pp. 2155–2162.

[4] I. Antoniadis and D. Economou, "Robust residual vibration suppression for linear time invariant systems by digital filtering of the guidance function," *Mechanical Systems and Signal Processing*, vol. 15, no. 3, pp. 565 – 580, 2001. [Online]. Available: http://www.sciencedirect.com/science/article/pii/S0888327000913840

[5] A. K. Banerjee and W. E. Singhose, "Command shaping in tracking control of a two-link flexible robot," *Journal of Guidance, Control, and Dynamics*, vol. 21, no. 6, pp. 1012–1015, 1998.

[6] P.-J. Barre, R. Béarée, P. Borne, and E. Dumetz, "Influence of a jerk controlled movement law on the vibratory behaviour of high-dynamics systems," *Journal of Intelligent and Robotic Systems*, vol. 42, pp. 275–293, 2005.

[7] R. Béarée, "New damped-jerk trajectory for vibration reduction," *Control Engineering Practice*, vol. 28, no. 0, pp. 112 – 120, 2014.

[8] J. Bemfica, C. Melchiorri, L. Moriello, G. Palli, U. Scarcia, and G. Vassura, "Mechatronic design of a three-fingered gripper for underwater applications," in *6th IFAC Symposium on Mechatronic Systems, Hangzhou, China*, 2013, pp. 307–312.

[9] L. Biagiotti and C. Melchiorri, *Trajectory Planning for Automatic Machines and Robots*. Springer Berlin Heidelberg, 2008.

[10] ——, "B-spline based filters for multi-point trajectories planning," in *Robotics and Automation (ICRA), 2010 IEEE International Conference on*, Anchorage, Alaska, May 2010, pp. 3065–3070.

[11] ——, "Input shaping via b-spline filters for 3-d trajectory planning," in *IEEE/RSJ International Conference on Intelligent Robots and Systems (IROS)*, San Francisco, California, September 25-30 2011.

[12] ——, "Online planning of multi-segment trajectories with trigonometric blends," in *Proceedings of the 18th IFAC World Congress*, 2011.

[13] ——, "FIR filters for online trajectory planning with time- and frequency-domain specifications," *Control Engineering Practice*, vol. 20, no. 12, pp. 1385 – 1399, 2012.

[14] ——, "Online trajectory planning and filtering for robotic applications via b-spline smoothing filters," in *IEEE/RSJ International Conference on Intelligent Robots and Systems (IROS)*, Nov 2013, pp. 5668–5673.

[15] L. Biagiotti, C. Melchiorri, and L. Moriello, "Optimal trajectories for vibration reduction based on exponential filters," *Control Systems Technology, IEEE Transactions on*, vol. PP, no. 99, pp. 1–1, 2015.

[16] L. Biagiotti, L. Moriello, and C. Melchiorri, "A repetitive control scheme based on b-spline trajectories modification," *IFAC-PapersOnLine*, vol. 48, no. 19, pp. 262 – 267, 2015, 11th {IFAC} Symposium on Robot Control {SYROCO} 2015Salvador, Brazil, 26âĂŞ28 August 2015. [Online]. Available: http://www.sciencedirect.com/science/article/pii/S2405896315026671

[17] ——, "A repetitive control scheme for industrial robots based on b-spline trajectories," in *IEEE/RSJ International Conference on Intelligent Robots and Systems (IROS)*, 2015.

[18] ——, "Feedforward control of variable stiffness joints robots for vibrations suppression," in *Submitted to IEEE/RSJ International Conference on Intelligent Robots and Systems (IROS)*, 2016.

[19] A. Bicchi, "A criterion for optimal design of multi-axis force sensors," *Robotics and Autonomous Systems*, vol. 10, no. 4, pp. 269–286, 1992.

[20] A. Bicchi, S. Rizzini, and G. Tonietti, "Compliant design for intrinsic safety: general issues and preliminary design," in *Intelligent Robots and Systems, 2001. Proceedings. 2001 IEEE/RSJ International Conference on*, vol. 4, 2001, pp. 1864–1869 vol.4.

[21] A. Bicchi, J. Salisbury, and D. Brock, "Contact sensing from force measurements," *International Journal of Robotics Research*, vol. 12, pp. 249–262, 1990.

[22] M. Catalano, G. Grioli, M. Garabini, F. Bonomo, M. Mancinit, N. Tsagarakis, and A. Bicchi, "Vsa-cubebot: A modular variable stiffness platform for multiple degrees of freedom robots," in *Robotics and Automation (ICRA), 2011 IEEE International Conference on*, May 2011, pp. 5090–5095.

[23] J. Choi, S. Park, W. Lee, and S. C. Kang, "Design of a robot joint with variable stiffness," in *Robotics and Automation, 2008. ICRA 2008. IEEE International Conference on*, May 2008, pp. 1760–1765.

[24] A. Cicchetti, A. Eusebi, C. Melchiorri, and G. Vassura, "An intrinsic tactile force sensor for robotic manipulation," in *Proc. 7th. Int. Conf. on Advanced Robotics, ICAR'95, Sant Feliu de Guixols, Spain*, 1995, pp. 889–894.

[25] L. Cuiyan, Z. Dongchun, and Z. Xianyi, "A survey of repetitive control," in *Intelligent Robots and Systems, 2004. (IROS 2004). Proceedings. 2004 IEEE/RSJ International Conference on*, vol. 2, Sept 2004, pp. 1160–1166 vol.2.

[26] R. Dahiya, G. Metta, M. Valle, and G. Sandini, "Tactile sensing Ũ from humans to humanoids," *IEEE Transactions on Robotics*, vol. 26, no. 1, pp. 1–20, 2010.

[27] A. De Luca and W. Book, *Springer Handbook of Robotics*. Berlin: Springer Verlag, 2008, ch. Robots with Flexible Elements, pp. 287–317.

[28] A. De Luca, R. Farina, and P. Lucibello, "On the control of robots with visco-elastic joints," in *Robotics and Automation, 2005. ICRA 2005. Proceedings of the 2005 IEEE International Conference on*, April 2005, pp. 4297–4302.

[29] G. De Maria, C. Natale, and S. Pirozzi, "Force/tactile sensor for robotic applications," *Sensors and Actuators A: Physical*, vol. 175, pp. 60–72, 2012.

[30] J. S. Dewey and S. Devasia, "Experimental and theoretical results in output-trajectory redesign for flexible structures," in *Decision and Control, 1996., Proceedings of the 35th IEEE Conference on*, vol. 4, Dec 1996, pp. 4210–4215 vol.4.

[31] R. C. E. Torres-Jara, I. Vasilescu, "A soft touch: compliant tactile sensors for sensitive manipulation," in *CSAIL Technical Report MIT-CSAIL-TR-2006-014*, 2006.

[32] D. Economou, C. Mavroidis, I. Antoniadis, and C. Lee, "Maximally robust input preconditioning for residual vibration suppression using low-pass fir digital filters," *ASME Journal of Dynamic Systems, Measurement, and Control*, vol. 124(1), pp. 85–97, 2000.

[33] J. Feddema, C. Dohrmann, G. Parker, R. Robinett, V. Romero, and D. Schmitt, "Robotically controlled slosh-free motion of an open container of liquid," in *Robotics and Automation, 1996. Proceedings., 1996 IEEE International Conference on*, vol. 1, Apr 1996, pp. 596–602 vol.1.

265

[34] J. Fortgang, W. Singhose, and J. d. J. Márquez, "Command shaping for micromills and cnc controllers," in *Proc. American Control Conference*, 2005.

[35] B. Francis and W. Wonham, "The internal model principle for linear multivariable regulators," *Applied Mathematics and Optimization*, vol. 2, no. 2, pp. 170–194, 1975.

[36] R. R. G. Hellard, "A robust, sensitive and economical tactile sensor for a robotic manipulator," in *Proc. of Australasian Conference on Robotics and Automation*, 2002, pp. 100–104.

[37] S. Hara, Y. Yamamoto, T. Omata, and M. Nakano, "Repetitive control system: a new type servo system for periodic exogenous signals," *Automatic Control, IEEE Transactions on*, vol. 33, no. 7, pp. 659–668, Jul 1988.

[38] P. Henry, M. Krainin, E. Herbst, X. Ren, and D. Fox, "Rgb-d mapping: Using depth cameras for dense 3d modeling of indoor environments," in *In the 12th International Symposium on Experimental Robotics (ISER*, 2010.

[39] J. Heo, J. Chung, and J. Lee, "Tactile sensor arrays using fiber bragg grating sensors," *Sensors and Actuators A: Physical*, vol. 126, no. 2, pp. 312–327, 2006.

[40] S. Hirose and K. Yoneda, "Development of optical 6-axial force sensor and its signal calibration considering non linear calibration," in *Proc. IEEE Int. Conf. on Robotics and Automation*, vol. 1, Tsukuba, Japan, 1990, pp. 46–53.

[41] E. G. M. Holweg, H. Hoeve, W. Jongkind, L. Marconi, C. Melchiorri, and C. Bonivento, "Slip detection by tactile sensors: algorithms and experimental results," in *Proc. IEEE Int. Conf. on Robotics and Automation*, vol. 4, Apr 1996, pp. 3234–3239.

[42] K.-T. Hong and Hong, "Input shaping and vsc of container cranes," in *Proc. IEEE International Conference on Control Applications*, 2004, pp. 1570–1575.

[43] J. Hyde and W. Seering, "Using input command pre-shaping to suppress multiple mode vibration," in *Robotics and Automation, 1991. Proceedings., 1991 IEEE International Conference on*, Apr 1991, pp. 2604–2609 vol.3.

[44] T. Inoue, S. Iwai, and M. Nakano, "High accuracy control of a proton synchrotron magnet power supply," in *Proc. 8th IFAC World Congress*, vol. 20, 1981, pp. 3137–3142.

[45] T. Inoue, M. Nakano, and S. Iwai, "High accuracy control of servomechanism for repeated contouring," in *Proc. 10th Annual Symp. Incremental Motion Contr. Syst. and Device*, 1981, pp. 258–292.

[46] K. Kamiyama, K. Vlack, T. Mizota, H. Kajimoto, N. Kawakami, and S. Tachi, "Vision-based sensor for real-time measuring of surface traction fields," *Computer Graphics and Applications, IEEE*, vol. 25, no. 1, pp. 68–75, 2005.

[47] C. Kang, "Performance measure of residual vibration control," *ASME Journal of Dynamic Systems, Measurement, and Control*, vol. 133(4), 2011.

[48] C. G. Kang and M. T. Ha, "Partially analytical extra-insensitive shaper for a lightly damped flexible arm," in *Intelligent Robots and Systems (IROS 2014), 2014 IEEE/RSJ International Conference on*, Sept 2014, pp. 2401–2406.

[49] M. K. Kang, S. Lee, and J. H. Kim, "Shape optimization of a mechanically decoupled six-axis force/torque sensor," *Sensors and Actuators A: Physical*, vol. 209, no. 0, pp. 41–51, 2014.

[50] S. Kasap, *Optoelectronics and Photonics: Principles and Practices*. Englewood Cliffs, NJ: Prentice Hall, 2001.

[51] G. A. P. Kim, G. J. Shin, and J. Yoon, "Development of 6-axis force/moment sensor for a humanoid robot's intelligent foot," *Sensors and Actuators A: Physical*, vol. 141, no. 2, pp. 276–281, 2008.

[52] J. J. Kim and B. Agrawal, "Experiments on jerk-limited slew maneuvers of a flexible spacecraft," in *Guidance, Navigation, and Control and Co-located Conferences*. American Institute of Aeronautics and Astronautics, Aug. 2006, pp. –.

[53] K. Kozak, W. Singhose, and I. Ebert-Uphoff, "Performance measures for input shaping and command generation," *Journal of Dynamic Systems Measurement and Control*, vol. 128, no. 3, pp. 731–736, 2006.

[54] B. C. Kuo and F. Golnaraghi, *Automatic Control Systems*, 8th ed. New York, NY, USA: John Wiley & Sons, Inc., 2002.

[55] P. Lambrechts, M. Boerlage, and M. Steinbuch, "Trajectory planning and feed-forward design for electromechanical motion systems," *Control Engineering Practice*, vol. 13, pp. 145–157, 2005.

[56] W. Lorenz, M. Peshkin, and J. Colgate, "New sensors for new applications: force sensors for human/robot interaction," in *Proc. IEEE Int. Conf. on Robotics and Automation*, vol. 4, 1999, pp. 2855–2860.

[57] J. Ma and A. Song, "Fast estimation of strains for cross-beams six-axis force/torque sensors by mechanical modeling," *Sensors*, vol. 13, no. 5, pp. 6669–6686, 2013.

[58] J. Ma, A. Song, and J. Xiao, "A robust static decoupling algorithm for 3-axis force sensors based on coupling error model and Îţ-svr," *Sensors*, vol. 12, no. 11, pp. 14 537–14 555, 2012.

[59] D. Magee and W. Book, "Optimal filtering to minimize the elastic behavior in serial link manipulators," in *American Control Conference, 1998. Proceedings of the 1998*, vol. 5, Philadelphia, PA , USA, 1998, pp. 2637 – 2642.

267

[60] P. Meckl and P. Arestides, "Optimized s-curve motion profiles for minimum residual vibration," in *Proceedings of the American Control Conference*, Philadelphia, Pennsylvania, 1998, pp. 2627–2631.

[61] C. Melchiorri, "Tactile sensing for robotic manipulation," in *Articulated and Mobile Robotics for SErvices and TEchnologies (RAMSETE)*. Springer, 2001, pp. 75–102.

[62] C. Melchiorri, L. Moriello, G. Palli, and U. Scarcia, "A new force/torque sensor for robotic applications based on optoelectronic components," in *Robotics and Automation (ICRA), 2014 IEEE International Conference on*, May 2014, pp. 6408–6413.

[63] ——, "Optoelectronic system for the measurement of position and orientation," Italian Patent 0 001 420 480, January, 2016. [Online]. Available: http://www.uibm.gov.it/uibm/dati/Codice.aspx?load=info_uno&id=2199025&table=Invention#ancoraSearch

[64] C. Melchiorri, G. Palli, G. Berselli, and G. Vassura, "Development of the ub hand iv: Overview of design solutions and enabling technologies," *Robotics Automation Magazine, IEEE*, vol. 20, no. 3, pp. 72–81, Sept 2013.

[65] Z. Mohamed and M. Tokhi, "Command shaping techniques for vibration control of a flexible robot manipulator," *Mechatronics*, vol. 14, no. 1, pp. 69–90, 2004.

[66] R. Norton, *Cam design and manufacturing handbook*. Industrial Press, 2009.

[67] K. Ogata, *Modern control engineering (3rd ed.)*. Upper Saddle River, NJ, USA: Prentice-Hall, Inc., 1997.

[68] G. Palli and C. Melchiorri, "Velocity and disturbance observer for non-model based load and friction compensation," in *Proc. Int. Workshop on Advanced Motion Control*, Trento, Italy, 2008, pp. 194–199.

[69] G. Palli, C. Melchiorri, and A. De Luca, "On the feedback linearization of robots with variable joint stiffness," in *Robotics and Automation, 2008. ICRA 2008. IEEE International Conference on*, Pasadena, CA, May 2008, pp. 1753–1759.

[70] G. Palli, L. Moriello, and C. Melchiorri, "An intrinsic tactile sensor for underwater robotics," in *19th IFAC World Congress*, August 2014, pp. 3364–3369.

[71] ——, "On the bandwidth of 6-axis force/torque sensors for underwater applications," in *OCEANS 2015 - Genova*, May 2015, pp. 1–6.

[72] G. Palli, L. Moriello, U. Scarcia, and C. Melchiorri, "Development of an optoelectronic 6-axis force/torque sensor for robotic applications," *Sensors and Actuators A: Physical*, vol. 220, pp. 333 – 346, 2014. [Online]. Available: http://www.sciencedirect.com/science/article/pii/S092442471400418X

[73] G. Palli and S. Pirozzi, "Force sensor based on discrete optoelectronic components and compliant frames," *Sensors and Actuators A: Physical*, vol. 165, pp. 239–249, 2011.

[74] U.-H. PARK, J.-W. LEE, B.-D. LIM, and Y.-G. SUNG, "Design and sensitivity analysis of an input shaping filter in the z-plane," *Journal of Sound and Vibration*, vol. 243, no. 1, pp. 157 – 171, 2001. [Online]. Available: http://www.sciencedirect.com/science/article/pii/S0022460X0093414X

[75] M. Paz, *Structural Dynamics: Theory and Computation*. Chapman & Hall, 1997.

[76] F. Petit and A. Albu-Schäffer, "State feedback damping control for a multi dof variable stiffness robot arm," in *Robotics and Automation (ICRA), 2011 IEEE International Conference on*, May 2011, pp. 5561–5567.

[77] F. Petit, A. Daasch, and A. Albu-Schaffer, "Backstepping control of variable stiffness robots," *Control Systems Technology, IEEE Transactions on*, vol. PP, no. 99, pp. 1–1, 2015.

[78] A. Piazzi and A. Visioli, "Minimum-time open-loop smooth control for point-to-point motion in vibratory systems," in *Robotics and Automation, 1998. Proceedings. 1998 IEEE International Conference on*, vol. 2, May 1998, pp. 946–951 vol.2.

[79] ——, "Minimum-time system-inversion-based motion planning for residual vibration reduction," *Mechatronics, IEEE/ASME Transactions on*, vol. 5, no. 1, pp. 12–22, Mar 2000.

[80] ——, "Optimal dynamic-inversion-based control of an overhead crane," *Control Theory and Applications, IEE Proceedings* -, vol. 149, no. 5, pp. 405–411, Sep 2002.

[81] *QBMove - maker pro datasheet*, Q.B. Robotics. [Online]. Available: http://media.wix.com/ugd/45c5a1_792590e00b134129b2b6363a1ea7de45.pdf

[82] J. Salisbury, "Interpretation of contact geometries from force measurements," in *Robotics and Automation. Proceedings. 1984 IEEE International Conference on*, 1984, pp. 240–247.

[83] B. Siciliano and O. Khatib, Eds., *Springer Handbook of Robotics*. Springer, 2008.

[84] N. Singer, W. Singhose, and W. Seering, "Comparison of filtering methods for reducing residual vibration," *European Journal of Control*, vol. 5, no. 2Ũ4, pp. 208 – 218, 1999. [Online]. Available: http://www.sciencedirect.com/science/article/pii/S094735809970155X

[85] N. C. Singer, "Residual vibration reduction in computer controlled machines," MIT Artificial Intelligence Laboratory, Cambridge, MA, USA, Tech. Rep., 1989.

[86] N. C. Singer and W. P. Seering, "Preshaping command inputs to reduce system vibration," *ASME Journal of Dynamic Systems, Measurement, and Control*, vol. 112, pp. 76–82, 1990.

[87] W. Singhose, E. Crain, and W. Seering, "Convolved and simultaneous two-mode input shapers," *Control Theory and Applications, IEE Proceedings -*, vol. 144, no. 6, pp. 515–520, Nov 1997.

[88] W. Singhose, D. Kim, and M. Kenison, "Input shaping control of double-pendulum bridge crane oscillations," *ASME Journal of Dynamic Systems, Measurement, and Control*, vol. 130(3), 2008.

[89] W. Singhose, W. Seering, and N. Singer, "Residual vibration reduction using vector diagrams to generate shaped inputs," *ASME Journal of Mechanical Design*, vol. 116(2), pp. 654–659, 1994.

[90] W. Singhose, N. Singer, and W. Seering, "Comparison of command shaping methods for reducing residual vibration," in *Third European Control Conf*, 1995, pp. 1126–1131.

[91] W. Singhose and J. Vaughan, "Reducing vibration by digital filtering and input shaping," *Control Systems Technology, IEEE Transactions on*, vol. 19, no. 6, pp. 1410–1420, Nov 2011.

[92] W. Singhose, L. Porter, and N. Singer, "Vibration reduction using multi-hump extra-insensitive input shapers," in *American Control Conference, 1995*, 1995.

[93] W. Singhose, L. Porter, T. Tuttle, and N. Singer, "Vibration reduction using multi-hump input shapers," *ASME Journal of Dynamic Systems, Measurement, and Control*, vol. 119(2), 1997.

[94] W. Singhose, W. Seering, and N. Singer, "Shaping inputs to reduce vibration: a vector diagram approach," in *Robotics and Automation, 1990. Proceedings., 1990 IEEE International Conference on*, May 1990, pp. 922–927 vol.2.

[95] O. Smith, "Posicast control of damped oscillatory systems," *Proceedings of the IRE*, vol. 45, no. 9, pp. 1249–1255, Sept 1957.

[96] H. C. So and G. J. Thaler, "A modified posicast method of control with applications to higher-order systems," *American Institute of Electrical Engineers, Part II: Applications and Industry, Transactions of the*, vol. 79, no. 5, pp. 320–326, Nov 1960.

[97] A. Song, J. Wu, G. Qin, and W. Huang, "A novel self-decoupled four degree-of-freedom wrist force/torque sensor," *Measurement*, vol. 40, no. 9–10, pp. 883–891, 2007.

[98] SPIE, Ed., *Optimal design of a mechanically decoupled six-axis force/torque sensor based on the principal cross coupling minimization*, vol. 9061, 2014.

[99] M. W. Spong, "Modeling and control of elastic joint robots," *Journal of Dynamic Systems Measurement and Control-transactions of The Asme*, vol. 104, no. 4, pp. 310–319, 1987.

[100] G. Tallman and O. Smith, "Analog study of dead-beat posicast control," *Automatic Control, IRE Transactions on*, vol. 4, no. 1, pp. 14–21, Mar 1958.

[101] A. Tar and G. Cserey, "Development of a low cost 3d optical compliant tactile force sensor," in *Proc. IEEE/ASME Int. Conf. Advanced Intelligent Mechatronics*, 2011, pp. 236–240.

[102] M. Tomizuka, T. Tsao, and K. Chew, "Discrete-time domain analysis and synthesis of repetitive controllers," in *American Control Conference, 1988*, June 1988, pp. 860–866.

[103] G. Tonietti, R. Schiavi, and A. Bicchi, "Design and control of a variable stiffness actuator for safe and fast physical human/robot interaction," in *Robotics and Automation, 2005. ICRA 2005. Proceedings of the 2005 IEEE International Conference on*, April 2005, pp. 526–531.

[104] N. Tsagarakis, I. Sardellitti, and D. Caldwell, "A new variable stiffness actuator (compact-vsa): Design and modelling," in *Intelligent Robots and Systems (IROS), 2011 IEEE/RSJ International Conference on*, Sept 2011, pp. 378–383.

[105] M. Tsai, G. Anwar, and M. Tomizuka, "Discrete time repetitive control for robot manipulators," in *Robotics and Automation, 1988. Proceedings., 1988 IEEE International Conference on*, Apr 1988, pp. 1341–1346 vol.3.

[106] T. Tuttle and W. Seering, "A zero-placement technique for designing shaped inputs to suppress multiple-mode vibration," in *American Control Conference, 1994*, vol. 3, 1994, pp. 2533 – 2537.

[107] M. Van Valkenburg, *Analog Filter Design*, ser. Oxford series in electrical and computer engineering. Oxford University Press, 1982. [Online]. Available: https://books.google.it/books?id=VMDaJvK5_OAC

[108] J. Vaughan, A. Yano, and W. Singhose, "Comparison of robust input shapers," *Journal of Sound and Vibration*, vol. 315, no. 4Ű5, pp. 797 – 815, 2008. [Online]. Available: http://www.sciencedirect.com/science/article/pii/S0022460X08001375

[109] Y. Wang, F. Gao, and F. J. Doyle, "Survey on iterative learning control, repetitive control, and run-to-run control," *J. of Process Control*, vol. 19, pp. 1589 – 1600, 2009.

[110] S. Wolf and G. Hirzinger, "A new variable stiffness design: Matching requirements of the next robot generation," in *Robotics and Automation, 2008. ICRA 2008. IEEE International Conference on*, Pasadena, CA, May 2008, pp. 1741–1746.

[111] B. Wu and P. Cai, "Decoupling analysis of a sliding structure six-axis force/torque sensor," *Measurement Science Review*, vol. 13, no. 4, pp. 187–193, 2013.